Andrzej GĘBURA, Mariusz ZIEJA

MONITORING THE TECHNICAL CONDITION OF PROPULSION UNIT BEARING ASSEMBLIES AND SELECTED TRANSMISSION COMPONENTS

PUBLISHING HOUSE OF THE AIR FORCE INSTITUTE OF TECHNOLOGY

WARSAW 2024

FIRST EDITION REVIEWERS
prof. Ph.D. D.Sc. Eng. Jerzy GIRTLER
prof. Ph.D. D.Sc. Eng. Paweł LINDSTEDT

SECOND EDITION REVIEWERS
Ph.D. D.Sc. Eng. Rafał KOWALIK, prof. at LAW

TRANSLATION FROM POLISH
TooMuch – pogotowie językowe

TECHNICAL EDITING
Krzysztof BUBRZYK

TYPESETTING
Piotr TARASIEWICZ

COVER DESIGN
Piotr TARASIEWICZ

Photos: archives of the authors, unless captioned otherwise

Project co-financed from the State budget allocated by the Minister of Education and Science under the Programme „Doskonała Nauka II" (Excellent Science II).

Ministry of Science and Higher Education
Republic of Poland

Doskonała Nauka

ISBN 978-83-61021-63-6

PUBLISHING HOUSE OF AIR FORCE INSTITUTE OF TECHNOLOGY
01-494 Warszawa, ul. Księcia Bolesława 6, Poland

Printed at the Air Force Institute of Technology

TABLE OF CONTENTS

Abstract **9**

Basic definitions and designations **13**

Preamble **21**

1. INTRODUCTION **25**

1.1. Requirements and development of integrated aviation safety 25

1.1.1. Determinants and directions of air transport security system integration 25

1.1.2. Maintaining aircraft airworthiness throughout a long-term operation process 26

1.1.3. Methodology for maintaining aircraft airworthiness throughout long-term operation 28

1.1.4. Monitoring the fitness of AC structures 32

1.2. General information on diagnostic methods in aviation 33

1.3. Pros and cons of the FAM-C and FDM-A methods compared to other diagnostic methods 36

1.4. Monograph structure description 46

2. CURRENT STATE OF RESEARCH, ORIGIN OF PRESENTED METHODS AND HYPOTHESES **49**

2.1. Origin of FAM-C and FDM-A discrete and frequency methods 49

2.1.1. Theoretical premises 49

2.1.2. Author's operational experience-based premises 51

2.2. Description of the FAM-C and FDM-A methods 53

2.2.1. Method for obtaining and sampling signals employing AC generators-transducers 53

2.2.2. Instantaneous frequency measurements 62

2.2.3. Method for creating points on a plane (f_p, ΔF) 63

2.2.4. General description of the relationship between a kinematic pair defect parameter and generator-transducer frequency modulation parameters 65

2.2.5. Conditions for the discrimination of primary signal spectrum components in the FAM-C and FDM-A methods 66
2.2.6. Method for signal acquisition and analysis using DC generators-transducers 69
2.2.6.1 General characteristics of DC generator commutator pulsation 70
2.2.6.2. Slot pulsations as a carrier of diagnostic information on the condition of a propulsion unit 74
2.2.6.3. Polar pulsations 75
2.2.6.4. Commutator pulsations 79
2.2.6.5. Compared sensitivity of the FAM-C and FDM-A methods 80
2.2.7. Summarized description of the FAM-C and FDM-A methods 81
2.3. Research hypotheses – diagnostic features of generator-transducers and their application within the FAM-C and FDM-A methods 82
2.3.1. Specific features employed at the primary sampling (electromechanical) stage 82
2.3.2. Specific FAM-C and FDM-A features that can be applied at the secondary sampling stage 90

3. RELATIONSHIPS BETWEEN INDIVIDUAL DEFECTS OF MECHANICAL PROPULSION UNIT KINEMATIC PAIRS WITH FAM-C AND FDM-A IMAGING 97

3.1. Typical mechanical defects in simple machines and their reflection within instantaneous speed waveform and narrowband characteristic sets 97
3.1.1. Eccentricity of connections without circumferential backlash 97
3.1.2. Eccentricity of connections with circumferential backlash 99
3.1.3. Circumferential backlash of a kinematic pair in the universal sense and its imaging using the FDM-A method 102
3.1.4. Circumferential backlash of gear wheel pairs and splined connections 103
3.1.5. Mechanical connection skewing 105
3.1.6. Simultaneous action of skewing and eccentric displacement 111
3.1.7. Summary of considerations in relation to narrowband mechanical faults 114
3.2. Broadband mechanical defects 115

3.2.1. Slide of rolling bearing rolling elements and rolling coefficient 116
3.2.1.1. Motion geometry of a “perfect” rolling bearing 116
3.2.1.2. Slide and rolling coefficient. Their significance for the rolling bearing classification criterion 120
3.2.2. Misalignment and miscylindricity of shaft bearing supports 123
3.2.2.1. Misalignment of shaft bearing supports 123
3.2.2.2. Miscylindricality of shaft bearing support seats 124
3.2.3. Rolling bearing spacer-cage falling onto the inner race 126
3.2.4. Rolling bearing resonance and its reflection in the FDM-A characteristic set shape 131
3.2.5. Condition arising from an excessively tightly clamped rolling bearing and its reflection in the shape of characteristic sets 136
3.2.6. Condition of excessive internal passive rolling bearing anti-torques and its reflection in the shapes of characteristic sets 141
3.2.7. Spacer sleeve fracture 143
3.3. Selected mechanical defects manifested by stochastic quasi-pulsed motion dynamics phenomena 145
3.3.1. Spontaneous decoupling of one-way couplings 146
3.3.2. Air lock phenomena within the rotational speed controller hydraulic systems 149
3.3.3. Breaking out of rolling bearing separation elements and cracking of the spacer-cage perimeter 150
3.3.4. Breaking out of a transmission gear tooth 151
3.3.5. Broken clamp fit between the rolling bearing ring and shaft or bearing seat 153
3.4. The role of a mechanical failure catalogue in propulsion unit diagnosis 156

4. METROLOGICAL PROPERTIES OF THE FAM-C AND FDM-A METHODS 157

4.1. Overall metrological structure of the FAM-C and FDM-A methods 157
4.2. Primary sampling – electromechanical 162
4.2.1. Primary sampling not taking mechanical transmission backlash into account 162

4.2.2. Primary sampling taking mechanical transmission backlash into account ... 170
4.2.3. Primary sampling for multi-phase measurement systems ... 171
4.3. TTM secondary sampling ... 172
4.3.1. General issues associated with secondary sampling within the FAM-C and FDM-A methods ... 172
4.3.2. Signal conditioning system – error analysis ... 173
4.3.3. The role of a meter sheet and its interaction with a computer within a FAM-C and FDM-A measurement system ... 174
4.3.4. Selected issues from the theory and practice of the frequency measurement technique ... 177
4.3.5. The possibilities of synchronizing the measurement chains of two different generator-transducers ... 179
4.3.6. Impact of generator-transducer voltage signal interference on the secondary sampling error ... 183
4.3.7. Possible applications of quadrature modulation in the FAM-C and FDM-A methods ... 188
4.4. Significance of FAM-C and FDM-A method metrological properties in verifying study hypothesis – summary ... 190

5. APPLICATION OF THE FAM-C AND FDM-A METHODS WITHIN THE TECHNICAL OBJECT MONITORING PROCESS ... 193

5.1. Scope of FAM-C and FDM-A method implementation in relation to actual objects ... 193
5.2. Diagnostic systems and semi-automatic diagnostic testers for assessing the technical condition of aviation propulsion units ... 196
5.2.1. SD-KSA diagnostic system and DIA-KSA-CM diagnostic tester for the propulsion unit of a MiG-29 aircraft ... 197
5.2.1.1. Technical description and operation of the DIA-KSA-CM diagnostic tester ... 197
5.2.1.2. Description of the SD-KSA diagnostic system ... 199
5.2.2. DIA-SO3 diagnostic tester for the propulsion unit of a TS-11 Iskra aircraft ... 201
5.2.2.1. Operation algorithm of a DIA-SO3 diagnostic tester ... 201
5.2.2.2. Tester tribological process recognition algorithm ... 207
5.2.2.3. DIA-SO-3 diagnostic tester structural description ... 210
5.3. Monitoring military aircraft propulsion units at airfields ... 214

5.3.1. Detecting a damaged bearing in the Mi-24 helicopter main rotor shaft using the FAM-C method 214
5.3.2. Diagnosing the Mi-24 generator gearbox 218
5.3.3. Detecting a damaged bearing of a Mi-17 helicopter swash plate 223
5.3.4. Using the FAM-C method to detect increased circumferential backlash of a Mi-17 helicopter swash plate mobile disc synchronizer 226
5.4. Using the FAM-C method to measure non-aviation propulsion units 231
5.4.1. Studying the propulsion units of marine power plants 231
5.4.1.1. Description of a marine power plant and its diagnosis capacity with the FAM-C method 231
5.4.1.2. Three-phase measurements of the Pomerania ferry propulsion unit 233
5.4.1.3. Single-phase measurements of the Polonia ferry propulsion unit 235
5.4.2. Studying electromechanical transducers 236

6. STUDYING THE TRIBOLOGICAL PROCESSES IN ROLLING BEARINGS USING THE FAM-C AND FDM-A METHODS 247

6.1. Basic wear models for single-shaft engine bearings based on empirical studies, taking into account their monitoring with the FAM-C and FDM-A methods 247
6.1.1. Model of increased passive resistance 248
6.1.2. Model of rolling elements clamped between races 253
6.1.3. Model of increased radial clearance 255
6.1.4. Model of increased longitudinal clearance 258
6.1.5. Rolling bearing tribological wear test result summary – potential assessment of the current technical condition 262
6.2. Long-term tribological wear processes and their monitoring using the FAM-C and FDM-A methods 263

7. SUMMARY OF STUDY RESULTS – CONCLUSIONS AND FINAL REMARKS 269

7.1. General monograph content summary 271
7.1.1. The concept behind the FAM-C and FDM-A methods 271

7.1.2. Catalogue of mechanical failures and their reflections in FAM-C and FDM-A 274
7.1.3. Metrological properties 274
7.1.4. Implementations and applications of the FAM-C and FDM-A methods 276
7.1.5. Studying bearing node tribological processes and their changes using the FAM-C and FDM-A methods 280
7.2. Final conclusions – FAM-C and FDM-A methods as a novel element in the scientific theory 281
7.2.1. General remarks 281
7.2.2. FAM-C and FDM-A methods vs the theory of signals 283
7.2.3. Onboard generator as a diagnostic transducer 284
7.3. Practical aspects of the FAM-C and FDM-A methods 285
7.4. Final remarks 285

REFERENCES 287

LIST OF FIGURES 309

LIST OF TABLES 319

"...everyone believes the test results, except the person who made the measurements, and nobody believes the theoretical results, except the person who calculated them..."

Gareth D. Padfield

ABSTRACT

The monograph discusses novel methods for monitoring destructive phenomena ongoing within mechanical propulsion units. It contains a description of these discrete and frequency-based methods and numerous issues related to the motion of various mechanical elements and subassemblies (e.g., rolling bearings), the observation of which they enable. A practical application of these methods allows a more accurate investigation of the tribological processes and other phenomena associated with machine dynamics. Accordingly, an onboard direct or alternating current generator takes on the role of monitoring the technical conditions of the powerplant (engine with bearing supports propulsion unit+ mechanical power transmission elements + mechanical power consumers). Due to the different properties of these generators, two research methods were developed: FAM-C for an alternating current generator and FDM-A for a direct current generator. These methods do not require any additional sensors, but rather utilize the power or rate generators existing within the object structure (intended for completely different purposes). The methods are based on the TTM (*tip timing method*[1]) idea proposed by Campbell in 1924 [37, 302] to monitor steam turbine blade deflections, also applied later in practice in radiolocation and diagnostics. However, none of the known TTM-based diagnostic methods employs an onboard generator as a diag-

[1] In Polish and Russian source literature [303, 274], TTM is known as the discrete-phase method.

nostic transducer. Moreover, TTM utilizes sensors [39, 145, 151, 298, 307] (reluctance, optical, eddy current, capacitive, microwave) assigned to individual (single) mechanical sub-assemblies. In the case of FAM-C and FDM-A methods, a single generator-transducer can simultaneously provide data on the technical conditions of numerous (virtually all) mechanical nodes. These can also be displayed as separate characteristic sets. This feature can be called the method's "versatility". Every generator type exhibits the properties of a band-pass filter for the observed motion dynamics processes within individual mechanical sub-assemblies.

Every generator type, depending on the design, has a specific observable band, hereinafter referred to as the "observable window". At the same time, mechanical nodes, particularly aerospace propulsion units, have very diverse[2]: bands related to their motion dynamics and rated frequencies (called "subcarrier frequencies" [3]) related to the rated rotational speed specified in the kinematic diagram. Therefore, a single generator is able to cover only some of these mechanical nodes with its observable window. Usually, the observable window is for lower frequency bands in alternating current generators, and higher bands in direct current generators. In order to expand the monitoring capacity onto a greater number of mechanical nodes of a given propulsion unit, the authors suggest to execute diagnostic measurement employing several types of onboard generators simultaneously. They also propose different measurement set-ups for individual generators, modifying their observable band. This allows to control the monitoring capabilities of the various propulsion unit components, the observation resolution and the observable band window of their motion dynamics.

The initial diagnostic signals of individual kinematic pairs are synchronised with their rated frequencies, hereafter referred to as "subcarriers" [3]. These relationships are maintained after being converted to a higher frequency band by a generator-transducer acting as a modulator (frequency mixer) and amplifier (electromechanical) [100, 101, 189]. Moreover, transformed primary diagnostic signals (angular velocity modulations) are converted into voltage signals synchronously. In addition, stator pole pieces and rotor slots form a peculiar generator vernier. Signal conversion synchronicity and the aforementioned vernier enable achieving much higher sensitivities and resolutions than in other TTM-based diagnostic methods. The FAM-C and FDM-A methods may be applied to easily determine the technical condition and the associated, so-called "mechanical quality factor" of individual propulsion unit mechanical nodes. In consequence, one can detect local and

[2] Band diversity – this applies both to the diversity of the rated frequencies of various components (e.g., a helicopter propulsion unit from 4 Hz for the propeller shaft of the carrier, to 40 kHz for the compressor shaft) and to the emitted bandwidth (e.g., a faulty rolling bearing may emit a frequency spectrum much wider than its rated frequency).

structural resonance [123]. The onboard generator is therefore a good tool for observing and identifying the technical conditions of both individual kinematic pairs and entire propulsion units. This is confirmed by active and passive experiments involving actual objects. The authors present numerous practical applications for these methods within the process of diagnosing bearing nodes and propulsion unit transmission elements. Their observations on the dynamics of the sub-assemblies, as well as the various types of failures, have been organised herein – into groups, depending on the relative band occupied by individual sets of characteristic points generated by the sub-assembly. The monograph also presents a systematic approach to recognising the rolling bearing tribological wear model and criteria for assessing its technical conditions based on parameters obtained from generator-transducers. All bearing characteristics are determined for several, consecutive rated rotational speeds. Therefore, diagnostic observations of individual kinematic pairs with the FAM-C and FDM-A methods are conducted within a 3D space:

- frequency deviation ΔF [Hz],
- modulation process frequency f_p [Hz],
- rated speed n [rpm] of a given propulsion unit drive engine main shaft.

The introduction of a third 0-n axis enables observing changes within a number of tribological processes, such as the impact of hydromechanical forces on rolling elements or the emergence and development of resonant processes within the moving elements of rolling bearings. In the case of issues related to long-term tribological processes of rolling bearings, the authors also introduce a fourth axis – operating time θ [h]. Owing to the introduction of this axis, changes in the type of tribological model and, hence, changes in the technical conditions for the same bearing in the course of its operation have been observed on real objects.

The FAM-C and FDM-A methods do not eliminate other diagnostic methods (e.g., vibroacoustic) from the diagnostic process, but rather supplement them. However, in the case of many facilities and many significant phenomena associated with the motion dynamics of mechanical power transmissions systems and their monitoring, in the future, they can become leading methods in diagnostic tests. What is more, they easily undergo automation and computer processing. Therefore, it is easy to construct onboard and ground diagnostic systems, as well as systems warning and prompting about a threat to the mechanical structure of a propulsion unit. As it turns out, these methods can be employed in relation to all types of propulsion units, coupled structurally with a DC or AC generator, a rate generator or a motion sensor with a voltage output. Modulated diagnostic information is transmitted via the onboard electrical network between the generator-transformer and the measuring system, therefore, a measuring device based on the FAM-C and FDM-A methods can be hooked-up to any point on the electrical grid. This is an important ergonomic and economic aspect that increases the possibility of applying these methods

to diagnose hazardous or difficult-to-access areas, which are characterised by high temperatures, significant heights (relative to the ground), high pressure and hindered access to the component (clustering of many mechanical or electrical components around it). FAM-C and FDM-A methods do not require any additional sensors – therefore, they are fast in test set-up and non-invasive in operation.

BASIC DEFINITIONS AND DESIGNATIONS

A. BASIC TERMS

Diagnostic test – test of an object (its features) aimed at gathering information required to determine the technical conditions of the object or its elements.

Comprehensive test – test of a propulsion unit mounted on an aircraft or vessel under actual conditions.

Characteristic set height characteristics – a graph (e.g., bar chart) illustrating the heights of characteristic sets as a function of the main propulsion engine shaft speed rating or bearing journal speed.

Bathtub characteristics – characteristic set height characteristics, where the envelope of their vertices (bars) resembles the cross-section of a bathtub (this concept is taken from the object failure probability theory).

Resonant characteristics – characteristic set height characteristics, where the envelope of their vertices (bars) resembles the characteristics of an electrical resonant circuit – there is a noticeable uplift of the characteristic set height in relation to average main propulsion engine shaft rotational speed or bearing journal rotational speed values.

Average frequency – arithmetic mean for the generator output voltage instantaneous frequency set within in the course of a diagnostic observation.

Kinematic pair rated frequency – the frequency of the first harmonic of a given kinematic pair.

Kinematic pair sub-carrier frequency – the frequency arithmetically equal to the value of the kinematic pair rated frequency.

Generator rated frequency – generator output voltage frequency at rated rotor speed in a steady state.

Frequency modulation process frequency – the inverse doubled duration of the generator output voltage instantaneous frequency waveform deviation from the average frequency.

Mechanical process frequency – a given kinematic cell or mechanical component angular velocity change output frequency, manifested as changes (fluctuations) in the instantaneous angular value around the rated speed value of that cell (component).

Diagnosis – results of a diagnostic test; a credible hypothesis on the technical condition of an object.

Power plant mechanical monitoring – a type of diagnostic process wherein a condition check is repeated periodically (periodic or aperiodic) in order to detect a failure in the inspected mechanical propulsion unit soon enough after it has occurred, so as not to jeopardise operation safety.

Harmonic (harmonic component) – the Fourier component of an analysed signal – a waveform component with a frequency that is the total multiple of the fundamental frequency.

Instantaneous frequency decay pulse – a pulse of an instantaneous frequency waveform, the amplitude of which is less than the rated frequency level.

Mechanical power unit – in this monograph, this means a mechanical unit comprising a primary power source (e.g., engine gas-dynamic turbine), mechanical power transmission elements (gears, couplings, transmission shafts, gears), bearing supports, and mechanical power consumers (hydraulic, fuel pumps and oil pumps, onboard generators, tachometric generators, a propeller).

Mechanical propulsion unit monitoring - tracking changes in the parameters of the tested mechanical propulsion unit.

Instantaneous frequency deviation from average frequency – the fragment of generator output voltage instantaneous frequency waveform of unilateral "departure" from the average frequency level until returning.

Kinematic pair – two mechanical elements (or sub-assemblies) of a propulsion unit capable of transmitting mechanical energy.

Shaft generator – in shipbuilding, a generator coupled kinematically with a screw propeller shaft.

Onboard generator – in aviation, a generator powered by a given propulsion unit.

Generator output voltage instantaneous frequency waveform – a discrete waveform of instantaneous frequency values as a function of time.

Instantaneous frequency value – the inverse duration of a successive instantaneous value passage through the zero level.

Slot pulsation – the course of changes to the generator output voltage variable component instantaneous value caused by a reluctance change (magnetic resistance) induced by the rotation of a toothed rotor within the stator magnetic field.

SBK – the total error in the value of the parameter characterising the shape of a mechanical component relative to the shape parameter set out in the design documentation [73].

Observable band – the band of the primary signal (herein: kinematic pair angular velocity speed fluctuations) range (harmonics) observed by the measuring and diagnostic system.

Characteristic points – points on the plane of rectangular coordinates, wherein the ordinates are the extreme values of the i deviation of the instantaneous frequency (generator output voltage) from the average frequency, and the abscissa is the process frequency of the i deviation of the instantaneous frequency.

Characteristic set band – the distance Δf_{p} measured in the horizontal axis between the extreme points of a given characteristic set j:

$$\Delta f_{pj} = \left| \{\Delta f_{pj}\}_{\max} \right| - \left| \{\Delta f_{pj}\}_{\min} \right|$$

Kinematic pair defect – a condition caused by manufacturing and assembly errors or tribological wear throughout the service life of a propulsion unit.

Rolling bearing rolling coefficient – the ratio of average angular velocity of the rolling element (shaft) main axis of symmetry relative to the bearing symmetrical centre and the angular velocity of that bearing's journal. In practice, it is the quotient of the angular velocity of the cage to the velocity of that bearing's journal.

Rolling characteristic "dynamic tilt" coefficient – the quotient of the maximum rolling coefficient and minimum rolling coefficient for each rotational speed in the course of successive measurement exposures.

Technical requirements – official (approved) listing of technical parameters required for the correct manufacturing and operation of an element, sub-assembly, device or technical system, developed by the manufacturer or user.

Characteristic set height – the distance ΔF measured in the vertical axis between the extreme points of a given characteristic set j:

$$A_j = \left| \{\Delta F_i\}_{\max} \right| - \left| \{\Delta F_i\}_{\min} \right|$$

Primary diagnostic signal interference – action of external factors and internal changes within a measurement chain and object impacting a measurement chain and object, leading to a negative diagnostic measurement result.

Kinematic pair characteristic set – set of characteristic points describing a j kinematic pair.

B. BASIC DESIGNATIONS

B1. Mechanical motion kinematics and dynamics

t – time [s];
s – Laplace′ operator;
ϑ – instantaneous angular position [rad];
$\dot{\vartheta}, \ddot{\vartheta}$ – first and second rotation angle derivative [rad/s; rad/s^2];
$\omega(t)$ – kinematic pair or subassembly (e.g., shaft, gear) kinematic pair instantaneous velocity as a function of time;
$\omega(s)$ – kinematic pair or subassembly (e.g., shaft, gear) velocity as an operator;
M_n – driving torque [N·m];
M_o – preset (source) torque [N·m];
M_t – friction moment [N·m];
W_ω – peculiar matrix determinant (relative to variable ω);
W_Δ – general matrix determinant;
n_N – generator rotor rated speed [rpm];
n_{smax} – engine main shaft maximum speed [rpm];
n_{smin} – engine main shaft minimum speed [rpm];
ω – instantaneous angular velocity [rad/s];
p_s – rolling bearing rolling coefficient;
$p_{smaxmax}/p_{sminmin}$ – rolling characteristic “dynamic titl” coefficient;
T_{np} – rated fluctuation period of a given kinematic pair;
f_p – mechanical process frequency;
f_{pN} – (observed) mechanical process rated frequency; kinematic fringe rate frequency.

B2. Mechanical element structural values

β – skewing angle between the rotation angle of a propulsion element and the rotation angle of the driven element [°];
a – linear displacement between the rotation angle of a propulsion element and the rotation angle of the driven element, measured within the rotation plane (eccentricity) [m];
J_1 , J_2 – mass inertia moments [kg · m^2];
k – elasticity coefficient [rad/N · m];
Dj – viscous damping coefficient of the j kinematic cell [N·m·s/rad];
z – toothed wheel teeth number;

d_{pr} – generator shaft diameter [m];
D_N – propulsion seat sleeve internal diameter [m];
m – toothed wheel modulus;
i – number of subsequent crossing of the onboard generator output voltage waveform through level "zero"
j – number of kinematic pair or subsequent waveform deviation $f_i(t)$ from the reference level (usually from $f_{śr}$);
d_k – rolling bearing rolling element diameter;
D_w – rolling bearing internal race diameter.

B3. Electric and magnetic values

B – magnetic induction in the gap between the stator pole piece and generator rotor [T];
I – current intensity [A];
l – length of section (coil frame) within the stator magnetic field [m];
f_{pi} – frequency of a "mechanical process" (modified angular velocity of a given kinematic cell) for the i sample of a characteristic set [Hz];
ΔF_i – amplitude of the i instantaneous frequency deviation (generator output voltage) from the average frequency [Hz];
$f_{śr}$ – average frequency – arithmetic mean of the set of instantaneous frequency values [Hz];
t_{odi} – duration of the i instantaneous frequency deviation from the average frequency [s];
p – number of generator pole pairs;
K – number of generator commutator segments;
$\dot{Z}$ – number of generator rotor slots;
E – electromotive force (EMF) effective value [V];
e – electromotive force (EMF) instantaneous value [V];
U_{max} – maximum voltage [V];
U_N – rated effective voltage [V];
AC – alternating current;
DC – direct current;
T_{NG} – generator output voltage waveform duration;
1fAC – single-phase measurement of the AC measurement chain (FAM-C method);
3fAC – three-phase measurement of the AC measurement chain (FAM-C method);
$u(t)$ – voltage analogue waveform;

$U_{\sim}$ – direct current generator pulsation component (AC component) amplitude value;

U= – direct current (DC) generator output voltage constant component value;

o – natural number – subsequent polar pulsation period number.

B4. Signal theory, radio engineering and electronics values

FM – frequency modulation;

AM – amplitude modulation;

LF – low frequency – in this study, the primary diagnostic signal, i.e., a spectrum of frequency components in the waveform of the instantaneous angular velocity of individual kinematic pairs within a studied propulsion unit;

HF – high frequency – in this study, the rated frequency of the generator – transducer;

$f_{poj} \equiv f_{Nj}$ – carrier frequency of a given j characteristic set – in the source literature of the radioengineering domain [3, 32] also called the "signal sub-carrier frequency", and the "kinematic frequency" in the diagnostic source literature [25, 85];

Δf_{pj} – bandwidth of the j characteristic set (designated with the $\boldsymbol{B}_{\mathbf{j}}$ letter, as in *band*, in the source literature on radioengineering);

κ – amplifier gain.

B5. Other designations, symbols and abbreviations

DSS – engine control lever;

SIL – Engineering-Air Service (aircraft user);

SHM – structural health monitoring;

TTM – (*tip timing method*); a method for monitoring the dynamics of a rotating machine based on a synchronous signal associated with rotating mechanical elements (compressor or turbine blade, toothed wheel gear) generating "time markers", which enables calculating time increments between successive passages of rotating mechanical elements, i.e., secondary discrete determination of rotating machine subassembly motion dynamics;

TOA – time of arrival – time increment between "time stamps";

TR – technical requirements;

K – number of tests or the successive test number for a given tested propulsion unit;

Θ – duration of a single test or total operation time of a tested propulsion unit;

Θ_k – time counted from the start of operation until the last overhaul of a tested propulsion unit, followed by a k diagnostic test;

$\Delta\Theta$ – operation time of a tested propulsion unit between successive diagnostic tests;

A – height of the characteristic set determined on the plane (f_p, ΔF);

A_j – height of the j characteristic set determined on the plane (f_p, ΔF);

A_o – height of a characteristic set with the frequency of the engine main shaft speed first harmonic frequency modulation process;

A_{05} – height of a characteristic set with the frequency of the engine main shaft speed first subharmonic[3] frequency modulation process;

[3] First subharmonic process frequency – frequency f_p equal to the value of the first subharmonic frequency of engine main shaft speed $\boldsymbol{n}_N$ or bearing journal speed ($f_p = 0.5 \cdot \boldsymbol{n}_N/60$).

PREAMBLE

The development of watercraft and aircraft for transporting people and/or commodities is an indisputable economic, social and military necessity. For the purposes of making these measures safe and, at the same time, economical, carriers are interested in installing reliable diagnostic and monitoring systems, in relation to propulsion units, in particular [10, 13, 177, 190, 226, 234, 290]. In the race for speed and payload, propulsion units are experiencing increasing burdens and, therefore, continuous improvement of their diagnostic systems is of fundamental importance. The diagnostic system (installation) must have sensors and parameter transducers. Currently, there are a significant number of different types of sensors and transducers associated with various parameters on the market. It is, therefore, not a technical issue to route their signals to the aircraft or watercraft crew commander cockpit. However, such a proliferation of different types of indicator instrumentation was severely criticised and inhibited as early as the late 1960s. The pilot, especially a military pilot, burdened with numerous activities, was even then unable to concentrate on analysing aircraft technical structure. Therefore, a clear trend towards the automation of danger alert systems for pilots began already.

By the end of the 1970s, conflicts of local importance were being considered to be of strategic relevance. Therefore, the operation of military aircraft had to be cheaper and predictable. Onboard diagnostic systems (installation) were also supposed to provide much greater failure detection and long-lasting operation. These aspirations evolved into a structural strategy of operation based on technical conditions [234, 303, 290]. In this case, diagnostic systems (onboard and ground-based) were to support technical maintenance to such an extent that replacements and overhauls of onboard units were to be kept to a minimum. Therefore, scheduled overhauls linked strictly to the number of flight hours or the calendar period of operation were to be eliminated.

All this came about because it turned out that units in sound technical conditions were often sent for overhaul, while at the same time, dangerous system failures occurred as a result of damage to similar units in the period between the overhauls. Simultaneously during this period in aviation, the flight capability of new

aircraft designs became increasingly dependent on the fitness of the propulsion unit. The problem involved increasing take-off, cruising and rate of climb speed and flexibility. To this end, the designers had to adjust the aerodynamics of the aircraft's airframe (slanted edges of attack of the lifting airfoils and reduced lifting airfoil surface to reduce aerodynamic drag forces). In such a situation, glide (often applied in older aircraft designs) was severely restricted in situations of power unit failure. These relationships were certainly an important cause behind the development of HUMS *Health and Usage Monitoring System*) [7, 9, 95, 316].

It quickly became apparent that a helicopter was much more dependent on the fitness of a propulsion unit than an airplane. Armed conflicts of the last two decades based on the operations of relatively small infantry forces have prioritized helicopters, particularly in areas with significant terrain obstacles, such as mountainous regions. The critical issue in helicopters is the strong dynamic impacts of main rotor blade vibrations, (specific vibrations, the impact of aerodynamic forces, ground resonance resulting) due to forward speed (helicopter fuselage) overlapping the main rotor blade airflow speed during rotational movement [13, 225]. The accumulation of these two phenomena is an important aspect in the accelerated wear of the broadly understood propulsion unit (engine + transmission system + lift system + flight control system). It should be added that, while the carrier force generation phenomenon in an aircraft has almost no effect on the propulsion system, the two are closely linked in the case of a helicopter. Therefore, when a helicopter starts a climb or changing flight direction, the dynamics of the forces impacting numerous nodes of the propulsion unit – the transmission shafts, numerous gearbox components and the control disc bearing – increase. The opposite relationships are also observed – if mechanical components of the propulsion unit become abnormally worn, this may lead to extraordinary vibrations of anomalously high amplitude disturbing flight aerodynamics or to a deterioration of control precision. When the transmission elements transmitting propulsion to the tail rotor wear out, this entails hindrances in maintaining flight direction [7, 13, 95, 225].

A helicopter with an engine failure can theoretically land based on so-called "autorotation", similar to the gyroplanes developed in the interwar period. This requires full fitness of control elements and, above all, a significant altitude reserve. This is a difficult operation, which is sometimes impossible for combat helicopters that are often tasked with supporting infantry at low altitudes or for deployment. This even more necessitates developing propulsion unit monitoring and diagnosing systems.

In practice, a HUMS comprises sets of vibroacoustic sensors (and, also, temperature sensors) arranged at crucial locations. The CH-47 Chinook helicopter has the best-developed system with numerous piezoelectric sensors deployed by the propulsion motors of both transmissions and along the control assemblies, as well as near the control discs [95, 316,303].

The vibroacoustic method is, however, burdened with numerous structural errors. Firstly, the primary vibroacoustic signal passes through a variety of centres – air layers, seals, oil film layer – which weaken its energy [40, 39, 208]. Some of the energy, in turn, passes from the source to the signal receiver via a circuitous route through very good vibration conductors (e.g., through a gearbox casing metal segments), but become mixed due to interference with numerous other vibroacoustic signals of no diagnostic interest. Furthermore, components that are not relevant from the diagnostic perspective (e.g., housings), often exhibit mechanical vibration filtering properties. These have their own resonant frequencies (natural frequencies) – band-wise amplification of the primary diagnostic signal harmonics near the resonant vibration frequency of this component takes place. In turn, within the remaining frequency range, the spectrum of the vibroacoustic signal is attenuated.

Such filtering of mechanical vibrations can significantly distort the spectral distribution of the vibroacoustic kinematic pair. In addition, in the case of a highly spatially packed sub-assembly, e.g., an aviation reducer, it is difficult to identify individual kinematic pairs due to the geometric densities of the diagnostic signal primary sources. With minute distances between the sources of vibroacoustic signals and relatively large distances of the embedded receiver from individual sources, the individual signal spectra are more likely to interfere with each other. Therefore, the authors believe that the HUMS system is an opportunity for applying FAM-C and FDM-A methods [95, 98].

The generator-transducer provides data on the technical conditions of multiple mechanical nodes simultaneously, and this is depicted in the form of separate characteristic sets, easily applicable within automatic signalling systems. Furthermore, in the case of the FAM-C method, using natural summation nodes and tracts of the mechanical propulsion chain of the various kinematic cells, the primary signal is converted to higher electrical vibration frequencies within the original (same) propulsion unit by means of a generator-transducer that constitutes an integral part of the tested mechanical propulsion unit (Fig. 1.1) [100, 129, 101]. Herein, the original spectral oscillations of individual mechanical kinematic pairs become the modulator for the generator-transducer output signal.

As in the case of a radio broadcasting station, the diagnostic information of certain kinematic pairs may be somewhat impoverished during modulation (in a generator-transducer), since each type of a generator-transducer has its own passband (electromechanical filtering). At the same time, such an operation of shifting the original diagnostic data ensures its protection against various interference types. In practical terms, complete immunity of the transmitted signal against mechanical modulations is achieved through further transmission (through the medium of the onboard electrical network) – the electrical wires can pass freely close to other mechanical assemblies, while those contained in the electrical signal (FM electrical

modulations) are immune to all kinds of mechanical vibrations or angular velocity modulations in relation to these mechanisms.

Measurements with the FAM-C or FDM-A methods involve reading the frequency-modulated voltage signal from the onboard electrical network, followed by its mixing with the measuring system internal clock pulses. This is, in turn, followed by detection. Individual kinematic pair vibration spectra are "unpacked". It should be noted that each kinematic pair of a mechanical propulsion unit has its own lift frequency. This is nothing else but the rated speed of the respective kinematic pair and can be easily retrieved from the kinematic diagram or from the technical specification of the respective propulsion unit type. Subcarrier frequencies [3], i.e., the rated frequencies of individual kinematic pairs, are also recovered during demodulation. This enables identifying individual vibration spectra. The ability to easily identify individual kinematic pairs under the FAM-C method is a major advantage. Sensors in the usually applied vibroacoustic methods are rarely attached directly to a tested kinematic pair. In most cases, the sensors are mounted to the housing of such a kinematic pair or some other accessible area of the airframe or propulsion unit structure. Therefore, vibroacoustic systems exhibit major problems in identifying the components of received signals with assignment to individual kinematic pairs [39, 40].

In order to assess individual mechanical nodes as comprehensively as possible, the authors measured the parameters at successive rotational speeds of the engine main shaft. They thus obtained whole families of characteristics that are rotational speed functions. Hence, a kind of discrete variation of the observed parameters measured by the FAM-C and FDM-A methods as a function of rotational speed, takes place. This is necessary due to the impact of the oil film on the tribological processes [55, 177, 179, 261]. It enables tracking, among others, tribological processes depending on the rotational speed [113, 119, 120], and the observations enable developing a particular catalogue of tribological dependencies.

1

INTRODUCTION

1.1. Requirements and development of integrated aviation safety

"Safety" is usually construed as the lack of a hazard, and a state of calmness and certainty. Safety in transport is a system property that allows transport operations to be implemented under given environmental conditions and without accidents or adverse events. Operational security of technical systems is a new emerging scientific discipline and therefore has relatively poorly established basic concepts, standards and measures. Studying safety hazards and assessing safety condition remain open issues.

1.1.1. Determinants and directions of air transport security system integration

The process of improving security in transport is a complex activity that requires coordinating the work of various professional groups. In designing large and complex technical and organisational systems, transport being one of those, ensuring an adequate level of safety is as important as achieving transport readiness. Studying system safety status can most generally be reduced to an analysis of the following factors:

- the risk of safety threats arising within the transport system and its environment;
- the ability of a transport system to deal with hazards involved and the ability of external emergency systems to deal with the consequences of those hazards;

- the inter-relationship between a safety risk and the effectiveness of counteracting and mitigating the effects of the incident that has occurred.

Individual transport modes have different units investigating and monitoring the safety status and various ways of managing it. All this leads to a multitude of partial safety management systems, each with different definitions and interpretations of basic concepts, standards, regulations and even causes of incidents, and a preference for different risk prevention measures. The ambiguity in definitions and interpretation of terms indicates that there is a need to review, compare and evaluate:

- safety management methods,
- standards and organisational structures,
- safety measures.

For overall society-related reasons, as well as for economic reasons, the solutions recognized as best by the milieu should be adapted to individual transport modes and put into practice. This will result in improved effectiveness of transport safety measures and, consequently, an increase in the quality of life.

In the case of aviation, there are notable safety risks originating from the environment and from ground-based flight safety systems. These include:

- air and terrain obstacles, as well as bird overflights surprising the pilot,
- erroneous airspace management,
- unexpected weather and visibility changes,
- inadequate supplies (fuels, utilities),
- inadequately prepared aerodromes (take-off and landing runways),
- improperly functioning airport infrastructure,
- ineffective aircraft diagnostics.

All the above-mentioned safety components and the methods of analysing, in particular, them, can be integrated.

1.1.2. Maintaining aircraft airworthiness throughout a long-term operation process

A major challenge for aeronautical companies is the ageing fleet of aircraft (AC). Examples include, for example, two US companies: Midwest, where the average age of aircraft in service is 26 years, and Northwest, where it is 20 years. Aviation companies are usually guided by economic considerations when deciding to operate aircraft (AC) with service lives longer than those established at the design stage. The primary condition to be satisfied when extending AC service life is to ensure an acceptable flight safety level. Increasing hourly- and calendar-based operation times lead to the appearance of various ageing process consequences that undermine the structural and functional integrity of advanced-age AC. To this end,

integrated programmes are agreed between the user and the industry to extend the AC service life. This task includes assessing the equipment and its components, the impact of ageing issues on structural and functional integrity, and the influence of ageing-related failures on flight safety. Revised restrictions, inspection schemes and maintenance regimes are developed to enable formal AC certification in relation to the extended service life.

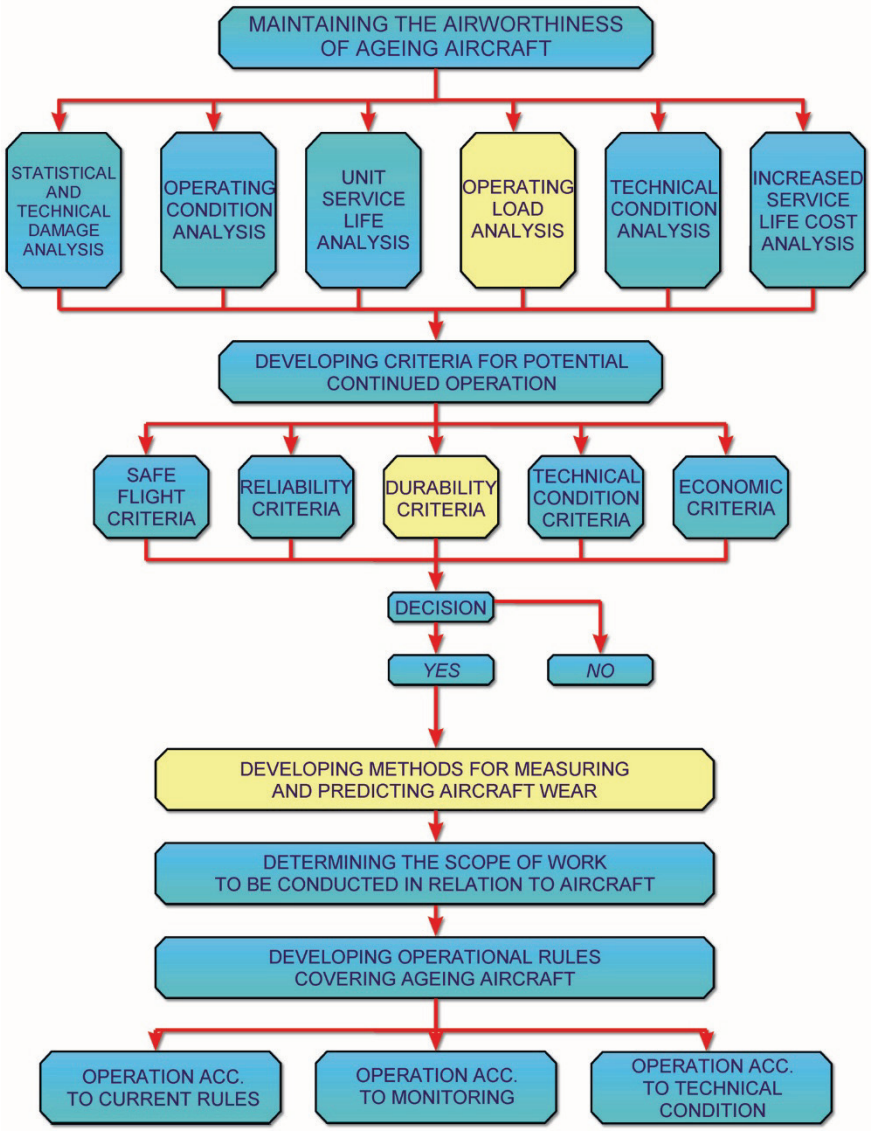

Fig. 1.1. Algorithm to maintain the airworthiness of ageing AC (developed by AFIT)

Plans of ventures associated with long-term AC operation include, among others (Fig. 1.1):

- modernising the existing operating system (including, but not limited to, analysis and forecasting of reliability and safety indicators, economic analysis (cost analysis), operating conditions (including loads), analysis of residual life of assemblies and units, technical condition analysis, modernisation of maintenance procedures,
- ensuring structural integrity (e.g., fatigue tests, localization of corrosion, forecasting corrosion development, non-destructive testing, analysing the form and effects of damage),
- ensuring subsystem integrity (e.g., testing and possible replacement of electrical networks for flight-critical subsystems).

1.1.3. Methodology for maintaining aircraft airworthiness throughout long-term operation

Methodology for maintaining aircraft airworthiness throughout long-term operation (AASP - Ageing Aircraft Systems Program) was developed with the intention of studying ageing aviation technology in a proactive manner to enhance operation safety. Despite the fact that the methodology focuses on an aviation group defined as ageing, it should be noted that all categories of failure events should be taken into account, not just those designated as ageing- or wear-related failures. The AASP methodology proactively mitigates risk associated with ageing aviation technology that has accumulated significant service life since the initial assessment during structural design and certification.

Description of the methodology for maintaining AC airworthiness throughout long-term operation

The AASP methodology is an approach applied to study ageing aircraft technology in order to better understand the current risks that may occur in relation to aircraft systems. AASP can serve as a standardised, proactive approach to managing ageing aircraft. A simplified diagram of the AASP is shown in Fig. 1.2. This diagram is the best description of the methodology without going into detail on the individual activities and assessment criteria. The activities that supplement the process include complex steps concerning data collection, analyses, risk assessment and documentation. They are described later in this chapter. The AASP methodology is based on researching of various sources (e.g., military service documents, government standards, industrial resources, internal military and civil aviation authority reports, as well as safety and reliability manuals). Most of the initial AASP tasks involve data collection. All deficiencies, non-conformities, potential risks and inaccuracies detected at all AASP stages should be documented. The main documentation of all activities is

contained in a so-called "Potential Studies List" (PSL). This list should be developed at the beginning of methodology implementation and updated throughout the process. The final PSL forms part of the study documentation.

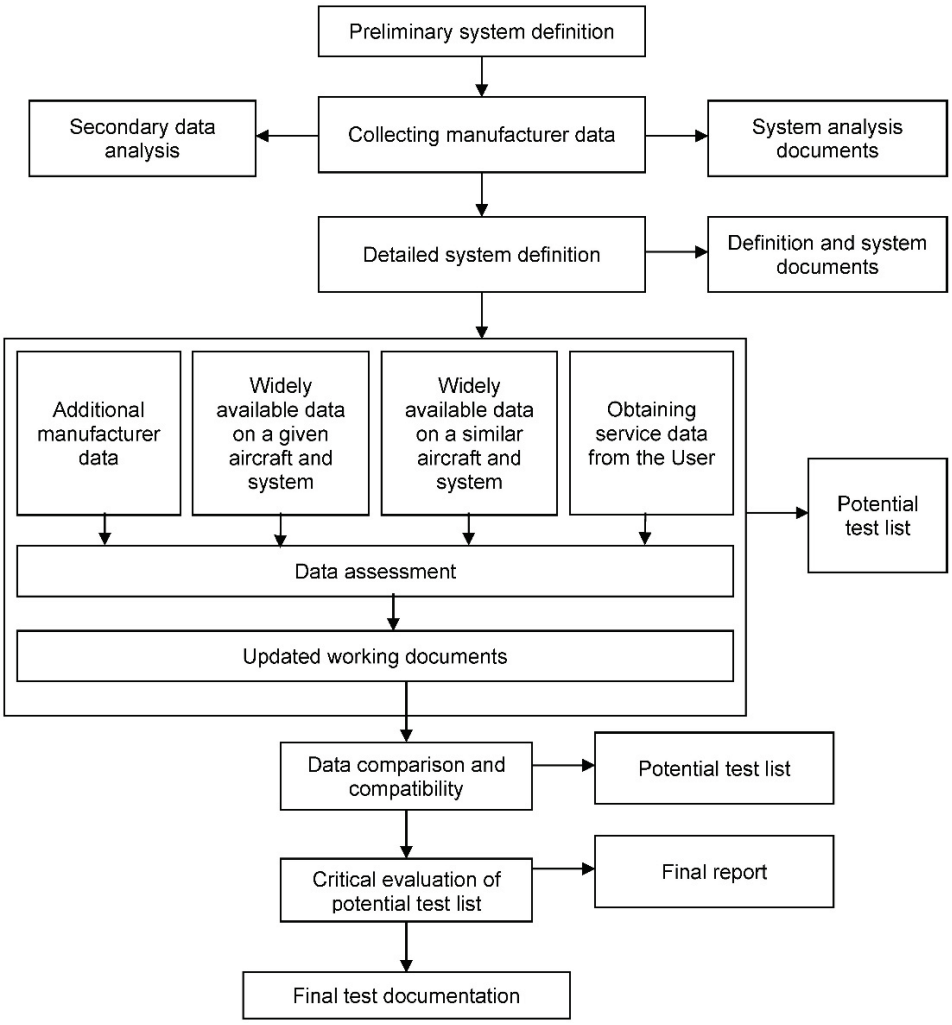

Fig. 1.2. AASP methodology structural diagram [1]

System definition

The first task of the AASP is to select an ageing aircraft and an appropriate system to investigate. As AASP is a safety-related process, therefore, it is important to limit the selection to systems that are critical to aircraft safety. Once a system is

selected, a detailed definition process follows. The system definition process employs two important concepts, namely, control area (Control Volume – CV) and symbiotic systems. In order to conduct an AASP study, a control area is defined for the system under study. A detailed list of specific equipment is then developed. In the case of AASP, symbiotic systems are aircraft systems that are not part of the control area, but are closely related to the test system. An example would be the relationship between an aircraft hydraulic system and a test system with hydraulic components. A preliminary system definition is a brief and written description of the mechanical system to be tested, and includes an identification of the control area. An example of a preliminary system definition: "The test system is the ailerons and their associated control system. The system contains specific hydraulic components that activate the ailerons, but do not activate the entire aircraft hydraulic system. All electrical components are located outside the control area".

Collecting and assessing manufacturer's data

The most critical source of AC system data to be added in the AASP study is the manufacturer. The manufacturer owns all original design and certification data and is the originator of all aircraft service bulletins. As an entity vividly interested in aircraft systems, the manufacturer receives and collects data from many public sources and airlines. Manufacturer's data becomes the grounds for the rest of the analysis. Thus, cooperation with the manufacturer must be established before data collection can begin. To this end, the following information should be provided to the manufacturer:

- purpose of the AASP study,
- aircraft and system to be studied,
- required data types,
- required assistance of the manufacturer's staff,
- conclusion of a non-disclosure agreement.

Data from the manufacturer is assessed as received. The detailed assessment concludes with the identification of potential risk areas (added to the PSL), documentation of data deficiencies (document for additional data requests), and determination of initial data compliance.

Collecting and assessing public data

There are many sources of public data on aircraft systems. Once certain initial data from the manufacturer has been assessed, an intensive search for data from public sources follows. The key to a successful and efficient public data collection process is conducting an analysis based on knowledge of available data types and its sources. Government websites should be used for research, followed by commercial websites and, finally, private websites.

A unique problem associated with collecting data from public sources is that searches provide too many records. The challenge is to strike the right balance between efficiency and completeness. If the data is insufficient for a particular aircraft, it may be necessary to use data related to another aircraft with a similar system to complete the dataset.

If the analysis is done at the component level, it may be possible to reuse data from the same or a similar component not within the aerospace industry. The evaluation of public data commences with a review of records in search of the most appropriate sources. Most records represent a specific event or event group. If possible, each event should be carefully considered so as to understand the causes of the event. This information will be applied intensively in comparing and assessing the compatibility of activities and will be part of the PSL.

Collecting and assessing user data

Although aircraft certification is the responsibility of the manufacturer, the certification holder (the user) is responsible for maintaining the airworthiness of the aircraft and its operation in accordance to established rules. The user is, therefore, another valuable source of information in relation to ageing aircraft systems. The user is selected at the beginning of the study, and the manufacturer recommends the selection process. The manufacturer can also be of assistance in establishing a working relationship with the user.

The best place to start data collection is the organisation where the selected aircraft is operated. The perfect time to visit the organisation is during a scheduled maintenance covering the aircraft of choice. If the service planner, quality control engineers or reliability analysts are not seated at the maintenance centre, every effort should be made to collect information from these sources. As the Airline Operator Query List is long and based on many different sources, it may be that some of the queries will not be relevant to a specific study. Data collected from relevant queries should be documented in relation to the study. An easy way to document and validate airline responses is to record the answers to each question as a written document that can be sent to staff for review. This technique facilitates collecting required and sequential data. As with other sources, the collected data from the airlines is then evaluated and the items are added to the PSL accordingly.

Critical assessment of PSL

Before the PSL is subjected to a final assessment, the collected data has to be reviewed in terms of the occurrence date. The purpose is to ensure that the entire maintenance system contains smooth transitions at each stage of its service life, and to identify any potential areas arising as a result of inadequate data or practices. Items are added to the PSL list throughout the entire AASP study. The items have usually not been thoroughly assessed up to this point. It must be underlined that any

item identified as potentially safety-related has been considered as a significant addition to the list. If the assessment suggests that action is required, a recommendation should be made. Recommendations will depend on the conclusions drawn in the course of all AASP analyses. Recommendations may include changes to the maintenance programme, guidelines on design changes, and the need for further data collection and analysis. Several important factors should be considered when developing appropriate actions related to the existing system, such as inspections, reliability and maintenance tasks.

Final test documentation

The ultimate task within the AASP process is supplementing the study documentation drawn up so far. The study summary contains two parts, namely, conclusions and recommendations. In addition, the most up-to-date version of the following documents should be attached to the study summary:

- list of potential study areas (PSL),
- system definition documents,
- data evaluation documents from the manufacturer,
- final data from the User,
- copies of important data from all relevant public data.

1.1.4. Monitoring the fitness of AC structures

Monitoring operating loads of AC structures

The main objective of the structural health monitoring system is predicting the current fatigue life status for each individual aircraft (Fig. 1.3).

The originally planned service life is guaranteed based on the experience gained from fatigue tests conducted at the engineering stage. The service life extension process is impacted by the experience from operational use, which may differ from the engineering stage assumptions. These become very important since changes in boundary conditions, such as modification of operating parameters, require a high degree of accuracy in assessing individual operating loads.

The current concept of fatigue life monitoring involves three stages: in-service measurements, mathematical modelling/failure estimation, and maintenance planning. This concept has resulted in improved maintenance planning that takes into account the occurrence of stresses in specific critical fatigue areas. All processes are essentially based on the acquisition of flight parameters specific to external loads, but differ in terms of the range of data measured. Furthermore, the operation involves continuous measurement and collection of the Pilot Parameter Set (PPS) and its submittal to a database so as to calculate individual failure indexes for critical fatigue areas using a computer aided aircraft structural life monitoring system.

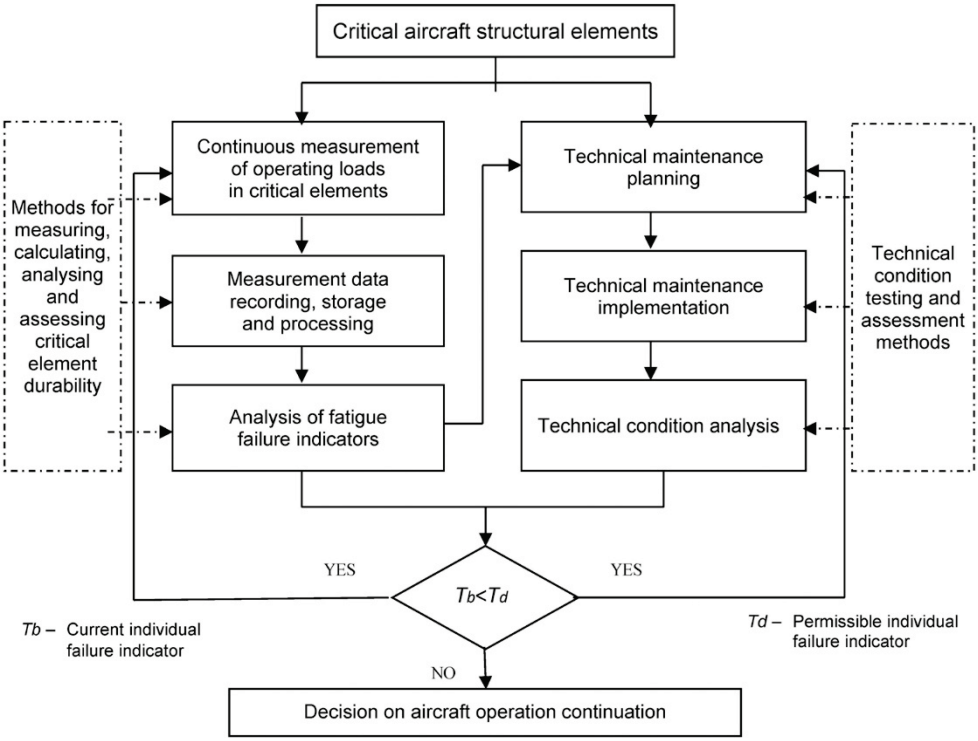

Fig. 1.3. Algorithm for monitoring the airworthiness of AC structures (developed by AFIT)

Selecting appropriate methods to study AC structural health

There is a need to conduct diagnostic tests of structures during the aircraft operation process in parallel with the monitoring of operational loads mainly due to wear and ageing processes. The negative products of these processes are the failures to the airframe structure of aircraft and helicopters.

1.2. General information on diagnostic methods in aviation

First, the author has developed and implemented the FAM-C and FDM-A diagnostic methods in relation to LUZES ground-based aircraft power supply units, where the magnitudes of skew and eccentric displacements of drive shafts, as well as the dynamics of the rotational motion causing the twisting of generator drive shafts were monitored. Subsequently, the methods have found many applications in monitoring the condition of numerous gearbox types (reducers, generator drive

boxes). The developed diagnostic methods have been applied for several years to diagnose bearing supports of the TS-11 "Iskra" aircraft. They also have been employed to monitor electromechanical converters [112, 115, 117]. Moreover, successful attempts have been made at monitoring spontaneous ignition diesel propulsion units on sea ferries [103, 116, 129]. Of note, intensive research work on the monitoring of military helicopter power units has been on-going for several years [7, 95, 98].

These methods are still classified as prototypes, being at the stage of research and implementation with a relatively narrow object population range, virtually limited to the airborne equipment of the Polish Armed Forces alone. Thus, they are complementary to the still officially valid "old" methods. For this reason, it is necessary to discuss them in general terms.

The following tests have been used previously for diagnostic measurements of mechanical propulsion units:
vibroacoustic tests with modal analysis,

a) analysis of wear products in lubricating oil,
b) temperature field analysis,
c) strain gauge measurements,
d) diagnostic methods related to TTM – indirect measurement of rotational speed and displacement of rotating elements (e.g., compressor blades) using electromagnetic, optical, microwave, capacitive, eddy current and microwave sensors. On a similar basis, torque meters for propulsion units have been constructed since the early 1970s [68, 201, 202, 206, 256, 295-297]. In practical terms, the FAM-C and FDM-A methods should be classified in this group, since, although they were under development for a long time independently of TOA, they, in fact, apply the TOA principle described by Campbell [37] in TTM.

Re a) Vibroacoustic measurements require the installation of additional sensors. The primary signal (e.g., from a turbine engine bearing support bearing) is displaced towards the sensor through various damping media. At the same time, sound-inducting engine bodies and housings feed numerous interference signals to the same sensors [39, 40, 44, 205, 207]. This hinders locating failures, as well as determining the risk level.

Re b) Measurement of abrasion products in lubricating oil [15, 182, 268] – the scope of diagnostic process observation is limited only to tribological processes resulting in the release of particles (due to the abrasion process) or chemical changes in the oil. In practice, periodic sampling of onboard aircraft and ship system during shutdown at strictly-defined intervals after downtime is applied. The investigator must be well acquainted with the material composition of various propulsion unit components. If the material composition of these components is not diverse, it is not possible to locate the defective component.

Onboard oil systems are fitted with abrasion wear sensors (so-called "filing sensors"). However, they are unable to analyse the composition of abrasion products, but only carry information for the crew about the total concentration of abrasion wear products in the lubricating oil.

Re c) Temperature field measurements [62] – due to the high packing (concentration in a volume unit) of components, particularly of aircraft propulsion units, these are difficult to conduct and the installation of temperature sensors complicates the design. There are also non-contact measuring devices (e.g., based on the principle of light spectrum analysis). These require optical contact between the gauge and the tested component - which is not always possible. What is more, temperature measurement is burdened with a large and difficult-to-precise dynamic error [232], which is important in the case of the cascade build-up of specific mechanical destruction processes.

Re d) Strain gauge measurements – they involve applying a special local stress sensor to the tested component. This is most often a resistance strain gauge. They require the installation of additional sensors and measuring bundles, as well as cumbersome[1] commutators [36, 269, 303].

Re e) Using electromagnetic sensors (CRL) for measuring the rotational speed of rotating elements in a transmission gear involves changing the reluctance (magnetic resistance) of a single-side open magnetic circuit of the electromagnet (sensor). A sensor is mounted on the inlet diffuser, while a metal compressor blade (steel or tantalum) serves as the modulator. The flexibility of the blade means that dynamic processes, such as the natural vibrations of bearing supports, are naturally filtered out. Many aerospace propulsion designs employ a similar system to measure local angular velocities of various components. In such a case, the modulator is a mechanically loaded gear tooth in a mechanical power transmission system or a mechanically unloaded tooth (specially coupled to cooperate with a reluctance or eddy current sensor). Similar systems are also utilized in the load diagnosis in individual cylinders of marine diesel engines [57]. Optical or microwave sensor systems [63, 248, 275] also require the installation of additional components.

The above brief and general overview does not exhaust the entire subject. The overriding aim of this monograph is to present the FAM-C and FDM-A methods, therefore it seems plausible to highlight two themes in the initial review:

[1] [274], p. 19, chapter 4. A non-contact device for vibration testing of rotor blades in aeronautical turbine engines; "Using traditional strain gauges to test vibrations and stresses in rotor blades of flow machines has always entailed considerable difficulties associated with the need to pre-prepare the engine for testing through drilling holes and channels to install the strain gauges. The number of blades observed (and measured) was limited by the number of strain gauge bridge channels, as well as the ability to route high-power strain gauge wires through the engine...".

- the importance of vibroacoustic diagnostic methods in modern diagnostics owing to their widespread application, and a review of their main drawback (relative to FAM-C and FDM-A) – no synchronisation,
- TTM methods and, in particular, the measurement of the test object rotational speed with CRL sensors in the light of their operating principle being similar to FAM-C and FDM-A.

A comparison of the practical significance of the characterised types of diagnostic measurements must stress that vibroacoustic measurements reign supreme in the pantheon of propulsion unit diagnostic methods. It is apparently the oldest way of locating and assessing component wear level. Such measurement originally relied on the use of natural human perceptual abilities in the field of auditory recognition of sound intensity and timbre. Vibroacoustic measurement practices, enhanced by modern technology (modern sensors, e.g., piezoelectric, modern filtration methods, analysis software), are still most powerful and widespread in the field of diagnostics. Along with system expansion, these measurements are becoming increasingly expensive, complex and, unfortunately, often unreliable. Their basic downside is the lack of natural synchronism between the primary diagnostic signal and the rated and carrier frequency (if any), making it difficult to locate the faulty area. The FAM-C and FDM-A are not burdened with this disadvantage.

1.3. Pros and cons of the FAM-C and FDM-A methods compared to other diagnostic methods

The FAM-C and FDM-A methods (Fig. 1.4) exploit the natural relationships between the spectrum of the primary diagnostic signal (generating the frequency modulation spectrum, e.g., kinematic pair no. 1: $\Delta\omega_1$) and the rated angular velocity of a given kinematic pair (kinematic pair no. 1: ω_{N1}) [303]. The FAM-C method involves the generator-transducer modulating, i.e., transferring this signal (as well as signals from other kinematic pairs) to a high-frequency level (abbreviated as HF) by naturally "mixing" the low-frequency (LF) signal with the rated "carrier" frequency of the generator-transducer in question. It should be noted at this point that the "carrier" wave is naturally synchronous with the HF signal. Synchronism is also maintained between the individual HF signals (between the signals from the individual kinematic pairs). When modulated, a HF signal gains protection from interference induced by any mechanical devices. This signal, transferred via the onboard electrical network to the HF band, is picked up by the FAM-C or FDM-A measuring equipment at a location convenient to the diagnostics technician. It is then subjected to demodulation, during which the HF signal is "recovered". The primary signal spectrum of

a given kinematic pair is recovered, as well as the associated nominal subcarrier frequency. The synchronous relation between individual kinematic pairs is maintained, which significantly increases the sensitivity and accuracy of the subassembly rotational motion dynamics analysis, hence, the efficiency of cause-and-effect inference increases again. Meanwhile, the vibroacoustic signal is acquired in a markedly different manner. The main differences lie in the method of extracting the primary diagnostic signal from the propulsion unit under investigation.

The first problem concerns the clarification of the primary diagnostic signal concept – in FAM-C and FDM-A, the angular motion dynamics of a given kinematic pair is considered to be the primary diagnostic signal. In vibroacoustics, the vibration of a given kinematic pair is thought to be the primary diagnostic signal. However, the author of this elaboration believes that it is rather the effect (secondary effect) of the fluctuation in the angular velocity of a given kinematic pair, at least in the case of rotor machines. Therefore, some of the original diagnostic information is lost already at this stage.

The second issue concerns the mutual synchronisation of vibroacoustic signals from individual kinematic pairs. Each kinematic pair emits its own vibroacoustic spectrum, which is measured at different, more or less, remote locations. However, the varying distance of the individual kinematic pairs from the sensor results in diverse phase shifts between the signals, which do not preserve natural relationships when they reach the sensor [39, 40, 207]. What is more, as mentioned in the introduction to this monograph, the primary vibroacoustic signal passes through numerous media – air layers, seals, oil film coat. Each of these media has a different sound propagation rate, hence, the signal displacement can vary even more. Moreover, a signal passing through media boundaries (Fig. 1.5, marked with dashed-line arrows) experiences reflections, which, depending on the phase, can reduce the signal amplitude, along with its damping, through interference.

The third issue related to the HF carrier wave. Vibroacoustic sensors often have their own carrier frequency. It is applied "obligatorily" in the teletransmission of the vibroacoustic signal [3, 100, 101]. The carrier wave is not synchronized with the received primary signal of the respective kinematic pair. An additional sensor, most often a reluctance one (Fig. 1.5, "Cz Obr") is installed in certain vibroacoustic systems. It monitors the "rotational speed phase" [28]. Due to the distortion of the phase between the primary signal of a given kinematic pair and the signal received by the sensor, only information regarding the current rated (averaged for an adopted time interval) rotational speed of the propulsion unit can be transmitted.

Apart from vibroacoustic methods, also noteworthy are the diagnostic methods associated with the TTM concept, especially rotational speed measurements of a test object using electromagnetic sensors (CRL).

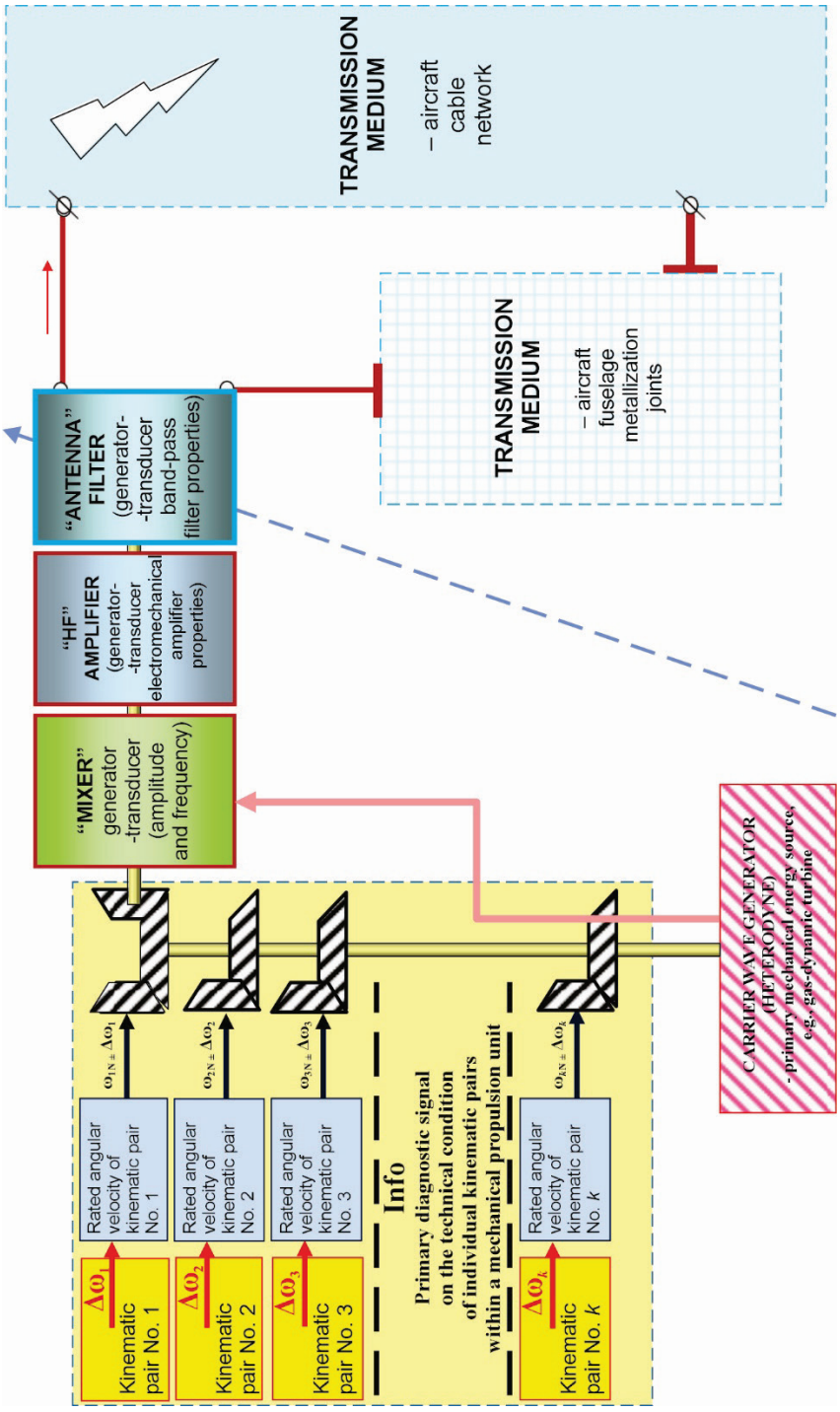

Fig. 1.4. Block diagram of a "transmitting station" used in the circulation of diagnostic information on the technical conditions of a mechanical propulsion unit under FAM-C and FDM-A methods

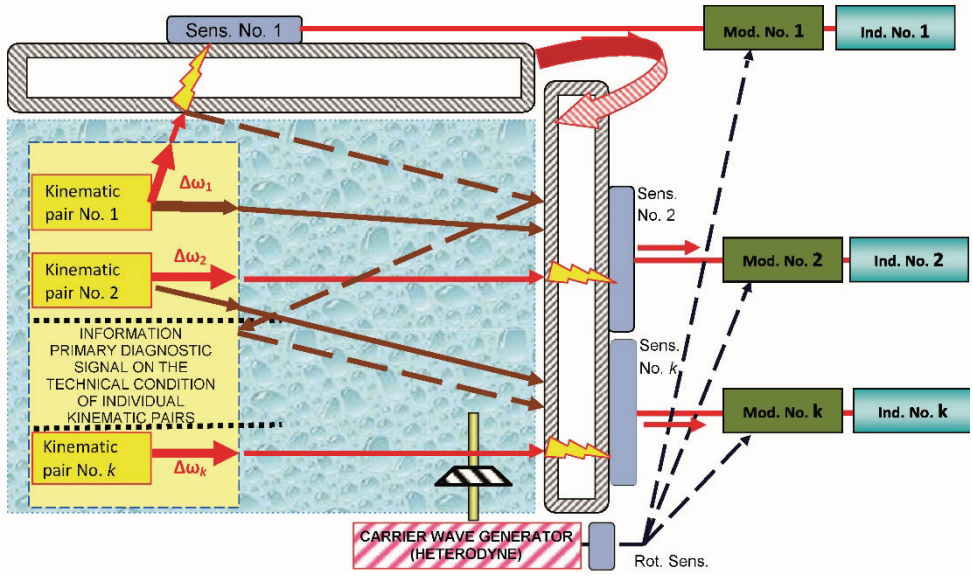

Fig. 1.5. Block diagram showing the circulation of diagnostic information on the technical conditions of a mechanical propulsion unit using the vibroacoustic method

As mentioned above, the idea of measuring rotational speed using electromagnetic sensors (CRL) is very similar to the collection and conversion of the primary diagnostic signal using FAM-C and FDM-A methods. Important **similarities** that can be distinguished include (Figs 1.6 and 1.7):

Above all, both methods have a natural synchronism loop. This increases the sensitivity and resolution of the method, and mitigates the possibility of aliasing [29, 77, 302].

Secondly, both methods have one peculiar element [183-186], which collects (based on a logical adder) individual spectra of primary signals (through modulating angular motion) of individual kinematic pairs. In addition, each kinematic pair has its own subcarrier frequency [3]. This enables identifying and localising failures.

There are also **differences** (Fig. 1.15 and 1.16) resulting primarily from the execution technology of the modulating element – sensor:

Firstly, the modulating elements in both methods have different and magnetic properties:

a) The generator teeth have a much larger cross-sectional area than the compressor blades, which makes it more difficult for them to enter a state of magnetic saturation under normal conditions [212, 215], particularly as there are provisions in all bulletins, methodologies and manuals [80, 86, 87, 91, 92] on the limits to the electricity consumption from a generator-transducer during a FAM-C or

FDM-A test; the onboard electrical network has effective means of monitoring and correcting this electricity consumption.

b) The generator teeth are made of materials with a high magnetic saturation field intensity – the generator is of linear magnetisation character, hence, no angular velocity modulation conversion distortions to generator-transducer frequency modulation occurs. No double frequency is generated[2] in the generators, as the rotor virtually never exceeds the magnetic saturation level [100, 129]. Thus, the generator as a transducer is of linear magnetisation character and therefore, enables reproducing the undistorted waveform of the angular velocity oscillations of individual kinematic pairs.

Secondly, both FAM-C and FDM-A methods exhibit a much better phase reflection of primary diagnostic signals owing to better modulator rotor rigidity – it is characterized by much lower pitch errors than a compressor blade grid; (tooth pitch is stable in the course of generator operation, while changing in the case of a blade grid (Fig. 1.8) [303].

Thirdly, the angular position reference baseline (the mounting location of the CRL reluctance sensor) is subject to much greater displacements than the angular position changes of the generator-transducer pole pieces in the FAM-C and FDM-A methods (Fig. 1.6). Both the compressor body and the sensor itself are exposed to intense forces that modify the angular and radial position relative to the blade grid. The compressor body is, however, commonly split circumferentially to facilitate installation, which usually reduces the rigidity of this design. In addition, air compressed in the subsequent stages of the compressor heats up to 400÷600 ^{o}C, which causes additional compressor body strains and changes the baseline position of the CRL sensor symmetry axis [301, 303]. Meanwhile, generator magnetic cores are made of silicon sheet metal executed in the same technology as the generator rotor – the package is pressed into a uniform, cast-steel cylindrical body of the generator. The cast-steel body itself has a diameter of 100÷400 mm and the cast walls thickness is is 5÷15 mm, which provides it with considerable rigidity.

Fourthly, in the case of the TTM method with a CRL sensor, the initial magnetism of the modulator and eddy currents – much lower in a generator-transducer are important for the phase error, because:

a) the directional properties of the generator rotor residual magnetism (sheet metal anisotropy due to steel treatment process, e.g., rolling) are structurally weakened through the use of a sheet metal package, each of which is rotated by one slot pitch, which is not the case in a blade rim,

[2] This does not apply to internal or external short-circuit conditions or to generator loading above rated current.

b) the impact of eddy currents within the magnetic circuit of the generator-converter is reduced by [129, 189, 203, 240]:
   – isolating individual package sheets from each other (formerly by interleaving with insulating tissue paper, nowadays by coating the surfaces of individual sheets with a phosphate layer),
   – incorporating silicon grains into the steel sheet (silicon sheets) structure, which increases the resistance to eddy currents.

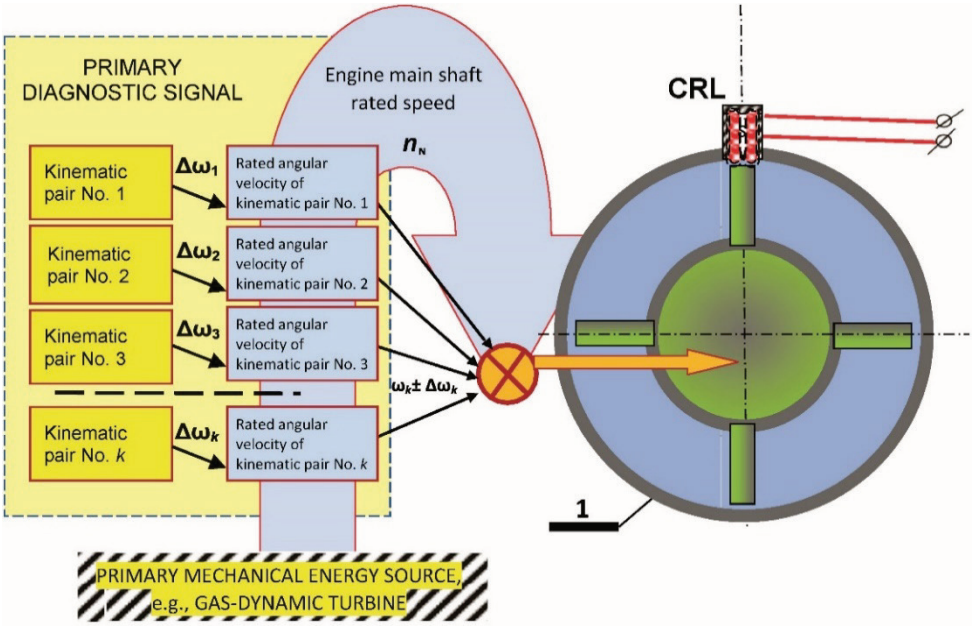

Fig. 1.6. Reluctance sensor (CRL) in a turbine engine compressor blade grid unit as a singular element for monitoring primary diagnostic signals (individual kinematic pairs) of a mechanical propulsion unit: CRL – reluctance sensor – compressor blade angular position signal receiver; 1 – compressor blade

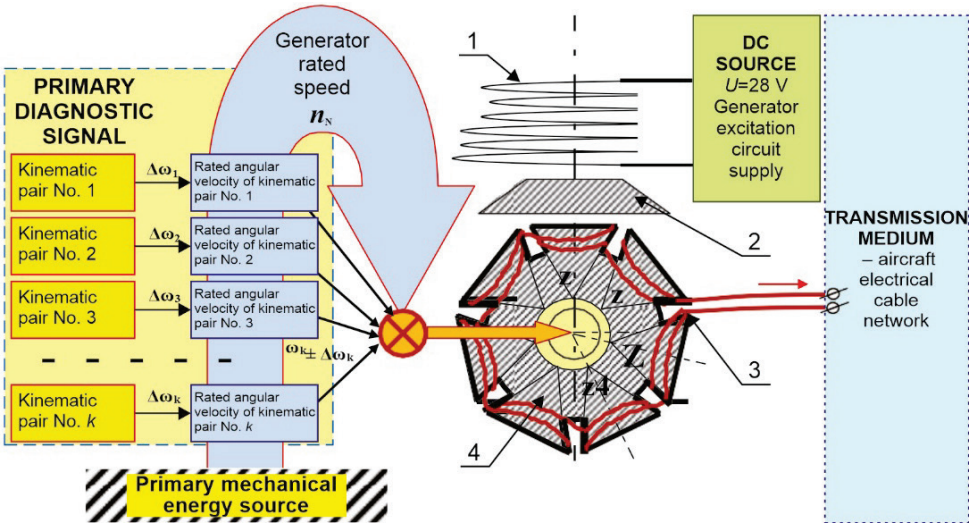

Fig. 1.7. Generator-transducer as a singular element for monitoring primary diagnostic signals (individual kinematic pairs) of a mechanical propulsion unit. 1 – generator-transducer stator excitation winding, 2 – generator-transducer stator pole piece, 3 – generator-transducer rotor winding, 4 – generator-transducer rotor

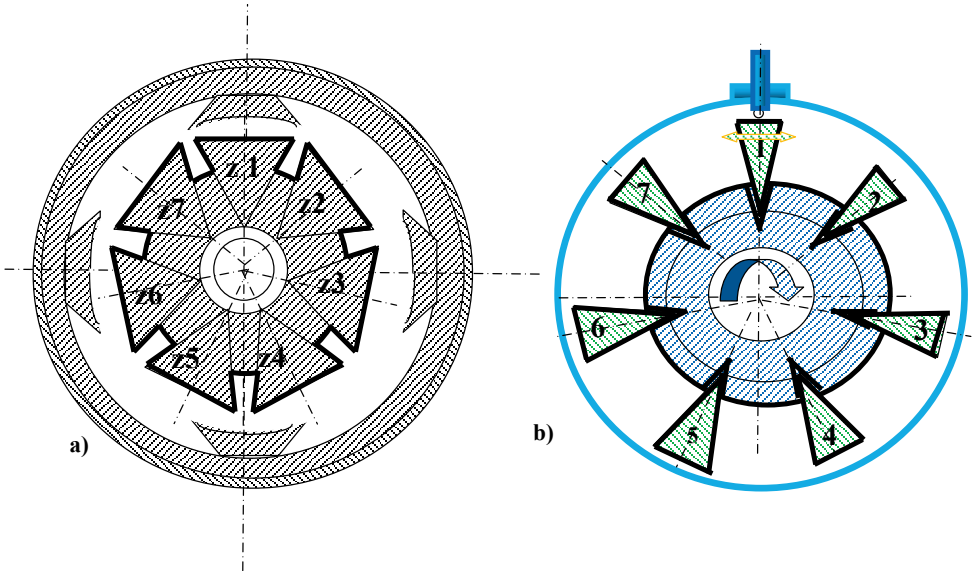

Fig. 1.8. Compared geometry of electrical generator rotor teeth with a turbine engine compressor blade grid: a) silicon sheet of the generator rotor core package, b) blade grid of a turbine engine compressor

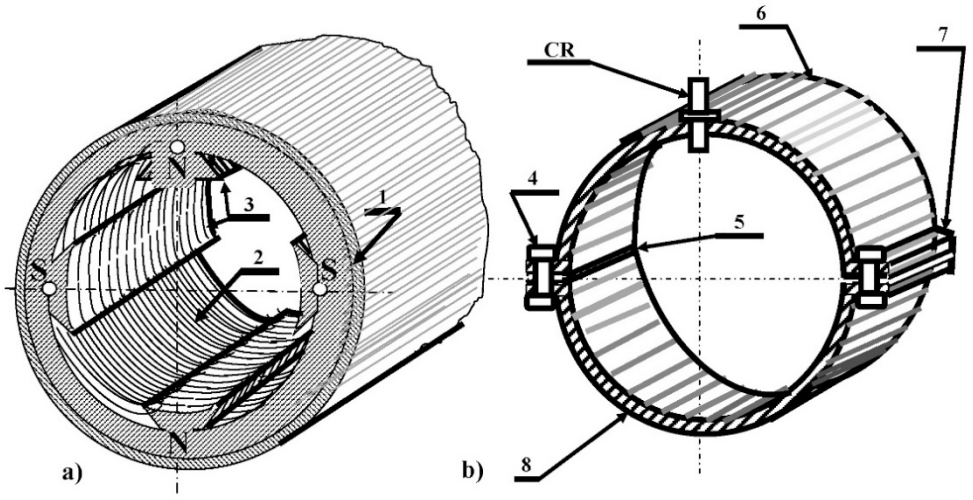

Fig. 1.9. Compared geometry of electrical generator stator pole pieces with a turbine engine compressor body: a) silicon sheet of the generator rotor core package:
1 – cylindrical cast-steel body, 2 – silicon sheet package, 3 – stator pole pieces, b) turbine engine compressor inlet diffuser body: CRL – reluctance sensor (inside in the engine body), 4 – "shoulder" screw mounted in the calibrated orifice holes of both engine body halves, engine body pitch plane, 5 – body pitch plane, 6 – engine body upper half, 7 – engine body orifice (upper body half), 8 – engine body lower half.

In the previous subsections, the author presented the features of the novel FAM-C and FDM-A methods against the background of the "old" diagnostic methods. While reading these considerations, readers might have the impression that the authors consider their novel methods to be perfect. The application of these methods, just like with any other, also has its limitations. It is difficult to determine at the very brink of developing a novel method whether all the limitations and risks associated with their application have been identified.

Disadvantages and application limitations of the FAM-C and FDM-A methods

There are also phenomena which, under certain conditions, can interfere with the measurement, and result from a non-diagnostic purpose of generator-transducers:

a) The effect of magnetostriction [16, 34, 72, 241, 258, 300, 303] – changes in the air gap between the stator and rotor, and changes of the rotor tooth thickness and/or stator pole piece width due to strains caused by the strong electromagnetic fields in the stator and rotor – the effect is almost eliminated in relation to

FAM-C and FDM-A method errors through minimizing the intensity of the current drawn from the generator and through a ban on the activation and deactivation of any electric consumers during FAM-C and FDM-A testing.

b) The effect of electric machine transverse magnetic field [49] occurring in the event of significant current load on the generator, causing angular displacement of a magnetically neutral line, i.e., in the FAM-C and FDM-A methods, it is a measurement error – eliminated similarly as in point a).
c) The effect of a change in the field force lines due to internal structure irregularity of the broadly understood mechanical stresses, including heterogeneity of the internal structure (technological drilling in the silicon sheets of the generator stator or rotor, non-uniformity of the compression or tensile force of these sheets, etc.). – i.e. an effect opposite [188, 212] to magnetostriction. In the FAM-C method, it is considered as negligible, a kind of "fingerprint" for a given generator unit.
d) The effect of rotor sway due to electromagnetic forces present during changes of the current load [189, 199, 230, 315] – it is virtually eliminated in relation to FAM-C and FDM-A method errors through a ban on the activation and deactivation of any electric consumers during FAM-C and FDM-A testing.
e) The effect of distorting the generator-transducer voltage waveform during and after being exposed to electrical load comparable to rated power – eliminated analogously as in a).

Summarised preliminary properties of the FAM-C and FDM-A methods compared to other diagnostic methods

The differences between individual diverse diagnostic methods and their common features can be illustrated based on the example of a dummy aircraft (Fig. 1.7). In general, all previous methods required either local mechanical contact with the tested kinematic pair or its housing, or "optical" access to the propulsion unit component diagnosed. Therefore, it is required to install an additional sensor (not being part of the "standard" structure of the tested power train), near the tested kinematic pair or in direct "visual contact" with the studied element. In most of these methods, the installation of sensors on the object under diagnosis usually entails disturbing its mechanical structure. At the same time, the electric bundles of the sensors further complicate the structure of the electrical equipment of the diagnosed object [274, 303]. In the case of a remote signal reception option, direct (optical) visibility of the component under test by the diagnostic signal receiver is required, which is often a condition that cannot be satisfied. In turn, some of these methods require shutting down the propulsion unit.

Meanwhile, the FAM-C and FDM-A methods require neither an additional sensor, nor additional electrical bundles within the aircraft structure or the observability of a tested component by the sensor. Moreover, the collection of diagnostic information is implemented under the natural operating conditions of the machine [81, 83, 84, 99, 124, 125, 129, 168, 303]. At the same time, it is an ergonomic method – a diagnostician connects the instruments to any connector exhibiting a particular voltage range and conducts the measurement far away from dangerous places – no mechanical access to the tested nodes of the propulsion unit is necessary, rather, onboard generators and the aircraft power grid are used. These are intended to generate and supply electricity to consumers. The methods use a "by-product" of energy flow in the form of frequency modulation reflecting the dynamics of the propulsion unit motion. Because the dynamics of frequency modulation changes is the same for all locations of a given electrical circuit, a FAM-C or FDM-A measurement may take place at any point of the grid that is safe and ergonomically convenient to the diagnostician. Locations away from hazardous regions, such as the motor hot zone (Fig. 1.10) are usually selected [80, 81, 83, 84, 125].

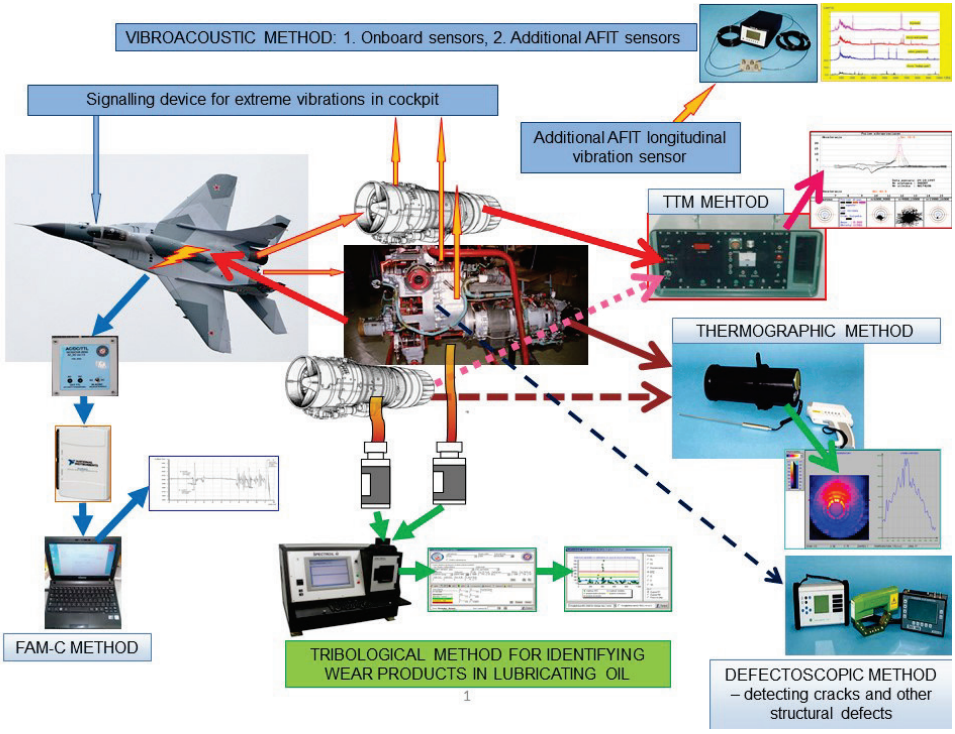

Fig. 1.10. FAM-C method compared to other diagnostic methods in terms of monitoring the technical conditions of a MiG-29 aircraft propulsion unit – overview

1.4. Monograph structure description

Successive chapters of the monograph thoroughly present the concept behind the FAM-C and FDM-A methods and their implementation.

Chapter 2 discusses the current state of research on the topic and the principle author's research hypotheses. It also describes the FAM-C and FDM-A methods, their origin, development and implementation procedure. The basic relationships undergoing within a diagnosed propulsion unit, a generator, and a detection system, as well as between them, are defined. An attempt is also made to formulate hypotheses through describing the diagnostic features of generator-transducers and their application as part of FAM-C and FDM-A methods.

The cycle of converting the primary diagnostic signal (modulating the angular velocity of the mechanical components) into a frequency-modulated voltage signal by the generator-transducer is to be compared for tele-transmission purposes. This enabled adopting a number of relationships from radio engineering and telecommunications. In this chapter, the authors attempt formulating a multi-vector model, taking into account relationship and interaction between kinematic pairs of a given propulsion unit, the processing of these relationships by an onboard generator, FAM-C and FDM-A measurement and diagnostic analysis. A plan for justifying the veracity of the observations, with regard to active and passive experiments, as well as theoretical analyses will also be also presented.

Chapter 3 presents the relationship between individual defects in mechanical propulsion unit kinematic pairs and their depictions in FAM-C and FDM-A methods.

The subject matter is structurally divided into separate subsections discussing the representation of periodic and stochastic phenomena. Periodic phenomena will be sectioned with respect to the relative width of the primary diagnostic signal generated by a given kinematic pair or component of a mechanical propulsion unit, into narrowband and broadband. This division was adopted by the author from the theory of teletransmission [3] and radioelectronics to reflect mechanical phenomena (e.g., the broadband model of rolling bearing vibration dynamics is quite often referred to in the source literature on rolling element bearing dynamics [73]). This chapter classifies and systematizes the links between various defects of propulsion unit components, and the phase and frequency modulation parameters obtained from the onboard generator voltage waveform via the FAM-C and FDM-A methods.

In **Chapter 4**, the author discusses the metrological properties of the FAM-C and FDM-A methods and their structural errors as linked with the process of monitoring mechanical propulsion units. The main focus is on the measuring system and errors associated with it. In particular, the author thoroughly analysed the issues

related to converting the generator--converter voltage analogue signal into a digital one.

Chapter 5 provides a review of the FAM-C and FDM-A method embodiments based on real objects operating within the operating system: ground-based power supply systems, the engine rooms of aircraft, helicopters and floating ferries, as well as machine converters.

Chapter 6 describes the tribological phenomena observed during long-term monitoring of bearing nodes in aircraft single-shaft turbine engines.

Chapter 7 summarises the deliberations. The positive features of a signal obtained from an onboard generator coupled with a tested propulsion unit that arise from natural physical phenomena will be stressed. One of those is the mutual synchronism of signals from all mechanical nodes. There is a mutual synchronism of angular velocity changes in individual kinematic pairs with their reflection in the instantaneous frequency changes obtained from the generator-transducer. Therefore, the signal recognition barrier established by the Kotielnikov-Shannon condition has been overcome in practice. At the same time, the authors will point to the high resistance to interference associated primarily with shifting the frequency band of the primary diagnostic signal into the frequency band of the onboard electrical grid. The possibility of controlling the diagnostic observation resolution by adjusting the phase configuration of signal acquisition and synchronising the measurement from several generators (mounted on the same propulsion unit) is to be demonstrated. Future directions for the development of the FAM-C and FDM-A diagnostic metho ds, such as, e.g., using a quadrature method for collecting and analysing a signal, were also indicated.

2

CURRENT STATE OF RESEARCH, ORIGIN OF PRESENTED METHODS AND HYPOTHESIS

2.1. Origin of FAM-C and FDM-A discrete and frequency methods

The methods are derived from operational practice, taking into account certain theoretical analyses covering source literature. They are based on the analysing power quality parameters. These enable determining the technical conditions of individual propulsion unit components. Through discrete time increment counting, it resembles the TTM idea developed by Campbell [37] in 1924 (at the time, still in the form of analogue measurement) for diagnosing the technical conditions of steam turbine blades. The idea has seen numerous implementations (since the 1980s, already in the form of discrete successive time increment determination) for various mechanical assemblies [8, 38, 50, 51, 58, 144÷147, 153, 173, 233, 248, 249, 253, 255, 272÷282, 298, 301].

2.1.1. Theoretical premises

The first theoretical premise noted by the primary author was an entry in standard [213] claiming that "...frequency modulation depends on the failures in the propulsion system of an aircraft generator...". While reviewing the source literature on vibroacoustic testing, the author found a statement that the foremost me-

chanical signal of a given kinematic pair (associated with its defect or failure) generates the following angular velocity frequency ranges: a carrier frequency dependent on the location of the kinematic pair in the propulsion unit structure and a certain range of amplitude-frequency modulation dependent on the type of defect. An interesting and inspiring statement was made in [203], presenting the electromechanical transducer as a "six-piece" with such parameters as voltage U and frequency f, two mechanical leads defined by torque M and spin speed n, as well as unit heat q and temperature τ. Furthermore, [203] pointed to the interdependence of all these parameters. Therefore, it is consequently required to monitor certain available parameters of this "six-piece" to monitor other parameters. According to the authors of this monograph, logical consequences include, tracking the changes in mechanical moments (M), both torsional and bending, by following the frequency change dynamics at different speeds.

On the other hand, the source literature in the field of vibroacoustics [39, 40] demonstrates that amplitude modulations are attenuated when passing through successive (different) kinematic pairs, while frequency modulations remain unchanged. In contrast, the literature on electrical machines [310, 311] presents the effect of skew and eccentricity of a tach generator connection on speed modulations, treating them as an interference signal. In the light of the above, an idea came to life that a reverse statement should also be true (assuming the linearity of the generator-transducer characteristics), i.e., that developing appropriate methods for testing the frequency modulation of the voltage generated by an onboard generator will enabled making a diagnostic assessment of the failure magnitude (e.g., circumferential backlash, spline joint skewing angle, etc.) in the propulsion mechanism, and identifying the kinematic pair, as well as the type of failure and its magnitude.

The source literature on tribology and motion dynamics of mechanical machines, reveals how important the rated speed of the kinematic pair under consideration is for the form of rotational speed frequency modulation change waveform [119, 139, 180, 219]. It is primarily associated with the phenomena of increase in hydromechanical (lubricant-related) and centrifugal forces being directly proportional to the rated rotational speed. Hence, the primary author decided to introduce several levels of this speed for the individual measurements – virtually every parameter calculated in the course of FAM-C and FDM-A measurements should be presented in relation to speed.

However, the issue related to measurement implementation still remained. Source literature on electrical engineering [304÷306] indicates that the least interference to an AC voltage signal exists when passing through the zero level. Therefore, the author decided to base the measurement idea behind counting time increments at the points where voltage waveform passes through this level. In turn, researchers dealing with radio location discussed methods of measuring altitude

(pulse radio altimeter) or distance (pulse radio station) and further hyperbolic navigation systems (LORAN, DECAN), where the time increment related to sending the probing signal to the return reflection (from the object) was measured by counting the number reference generator pulses [164, 174, 246]. The primary author found that he could similarly track the mechanical propulsion unit motion dynamics through measuring successive crossings of the generator output voltage through the zero level. Counting the pulses induced in a CRL (or other) reluctance sensor in a TTM (since the 1970s, when the digital version began to be used) between successive displacements of a compressor or turbine blade underneath it was similar [8, 38, 51, 58, 71, 145÷147, 150, 151, 153, 173, 233, 248, 249, 253, 272÷279, 281, 282, 298, 301]. The fact that source literature [274] confirms that the more reluctance sensors there are, the higher the sensitivity and resolution of the measurement is, was very important to the author of this monograph. This is indirect evidence that the generator design is a good transducer in TTM. The idea behind TTM is also applied in torque meters with a reluctance transducer [68, 201, 202, 204, 206, 256, 295÷297]. Its design resembles an induction generation; however, there is a spring shaft with appropriate torsion angle as a function of torque between the rotor and stator. A device of this type was one of the elements that inspired the primary author to develop the FAM-C [88] and FDM-A [25] methods.

2.1.2. Authors' operational experience-based premises

The first measurements of frequency modulation changes using the FAM-C method were conducted in 1991 on a LUZES-V propulsion unit with a GTD-350 engine [116, 194]. Initially, a [1] K-20 loop recorder was used for the measurements. Due to the value of the observed waveform's frequency (f_N = 400 Hz), the highest travel speed of the photographic plate of n = 5 m/s was set.

Thus, the geometric distance between successive zero-level crossings was, for the rated frequency, ΔL = 6.25 mm. These distances were measured using callipers with a resolution of 0.1 mm. The relative error of the half-period measurement was δ = 1.6%. In practical terms, frequency modulations at short tape lengths were imperceptible. Only by collating the time increments from numerous successive zero-level crossings and plotting them on a graph enabled observing instantaneous frequency changes. These observations were necessary due to the repeated twisting of generator shafts during the step-down of the current load from the generator of this propulsion unit (Fig. 2.1). Based on this theory and diagnostic practice based on

[1] Loop recorder – a mirror galvanometer (an electrical coil connected to a miniature mirror in turn connected, together with a serially hooked-up resistor, to the output voltage of a generator-transducer, moving within the magnetic field of a permanent magnet).

recording instantaneous frequency waveforms on a loop oscillograph, the primary author developed the concept, followed by constructing the first system for measuring AC generator output voltage instantaneous frequency with a group of coworkers. The FAM-C measurement system consisted of the following blocks [99, 129]:

a) an AC voltage signal truncation circuit (at U = ±0.1 (V),
b) a zero-level crossing comparator (triggered successively by the positive and then negative edge of the signal received from the signal truncation system),
c) a measuring computer with a counter card (timer) with PCL-830, and an internal counter card generator f_z = 1.6 MHz.

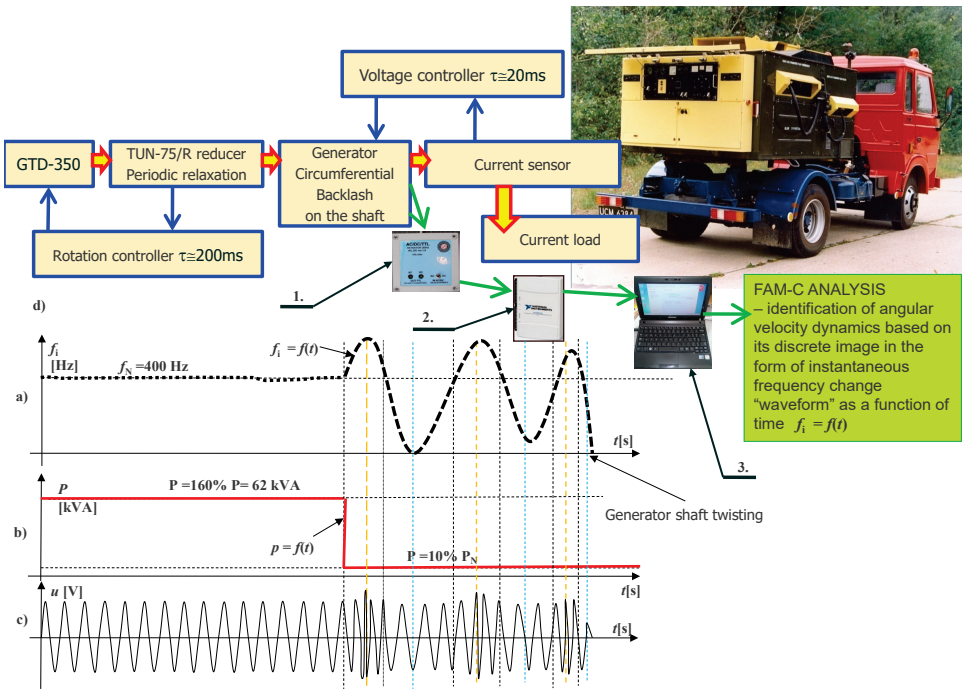

Fig. 2.1. Testing of the LUZES-V unit with the GTD-350 turbine engine after step-down of the current load: a) instantaneous frequency waveform as a function of time; b) current load change waveform, P – load power of the GT-40PCz6 three-phase generator of the LUZES-V, P_N – generator rated power, f_N – generator rated frequency; c) generator output voltage waveform (single-phase); d) block diagram of the tested propulsion unit and components of the single-phase FAM-C measuring system

Using this system, the primary author observed speed variations of another GT40-PCz6 AC generator mounted on a LUZES-V ground power supply device, as described in [129]. By observing the changes in frequency over time, the relationship of the shaft-breaking phenomenon of the GT-40PCz6 generator with specific changes in engine speed, manifested by the modulation of this frequency, was confirmed. The obtained results (instantaneous frequency waveforms reflecting the dynamics of the engine instantaneous speed) led turbine engine specialists to a conclusion that the control system used in the turbine jet engine studied was too slow. This led to the decision to replace this engine with a diesel engine – the LUZES-VD version was developed [194].

The FAM-C method was applied for the first time on-board a MiG-29 aircraft [80, 81, 87, 125].

2.2. Description of the FAM-C and FDM-A methods

2.2.1. Method for obtaining and sampling signals employing AC generators-transducers

The FAM-C method is based on employing the output signal from an AC generator. There are two types of AC generator on board aircraft, as well as ships and ground motor vehicles:

- tach generators, mostly three-phase,
- power generators.

AC tach generators mainly serve as a three-phase voltage transmitter, driving the synchronous indicator motor in the cabin. They are also used as part of automatic control systems. On the other hand, aircraft AC power generators served (until the development of the FAM-C and FDM-A methods) solely to supply electricity to consumers. Their parameters are tracked by numerous measuring and I&C systems to correct the quality of electricity and, under extreme deviations, to automatically disconnect the generator (when, for whatever reason, it does not satisfy the formally required electrical parameters, namely, voltage or frequency). However, none of the aeronautical SV power generators known to the author serve as a source of diagnostic information in propulsion unit diagnostics. The primary author proposes to use AC or DC synchronous generators in the technical diagnosis of a propulsion unit. Although the method of measuring the frequency of tachometric generator output voltage has been applied (to a very limited extent) for many decades, the frequency was measured over averaged long (at least several signal periods) time intervals [304, 305, 307]. The counting and averaging period was many times

longer than the oscillation period for the output voltage of an AC voltage source. The available source literature does not mention the possibility of employing frequency measurements to diagnose individual mechanical kinematic pairs of a propulsion unit. Very few authors treated them as parasitic when describing these relationships [309÷311].

In the method proposed by the primary author, the frequency averaged over short time intervals is measured – single periods or even half-periods of the t_i waveform (the inverses of these time intervals are instantaneous frequencies) – this measurement method is dubbed the indirect frequency measurement method and is utilized by digital frequency meters [265]. This method has been employed in TTM technology since the 1980s [303]. Such a generator type is presented in Fig. 2.2.

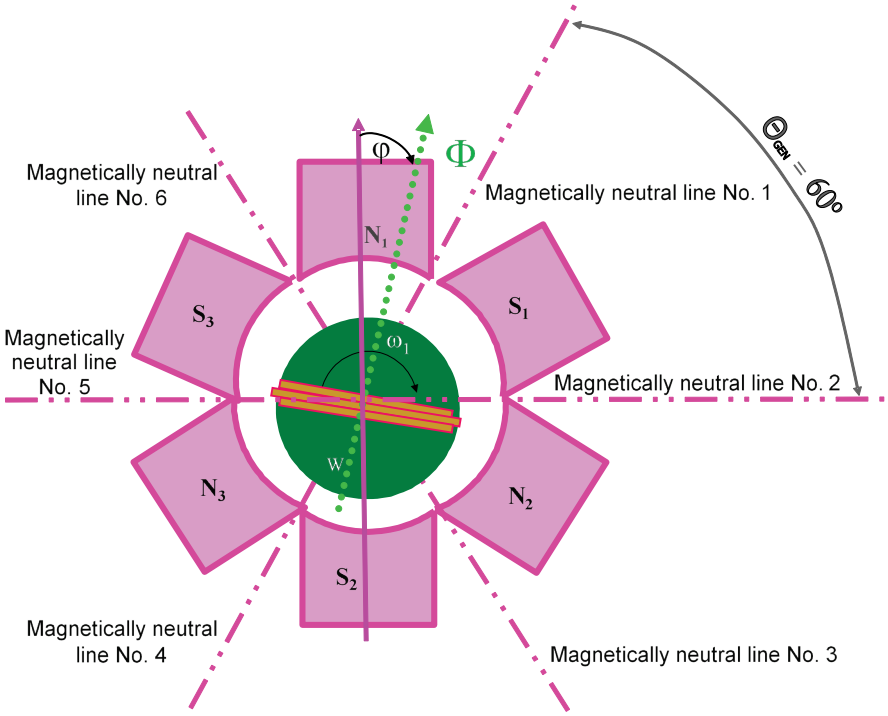

Fig. 2.2. Alternating current generator (alternator) with three pole pairs: N_1, N_2, N_3, S_1, S_2, S_3 – generator stator magnetic poles; zero line (No. 1, 2, 3, 4) – generator stator magnetic field magnetically-neutral zone (line)

An electromotive force (EMF) with rms value defined by the formula below is induced in the rotor windings of an AC generator:

$$E = k \cdot B \cdot \Omega_w \tag{2.1}$$

where:

k [m^2 /rotation] – constant design factor, B [T] – magnetic induction in the gap between the rotor and pole (N, S) with a constant value, Ω_w [rps] – rotor speed.

The EMF instantaneous value can be determined with the formula:

$$e = k \cdot B \cdot \sin(\omega_2 \cdot t \cdot p) \tag{2.2}$$

where:

p – number of pole pairs; ω_2 – instantaneous rotor angular velocity of the AC generator [rps].

The EMF induced in the windings reaches an instantaneous value of zero at the angular position:

$$\vartheta_2(t) = \omega_2 \cdot t \tag{2.3}$$

corresponding to the rotor coil reaching a magnetically neutral axis (Fig. 2.2 – zero line 1, 2, 3, 4). Changes in the instantaneous speed of the AC generator rotor cause the EMF induced in the armature to be frequency-modulated. Time increments are usually not uniform – they depend on the generator rotor angular speed change characteristics. The waveform of a "perfect" generator output voltage without such changes is shown in Fig. 2.3.

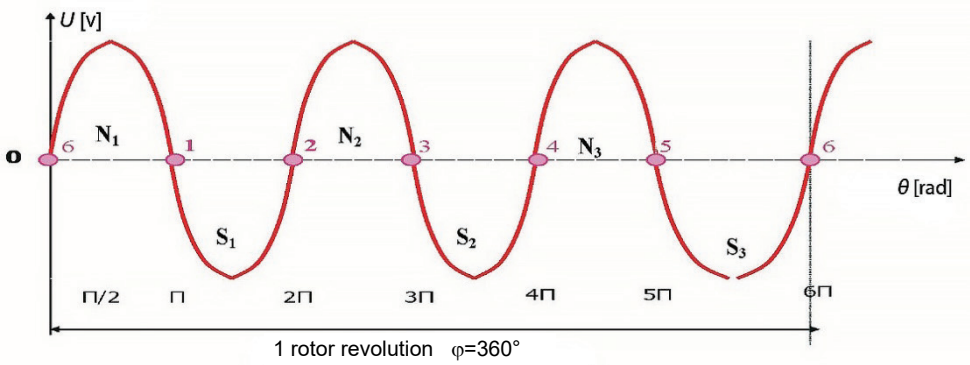

Fig. 2.3. AC generator output voltage waveform with three pairs of poles at constant angular velocity without modulation: N_1, N_2, N_3, S_1, S_2, S_3 – generator stator magnetic poles; zero line (No. 1, 2, 3, 4, 5, 6) – generator stator magnetic field magnetically-neutral zone (line)

Mechanical faults in a propulsion unit induce changes in speed modulation $\vartheta_2(t)$, as revealed in Fig. 2.4.a, and these, in turn, cause the EMF frequency (and amplitude) modulations that are shown in Fig. 2.4.b. By counting the increments of time intervals between successive zero-level crossings, a set of successive time increment values $\{\Delta t_{1\text{-}2}, \Delta t_{2\text{-}3}, \Delta t_{3\text{-}4}, \Delta t_{4\text{-}5}, \ldots\}$ can be obtained, as demonstrated in Fig. 2.5.b. By juxtaposing the inverses of doubled time increment values, the following set can be obtained:

$$f_i(t) = \left\{ \frac{1}{2\Delta t_{c1}};\ f_2 = \frac{1}{2\Delta t_{c2}};\ f_3 = \frac{1}{2\Delta t_{c3}};\ \ldots\ldots;\ f_n = \frac{1}{2\Delta t_{cn}} \right\} \tag{2.4}$$

from which the instantaneous frequency waveform $f_i = f(t)$ can be obtained (Fig. 2.6.b). This waveform reflects speed modulations (instantaneous speed change waveform) of the generator-transducer shaft (Fig. 2.4.a). Since speed modulations reflect the kinematic pair modulations in the entire mechanical propulsion unit, the instantaneous speed change waveform reflects them. Observing the instantaneous frequency waveform, it can be noted that it mostly oscillates around the rated frequency of the generator-transducer. It can be approximated as an instantaneous frequency arithmetic mean:

$$f_{śr} = \frac{1}{n} \cdot \sum_{i=1}^{n} f_i \tag{2.5}$$

By determining the duration increment of the instantaneous frequency waveform deviation from the mean value, a set of deviation duration increments $\{t_{od1}, t_{od2}, t_{od3}, \ldots\}$ can be obtained (Fig. 2.8.a). The inverse of the doubled increment duration of these deviations exhibits a frequency dimension and can be denoted as f_p (mechanical process frequency). Therefore, following [191], it can be written for the j deviation:

$$f_{pj} = \frac{1}{2 \cdot \Delta t_{odj}} \tag{2.6}$$

By assigning each such deviation, in addition to f_{pj}, with an amplitude value ΔFj derived from the value of f_N (represented by $f_{śr}$), a set of consecutive points (f_{pj}, ΔF_j) can be obtained, which the author called characteristic points (Fig. 2.8.b). These points are grouped into sets, called characteristic [82], due to the fact that each such set reflects a defect of a different mechanical node. As will be shown later in the monograph, the sets have different shapes and positions throughout the

plane (f_p, ΔF). The principles of the image analysis theory [221] can therefore be applied to their analysis[2]. Each such set has a certain height – it can be tentatively agreed that it determines the power-related aspects of a given defect in a mechanical component.

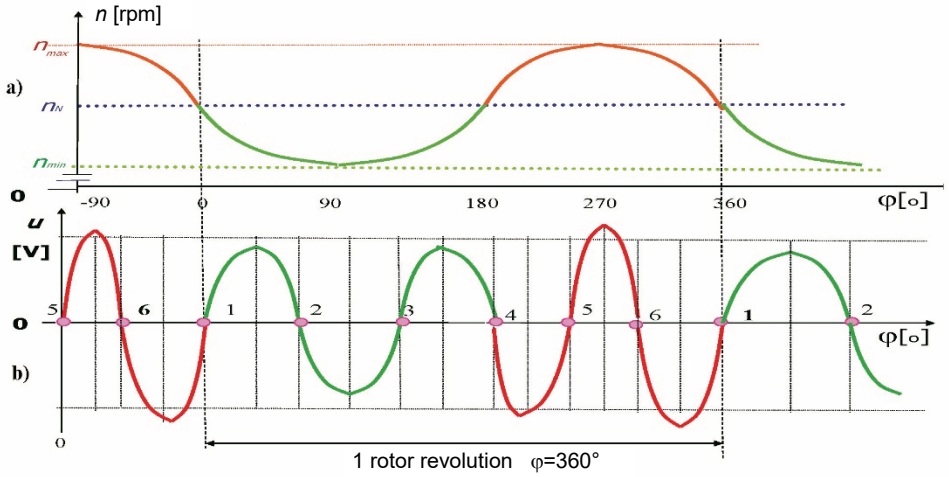

Fig. 2.4. Impact of a mechanical defect of the tested propulsion unit on generator-transducer voltage modulation: a) example of an instantaneous angular velocity waveform (instantaneous speed value) after modulation by a mechanical defect, b) output voltage waveform for an AC generator with three pole pairs at constant angular velocity

[2] [221], p. 166 "...The theory of image recognition has developed globally together with research related to artificial intelligence ... The Polish name of image recognition is not very precise in reflecting the scope of the issue in question and, therefore, requires comments... In general, the task of image recognition is to recognise the belonging of various types of objects (or phenomena) to certain classes. This recognition is to be conducted in the absence of aperiodic information on object classification rules, and the only information available in a learning sequence consisting of objects for which the correct classification is known ...".

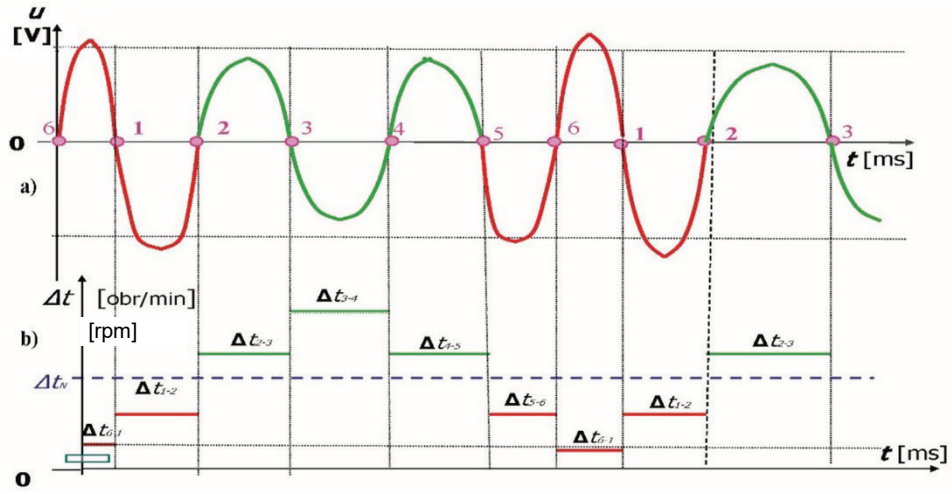

Fig. 2.5. Theoretical generator-transducer voltage modulations reflected in the waveform of time increments between successive voltage waveform zero-level crossings: a) generator-transducer voltage variation over time, b) time increment waveform

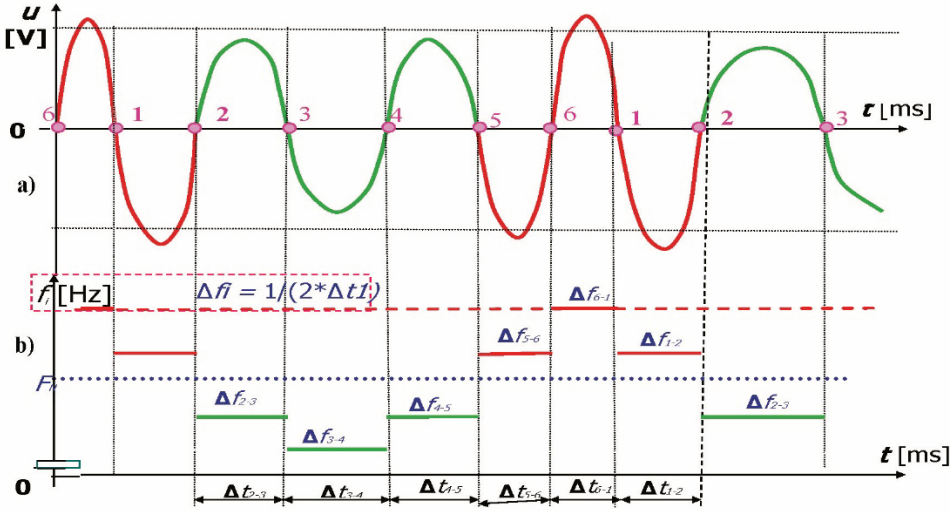

Fig. 2.6. Theoretical generator-transducer voltage modulations reflected in the instantaneous frequency change waveform: a) generator-transducer voltage variation over time, b) instantaneous frequency change waveform

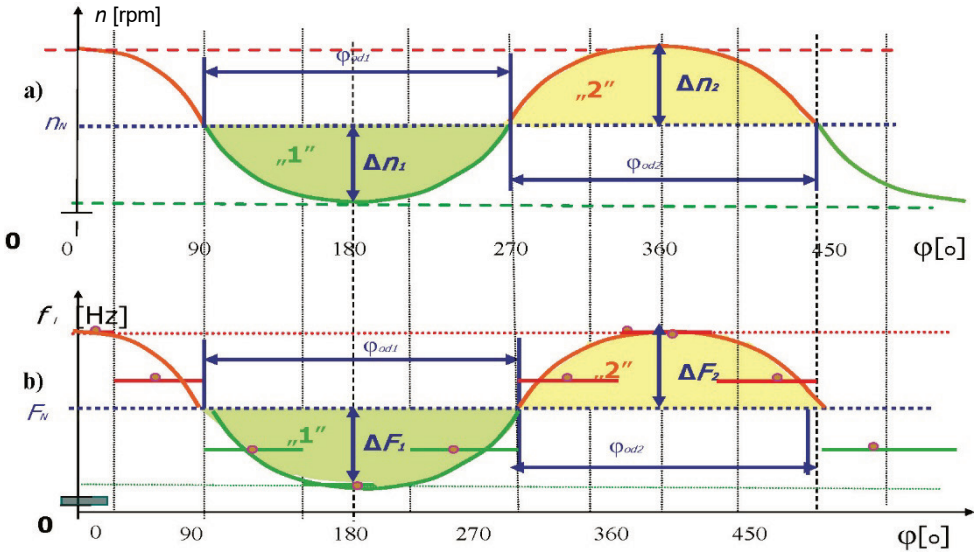

Fig. 2.7. Theoretical instantaneous rotational speed changes reflected in the generator-transducer instantaneous frequency waveform: a) input rotational speed changes, b) instantaneous frequency changes

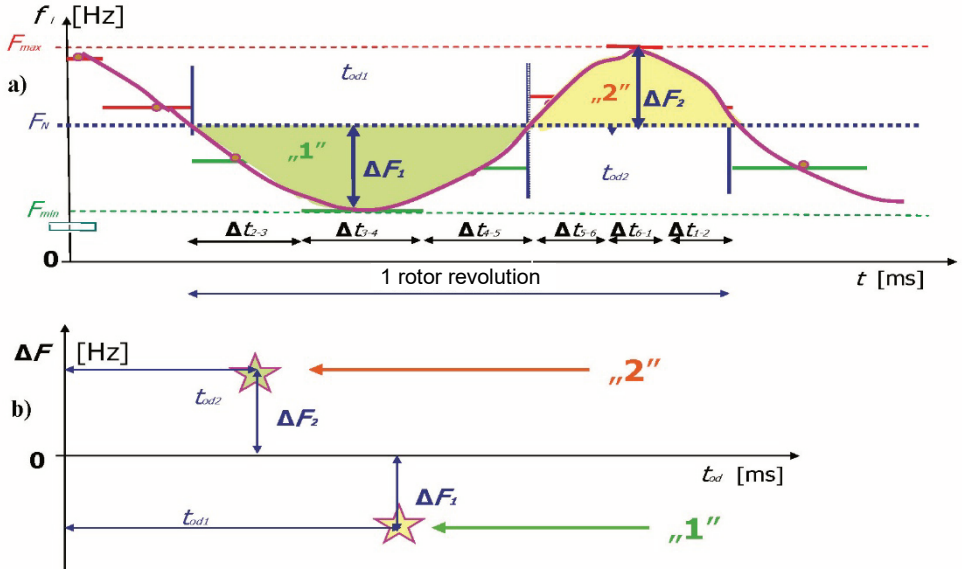

Fig. 2.8. Method of creating characteristic points: a) instantaneous frequency changes as a function of time, b) the reflection of frequency changes in the plane (ΔF,t_{od})

If the vertical symmetry axis of such a characteristic set is determined, its coordinate on the f_p axis will be close to the so-called "kinematic frequency", which is equal to the product of the rated speed and a coefficient defect type-dependent coefficient. These coordinates enable identification. Therefore, a diagnostician obtaining the characteristic sets in the (f_p, ΔF) plane using the FAM-C method, can identify the type of defects in individual mechanical propulsion unit components of a given generator-transducer and assess their power value. A given generator-transducer type under a specific measurement configuration has a determined mechanical process observability band (observability window) that covers a specific band on the 0-f_p axis. Therefore, the primary author has employed several generator-transducer types that simultaneously (in parallel) conduct diagnostic measurements. At the same time, the author applies measurement systems with different phase configurations, thus obtaining changes in the diagnostic observability bandwidth. This makes the diagnosis more complete, accurate and reliable [133, 134]. In the course of long-term diagnostic measurements [129] and literature analysis [55, 179, 180], a significant dependence of the characteristic set height and its bandwidth (of a given mechanical component) on the rated speed was found. Therefore, the primary author decided to introduce a third coordinate axis n. Thus, the parameters will be considered within a spatial coordinate system (f_p, ΔF, n), Fig. 2.9.

In summary – the path from defect formation to a diagnostic signal is as follows:

a) formation of a mechanical kinematic pair defect parameter, causing changes to angular motion smoothness;
b) formation of a periodic or non-periodic inducing function, manifested as modulation of the angular velocity of a given cell's driven element (Fig. 2.4.a);
c) transmission of the modulated angular velocity signal from a given kinematic link (via the propulsion path kinematic chain) to the aircraft onboard generator rotor;
d) conversion of the modulated angular velocity signal of the generator-transducer into an electrical signal – amplitude- and phase-wise modified voltage waveform (Fig.2.4.b). It can be shown [90, 94, 96, 127, 131] that output voltage frequency (Fig. 2.6.a) reflects, discretely, the generator-transducer rotor instantaneous angular velocity change waveform (Fig. 2.4.a).
e) analysis of frequency waveform parameters $f_i(t)$ extracted from the generator-converted output voltage waveform $u(t)$ (Fig. 2.4.a), which enables determining:
    - the duration t_{od} (Figs. 2.7 and 2.8.a) of the instantaneous angular velocity deviation from the mean (rated) level; the durations of these deviations,

according to the primary author's experience, are characteristic of the kinematic pair type;

- the depth of angular velocity modulation proportional to the defect parameter that can be determined by the depth of frequency modulation ΔF;
- the relative value of frequency modulation depth $\left(\frac{\Delta F_i}{f_{śr}}\right)$, i.e., the ratio of the frequency amplitude ΔF deviation to the mean frequency $f_{śr}$.

f) it can be observed that each kinematic pair is characterised by a different deviation duration. The results obtained for real objects show that the points in the plane (f_p , ΔF, n) are arranged into characteristic sets (Fig. 2.9). Points in the individual sets accumulate in bands with respect to the $0f_p$ axis. Characteristic frequencies f_{pj} of individual bands depend on the rated speeds of individual components (on the subcarrier frequencies) and on the type of individual faults (Fig. 2.9). Each of these sets characterises the wear status of a different kinematic link of a propulsion unit and its defect (performance- or wear-related). They exhibit varying shapes, heights, frequency bands ($f_{p\min}$, $f_{p\max}$) and "carrier" frequencies f_N. The height and band parameters vary depending on the operator-set value of the propulsion engine main shaft speed n [113, 114, 118÷120, 122, 123, 129, 136].

g) it can be observed that each generator-transducer has a different observability band for propulsion unit motion dynamics processes (different band with respect to the 0-f_p axis (Fig. 2.9)); changing the measurement set-up also leads to a change in the observability band (observability window) (Fig. 29). The lowest observability band for propulsion unit motion dynamics processes is exhibited by the AC single-phase generator, while a higher band is exhibited by the same generator, albeit in a three-phase configuration; the DC generator has the highest observability band [100, 129, 134].

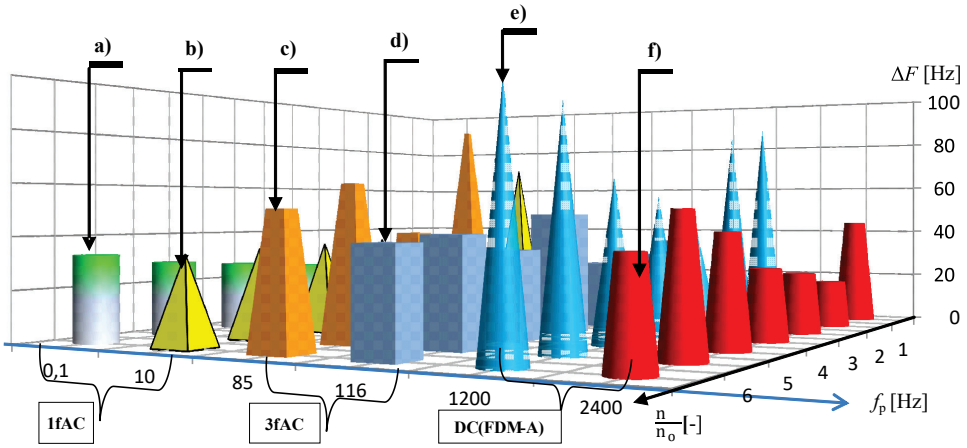

Fig. 2.9. Characteristic sets in a 3D space (f_p, n, ΔF) for typical aircraft propulsion unit failures – diagram showing characteristic set heights: a) hydraulic unit air blockage, b) excessive one-way coupling wear, c) compressor shaft skewing with respect to turbine shaft, d) excessive combined backlash of engine main shaft, e) front support bearing technical condition $N = 12$, f) centre support bearing technical condition $N = 22$, 1fAC – single-phase FAM-C measurement, 3fAC – three-phase FAM-C measurement, DC(FDM-A) – FDM-A measurement

2.2.2. Instantaneous frequency measurements

Defects in kinematic pairs cause the generator output voltage waveform frequency modulations, as shown in Fig. 2.4. Instantaneous frequency is measured through measuring time increments between adjacent successive crossings of the generator voltage signal through the zero-voltage level ($U = 0$V). The inverse double value of this time increment is the sought after instantaneous frequency f_i. Since for U = 0V the sinusoid reaches the largest change gradient, it can be inferred that the voltage waveform will be least distorted in these locations [304]. The period between successive crossings through $U = 0$V is measured by counting successive pulse packages of the time base generator ("internal clock") in the pulse counting circuit ("counter card") f_z. Measuring the time increments between successive crossings of this voltage through the reference level ($U = 0$V), i.e., through the zero level, enables obtaining the following values $\Delta t_{ci} = \{\Delta t_{c1}, \Delta t_{c2}, \Delta t_{c3}, ..., \Delta t_{cn}\}$. Subtracting the inverse of these doubled time increments determined by equation (2.8) enables obtaining the generator output voltage instantaneous frequency changes over time, i.e., the waveform of the function $f_i = f(t)$, as shown in Fig. 2.6.b (theoretical waveform) and Fig. 2.10 (actual waveform). At the same time, the arithmetic

mean for the instantaneous frequency defined by formula (2.8) can be determined for the entire diagnostic measurement duration.

Two parameters can be assigned to the deviation of the instantaneous frequency f_i from the mean value $f_{śr}$ (Fig. 2.8.b):

- deviation amplitude – ΔF [Hz],
- deviation duration – t_{od} [s].

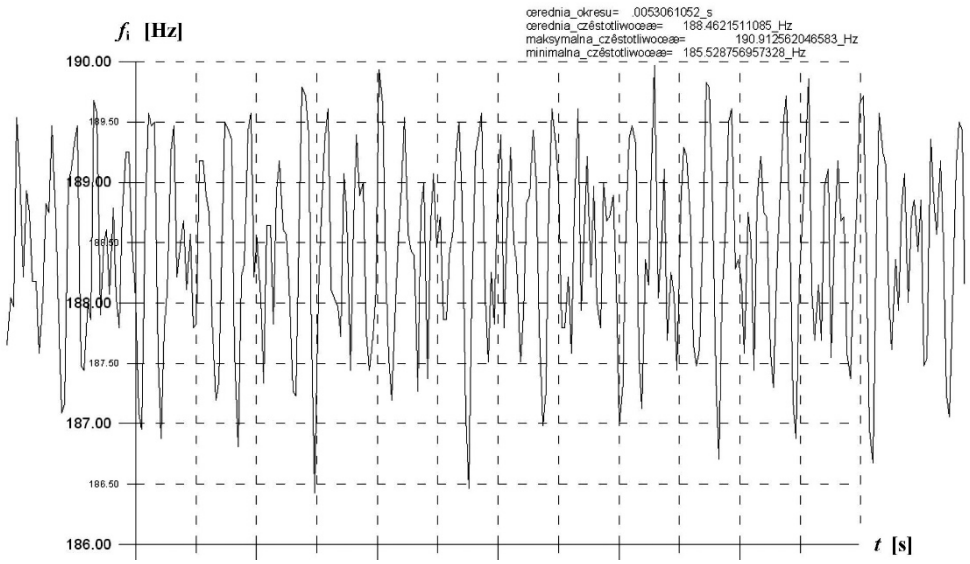

Fig. 2.10. Example of an actual instantaneous frequency waveform – waveform from a D-10/2 tach generator in a three-phase configuration from an SO-3W engine, at main shaft speed n = 15 100 rpm

2.2.3. Method for creating points on a plane (f_p, ΔF)

Observing changes in the instantaneous frequency enabled identifying relationships between increasing extreme frequency change deviations (ΔF_i) from the average frequency ($f_{śr}$) and the degree of monitored kinematic pair wear. Observations of the instantaneous frequency waveforms $f_i = f(t)$ required reviewing prolonged waveforms and noting extreme amplitude values (Fig. 2.10). In order to reduce the effort required to determine extreme frequencies and duration of deviations from the average frequency in the case of output voltage frequency changes as a function of time, it was decided to represent these changes in a rectangular coordinate plane (f_p, ΔF) – Fig. 2.11. The value of the modulating frequency generated by individual kinematic pairs of the propulsion unit under study was plotted

on the abscissa axis, while extreme frequency deviation ΔF values were plotted on the ordinate axis.

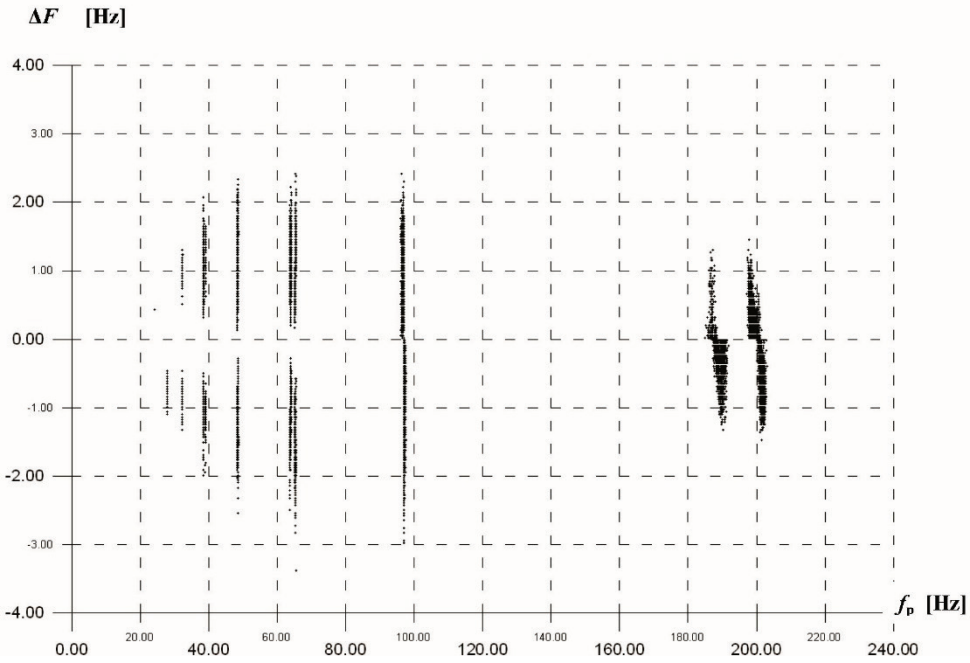

Fig. 2.11. Example of actual narrow-band characteristic sets obtained from a D-10/2 tach generator in a three-phase configuration from an SO-3W engine, at main shaft speed n = 15 600 rpm

By using the (f_p, ΔF) plane to plot the points with coordinates that constitute the parameters of successive deviations (e.g., according to Fig. 2.8.b for the negative deviation point 1) [82, 127, 129]:

a) ΔF_1, i.e., the extreme value of the instantaneous frequency deviation from the average frequency;
b) f_{p1}, hereinafter referred to as the mechanical process frequency, calculated as the converse doubled duration j of instantaneous frequency deviation Δt_{odj} from the reference level (usually, the average frequency level $f_{śr}$) determined by formula (2.10)), the successive characteristic points shown in Fig. 2.8.b are obtained.

Successive points with coordinates (f_{pj}, ΔF_j, n_j) obtained from the measurement form characteristic sets – an example of such sets is shown in Fig. 2.9.

2.2.4. General description of the relationship between a kinematic pair defect parameter and generator-transducer frequency modulation parameters

In the case of a propulsion unit, a distinction can be made between mechanical energy sources (e.g., a turbine of a turbojet engine powered by exhaust gas), transmission elements (transmitting rotary motion from the propulsion engine to mechanical energy consumers, such as gear assemblies, bearing nodes, couplings of various types) and elements that are mechanical energy consumers. One such consumer is the onboard generator (AC generator, DC generator, tach generator). Incomplete gearbox load conditions induce propulsion unit kinematic pair angular velocity modulations with an amplitude proportional to the magnitude of the defect, e.g., to the value of existing clearances or other parameters related to component wear or manufacturing and assembly errors. These modulations accumulate in the consumers (they modulate the rotational speed waveform for the drive shafts of these consumers) [183÷187], e.g., in the rotor of a generator-transducer in the form of an output velocity change ω_2 (Fig. 2.4.a), providing diagnostic information. An electromotive force (EMF) with an effective value is induced in the rotor's generator-transducer windings, as determined by formulae (2.5) and (2.6). The EMF induced in the windings reaches an instantaneous value equal to zero at the position corresponding to the rotor's coil reaching a magnetically neutral zone (Fig. 2.2 – zero lines 1, 2, 3, 4). AC generator's rotor angular velocity modulations ω_2 cause the electromotive force (EMF) induced in the armature to be exposed to frequency modulation. According to aeronautical standards (e.g., ISO-1540, EUROCADE ED-14/B/RTCA DO-160B), any cyclic or stochastic change in frequency is called a "frequency modulation". As this study primarily addresses aeronautical issues, it was decided to follow this definition of frequency. It deviates from definitions in other fields [67, 166, 220, 265, 294, 304], which usually characterize it as the number of complete periods per unit of time. Fig. 2.4.b shows the output voltage signal obtained from an AC generator, frequency-modulated by variations in the angular velocity of the onboard generator drive ω_2 (Fig. 2.4.a). The change in angular velocity ω_2 is shown in Fig. 2.6.b as a (discrete) change in frequency $f_i = f(t)$. Measuring the extreme values of the deviations from the level of the average frequency ($f_{śr}$), i.e., ΔF_1 i ΔF_2, and the inverse of doubled duration increments of the deviation from the level of the average frequency, enables illustrating the deviation of ΔF from the mechanical process frequency f_p (Fig. 2.8.b) [127, 129].

2.2.5. Conditions for the discrimination of primary signal spectrum components in the FAM-C and FDM-A methods

The change in rotational speed of the generator-transducer rotor can be represented by the sum of modulating sinusoidal functions derived from individual kinematic links. The steady-state response of a linear system to sinusoidal driving functions is equal to the sum of the sinusoidal responses to each sinusoidal driving function [1, 4, 41÷43, 52, 58, 139, 140, 154, 208÷211, 222, 250, 307, 314]. Each sinusoidal driving function associated with a faulty kinematic link after passing through propulsion system transmittance, retains its frequency, but changes its phase shift angle and amplitude [39, 40].

Research practical experience shows that a worn out given kinematic pair may lead to modulation-related changes of the angular velocity deformed from the sinusoid. Such an angular velocity waveform can be decomposed (Fourier decomposition) into harmonic components. The response of the propulsion unit (between the faulty link and the generator-transducer rotor – combined) is composed of harmonic components obtained in the generator-transducer rotor windings. Each harmonic of the driving signal generated from any propulsion unit link will have its response at the same frequency [39, 40] and at any point within the mechanical system, among others, in the generator-transducer rotor. As a result, the AC generator (synchronous machine) output voltage signal is frequency-modulated by the harmonics generated by individual kinematic links of the propulsion unit. The generator output voltage frequency waveform will therefore be a discrete representation of the conventional rotor coil angular velocity waveform in an AC generator rotor. There is a polarity of the voltage signal induced in the armature in the magnetically neutral zone (Fig. 2.2 – zero lines No. 1, 2, 3, 4), between the adjacent generator stator poles, i.e., the output voltage signal passes through the zero level. Therefore, the time increment between such polarity changes will be the discretisation time Δt_c. In order for a given speed harmonic with a frequency f_p to be distinguishable, the rated discretisation time Δt_N of the generator-transducer, i.e., the average duration of the crossing between adjacent neutral zones (Fig. 2.2), should satisfy the equation according to the modified Kotielnikov-Shannon theorem [264, 270, 305, 306]:

$$\Delta t_N \leq \frac{1}{2,5} \cdot \Delta t_{od} \tag{2.7}$$

where:

t_{od} – duration of the deviation of the observed instantaneous angular velocity value from the reference level.

Formula (2.7) is valid for small extreme deviations of instantaneous angular velocity ω. Based on Fig. 2.4, it can be construed that in the case of significant deviations (from the rated value):

– when decreasing the speed – the duration of the discretisation period increases,
– when increasing speed – the duration of the discretisation period decreases.

Thus, upon decreasing the speed, there is an increase in the time increments Δt_{ci} (Fig. 2.5) between successive zero lines (Fig. 2.2), and a decrease in the value of these increments when decreases occur in the said speed [129]. Therefore, formula (2.11), based on the assumption that the sampling period is invariant over time, can only be applied for relatively small instantaneous angular velocity amplitudes; in the case of larger ones, another formula can be used to satisfy the distinguishability condition:

$$\left\{\Delta t_{ci}\right\}_{\min} \le \frac{1}{2{,}5} \cdot \Delta t_{od} \tag{2.8}$$

where:

i – natural number representing the number of generator-transducer output voltage signal crossings through zero for the duration of Δt_{od} ; Δt_{ci} – duration of the output voltage waveform "half-period" (Fig. 2.5).

In order for the tested rotor instantaneous angular velocity change waveform (periodic or non-periodic) to be distinguishable, t_{od} must last for at least the duration corresponding to the crossing (of a conventional rotor coil) through 2.5 consecutive zero lines. Thus, prior to each measurement, it is necessary to carefully analyse what frequency of this mechanical phenomenon can be assessed by investigating the frequency of changes in the output voltage in a given type of generator. In the case of AC electrical machines, the rated frequency (carrier frequency) is:

$$f_N = \frac{n_N \cdot p}{60} \tag{2.9}$$

where:

n_N – rated rotational speed [rpm], p – number of pole pairs.

In the event of half-period (two-pole) counting (Fig. 2.5), this can be written as:

$$\Delta t_N = \frac{1}{2 \cdot f_N} \tag{2.10}$$

Substituting (2.9) into (2.10) enables obtaining the formula for the duration of the half-sinusoid ("half-period") of the rated voltage waveform $u(t)$ generated by an AC generator, at a given rated speed of its rotor:

$$\Delta t_N = \frac{60}{2 \cdot n_N \cdot p} \tag{2.11}$$

The rated frequency (the slot pulsation frequency at rated steady-state speed of the propulsion) for commutator electrical AC machines, at a specific calculated (based on rated revolutions and ratios) rated speed is:

$$f_N = \frac{n_N \cdot \dot{Z}}{60} \tag{2.12}$$

where:
$\dot{Z}$ – number of rotor slots.

After substituting (2.12) for (2.11), we obtain:

$$\Delta t_N = \frac{60}{2 n_N \cdot \dot{Z}} \tag{2.13}$$

Thus, for example, the GŻ-30 generator (a three-phase, non-contact AC generator with an excitation winding in the rotor and an armature in the stator), which has a rated frequency of f_N = 400 Hz, i.e., a half-sinusoid duration Δt_N = 1.25 ms, can be employed, based on formula (2. 13), to analyse angular velocity variations with a frequency below the limiting frequency f_{gr} (minimum rated frequency of the generator-transducer ensuring diagnostic signal distinguishability, i.e., the dynamics of angular velocity variations with a duration Δt_N – in the case in question, according to the relation (2.8) f_{gr} = 160 Hz).

The limiting frequency, provided by design features of AC generators, is usually sufficient to detect[3] rupture of one-way couplings, as well as eccentricity or skew of shaft connections, but it is commonly insufficient to detect inter-tooth backlash of gears or spline connections. It is impossible to monitor rolling bearings

[3] In addition to the detection phenomena associated with mechanical defects, there are issues related to the accuracy of the defect parameter measurement. These issues will be discussed in subsection 5.5 (verification of gearbox test results through modelling).

in most designs [162, 163, 173, 175, 176, 178, 179, 185, 190]. Therefore, the primary author attempted to utilize onboard commutator DC generator pulsation component frequency modulation. The considerably higher rated frequency of commutator DC generators (compared to AC generators) enables multiplying the sensitivity of diagnostic measurement.

Based on numerous studies of real objects, it was found that the characteristic points of instantaneous frequency deviations (from the average frequency) in the (f_p, ΔF) plane accumulate into sets. It was experimentally determined that each of such sets characterizes the wear condition of a different propulsion unit kinematic link. An example of such sets is shown in Fig. 2.9. They will be called "characteristic sets" in the remainder of the paper since each depicts the technical conditions of a different mechanical element. At the same time, the position of such a set with respect to the abscissa axis depends on the installation location within the kinematic system of the tested propulsion unit, and more precisely, on the rated speed of this element. The shape of the set is characteristic for each mechanical subassembly and its failure type. An illustration of the diagnostic symptom is the change in frequency modulation of the generator-transducer output voltage ΔF depending on modulation process frequency f_p.

Voltage signal frequency measurements are not difficult. Measurement accuracy can be determined by internal measuring system generator (clock) frequency, the number of AC generator pole pairs, and the ratio between the AC generator shaft and the tested kinematic link. It should be added that frequency modulation is characterised (in contrast to amplitude modulation) by its high resistance to all kinds of interference, which is why it is so important in the diagnostic process [67, 155]. This is why frequency modulation (FM) was first applied in radio broadcasting and telecommunications over short distances, since the primary advantage of this system is being highly insensitive to interference [67, p. 7]. Its additional benefit is that, in practice, a diagnostic test involves a certain current load on the generator-transducer (usually of approx. 10÷20% of the rated current), which induces strong attenuation of low-energy interfering signals, e.g., conducted or radiated radio interference.

2.2.6. Method for signal acquisition and analysis using DC generators-transducers

As in the case of the FAM-C method [88], the FDM-A method [25] is based on frequency modulation measurement. DC generators employ a slot pulsation component [24, 89, 106, 126]. Other pulsation types are treated as interference. Since the slot pulsation component is not symmetrical with respect to the time axis, it is possible to count crossings through zero only under full pulsation periods. In

addition, all phenomena related to the representation of tested propulsion unit kinematic pair defects through frequency modulation phenomena are analogous. In order for a given harmonic ω with a frequency f_p to be distinguishable, the rated discretisation time Δt_N of a generator-transducer, i.e., the average duration of the crossing between adjacent rotor slots (between stator neutral zones in the FAM-C method) should satisfy the equation (consistent with the Kotielnikov-Shannon theorem [264]), which can be expressed by the formula:

$$\Delta t_{odj} \geq \sum_{i=1}^{i>2} \Delta t_{ci} \tag{2.14}$$

where:

i – natural number representing the number of generator-transducer output voltage signal crossings through zero during the j deviation of the waveform $\Delta t_{odj;}$;

Δt_{ci} – duration of generator-transducer output voltage waveform periods.

The role of individual output voltage pulsation components in a commutator DC generator-transducer in the process of diagnosing the tested propulsion unit or in its disturbance is discussed below.

2.2.6.1. General characteristics of DC generator commutator pulsation

In the classical, academic view, a commutator DC generator is represented by a schematic diagram (Fig. 2.12.b) and the course of its electromotive force – as in Fig. 2.12.a. A commutator DC generator consists of:

- a stationary stator, which can be pictured as a pair of permanent magnets (Fig. 2.2: "N" – north pole, "S" – south pole) generating a constant magnetic field, with intensity B and direction from "N" to "S";
- a rotor rotated by an external mechanical force with an instantaneous angular velocity of ω_2. Coils are wound on the rotor, wherein the electromotive force e is induced. The electromotive force (EMF) induced herein can be described by the formula:

$$e = \left| k \cdot B \cdot \sin(\omega_2 t) \right| \tag{2.15}$$

where: k – design factor of a given generator, B – magnetic induction, ω_2 – instantaneous angular velocity of the generator rotor;

- a commutator, i.e., a ring made of electricity conductive material mounted on the rotor; this ring is divided into segments, which are electrically isolated from each other – forming the so-called "commutator bars"; each stave is connected to the end of the coil; the commutator acts as a mechanical current rectifier;
- electric brushes (commutator brushes – Fig. 2.16.a) "+" and "-", which slide on the commutator staves. Wires that conduct current to consumer circuits are connected to the brushes.

So as to increase the value of induction B, the coils are placed on the core made of a silicon sheet package, hence strengthening the electromotive force (EMF) (e) by approx. 10,000 times. In order for the coils on the rotor to be well bound mechanically with the core, they are arranged in specially prepared grooves called "slots". On the rotor core cross-section, these slots are shaped like teeth, hence, the term "rotor teeth" was used hereafter [49, 72, 160, 189, 258]. A comparison of the theoretical waveform for the function described by the equation (2.19), Fig. 2.16.c, with the real waveform of a commutator generator pulsation component (Fig. 2.12.a) shows no similarity between the two. This is because an unloaded commutator DC generator (for a generator loaded below 20% of the rated current) is dominated by slot pulsations and not commutator pulsations. Both pulsation types are presented in Figs. 2.15 and 2.16.

Slot pulsations arise as a result of a reluctance change caused by the rotation of a toothed rotor (Figs. 2.12.a, 2.15.a, 2.16). The frequency of slot pulsations $f_ż$, pursuant to source literature [309, 310], can be expressed by the formula (2.16). A detailed review of the properties exhibited by this pulsation is included in the next subsection (2.2.6.2).

Polar pulsations are associated by source literature with the so-called "rotational pulsations", due to their mutual similarity. The phenomenon of polar and rotational pulsations is evident in the form of a periodic increase in the peak voltage (either negative or positive, depending on the magnetic polarity of the stator pole) when the rotor coil passes under the pole piece – there is an extreme (A_{max}, A_{min}) of the voltage modulation envelope waveform shown in Fig. 2.15.a [106, 109, 309÷311]. This envelope modulation frequency is directly proportional to the product of the number of stator poles and the rotor angular velocity, while amplitude depth is proportional to the change in magnetic reluctance between the rotor and stator. Polar pulsation frequency f_b can be expressed through the formula:

$$f_b = 2p \cdot n/60 \tag{2.16}$$

where:
p – number of stator (DC generator) magnetic pole pairs.

The pole modulation signal carries information on the anisotropy (geometric variation of the generator's magnetic circuit magnetic sheet permeability) of the generator's magnetic circuit sheets in terms of the diverse magnetic flux values for successive stator pole pieces.

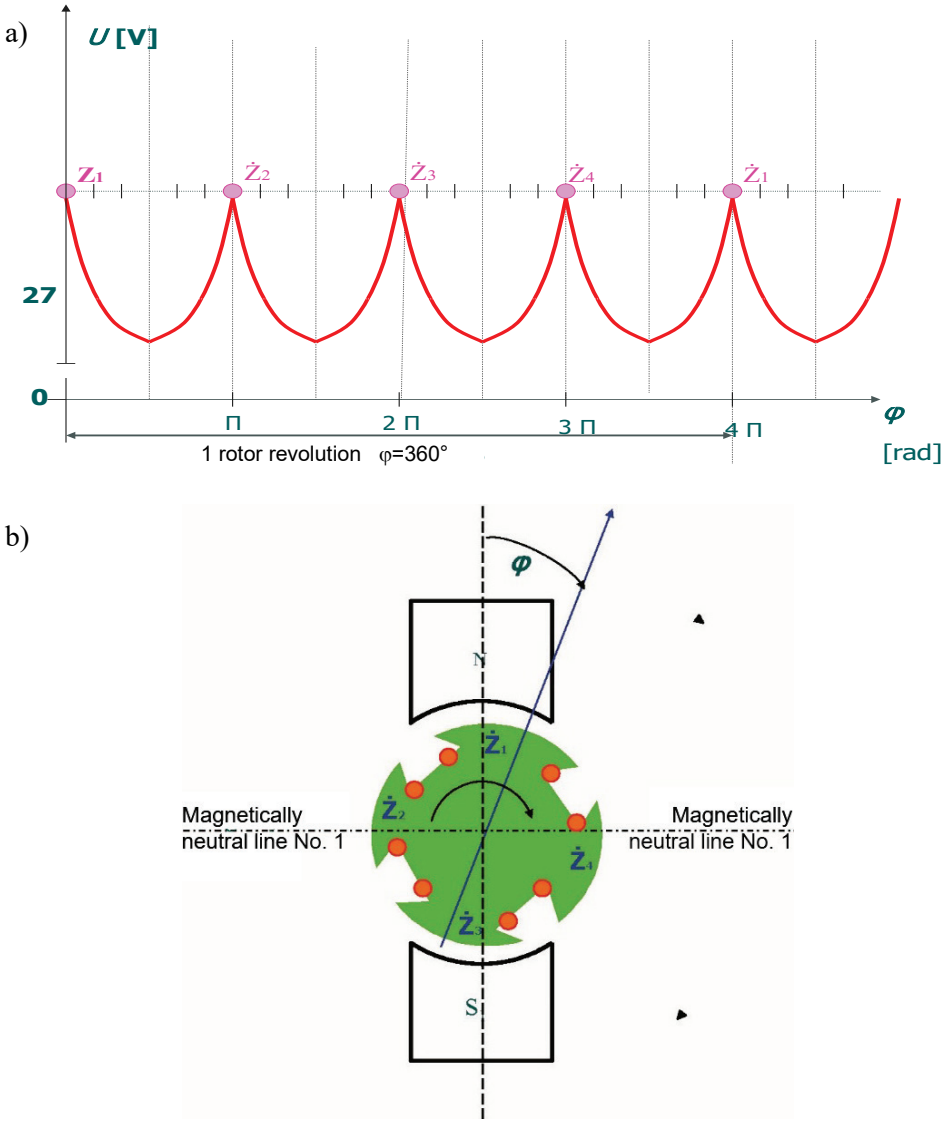

Fig. 2.12. Rotor with four slots and a graph of electromotive force variations between commutator brushes of a DC generator: a) waveform for components of voltage (electromotive force; EMF) induced in individual rotor coils – formation of commutator pulsation, b) overview

Envelope voltage amplitude is exposed to diversification– successive envelope peaks will reflect the varying permeability of the magnetic sheets in the magnetic circuits of successive stator pole pieces. These sheets exhibit a higher magnetic permeability in the rolling direction, than in the transverse direction. As a result, the magnetic resistance (reluctance) for one stator pole may be consequently higher than for another. Thus, changes in the output voltage envelope amplitude value (pulsation component) are observed. This can be conventionally called the "amplitude effect". However, there can also be a change in the phase value of the pulsation component envelope due to the angular shift of the poles relative to the reference pitch. These two polar pulsation effects (amplitude and phase) can be called the "signature" of a given generator unit. Unfortunately, this is topped up by the influence of the rotor bearing node and the commutator node (in the mechanical sense), the mechanical angular decelerations of which introduce "their" changes into the generator-transducer output voltage signal envelope. Therefore, in the future, it will be possible to precisely determine both the stator pole piece shift and the magnetic anisotropy of the magnetic circuits in individual stator poles.

Source literature usually associates polar modulation with **rotational modulation** [310, 311], which is characterised by the fact that the frequency of such modulation is equal to the frequency of the first, possibly the second harmonic (in some cases, the first sub-harmonic) of the generator rotor speed. Rotational modulation carries diagnostic information on the resultant generator rotor anisotropy. Theoretically, it is technologically mitigated by angular (by one angular pitch) displacement of successive (silicon) sheets during rotor bundling. The rotational modulation signal also carries diagnostic information on manufacturing and assembly geometry errors [310, 311] associated with:

- DC generator manufacturing, especially geometrical dimension inaccuracies, manifested by asymmetry in the air gap between the stator and the rotor;
- DC generator assembly geometry, such as the generator rotor shaft axis and drive shaft axis parallel displacement error, sometimes referred to as the "eccentricity error", and the generator rotor shaft axis and drive shaft skewness error.

In order to reduce polar and rotational pulsations, it is usually recommended to [310]:

- use selected rolling bearings with reduced radial clearance,
- carefully machine bearing discs leading to reduced eccentricity of the rotor rotational axis relative to the stator axis of symmetry,
- accurately set the symmetry of the rotor package during assembly relative to its axis of symmetry– such an offset should not exceed ±0.01 mm,
- minimise rotor unbalance.

Commutator pulsations of the DC generator output voltage are related to the brushes-commutator interactions. As the armature spins, the brushes alternately short-circuit a different number of winding coils, which leads to a change in the number of coils in parallel branches and induces periodic voltage pulsations on the brushes [109, 112, 159, 163, 240, 288, 289, 308÷310]. The frequency of these pulsations f_k depends on the number of commutator bars, which can be expressed by the formula:

$$f_k = K\,n\,/\,60 \tag{2.17}$$

where: K – number of commutator bars (staves).

According to numerous studies, commutator pulsations also include voltage pulsations caused by sparking occurring under the brushes during generator operation. This phenomenon, described in source literature, is caused by:

- unevenness of the commutator surface, causing mechanical vibrations of the brush-commutator interface,
- self-induction EMF, generated in a commutated coil that is shorted or opened by the brush,
- transformation EMF,
- rotation SEM – if part of the commutated coil gets under the stator magnetic field, sparking will occur. Therefore, constructors try to design the generator so that the commutated coil is in a magnetically neutral zone when the two commutator staves are shorted.

In order to prevent sparking under the brushes arising due to mechanical reasons, the surface of the commutator should be particularly smooth and the brushes carefully lapped [288, 289].

2.2.6.2. Slot pulsations as a carrier of diagnostic information on the condition of a propulsion unit

The phenomenon of diverse induction AC generator slot pulsations is well known [308, 309]. These generators do not have rotor windings – the useful signal is received from a winding on the stator. The rotor has slots (teeth), which enables permanent magnet field strength modulation. Slot pulsations in these generators are the primary phenomenon related to the formation of a diagnostic signal. Since there are no windings in the rotor, as in a classic commutator DC generator, only the variable component of the slot and pole pulsations is generated (commutator pulsations do not occur). According to the available source information, in order to obtain an output voltage signal as similar to a sine wave as possible, an oblique

tooth shape is most often used in induction generators. Rotors with dovetail or T-shaped slots are used in induction generators very rarely [129, 309÷311]. This produces an asymmetrical output voltage shape. On the other hand, this slot shape type is common in classic onboard commutator DC generators – it guarantees that the windings can be correctly mechanically fixed (locked) into the rotor slots. The time increments between slot pulsation waveform crossings through a preset reference level for the generator rotor angular velocity ω_2 = const will only depend on the angular error of the tooth notch. Since these errors occur cyclically after each full rotation of the rotor, they are easy filter out. In turn, fact of the rigid angular position of the slots relative to each other is undeniable. Therefore, for ω_2 = var, the time increments between successive crossings through the e = 0 V level (after filtering out possible rotor slot notch errors) will be a measure of instantaneous changes in the angular velocity of the rotor. The described slot pulsation properties became the reason for treating them as a source of diagnostic information on the technical condition of a generator propulsion unit, which gave rise to the development of the FDM-A method [25]. Measuring the slot pulsation amplitude value enables locating discontinuities in rotor windings. Based on the data collected during the primary author's experimental studies [126], it can be noted that a winding break is followed by a reduction in the relative value (related to the rms value of the generator output voltage U_w) of slot pulsations $\delta_{\dot{Z}}$. This value can be expressed through the formula:

$$\delta_{\dot{Z}} = \sum_{m=1}^{m=n} \frac{(U\max m - U\min m)}{\dot{Z}U\mathrm{w}} \cdot 100\% \tag{2.18}$$

where: m – natural number, number of the consecutive slot pulsation period, $U_{\max m}$ – maximum instantaneous value of the pulsation voltage component in a given slot pulsation period m, $U_{\min m}$ – minimum instantaneous value of the pulsation voltage component in a given slot pulsation period m, $\dot{Z}$ – number of rotor slots, n – number of observed pulsations.

At the same time, virtually imperceptible changes (decreasing) of the output voltage rms value ΔU_w, particularly for lower ω_2 values, follow a winding rupture. The relative value of these changes when one winding of the rotor breaks δU_w does not exceed 0.01%.

2.2.6.3. Polar pulsations

The phenomenon of polar pulsations can be well observed in the output voltage waveform of a DC generator in the form of output voltage waveform amplitude

envelope modulation (Fig. 2.13). Modulation frequency is directly proportional to the product of the number of stator poles and the rotor angular velocity, while amplitude depth is proportional to the change in magnetic reluctance between the rotor and stator. This signal carries information about the anisotropy of the generator's magnetic circuit sheets [129, 309÷311]. Modulation can lead to small errors in ΔT_i. measurement. It is easy to filter out due to its repetitive nature, which is specific to a particular generator unit. The relative value of polar pulsations δ_b can be expressed by the formula:

$$\delta_b = \{(U_{maxo} - U_{mino})100 / (U_{maxo} + U_{mino})\}_{MAX} \tag{2.19}$$

where: o – natural number denoting the number of the consecutive polar pulsation period; U_{maxo} – maximum instantaneous value of the polar pulsation voltage component; U_{mino} – minimum instantaneous value of the pulsation voltage component during a given period o.

Polar pulsations carry several diagnostic information [106, 108, 109, 126, 132, 310]:

a) the phase parameter indicates possible errors in the geometrical distribution of stator poles,
b) the pulsation amplitude (of the envelope waveform in Figs. 2.13 and 2.14) is indicative, in general, of an uneven magnetic field distribution under stator magnetic poles and, in certain cases, also of a short circuit (Fig. 2.15) or rotor or stator winding interruption [106, 109, 132, 288, 289]:
   – if polar pulsation amplitude reaches increased values close to rotor slot pulsation amplitude, this indicates an overload of one coil due to increased leakage conductance of its insulation or a partial short-circuit with the ground or between rotor coils in the respective slot (Fig. 2.15),
   – if the polar pulsation amplitude (Fig. 2.15) reaches values that are not uniform throughout the entire period, e.g., one peak value of this envelope decreases per one rotor revolution, this indicates an overload of one coil due to increased leakage conductance of its insulation or a partial short-circuit with the ground or between one stator pole coils;
   – if the polar pulsation amplitude (Fig. 2.13) decreases uniformly throughout the rotor rotation period, this may indicate a broken rotor winding.

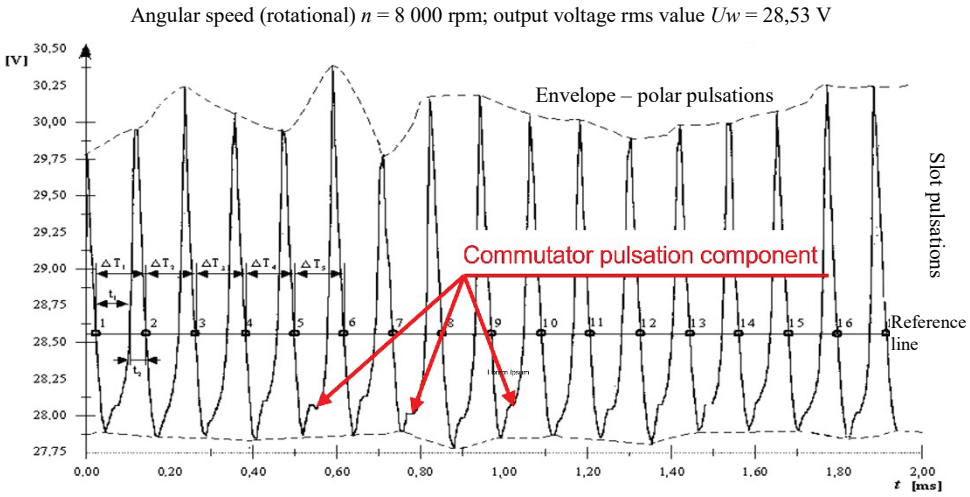

Fig. 2.13. Pulsation voltage component changes in the GSR-ST-1200WT commutator DC generator at minimum load (I≈1A)

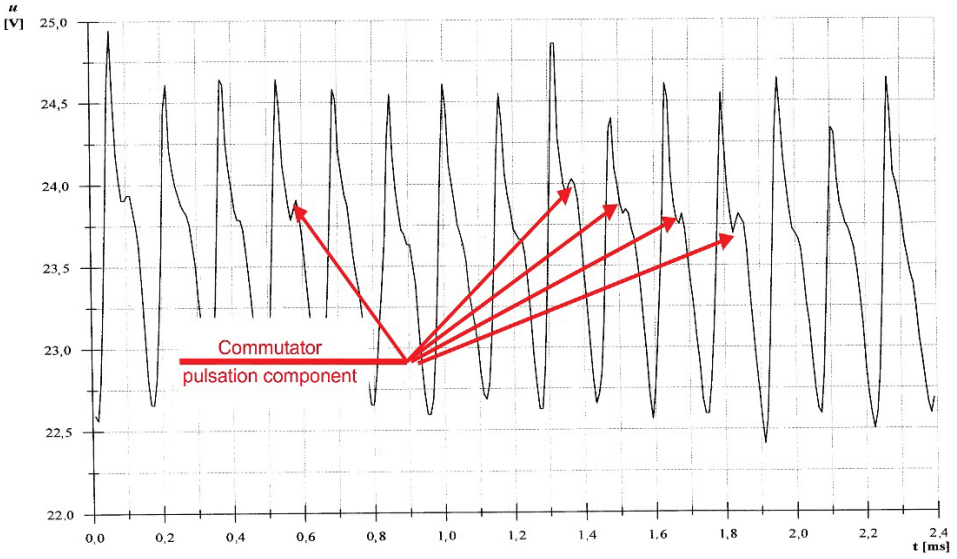

Fig. 2.14. Pulsation voltage component changes in the GSR-ST-1200WT commutator DC generator at rated load (I≈300 A)

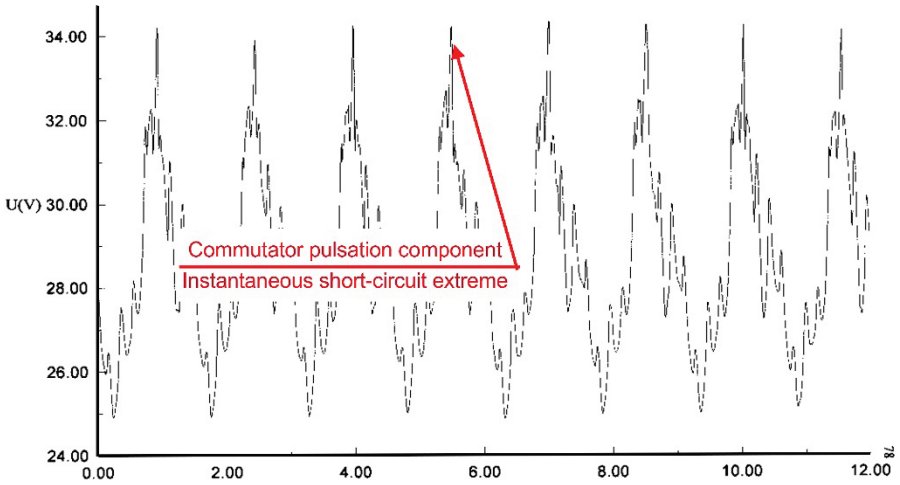

Fig. 2.15. Pulsation voltage component changes in the GSR-ST-1200WT commutator DC generator at rotor winding short-circuit

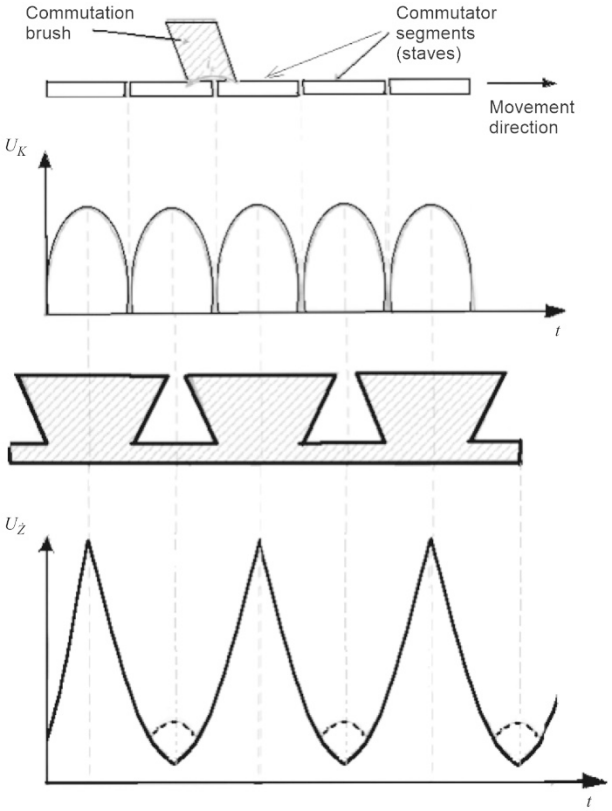

Fig. 2.16. Pulsation component waveform for a commutator DC generator

2.2.6.4. Commutator pulsations

The phenomenon of commutator pulsations (Figs. 2.14 and 2.16.d) is not yet applied in the FDM-A method. Previous studies implemented under the primary author's direction [106, 109, 111, 112, 126] have demonstrated that the amplitude of these pulsations is directly proportional to the current load level. When the DC generator is overloaded, the commutator pulsation amplitude exceeds the value of slot pulsations. Therefore, in a state of significant load on the generator-transducer, commutator pulsations would be measured by a measuring system – rated frequency would be accordingly higher and would be expressed by the formula [126, 129, 308÷311]:

$$f_N = \frac{n_N \cdot (\dot{Z} + K)}{60} \tag{2.20}$$

In current embodiments, the pulsation component is mitigated by prescriptively minimising the load on the generator-transducer below 10% of rated power. It is planned to employ the commutator pulsation component to diagnose the state of the electrical and magnetic generator circuits rather than the propulsion unit [49, 288, 289]. This, of course, requires numerous analyses and studies. The phase angle of commutator pulsation component periods is too unstable relative to the phase angle of slot pulsation. This is due to both the angular oscillations of the carbon brushes and the strongly non-linear phenomena associated with commutation and the electric arc [288÷289]. Therefore, the commutator pulsation component, at this stage of the research, is considered by the author as an interference signal. Fig. 2.16 shows the interrelationships between commutator pulsation, slot pulsation, rotor slot position and commutator bars. Tests conducted in the course of operating the GSR-ST-12000 WT[4] DC commutator generator show that at load currents below 10% of the rated value, the commutator pulsation amplitude is almost imperceptible compared to slot pulsations (Figs. 2.13 and 2.16.e). However, at rated load, these pulsations are already clearly visible on the output voltage waveform (Fig. 2.14). In such state, the value of the commutator pulsation amplitude reaches 60÷80% of the slot pulsation amplitude value. Angular displacements of individual commutator pulsation half-sinusoids (Fig. 2.13) vary with respect to the angular position of slot pulsations and modify their amplitude – they undergo individual angular and amplitude displacements during mechanical vibrations of the brushes in the holder and in the course of changes in the generator current load level. In the light of the

[4] GSR-ST-1200WT – generator-starter used as the primary source of electricity on MiG-21 fighters of all series – number of rotor slots $\dot{Z} = 64$, number of commutator bars $K = 128$.

above, commutator pulsations cannot be applied to diagnose a propulsion unit. Instead, they can be used to diagnose the commutator-brush node. At rated load (the current rating for GSR-ST-12000 WT under operation is $I_N = 300$ A), the commutator pulsation peak value reaches a level of approximately 60% of the slot pulsation amplitude (Fig. 2.12). When one of the rotor windings is shorted [108, 110, 132], the commutator pulsation peak value exceeds the amplitude of slot pulsations severalfold (Fig. 2.15). This means that tracking the commutator pulsation phase shifts will enable diagnosing the condition of the generator commutator-brush node. On the other hand, analysing amplitude changes enables detecting short circuits in the coils [108÷111, 132].

2.2.6.5. Compared sensitivity of the FAM-C and FDM-A methods

Prior to any FAM-C or FDM-A measurement, a diagnostician should carefully analyse the regularity of the mechanical phenomenon frequency he/she is able to assess by investigating the generator output voltage change frequency. For an AC generator, the rated frequency f_N can be expressed by the formula (2.13). For a DC generator, the slot pulsation frequency can be expressed by the formula (2.16).

Therefore, an AC generator, e.g., the GŻ-30 generator from a MiG-29, with a hydraulically stabilised input speed of 12,000 rpm, generating $f_N = 400$ Hz (i.e., half-sinusoid duration $\Delta t_N = 1.25$ ms) can be employed to analyse angular velocity variations with a frequency no higher than $f_{gr} = 320$ Hz. Such a low electromechanical sampling frequency [129] is usually sufficient for analysing quasi-resonant states of gearbox structures on a macro scale, but in most cases, it is mostly insufficient for the analysis of vibrations associated with the operation of gears or rolling bearings. Based on the design assumptions, the inter-teeth backlash has a value that depends on the tooth modulus (according to [18, 56, 152, 169, 245], this backlash "...usually ranges from 0.03 to 0.07 of the modulus value..."). Gears usually have between 8 and 200 or more teeth, thus so many individual inter-tooth backlash values are manifested per revolution. Therefore, at the rated speed of the generator rotor $n_N = 100$ rpm and a kinematically related gear wheel with 10 teeth, the rotor will complete a full rotation (by 360°) in 10 milliseconds. Decelerations with a duration of 0.03 ms to 0.07 ms, i.e., an average of 50 μs, will be marked every 1 millisecond; this range was initially adopted as the backlash "measurement" resolution range (class). In order to satisfy the Kotielnikov-Shannon condition (the test frequency must be at least 2.5 times the tested frequency [210, 264, 305, 306]), the duration of the rated frequency half-sinusoid f_N (calculated as the product of the number of pole pairs and the rated speed) must be 2.5 times shorter than the maximum time increment (Δt_c) during the period f_{od} of rotor deceleration when selecting the backlash. The duration of the frequency semi-sinusoid f_N would, therefore, have

to be at least $1/2f_N$ μ s: 2.5 = 20 μs. This duration will be ensured by a generator with a pole count of p = 10 ms ÷ 20 μs = 500 poles, i.e., with a pole pair count of p = 250. Assuming a backlash measurement resolution of 0.03 ***m***[5], the duration of the half-sinusoid at rated frequency would have to be at least 30 μs/2.5 = 16 μs; hence a generator with a pole count of $2p \cong 700$ poles, i.e., p = 350 pole pairs, would be required. Table 1 demonstrates that this condition is not met by any of the current aircraft generators. It is, thus, required to adopt a lower resolution class that will be easier for aircraft generator designs to meet.

Table 1

Minimum number of generator-transducer pole pairs required to detect meshing backlash with a given backlash measurement resolution

Number of teeth	10					30				
Assumed resolution	0.05 ***m***	0.10 ***m***	0.20 ***m***	0.50 ***m***	0.70 ***m***	0.05 ***m***	0.10 ***m***	0.20 ***m***	0.50 ***m***	0.70 ***m***
Minimum number of pole pairs	250	125	62	25	16	750	375	186	75	48

Therefore, for the GSR-ST-12000WT generator with 64 slots, it is possible to measure backlash values of a 30-teeth wheel with a modulus resolution of 0.55 at most. Only large (more than 50%) teeth chipping can therefore be detected by this generator. Comparisons of the output voltage waveforms obtained from DC and AC generators show a significant difference in the pulsation period duration [127, 129]. This is due to the engineering differences between these generators. In operating practice, several to several dozen more output voltage periods are induced during one full rotor revolution of a DC generator than during one full rotor revolution of an AC generator. The resolution of the FAM-C and FDM-A methods depending on the different types of generators is shaped proportionally to these relationships.

2.2.7. Summarized description of the FAM-C and FDM-A methods

This chapter includes a description of the FAM-C and FDM-A methods. It first describes the theoretical and practical premises arising from the primary author's operational practice that inspired him to develop the FAM-C and FDM-A

[5] Notation: "0.03 ***m***" means 3% of the modular pitch value "***m***".

measurement systems and apply them in practice. The implementation of the measurement and diagnostic analysis is described. The physical phenomena occurring in generators have also been thoroughly discussed. These generators act as transducers for the diagnostic methods in question. This chapter is in the form of analytical considerations required to understand the idea behind the FAM-C and FDM-A methods. Having gathered the analytical source material, it is time to synthesise the themes covered herein. At the same time, it will be an attempt to formulate a hypothesis (set of hypotheses).

2.3. Research hypotheses – diagnostic features of generator-transducers and their application within the FAM-C and FDM-A methods

2.3.1. Specific features employed at the primary sampling (electromechanical) stage

FUNDAMENTAL FEATURE

Each DC or AC synchronous generator coupled by a rigid pull rod (with limited energy dissipation) to a propulsion unit is a discrete-frequency transducer for the motion dynamics of kinematic pairs in that propulsion unit that enables monitoring its technical condition.

C1. Additional feature 1 – applies to dynamics phenomena within a propulsion unit monitored using the FAM-C and FDM-A methods. A kinematic pair is observable under the following conditions

The observed kinematic pair is in the main path of the mechanical power transmission between the primary energy source (e.g., a gas turbine and generator-transducer) – it induces frequency-phase modulations in the generator-transducer.
The observed kinematic pair is located outside the primary path of mechanical power transmission (located along the side path) – it can induce frequency-phase modulations in the generator-transducer if the moment of inertia of this pair (its vibration energy) is significant enough to modulate the kinematic chain between the side path and the generator-transducer.

C2. Additional feature 2 – applies to the processing of dynamic phenomena within a propulsion unit by a generator-transducer:

1) Each generator-transducer has its own rated frequency (for a given rated speed), which can be directly considered as the sampling ("electromechanical") frequency in the sense of the Kotielnikov-Shannon theorem.

At the same time, the generator-transducer rated frequency may be directly considered as a HF carrier frequency, according to the theory of modulation [230].
A generator-transducer rotor rotates synchronously to its input speed.
The input shaft is a summation of angular oscillations ($\omega_j = \omega_{Nj} \pm \Delta\omega_j$) from individual *j*- kinematic pairs of the monitored propulsion unit (including subcarrier frequencies ω_{Nj} of individual kinematic pairs obtained from the kinematic diagram and the oscillations $\Delta\omega_j$ depending on the size and type of mechanical defect).
The waveforms of subcarrier pulsations (rated frequencies of individual kinematic pairs) $\omega_{Nj}(t)$ and the waveforms of vibrations $\Delta\omega_j(t)$ (dependent on the size and type of mechanical defect of individual kinematic pairs) are synchronised with each other.
Points 3÷5 indicate that frequency modulations obtained at the output (in the output voltage) of the generator-transducer carry synchronous pulsation-value relationships: $\omega_j(t) = \omega_{Nj}(t) \pm \Delta\omega_j(t)$.

C3. Additional feature 3 – applies to the process of detecting a signal emitted by the generator-transducer (implemented after secondary sampling – subsection 2.3.2). Detecting a signal emitted (to the mains) by the generator-transducer using the FAM-C and FDM-A[6] methods enables:

- removing the carrier wave,
- creating images of characteristic sets for individual kinematic pairs,
- identifying individual kinematic pairs by their subcarrier frequencies (e.g., based on the kinematic diagram of the monitored propulsion unit),
- identifying the bands occupied by individual characteristic sets reflecting kinematic pairs based on the image recognition theory [5, 73, 221].

C4. Additional feature 4 – applies to analysing a signal emitted by the generator-transducer. Identifying the wear and tear of individual kinematic pairs requires:

1) Calculating the height values of individual characteristic sets.

Determining (calculating) the limits (upper and lower) of the bands occupied by individual kinematic pairs.

[6] In addition, the DC component of the signal emitted by the generator-converted is removed under the FDM-A method (as opposed to the FAM-C method).

Based on 2 and 3, determining coefficients that characterise the motion dynamics of individual kinematic pairs.
Analysing the technical condition of individual kinematic pairs within the monitored propulsion unit, based on a comparison with the benchmarks-models (Chapter 3 of this study: *Relationships between individual defects of mechanical propulsion unit kinematic pairs with FAM-C and FDM-A imaging*).
Error analysis (Chapter 4 of this paper: *Metrological properties of the FAM-C and FDM-A methods*).
The structural analysis of the degree the technical condition of individual kinematic pairs impacts the hazard status of the entire propulsion unit (Chapters 5 and 6 of this study).

The operations aimed at verifying the aforementioned features included:

a) Discrete-frequency modulation measurements with "serial" FAM-C or FDM-A instrumentation on real objects or their physical and mechanical or physical and electronic models:
   – active experiments on propulsion units (inflicting targeted mechanical damage and observation of modulations from generator-transducer signals),
   – active experiments on physical models of propulsion units in an AFIT laboratory (inflicting targeted mechanical damage and observation of modulations from generator-transducer signals),
   – active experiments on physical electronic models in the form of a system composed of generators and transducers at an AFIT laboratory involving the emission of frequency modulations similar to a specific-type generator in the event of specified mechanical faults of a propulsion unit,
   – passive experiments on propulsion units– observation of modulations from the object's generator-transducer signals during operation with FAM-C or FDM-A monitoring [20] (with conclusions drawn in relation to the wear of propulsion unit components), followed by dismantling of the subassembly and mechanical measurements.
b) Mathematical and physical analyses:
   • mathematical modelling,
   • comparative analyses with previously established knowledge in the field of diagnostic technology (other than FAM-C and FDM-A), e.g., TTM methods.

The FAM-C [88] and FDM-A [25] methods apply the TTM idea, which is based on calculating the time increments between the appearance of a successive physical element under a sensor. In classical TTM, this physical element is the turbine or compressor blade – in the FAM-C and FDM-A methods, it is a rotor tooth.

A generator-transducer has its rotor with slots and its stator with pole pieces. The toothed rotor is the equivalent of blades in the TTM, while the stator is the equivalent of sensors in the TTM. "Sensors" in FAM-C and FDM-A form a closed, evenly spaced ring. At the same time, slots are the equivalent of blades in the TTM. As noted earlier, generator-transducer slots have a much higher mechanical stiffness. Therefore, while only the classical TTM represents only local blade (turbine or compressor) jitter spectrum phenomena, the FAM-C and FDM-A methods represent the jitters of various kinematic pair vibrations within a monitored propulsion unit, i.e., numerous elements outside the local vibration jitter spectrum of generator-transducer teeth:

$$\{\zeta\Delta\omega_1 + \omega_{1N}, \zeta\Delta\omega_2 + \omega_{2N}, \zeta\Delta\omega_3 + \omega_{3N}, \dots, \zeta\Delta\omega_j + \omega_{jN}, \dots, \zeta\Delta\omega_m + \omega_{mN}\} \quad (2.21)$$

whereas: $\omega_{kN}=2\pi f_{kN}$

where:
m – number of observed (supervised) kinematic pairs,
f_{jN} – subcarrier frequency of kinematic pair no. j.

These vibrations can be presented, according to source literature [155, 228, 229], in the form of an upper and lower band with a zero subcarrier waveband (Fig. 2.17). The strip consists of correlated jitter bands (various oscillations of different kinematic pairs of the monitored propulsion unit) ζ_j and their subcarrier pulsations ω_{jN}. The generator-transducer transfers jitter oscillations of the different bearing nodes (kinematic pairs) into the HF band, thus providing them with immunity to all kinds of interference. The result is an HF signal:

$$2\pi f\mathrm{NG} + \sum_{j=1}^{j=m} \pm(\zeta\Delta\omega_1 + \omega_{1N}) \pm (\zeta\Delta\omega_2 + \omega_{2N}) \pm \cdots \pm \left(\zeta\Delta\omega_j + \omega_{jN}\right) \dots \pm (\zeta\Delta\omega_m + \omega_{mN}) \quad (2.22)$$

for kinematic pairs ($j = 1 \div m$) of the tested propulsion unit. Therefore, a main line f_{jN} with sidebands $\Delta\omega_j$ symmetrical relative to f_{jN} (Fig. 2.18) is formed according to the theory of teletransmission and radio engineering.

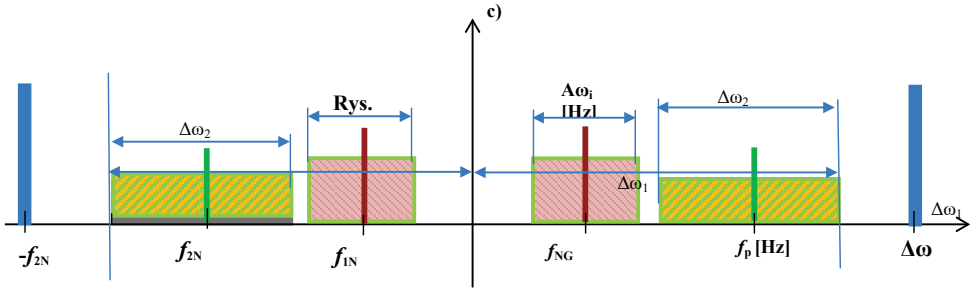

Fig. 2.17. Initial diagnostic signal lines – speed fluctuations of individual (two) kinematic pairs of the monitored propulsion unit: $\Delta\omega_1$, $\Delta\omega_2$ – instantaneous speed variation bands (reflecting Δn_1, Δn_2 speed variation bands) of individual kinematic pairs (No. 1, No. 2) in the tested propulsion unit; f_{1N}, f_{2N} – subcarrier (rated) frequencies of individual kinematic pairs (No. 1, No. 2) in the tested propulsion unit

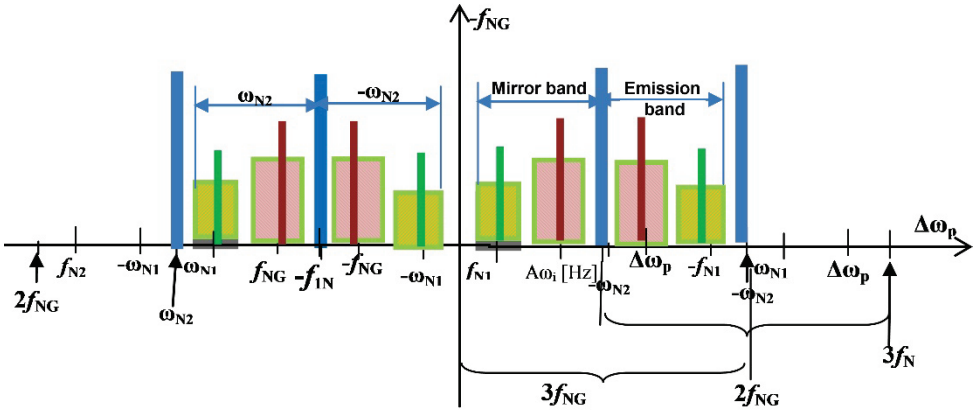

Fig. 2.18. Relationships between the main line of the carrier "wave" generated by a generator-transducer (f_{NG}) and the subcarrier frequencies of individual kinematic pairs in the propulsion unit under study: $\Delta\omega_1$, $\Delta\omega_2$ – instantaneous speed variation bands (reflecting Δn_1, Δn_2 speed variation bands) of individual kinematic pairs (No. 1, No. 2) in the tested propulsion unit; f_{1N}, f_{2N} – subcarrier frequencies of individual kinematic pairs (No. 1, No. 2) in the tested propulsion unit

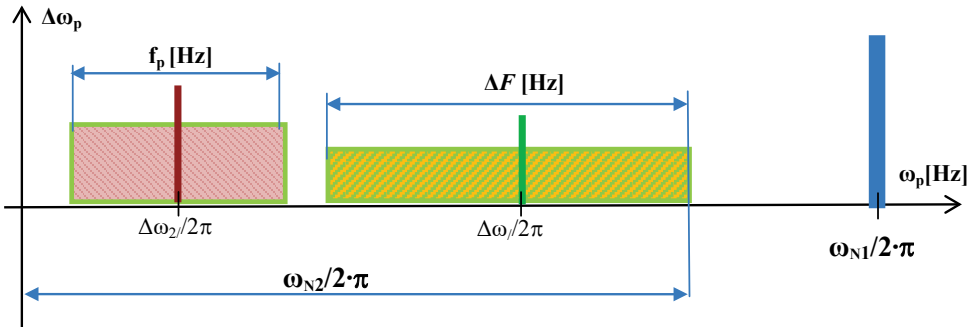

Fig. 2.19. Images after FAM-C or FDM-A detection: $\Delta\omega_1$, $\Delta\omega_2$ – instantaneous speed variation bands (reflecting Δn_1, Δn_2 speed variation bands) of individual kinematic pairs (No. 1, No. 2) in the tested propulsion unit; f_{1N}, f_{2N} – subcarrier (rated) frequencies of individual kinematic pairs (No. 1, No. 2) in the tested propulsion unit

After demodulation, the line with a carrier frequency f_{NG} is removed and the bands of individual kinematic pairs with their associated subcarrier frequencies are analysed (Fig. 2.19). According to the Kotielnikov-Shannon theorem [124, 127, 129, 155, 231, 303, 306], in the case of non-synchronised sampling, the maximum frequency distinguishable by the method would be determined by the relation:

$$f_{max} < 0{,}5 \cdot f_N \tag{2.23}$$

where:
f_{max} – maximum frequency (upper limit frequency of the generator-transducer observability), f_N – generator-transducer rated frequency.

The first sampling is an electromechanical, synchronised with the observed speed fluctuations within the tested propulsion unit [129], so the upper frequency of the recognised primary diagnostic signal f_{max} will shift significantly upwards (relative to the Kotielnikov-Shannon condition). According to the primary author's practical experiments, the sampling level reaches:

$$\frac{f_{max}}{f_{NG}} \approx 0.3\, f_{NG} \tag{2.24}$$

The lower level, on the other hand, is limited by the technical capabilities of the secondary sampling equipment [129] – it is limited by the capacity of the counter card and the throughput of individual pulse packets from the counter card to

computer memory, as well as the need to reset[7] the pulse gating circuit (activated in the electronic attachment, when the generator output voltage signal passes zero) [161].

A multi-phase physical measurement configuration of generator-transducer enables obtaining a much higher value of f_{max}, i.e., observability upper limit. This is achieved by assembling the phase vectors on a single time axis (in measurement practice, by simultaneously and independently measuring successive time increments on each phase of the generator-transducer) and then plotting the data onto a single time axis. Therefore, a three-phase measurement configuration allows to obtain a threefold increase in the carrier frequency of the generator-transducer (relative to a single-phase measurement) [129], as shown in Figs. 2.20-2.22. Thus, waveforms with three times the frequency spectrum can be observed.

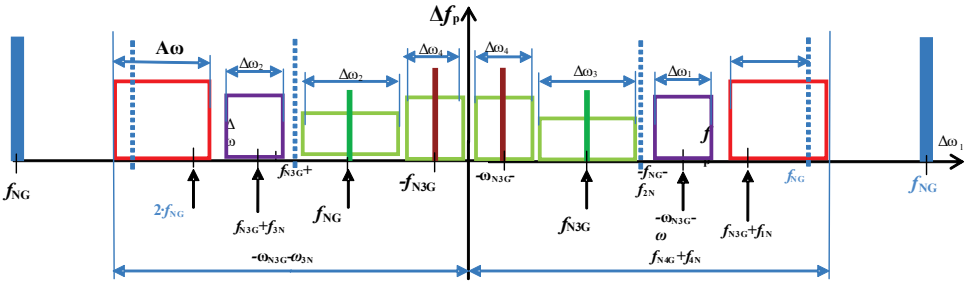

Fig. 2.20. Relationships between the main line of the carrier "wave" generated by a three-phase generator-transducer(f_{N3G}) and the subcarrier frequencies of individual kinematic pairs in the propulsion unit under study – basic characteristic set group: $\Delta\omega_1$, $\Delta\omega_2$, $\Delta\omega_3$, $\Delta\omega_4$,$\Delta\ \omega_5$ – instantaneous speed change bands (reflecting the speed change bands Δn_1, Δn_2, Δn_3, Δn_4, Δn_5) of individual kinematic pairs (No. 1, No. 2, No. 3, No. 4, No. 5) in the tested propulsion unit; f_{1N}, f_{2N} ,f_{3N}, f_{4N} ,f_{5N} – subcarrier (rated) frequencies of individual kinematic pairs (No. 1, No. 2, No. 3 No. 4, No. 5) in the tested propulsion unit; f_{NG} – rated frequency of the three-phase generator in a single-phase measurement configuration; f_{N3G} – rated frequency of the three-phase generator in a three-phase measurement configuration

[7] In [161], p.157, this time is referred to as "dead time". It is also stated there that "... using rapid logic circuits enables reducing the dead time to values in the order of microseconds, regardless of the sampling time value chosen... Dead time can a certain impact on measurement statistics and it is therefore necessary to know the dead time, especially when very short sampling times are applied...".

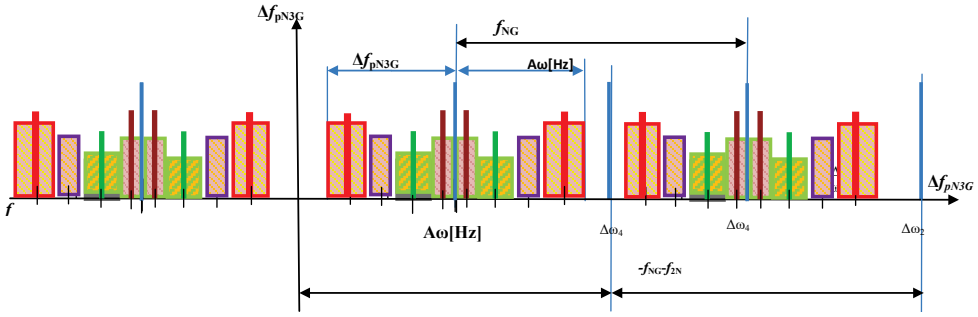

Fig. 2.21. Relationships between the main line of the carrier "wave" generated by a three-phase generator-transducer (f_{N3G}) and the subcarrier frequencies of individual kinematic pairs in the propulsion unit under study – full (extended) characteristic set group: $\Delta\omega_1$, $\Delta\omega_2$, $\Delta\omega_3$, $\Delta\omega_4$ – instantaneous speed change bands (reflecting the speed change bands Δn_1, Δn_2 , Δn_3, Δn_4, Δn_5) of individual kinematic pairs (No. 1, No. 2, No. 3, No. 4, No. 5) in the tested propulsion unit; f_{1N}, f_{2N} ,f_{3N}, f_{4N} ,f_{5N} – subcarrier (rated) frequencies of individual kinematic pairs (No. 1, No. 2, No. 3 No. 4, No. 5) in the tested propulsion unit; f_{NG} – rated frequency of the three-phase generator in a single-phase measurement configuration; f_{N3G} – rated frequency of the three-phase generator in a three-phase measurement configuration

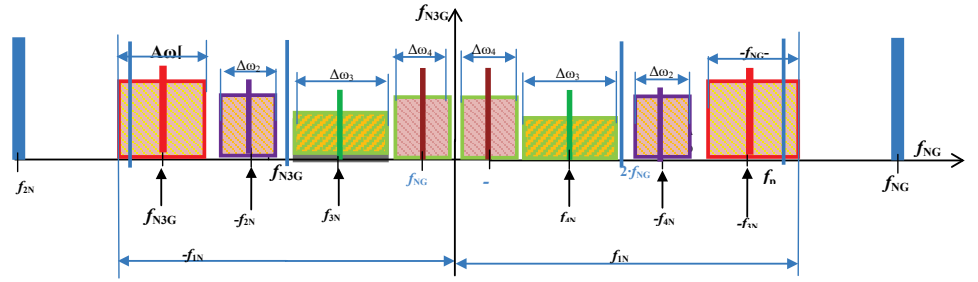

Fig. 2.22. Images after detection of the three-phase FAM-C measurement: $\Delta\omega_1$, $\Delta\omega_2$, $\Delta\omega_3$, $\Delta\omega_4$ – instantaneous speed change bands (reflecting the speed change bands Δn_1, Δn_2 , Δn_3, Δn_4, Δn_5) of individual kinematic pairs (No. 1, No. 2, No. 3, No. 4, No. 5) in the tested propulsion unit; f_{1N}, f_{2N} ,f_{3N}, f_{4N} ,f_{5N} – subcarrier (rated) frequencies of individual kinematic pairs (No. 1, No. 2, No. 3 No. 4, No. 5) in the tested propulsion unit; f_{NG} – rated frequency of the three-phase generator in a single-phase measurement configuration; f_{N3G} – rated frequency of the three-phase generator in a three-phase measurement configuration

Applying multi-phase configurations entails a simultaneous increase in the number of observed characteristic sets – characteristic sets of kinematic pairs with higher subcarrier frequencies (f_{jN}), and a wider spectrum of fluctuations ($\Delta\omega_j$) become visible.

In both single-phase and multi-phase measurement configurations, the subcarrier frequencies of individual characteristic sets are at the same locations on the 0-f_p abscissa axis.

2.3.2. Specific FAM-C and FDM-A features that can be applied at the secondary sampling stage

Secondary sampling is implemented in the typical TTM manner by counting the number of pulses f_s of the time base clock between successive crossings of the generator-transducer output voltage waveform through zero [99, 129, 302, 303]. The generator-transducer underwent earlier (in primary sampling, i.e., electromechanical sampling) discretisation of the mechanical modulation change spectrum involving the monitored propulsion unit and were encoded in the form of zero-level crossing time increment changes. Electromechanical sampling has many inherent advantages, with the most important being the synchronisation of mechanical and electrical phenomena. Secondary sampling aims to identify these changes and transpose them in a way that a digital machine can understand. The primary author currently only employs uniform sampling, which is not synchronised with the test voltage waveform. However, it would be advantageous in the future if the frequency of the time base clock f_s was increased[8] during a momentary increase in frequency (relative to the rated frequency) and vice versa [29, 303]. This would even out the error in the hyperbolic relationship between time increments and frequency.

$$f_{ik} = \frac{1}{\zeta_s + \Delta t_i} \tag{2.25}$$

where:
ζ_s – phase jitter of time base clock pulses, Δt_i – time increment between successive crossings through the zero-voltage level of the generator-transducer, determined by the number of time base clock pulses.

Due to such a relationship, the high-frequency component fluctuation amplitude is suppressed, which manifests itself through a lower (underestimated in relation to the actual) height of characteristic sets with high values of subcarrier frequencies close to the rated frequency of the generator-transducer. The aforementioned variations of the time base frequency would be possible if a delay line was

[8] [60], p. 25, "...quantisation intervals should be shorter for low amplitudes and longer for high amplitudes...".

connected at the input of the counter card in the main circuit (Fig. 2.23). On the other hand, the initial recognition of frequency deviation (ΔF) and deviation duration (t_{odch}) would take place within the auxiliary chain. The measurement error of frequency and deviation duration would be thus reduced. In the case of increased ΔF and decreased t_{odch} values, the frequency of the time base generator would increase. Ideally, the number of time base pulses should be approximately equal for different time increments. At the same time, it would be advantageous if the moment of triggering the frequency change was synchronised with the moment of the closest crossing of the generator-transducer voltage waveform through zero.

According to the systematics encountered in source literature, defects in drive components or subassemblies can be caused by errors made during the manufacturing process (machining, assembly errors) or can arise in the course of the operating process (tribological wear of components on mating contact planes, fatigue cracks, temperature strains). To simplify the nomenclature, manufacturing process errors are called "assembly defects", while defects arising from operational wear of components are called "wear defects" [129, 130, 176, 179].

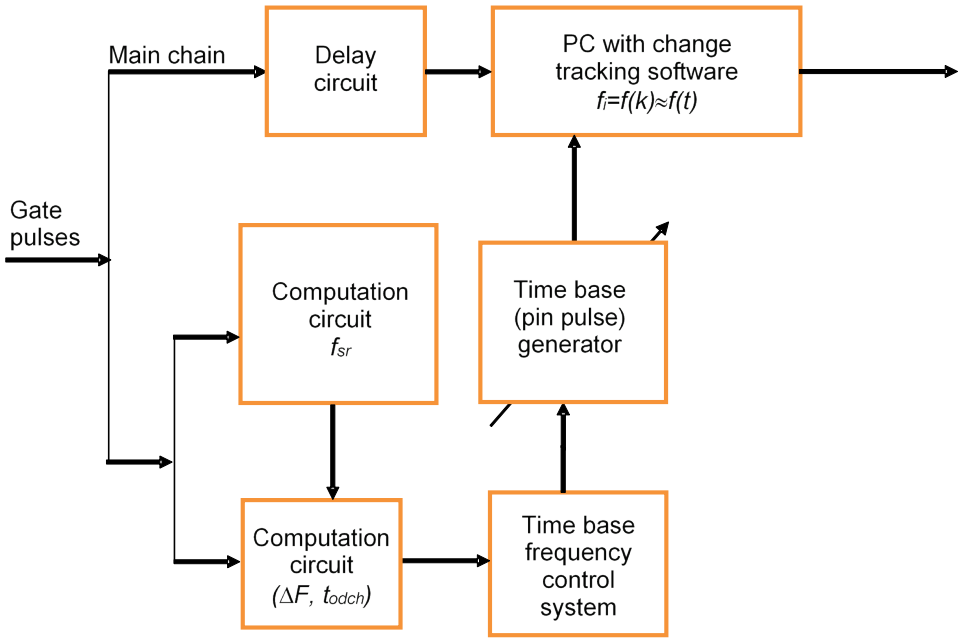

Fig. 2.23. Time base generator frequency tuning node for the imaging acquisition system (ΔF,f_p) – design – signal flow block diagram

These concepts were created by the authors only for the purpose of diagnostics to systematise the process of locating and determining the magnitude of certain mechanical defects within the diagnostic process [129]. According to the systematisation thus adopted, assembly defects can initially include:

- eccentricity defect,
- skew defect,
- misalignment and miscylindricity defects of rotor bearing supports,
- bearing journal skew,
- reduced rolling bearing radial clearance due to increased assembly clamping.

Wear defects, on the other hand, can include, e.g.:

- increased circumferential backlash of joints,
- increased inter-teeth backlash,
- the one-way coupling meshing discontinuity,
- increased bearing radial clearances.

The idea behind the method is based on modulating the angular velocity through the faulty kinematic pair according to [127, 129] (Fig. 2.24) and transferring these angular velocity modulations from the faulty mechanical component, to the rotor of the generator-transducer. These modulations are then converted into output voltage frequency modulation in the generator. Each generator-observer type has a well-defined observation band. This is a micro-scale diagram initially presenting the idea discussed in [127] and related to the observation of a single kinematic link, from a monitored mechanical propulsion unit, by a single generator-observer (Fig. 2.25). Both models (single kinematic link and single generator-transducer) have proven to be far from sufficient at the current stage of the primary author's research. The applications introduced over the last nine years have developed significantly – parallel measurements from several onboard generator-transducers have been applied simultaneously with their different phase configurations. The issue of diagnosing propulsion units with the use of the FAM-C and FDM-A methods should therefore be treated much more broadly. It can be stated that FAM-C and FDM-A diagnosis in 1998 [127] captured the problem on a micro-scale as simply processing the modulation of a single propulsion unit link and its simple reflection in the modulations of the onboard generator-transducer. Nowadays, it should be considered on a macro scale, i.e., it requires monitoring the widest possible range of the tested propulsion unit dynamic motion, depending on changes in the rated speed of a given plant and its operation time. The challenge is to adapt measurement structures constructed for the purposes of the evolving FAM-C and FDM-A methods so as to ensure that the individual propulsion units are effectively

monitored, which enables their safe operation. The comprehensive fitness assessment of an entire propulsion unit is a complex phenomenon. An initial model of this plant should be equally complex. Therefore, the task of the FAM-C and FDM-A methods should be to comprehensively capture:

a) interactions of all kinematic pairs with a given mechanical propulsion unit,
b) interactions of the primary power source (mechanical) of the monitored mechanical propulsion unit,
c) generator-transducer characteristics,
d) rotational speed controller properties of the monitored mechanical propulsion unit under test and the generator-transducer output voltage controller.

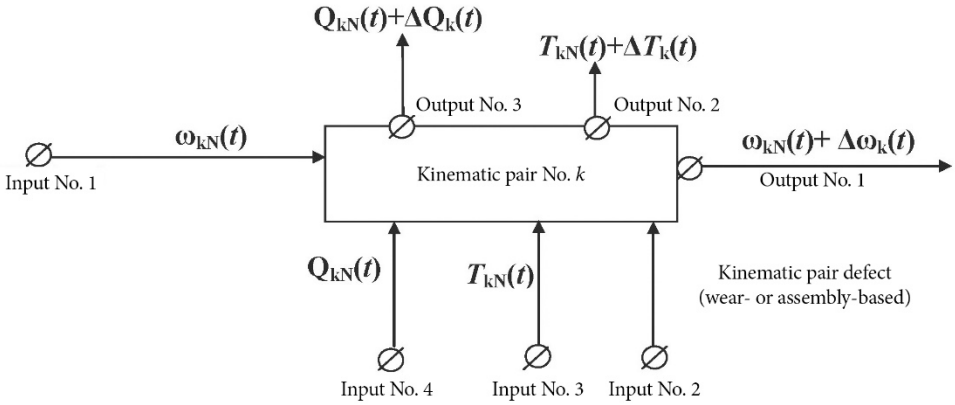

Fig. 2.24. Block diagram of a faulty kinematic pair as an angular velocity modulator: $\omega_{kN}(t)$ – rated angular velocity of kinematic pair no. k (value changed quasi-stepwise by the operator), $\Delta\omega_k(t)$ – angular velocity modulations due to the impact of kinematic pair defects and interference factors, $Q_{kN}(t)$ – value of thermal energy supplied from the operating environment, $\Delta Q_k(t)$ – value of thermal energy generated by kinematic pair k, $T_{kN}(t)$ – value operating environment temperature, $\Delta T_k(t)$ – value of the temperature generated by kinematic pair k

The study [203] that proposed a model of an electrical machine as a "six-piece" can be assumed as a starting point for a new (macro-scale) diagnosis. Herein, the driving torque M [Nm] and rotational speed n [rpm] can be considered at the input of the generator, while the temperature T [°C], voltage $u(t)$ [V], frequency [Hz] and load current [A] would be at the output (Fig. 2.24).

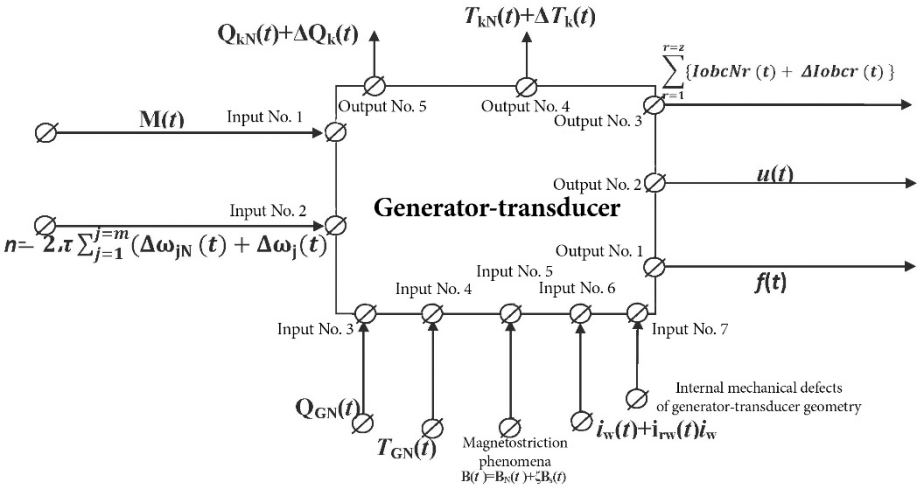

Fig. 2.25. Generator-transducer relative to input-output signals: $\omega_{kN}(t)$ – rated angular velocity of kinematic pair no. *k* (value changed quasi-stepwise by the operator), $\Delta\omega_k(t)$ – angular velocity modulations due to the impact of kinematic pair defects and interference factors, $Q_{kN}(t)$ – value of thermal energy supplied from the operating environment, $\Delta Q_k(t)$ – value of thermal energy generated by kinematic pair *k*, $T_{kN}(t)$ – value of operating environment temperature, $\Delta T_k(t)$ – value of the temperature generated by kinematic pair *k*, $i_w(t)$ – generator excitation current, $i_{rw}(t)$ – radio interference conducted through the generator excitation circuit into the generator structure

For the voltage frequency modulation parameters to reflect the defect parameters of a faulty component and enable its localisation within the structure of the tested propulsion unit, the elements of the entire signal transmission tract (transmission tract kinematic links) should satisfy a number of conditions. These can be summarised as general assumptions conditioning the minimization of distortions to diagnostic signal processing:

- the operating point of generator magnetic circuits is located within the rectilinear section of the magnetisation characteristic curve (below the magnetic core saturation);
- the hysteresis loop is negligibly narrow: the operating point is located within the rectilinear section of the magnetising characteristic;
- the generator is excited from an ideal DC source (no pulsation with dynamically varying component frequencies);
- little current is drawn in the generator output circuit – this does not affect the thermal or magnetic changes in the generator;
- the generator rotor and stator are rigid bodies;
- the rated speed of the drive motor is constant;

- the mechanical load on the propulsion unit is invariant over time – any changes are incomparably slower than the period of observed pulsations in propulsion unit kinematic pairs;
- the thermal state of the propulsion unit is fixed and does not impact electrical parameter changes;
- each gearbox kinematic pair exhibits its own disadvantage in the form of output angular velocity modulations relative to the input velocity (Fig. 2.17);
- the propulsion unit is a linear system in terms of transmitting rotational motion from a faulty kinematic pair to a generator-transducer;
- output angular velocity modulations of a given kinematic pair are transmitted to the rotor of the onboard generator.

It should be emphasised that practically all these conditions are satisfied in a typical FAM-C and FDM-A measurement procedure.

The possibility of attenuating the angular velocity modulation signal induced by a defective mechanical component inside the tested propulsion unit is even more important than the analysis of the electrical signal distortion in the generator-transducer. This is the case if one of the kinematic links in the propulsion unit on the path between the observed defective component and the generator-transducer has an incomparably higher moment of inertia than the adjacent links. High-frequency modulations of the angular velocity will then be attenuated. The energy of these modulations will be dissipated as heat. A given harmonic signal of angular velocity modulations from a defective mechanical component will not be reflected in the voltage frequency modulation if there is no continuity of mechanical energy transfer.

Typical *b* coefficients of kinematic pair angular velocity modulation phase

Based on numerous laboratory tests involving on propulsion benches, as well as analytical calculations [22, 129, 234], it is possible to formulate simple linear relationships between selected simple (elementary) mechanical defects of a given kinematic pair and the modulation frequencies (expressed as Fourier distribution harmonic numbers) at the output:

$$\omega_2 = h \cdot \omega_1 \tag{2.26}$$

where:
ω_1 – inlet pulsation of a given kinematic pair, ω_2 – outlet pulsation.

$$f_2 = h \cdot f_1 \tag{2.27}$$

- eccentric displacement of two shafts $h = 1$,
- skewing of two shafts $h = 2$,
- combined eccentricity and skewing of two shafts $h = 0{,}5$,
- gear pair inter-teeth backlash $h = z$, where z – number of gear teeth,
- represented correct operation of a rolling bearing $h = N \cdot p_s = N \cdot (1 \pm d_w / D_{śr} \cos \alpha)$, where: n - rotational speed [rpm], N – number of rolling elements of a given bearing, d_w – rolling element diameter, $D_{śr}$ – bearing average diameter, α – operation angle, p_s – rolling factor (in literature, for simplicity sake, a constant value $p_s = 0.5$[9] is usually assumed).

These straightforward relationships are relatively easy to observe in the case of simple machines, where only one kinematic link is subject to controlled failure [82÷87, 90, 94, 106, 127, 131]. More complex propulsion units usually involve multiple components with significant levels of wear – observation and localisation are not always easy. However, even when diagnosing the most complex propulsion units, mathematical and physical knowledge of the basic types of kinematic pair damage and the relationship between individual propulsion unit kinematic pair defects with FAM-C and FDM-A imaging is essential. This allows to create a basic set of benchmarks. This enables attempting an analysis of the technical condition exhibited by individual kinematic pairs of the studied propulsion unit based on a comparison with benchmarks-models.

[9] The cage-separator of a properly functioning rolling bearing rotates approximately twice as slow as the shaft [15, 36, 73, 113, 119, 122, 123]. Faster cage rotation indicates cage seizure or increased total bearing resistance due to e.g., internal contamination – then $p_s > 0{,}5$.

3

RELATIONSHIPS BETWEEN INDIVIDUAL DEFECTS OF MECHANICAL PROPULSION UNIT KINEMATIC PAIRS WITH FAM-C AND FDM-A IMAGING

3.1. Typical mechanical defects in simple machines and their reflection within instantaneous speed waveform and narrowband characteristic sets

3.1.1. Eccentricity of connections without circumferential backlash

A common assembly defect affecting connection of mechanical propulsion unit components is the parallel offset of drive shafts joined by claw couplings (Fig. 3.1) or splined connections (Fig. 3.2). These are of great importance especially when transmitting mechanical power via multi-segment (multi-support) transmission shafts (the transmission of power from the main gearbox to the tail rotor in aviation [95, 129, 190], and the propeller drive in ship building [28, 54]).

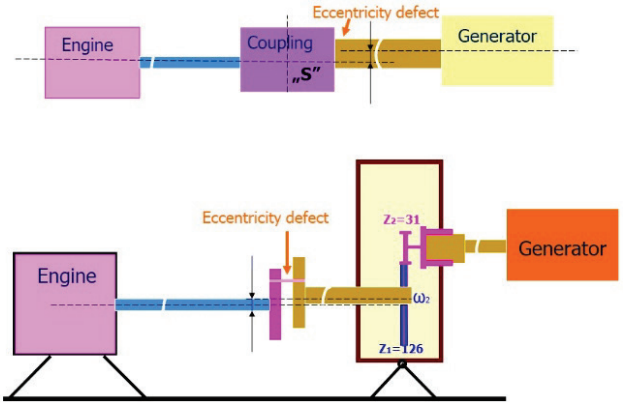

Fig. 3.1. Two shafts with an eccentricity defect connected by an "S" claw coupling: a) block diagram, b) overview cross-section of a test stand, z_1 , z_2 – transmission gears

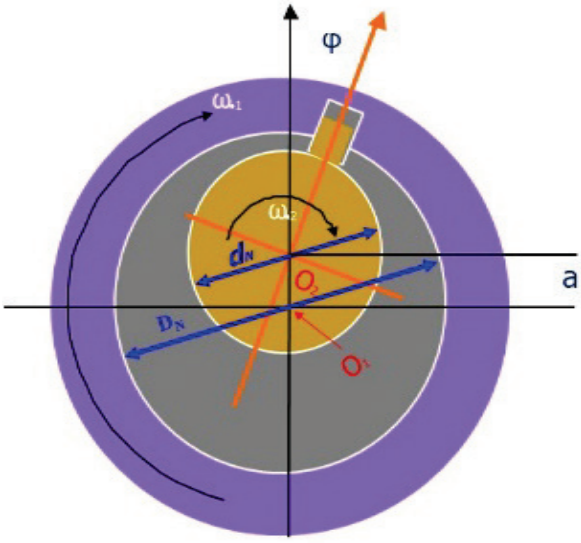

Fig. 3.2. Diagram of a splined connection between two shafts with an eccentricity defect, cross-section: D_N – driving sleeve diameter, d_N – driven shaft diameter, ω_1 – input angular velocity, ω_2 – output angular velocity

The relationship between the eccentricity displacement value *a* and the height of the characteristic set can be presented based on trigonometric relationships [129, 310, 311]:

$$a = \frac{D_N}{4} \cdot \frac{|\Delta F_{\max}| + |\Delta F_{\min}|}{f_{úr}} \tag{3.1}$$

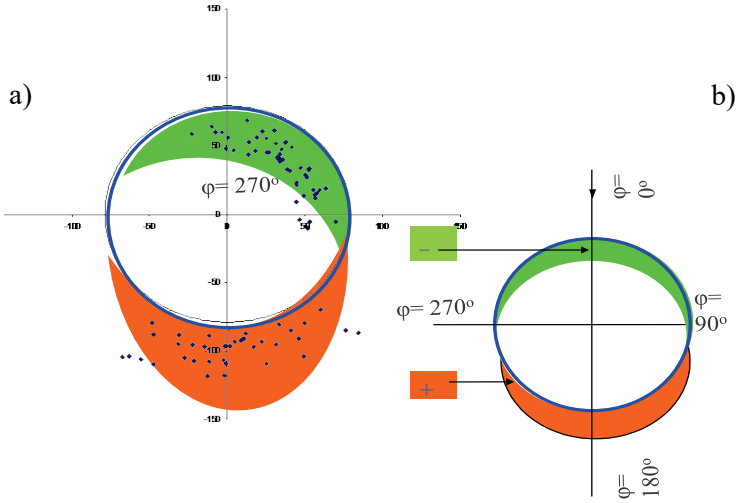

Fig. 3.3. Phase diagram of a splined connection between two shafts with an eccentricity defect, cross-section: a) phase image obtained from measurements on a LUZES-III drive bench, b) phase image obtained from a computer simulation

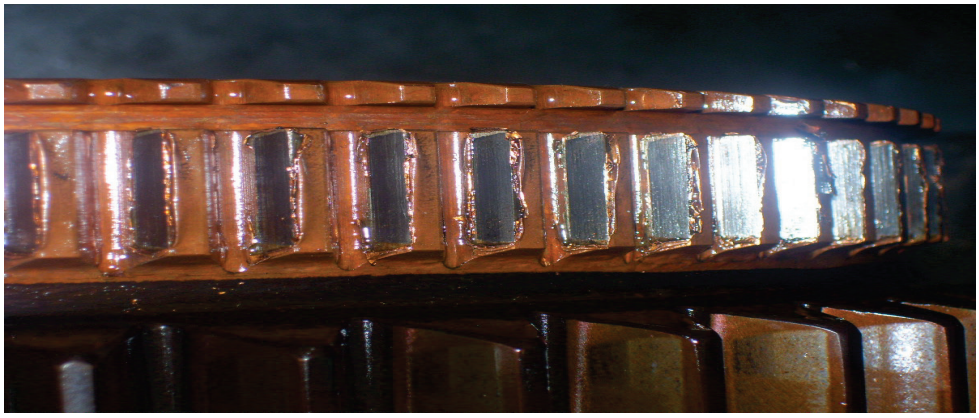

Fig. 3.4. Excessive wear of a gear wheel with an eccentricity defect

3.1.2. Eccentricity of connections with circumferential backlash

A generic formula for eccentricity will initially be the same as for a connection with no backlash. However, the existing backlash induces periodic loss of kinematic bond in the link (Fig. 3.5, section pt1-pt1bis and pt2). For these rotation angle sections, the formulae used for the moment of inertia (moment of inertia of the gearbox rotor and rotating elements) were applied, taking into account the coefficient of viscous damping and dry friction after kinematic bond loss. The changes

in kinematic link output velocity are divided into four zones in Fig. 3.5 (see link design in Fig. 3.6):

Zone 1. If $\omega_2 > \omega_n$ and ω_2 increases, then in pt. 1 there is a disconnection of tooth side 1 with the drive sleeve, this brings about braking of the shaft of the generator, together with its rotor. Here, generator rotor motion can be described by the equation (3.3), derived in [96, 104-105, 127, 129].

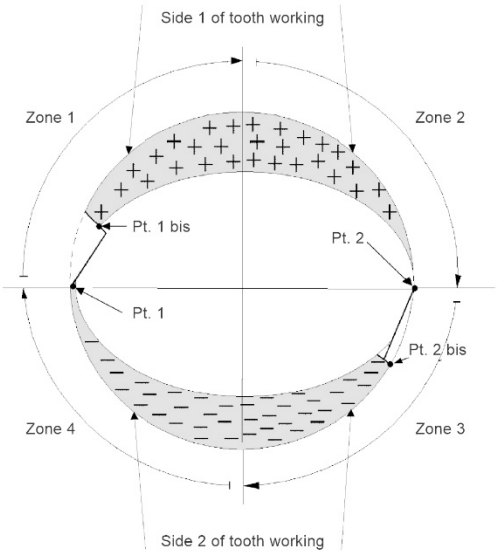

Fig. 3.5. Theoretical instantaneous angular velocity variations at an eccentric clearance connection

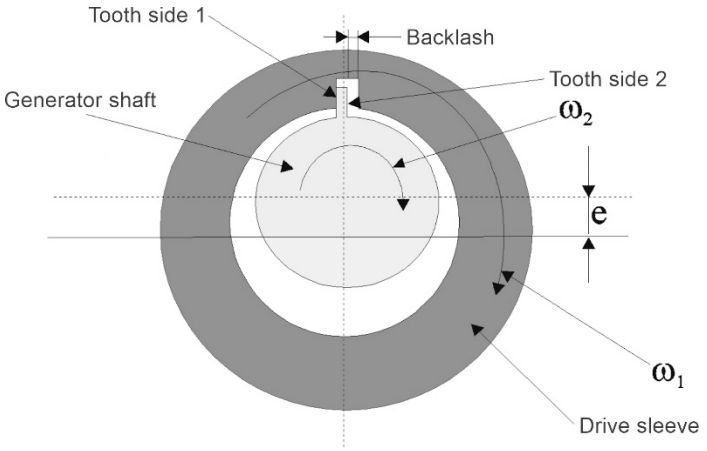

Fig. 3.6. Cross-section of the shaft-drive sleeve connection at an eccentric keyed connection with backlash

The solution to this differential equation will be an exponentially descending angular velocity function $\dot{\vartheta}_2(t)$ at the output of the kinematic pair in question. In pt. 2bis there is an impact of tooth side 1 combined with oscillations of the generator shaft and rotor. In such situation, the generator rotor motion can be described by the formula of two differential equations (derived in [87]):

$$\begin{cases} J_1\ddot{\vartheta}_1 + +D_1\dot{\vartheta}_1 + \dfrac{1}{K}(\vartheta_1 - \vartheta_2) = M_0 & (3.2) \\ J_2\ddot{\vartheta}_2 + D_2\dot{\vartheta}_2 + \dfrac{1}{K}(\vartheta_2 - \vartheta_1) = M_t & (3.3) \end{cases}$$

where:
D_1 – viscous damping coefficient, J_1 – resultant moment of inertia of the drive motor rotor and other drive elements between the motor and the considered eccentric link, M_0 – drive torque of the motor, where: J_2 – moment of inertia of the elements between the considered eccentric link and the generator rotor (included), D_2 – viscous damping coefficient for the elements above, K – resultant torsional flexibility coefficient of the shaft, M_t – dry friction torque on the bearings of the elements above, ϑ_2 – rotational angle of the generator rotor, ϑ_1 – output rotation angle of the considered eccentric link.

The solution to this system of differential equations will be an exponentially increasing velocity function $\dot{\vartheta}_2(t)$, with fading oscillations superimposed on it.

Zone 2. If $\omega_2 > \omega_n$ and ω_2 is decreasing, the generator shaft angular velocity waveform is according to theoretical calculations for the eccentric; tooth side 1 with the drive sleeve works.

Zone 3. If $\omega_2 < \omega_n$ and ω_2 is decreasing, then in pt. 2 there is braking of the generator shaft, together with its rotor; in pt. 2bis there is impact of side 2 of the tooth, combined with oscillations of the generator shaft and rotor.

Zone 4. If $\omega_2 < \omega_n$, tooth side 2 with a drive sleeve is operating.

Frequency modulation also changes proportionally. The distribution of characteristic set points in the (f_p, ΔF) plane also changes accordingly. Thus, the increase of eccentricity entails an increase in the value of the characteristic set height and the inclination angle of the vertical (longitudinal) axis of symmetry of this set in relation to the 0- f_p axis of abscissa decreases[1] (deviates from 90°, i.e., moves

[1] This refers to the inclination angle between the 0-fp axis and the axis of symmetry of the characteristic set. In the case of an increase in the circumferential clearances in characteristic set images on the $\Delta F = f(f_p)$ plane, a skewing of the characteristic set symmetry axis is also observed.

away from the normal (perpendicular) line towards the 0 f_p axis of abscissa). Of course, the intersection with the 0- f_p axis occurs for $f_p = \frac{n}{60}$, i.e., for the first harmonic ($h = 1$) of a given link (in this case, a combination of two shafts) speed frequency [124, 129].

3.1.3. Circumferential backlash of a kinematic pair in the universal sense and its imaging using the FDM-A method

Monitoring of increasing inter-tooth backlash of a pinion gear (type TUN-75/R) was described by the primary author in [96, 106, 127, 129]. An experiment involving the LUZES propulsion unit was conducted that included grinding up the plane of action of two consecutive gear wheel teeth (total number of teeth in this wheel $z = 26$) by 10% and 30% of the modulus value. Before grinding, the waveform $f_i = f(t)$ showed uniform fluctuations with a period equal to the motion period of one inter-tooth pitch. After grinding, two fluctuations of markedly increased amplitude appear after every 124 such fluctuations. As for the case of a claw coupling with increased circumferential backlash, the pulses upon increasing inter-tooth backlash result from the deceleration of the passive gear when the kinematic bond is broken, i.e., when the backlash is reduced. When the kinematic bond is re-established, there is a strong impact of the tooth contact surface of the drive wheel against the tooth contact surface of the driven wheel – imaged in the FAM-C method as a pulse with increased amplitude.

Another physical experiment included measurements on a LUZES propulsion unit that involved observing FAM-C imaging of increased circumferential backlash of the claw coupling [96, 106, 127, 129]. At the same time, the eccentricity or skewing of this coupling was changed. In this case, an imaging with a frequency and amplitude (instantaneous frequency) appropriate to the size and type of defect (skewing, eccentricity) was obtained on the time-dependent instantaneous frequency waveform in the slow-variable component. At the same time, the researchers obtained characteristic undercuts described in the previous section (3.1.2) and presented as a pie chart (Fig. 3.2). These are shown in Fig. 3.7 as expanded into a rectangular coordinate plane.

In a later study, the author noticed similar undercuts (dynamic component) during tests on rolling bearings in single-shaft turbine engines (Fig. 3.8) [122]. Simultaneously, the slow-variable component illustrated mechanical defects such as skewing or eccentricity of mechanical connections.

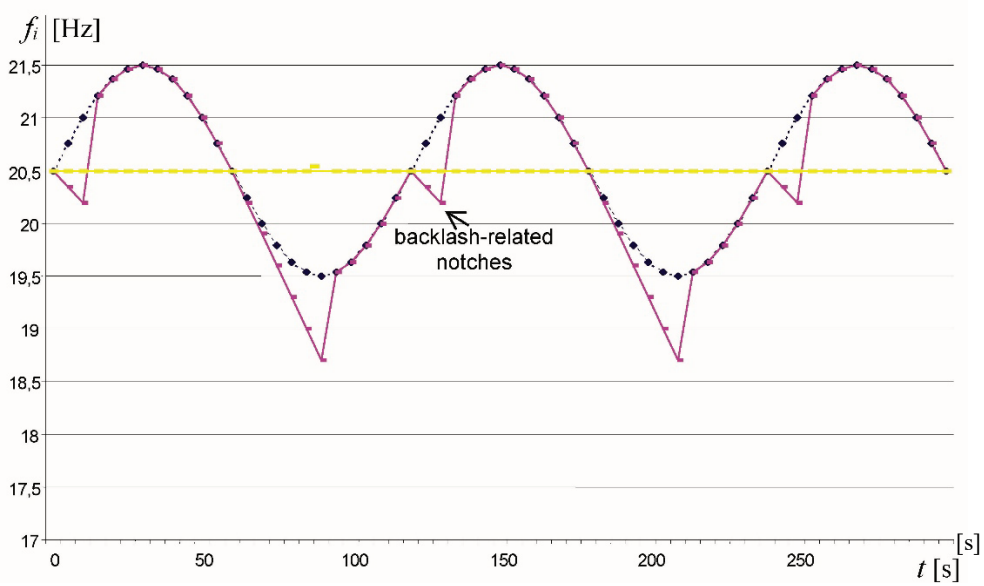

Fig. 3.7. Theoretical instantaneous frequency waveform for a kinematic pair exhibiting an eccentricity defect with backlash

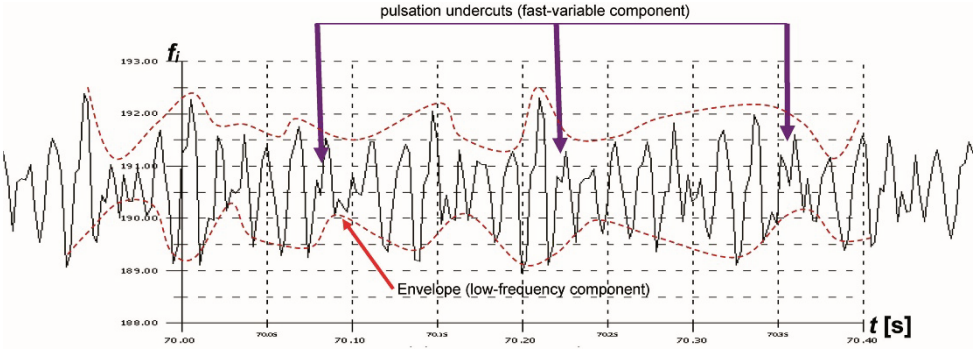

Fig. 3.8. Example of an actual instantaneous frequency waveform for a kinematic pair exhibiting an eccentricity defect with backlash

3.1.4. Circumferential backlash of gear wheel pairs and splined connections

The phenomena of initial angular velocity modulation by a pair of gear wheels and spline connections with circumferential backlash resembles the phenomenon described in subsections 3.1.2 and 3.1.3 – there is the same deceleration of velocity after the loss of the kinematic bond (frictional force, viscous damping forces) and

acceleration after the bond is established [1, 22, 35, 42, 52, 152, 218]. When a pair of gear wheels is bonded, this process is repeated every single pitch of the gear in question (Fig. 3.9). Sometimes, with significant decrements on some of the contact surfaces in certain teeth, a pulsed nature of the acceleration is also evident after this bond is established [106, 127, 129].

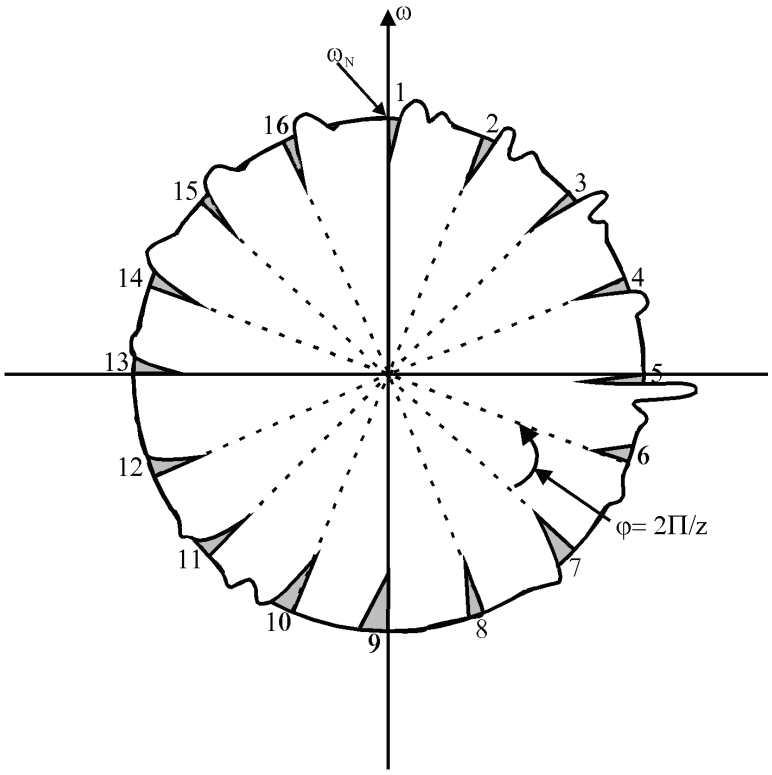

Fig. 3.9. Theoretical pie chart (in polar coordinates) of the instantaneous frequency waveform for a pair of gears with backlash

This issue has already been addressed in subsection 2.2.6.5 concerning the limited measurement resolution of the individual generator-transducer types. Only certain types of DC generator-transducers have enough slots that the images obtained using them approach the resolution limit for monitoring inter-teeth backlash even for new gear pairs with correct backlash. Undoubtedly, heavily worn tooth contact surfaces, above 10% of the modular pitch, are already "visible" to them – both the phase and amplitude in the instantaneous frequency waveform clearly show angular velocity accelerations (increase in the instantaneous frequency amplitude), (Fig. 3.9) [106, 108, 126, 129, 307].

3.1.5. Mechanical connection skewing

Papers in the field of aeronautical and marine mechanics have highlighted the significance of assembly defects such as eccentricity and skewing [35, 43, 171, 234], which can lead to numerous flight safety hazards. The primary author's observations and source literature [35, 41-44, 170] clearly indicate that the connection skewing defect induces more intense abrasive wear of the kinematic pair than the eccentricity defect. This is due to the nature of the spline teeth interaction, where abrasion occurs over the entire surface upon an eccentricity defect, while occurring spot-wise in the case of skewing (Figs 3.10 and 3.11, point "P"). The point concentration of stresses results in locally intensified heat generation and increased abrasive wear. Spline skewing induces more intensive spline wear than other types of connection defects. This is because, in the case of skewing, there is a mechanical point contact between a pair of splined connection teeth, rather than a linear contact such as with eccentricity. In addition, the point moves along the spline as the shaft rotates, resulting in heat concentration - particularly in the central part of the spline - where a characteristic barrel-shaped effect occurs (Fig. 3.13).

Cases of severe spline wear due to skewing of the spline shaft centreline relative to the drive sleeve centreline are known in the aerospace milieu. In some cases, this ends [35, 170] with:

- a malfunction of the generator, e.g., an aviation generator (short-lived overvoltages occur upon severe spline wear, which cannot be adjusted by the onboard regulator – the surge protector then disconnects the generator from the grid);
- a premise of an aircraft accident due to an uncoupled joint (e.g., disconnection of the connection between the electric starting motor and the shaft of a turbojet engine, and start-up interruption);
- an air crash, in the case of an interruption in the operation of circuits relevant to flight safety (e.g., disconnection of a hydraulic pump drive) due to incorrect operation of the unit or its disconnection in a specific air situation, which may cause, e.g., loss of controllability.

This section attempts to link and expand on two hitherto independently existing source literature themes:

- work in the field of electrical machinery, where modulations due to skewing have been described but treated as disturbances [310, 311],
- work in the field of mechanics, where the effects of skewing in splined connections were described [35].

Once the formulas for the modulation frequencies of the fundamental kinematic pair defects have been derived and systematised, an algorithm for calculating the so-called "baseline frequency" [82] of a kinematic line can be defined:

$$fp = h \cdot \omega_N \tag{3.4}$$

where:
ω_N [1/s] – rated angular velocity of a given kinematic pair, h – coefficient depending on the type of defect ($h = 1$ – eccentricity defect, $h = 2$ – skewing defect, $h = 0.5$ – complexity of eccentricity and skew defects).

Plotting the lines of kinematic fringes prior to the experiment enables identifying the characteristic sets formed during the measurements with individual defects in kinematic pairs of the propulsion unit under test. This makes it possible to determine, among other issues, the height of the characteristic set ($\left| \{\Delta F_i\}_{\max} \right| + \left| \{\Delta F_i\}_{\min} \right|$) "responsible" for the skewing of a given kinematic pair. Knowing the height of such a set, it is also possible to calculate the value of the rotating element axes skew β . Finding the geometrical relationships between these values requires some mathematical derivations in relation to eccentric connections with an invariant value of the eccentric displacement a. The position of contact point "P" at the intersection of two lines: generator shaft spline edge with the drive sleeve guide slot edge (Figs 3.10 and 3.11), can be described by the formula:

$$\mathrm{tg}\beta = a(\phi) / (L_{12} \cos\phi) \tag{3.5}$$

where:
$a(\phi)$ – value of the eccentric displacement depending on the instantaneous angular position of the drive sleeve.

Transforming equation (3.5) derives:

$$a(\phi) = \mathrm{tg}\,\beta \;\; L_{12} \cos\phi \tag{3.6}$$

Because $\omega_1 = \phi / t$, hence:

$$\phi = \omega_1 t \tag{3.7}$$

Eccentric connection output velocity (according to [91, 127]) can be expressed:

$$\omega_2 = (D_N \omega_1 - a \sin \omega_1 t) / (D_N + a^2 / D_N - 2a \sin \omega_1 t) \tag{3.8}$$

After substituting (3.6) to (3.8):

$$\omega_2 = (D_N\omega_1 - \text{tg}\,\beta\, L_{12} \sin\,\omega_1 t \cos\omega_1 t) / (D_N + \text{tg}^2\beta\, L^2_{12} \cos^2\omega_1 t / D_N - 2\,\text{tg}\,\beta\, L_{12} \sin\,\omega_1 t \cos\omega_1 t \quad (3.9)$$

Reduction gives:

$$\omega_2 = D_N\omega_1 / (D_N - 2\,\text{tg}\,\beta\, L_{12} \sin\,\omega_1 t \cos\,\omega_1 t) \quad (3.10)$$

Subsequent transformations produce:

$$\omega_2 = D_N\omega_1 / (D_N - 2\text{tg}\beta\, L_{12} \sin\,2\,\omega_1 t) \quad (3.11)$$

Assuming tg β >0, we obtain a maximum denominator value, i.e., minimum value $\omega_2(t)$ for:

$$\omega_1 t = \{135^o, 315^o, 495^o, ..., n \cdot 180^o) \quad (3.12)$$

where: n – natural number.

The minimum denominator value, i.e., minimum value $\omega_2(t)$ is generated for:

$$\omega_1 t = \{45^o, 225^o, 405^o, 585^o, ..., 45^o + n \cdot 180^o) \quad (3.13)$$

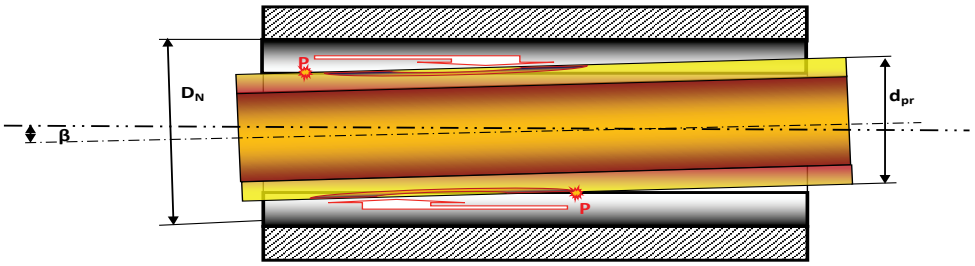

Fig. 3.10. Longitudinal section of the generator shaft connection in the drive sleeve when the connection is skewed by angle β: D_N – drive sleeve inner diameter, d_{pr} – shaft diameter of a driven component, e.g., generator, P – contact point between the generator shaft tooth edge and the drive sleeve tooth edge – the arrow indicates this point's movement direction, i.e., concentration of abrasive forces R at the contact edge of the SPLINES

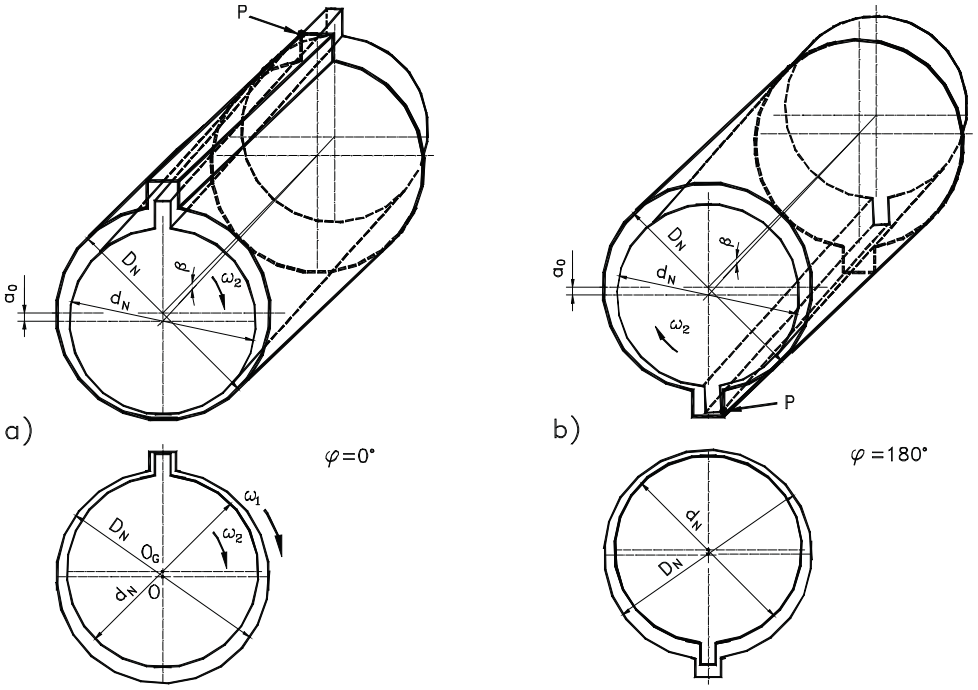

Fig. 3.11. Axiomatic view of the connection between the generator shaft and the drive sleeve with a skewed angle β: a) upper spline position; b) lower spline position. Designations: d_N – diameter of a driven component, e.g., generator; D_N – drive sleeve diameter; β – skew angle; P – generator shaft-drive sleeve point of contact; φ – rotation angle

Formula (3.12) indicates that connection skewing manifests itself as a sinusoidal waveform modulation of the instantaneous angular velocity of the driven element with a given kinematic pair rated velocity second harmonic frequency. Angular velocity instantaneous change waveforms can be presented as pie charts (Fig. 3.12). It can be seen that shaft skewing results in dynamic excesses twice the frequency (per full kinematic pair revolution) as in the case of an eccentricity defect. If tribological phenomena are taken into account – increased abrasion due to a spline contact point leading to stress accumulation and temperature increase, then splined connection skewing shall be considered as a dangerous assembly defect [35, 124, 131].

Skewing defect vs characteristic set height

The relative deviation of the angular velocity amplitude $\Delta\omega_2$ from the average value $\omega_{śr}$ can be described by the relationship:

$$\Delta\omega_2 / \omega_{śr} = (\omega_{2max} - \omega_{2min}) / 0.5\,(\omega_{2max} + \omega_{2min}) \qquad (3.14)$$

Given the assumption that generator output voltage frequency changes are a linear function of the generator rotor angular velocity, as in [129], one can obtain:

$$\Delta\omega_2 \,/\, \omega_{śr} = (\{\Delta F_i\}_{\max} + \{\Delta F_i\}\min) \,/\, f_{śr} \tag{3.15}$$

Equating the sides of equations (3.14) and (3.15) results in:

$$(\omega_{2\max} - \omega_{2\min}) \,/\, 0.5\,(\omega_{2\max} + \omega_{2\min}) = (\{\Delta F_i\}_{\max} + \{\Delta F_i\}\min) \,/\, f_{śr} \tag{3.16}$$

From the equation (3.11), the extreme values of the angular velocity can be determined - the minimum:

$$\omega_{2\min} = D_N\,\omega_1 \,/\, (D_N + \mathrm{tg}\beta\; L_{12}) \tag{3.17}$$

and the maximum:

$$\omega_{2\max} = D_N\,\omega_1 \,/\, (D_N - \mathrm{tg}\beta\; L_{12}) \tag{3.18}$$

Hence, after substituting (3.17) and (3.18) into (3.16) and after arithmetic transformations, one derives:

$$\mathrm{tg}\beta = D_N\,(\{\Delta F_i\}_{\max} + \{\Delta F_i\}\min) \,/\, (L_{12} f_{śr}) \tag{3.19}$$

Substituting $L_{12} = 0.5 \cdot L$ and using a trigonometric relation enables determining:

$$\beta = \mathrm{arctg}\,[D_N\,(\{\Delta F_i\}_{\max} + \{\Delta F_i\}\min) \,/\, (L_{12} f_{śr})] \tag{3.20}$$

Pie charts can be drawn based on mathematical relationships (Fig. 3.12). Figs. include angular velocity amplitude deviations of a kinematic pair with a skewing defect shown in polar coordinates. It can be seen that the skewing defect case is dominated by the given kinematic pair's rated angular velocity second harmonic. The operation of a splined connection with skewing, as mentioned at the beginning of this chapter, results in material loss at the edge of the drive shaft (Fig. 3.13).

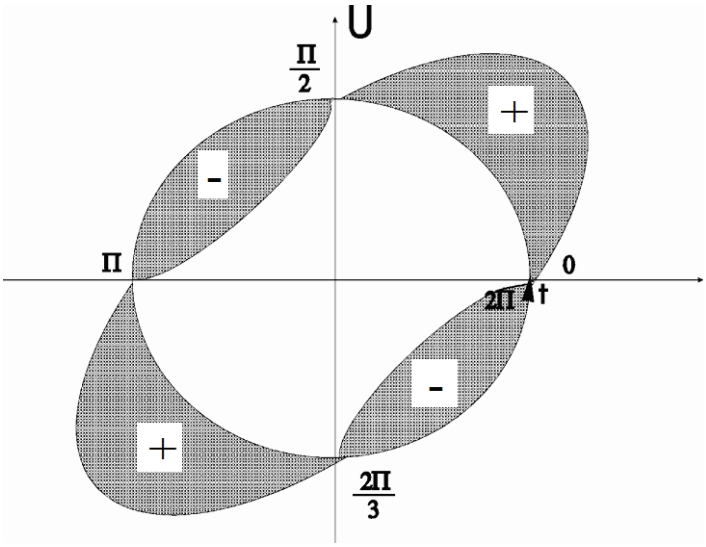

Fig. 3.12. Pie chart showing instantaneous angular velocity changes for a connection between shafts with skew

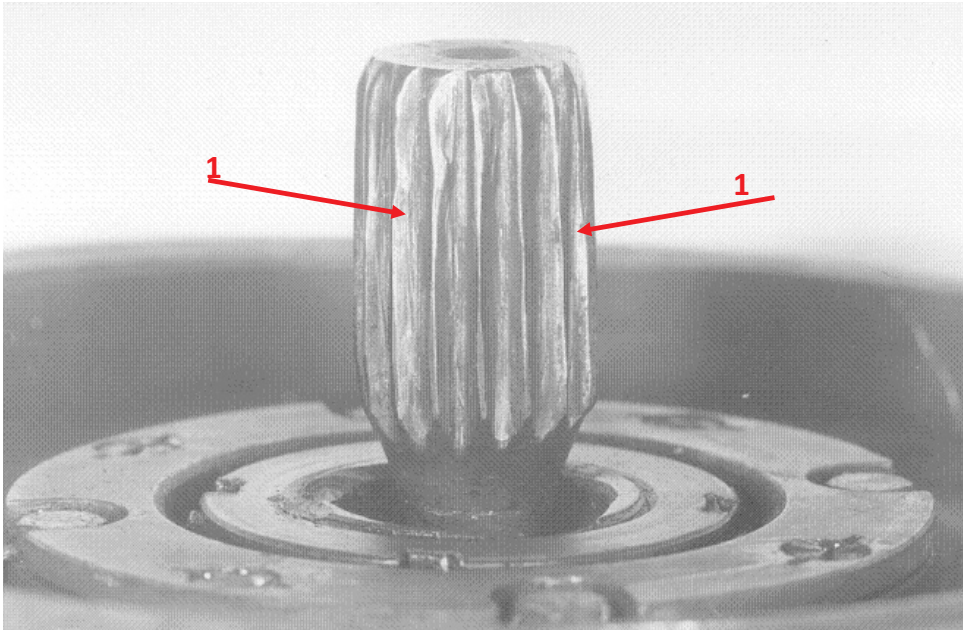

Fig. 3.13. Splined shaft of the SGO-8 AC generator after 800 h of operation on the LUZES-II laboratory propulsion bench with a skew of $\beta = 1.5^{\circ}$; 1 – trace of "barrel-shaped" material losses on the contact plane of drive shaft splines

3.1.6. Simultaneous action of skewing and eccentric displacement

The need to take interest in a complex defect – eccentricity and skewing – arose from the primary author's laboratory studies on the phenomenon of shaft skewing [96, 124, 131]. The certain degree of complexity exhibited by the tested propulsion units often lead to the interference of dynamic phenomena associated with eccentricity and shaft skewing. Therefore, when the skewing phenomenon was investigated, the first sub-harmonic of the considered kinematic pair's rated angular velocity appeared instead of the second harmonic.

$$\begin{cases} x_2 = x_1 & (3.21) \\ y_1 = (y_2 + a + e) \cdot \cos\beta & (3.22) \end{cases}$$

where:

$$\frac{a}{\frac{1}{2}l_A} = tg\beta \Rightarrow a = \frac{1}{2}l_A \cdot tg\beta \tag{3.23}$$

Because:

$$a = \frac{1}{2} \cdot \frac{l}{\cos\beta} \cdot tg\beta \tag{3.24}$$

so:

$$\begin{cases} x_2 = x_1 \\ y_1 = y_2 + \frac{1}{2}l \cdot (\frac{\sin\beta}{\cos^2\beta} + e) \cdot \cos\beta \Rightarrow y_2 = \frac{y_1 - \frac{1}{2}l \cdot \frac{\sin\beta}{\cos^2\beta} - e}{\cos\beta} \end{cases} \tag{3.25}$$

$$\begin{cases} x_2 = x_1 \\ y_2 = \frac{y_1}{\cos\beta} - \frac{\frac{1}{2}l\frac{\sin\beta}{1-\sin^2\beta} + e}{\cos\beta} \end{cases} \tag{3.26}$$

After converting to polar coordinates, using the formulas:

$$\sin\vartheta_1 = \sin\omega_1 t = \frac{y_1}{\frac{1}{2}D_N} \Rightarrow y_1 = \sin\omega_1 t \frac{1}{2} D_N \tag{3.27}$$

and:

$$\cos\vartheta_1 = \cos\omega_1 t = \frac{x_1}{\frac{1}{2}D_N} \Rightarrow x_1 = \cos\omega_1 t \cdot \frac{1}{2} D_N \tag{3.28}$$

after substituting, we achieve:

$$\begin{cases} x_2 = \cos\omega_1 t \cdot \dfrac{1}{2} D_N & (3.29) \\ y_2 = \dfrac{\sin\omega_1 t \dfrac{1}{2} D_N}{\cos\beta} - \dfrac{1}{2} l \dfrac{\sin\beta}{\cos^3\beta} - \dfrac{e}{\cos\beta} & (3.30) \end{cases}$$

$$\omega_2 = \frac{D_N^2 \cdot \cos^3\beta - D_N \cdot \sin\omega_1 t \cdot \cos\beta \cdot (l\sin\beta + 2e)}{\left(D_N^2 \cdot \cos^2\beta \cdot \sin^2\omega_1 t + D_N^2 \cdot \cos^4\beta \cdot \cos^6\omega_1 t\right) - \left(2D_N \cdot \sin\omega_1 t - l \cdot \sin\beta - 2e\right) \cdot \left(l \cdot \sin\beta + 2e \cdot \cos^2\beta\right)} \cdot \omega_1 \tag{3.31}$$

For *n* teeth:

$$\omega_2 = \vartheta_2 = \sum_{i=0}^{i=n} \frac{D_N^2 \cos^5\beta - D_N \sin(a) \cdot \cos^3\beta \cdot (b)}{\left(c \cdot \sin^2(a) + c \cdot \sin(a)\right)\left(\cos^2\beta - l\sin\beta - 2e \cdot \cos^2\beta\right)(b)} \tag{3.32}$$

where:

$$a = \omega_1 t + \frac{2\Pi}{n}(i-1);\ b = l\sin\beta + 2e\cos^2\beta;\ c = D_N^2 \cos^4\beta \tag{3.33}$$

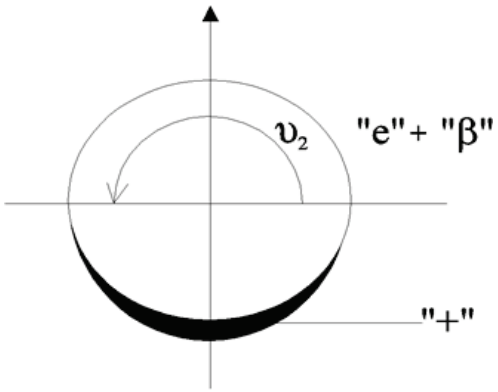

Fig. 3.14. Pie chart of the initial angular velocity in the case of combined connection skew and eccentricity

Angular velocity instantaneous change waveforms can be presented as pie charts (Fig. 3.14). In the case of a combination of skewing and eccentricity defects, there is a sinusoidal waveform modulation of the instantaneous angular velocity of the driven element with the frequency of the first sub-harmonic of the given kinematic pair's rated angular velocity appearing instead of the second harmonic. A longitudinal cross-section of the splined shaft-drive sleeve connection with the combined disadvantages of eccentric symmetry axes displacement defects in these elements and simultaneous skewing by angle β is shown in Fig. 3.15. The effects of long-term operation of a combination of the aforementioned elements leads to the accumulation of quasi-uniform wear of the contact edge of the involute joint (axis of symmetry eccentric displacement effect) and "barrel-shaped" material loss (Fig. 3.16, detail "1" – axis skewing effect) [35, 42, 247].

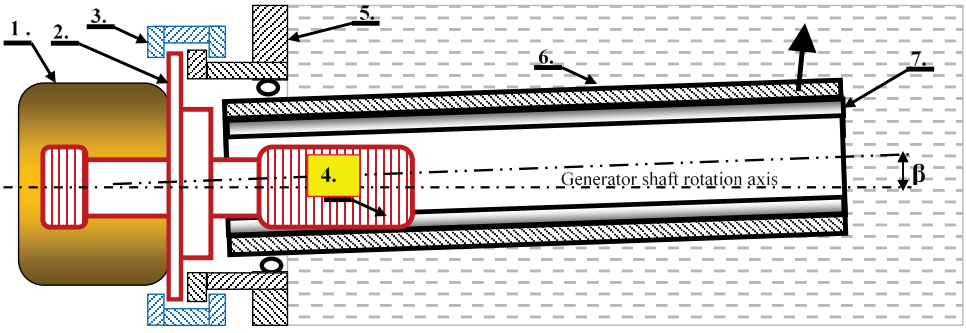

Fig. 3.15. Longitudinal section of a splined connection (generator shaft) with a drive sleeve exhibiting eccentricity and skew defects: 1 – generator body, 2 – generator mounting flange, 3 – mounting bracket, 4 – generator splined shaft, 5 – gearbox housing, 6 – drive sleeve with internal splined teeth, 7 – drive sleeve splined tooth

Fig. 3.16. Splined shaft of a GT-40PCz6 AC generator under long-term operation with skew and eccentric displacement: 1 – trace of material loss on the drive shaft splines in the shape of "conical" decrements on the contact plane

3.1.7. Summary of considerations in relation to narrowband mechanical faults

A comparison of actual (obtained from measurements of physical objects) properties shows that the sensitivity of DC generators is about 8÷20 times higher than that of AC generators. This is due to the design differences of DC and AC generators – the rotor of a DC generator has, on average, statistically 8÷20 times more rotor slots than an AC generator has stator pole pairs. Consequently, the rated frequency of a DC alternator is 8÷20 times higher than that of an AC generator [129]. However, even for the DC generators with the highest number of rotor slots, gear tooth backlash is the most difficult to monitor. This is caused by the small value of this backlash, which amounts to 0.3÷0.7% of the modular pitch in properly functioning, unworn gears. On the other hand, the following failure conditions [42, 96, 104, 127, 129] are detectable:

- tooth fractures,
- backlash increased to approx. 10% ÷20% of the modular pitch (0.1÷0.2·m).

An apparent conclusion comes to mind that, whenever possible, only DC generators should be used. In reality, the upper observable window frequency of a DC

generator is much higher than that of an AC generator. At the same time, a higher upper frequency also means a higher lower frequency of the observability window. Therefore, if a diagnostician wanted to rely only on a DC generator (abandoning the measurements taken with an AC generator), this would mean losing the opportunity to monitor slow-variable processes. This problem will be further addressed later in this paper, notably in Chapter 4, when discussing metrological properties of the FAM-C and FDM-A methods.

Kinematic pair backlash, as well as manufacturing and assembly errors in mechanical components are reflected in the periodic oscillations of the generator rotor angular velocity. The nature of the changes in these oscillations is transferred onto voltage frequency modulation parameters of the onboard generators. In the course of operating propulsion units, as tribological wear progresses, backlash values and other mechanical parameters of kinematic links undergo monotonic or oscillatory deviations, which, in turn, cause a change in the generator rotor periodic oscillation parameter values. The nature of these oscillations is synchronously transferred onto onboard grid voltage parameters. Tracking the changes in generator voltage frequency modulation enables observing the wear and tear of individual kinematic links within a mechanical power tract.

Backlash, skewing or eccentricity of the links are generally referred to as "kinematic pair faults". They cause a periodic change in the instantaneous angular velocity of the driven element. Each of these waveforms is characterised by a specific repetition period, depending on the kinematic pair design parameters (e.g., the number of gear wheel rim teeth).

The instantaneous angular velocity change amplitude is well-defined and proportional to the defect parameter, e.g.:

- in the case of kinematic pairs with backlash – indentation depth (in a slow-variable quasi-sinusoidal waveform) directly proportional to the backlash parameter,
- in the case of eccentricity – a value of the eccentric displacement,
- in the case of joint skewing – skewing angle β.

The repetition period of a given phenomenon enables deducing the type of damaged kinematic link, while from the amplitude – the magnitude of the given kinematic pair's defect parameter.

3.2. Broadband mechanical defects

According to [155], it is assumed that if the bandwidth of a frequency-modulated signal is greater than the upper frequency, this means broadband modulation.

The definition from the theory of teletransmission [3], where a signal with a bandwidth greater than the subcarrier frequency is considered to be broadband is more advantageous for the purposes of this study. In other words, in relation to this elaboration, a mechanical subassembly generating a signal bandwidth greater than the calculated subcarrier frequency value of that component will be considered as a subassembly generating broadband defect information.

Rolling bearings were presented by the author as representative. They are known to generate broadband vibrations [73]; moreover, their vibroacoustic signals are abundant with fast fluctuating signals. In principle, these signals represent a considerable number of independent rolling bearing characteristics. Their signal recognition and tangible description under the FAM-C and FDM-A methods [129] is essential for a correct diagnosis in terms of a rolling bearing technical condition. This will enable satisfying the postulate of the work [73] stipulating that the number of independent diagnostic signal parameters should be no less than the number of bearing condition parameters.

A rolling bearing is also capable of generating resonant vibrations [15, 39, 40]. According to [73], resonant vibrations are high-frequency (of the order of several kHz) and can only occur when the SBK (summed shape error) spectrum is broadband. A number of filtering processes had to be applied in order to track bearing parameters using previous vibroacoustic methods. These filters required labour-intensive tuning, when reaching resonance values, in particular. The FAM-C and FDM-A methods [129] do not require tuning of any filters – all parameters are comprehensively visible; furthermore – they enable not only simultaneous observations of all parameters of a given bearing, but also multiple bearings (as well as other mechanical components). They are only limited by the observability window of a respective generator-transducer.

3.2.1. Slide of rolling bearing rolling elements and rolling coefficient

3.2.1.1. Motion geometry of a “perfect” rolling bearing

The displacement of a rolling element between bearing races can be considered based on the model shown in Fig. 3.17. According to the first-class lever rule, linear displacement of the shaft’s centre of symmetry will amount to half of the displacement of the object being moved. At the same time, it can be experimentally determined that the smaller the diameter of the rolling element, the faster it rotates when moving the object on the top plate.

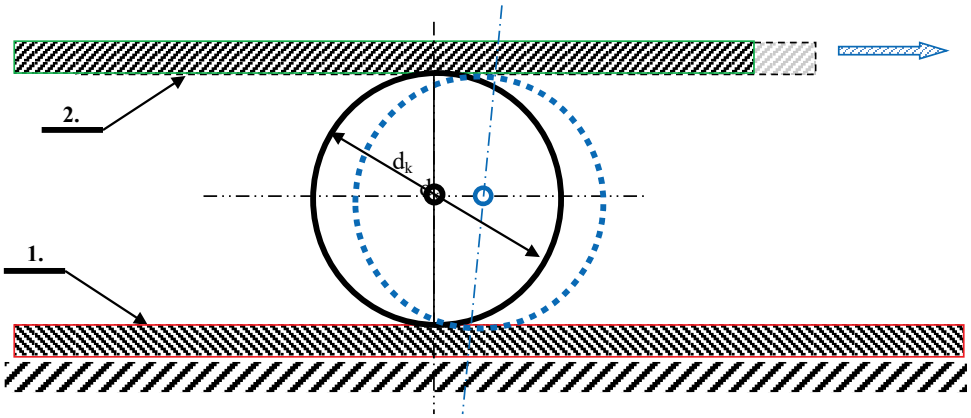

Fig. 3.17. Displacement of two flat plates on a rolling shaft relative to each other: 1 – stationary bottom plate, 2 – moving top plate (object being moved), dk – rolling element diameter (roller or ball)

It is also easy to determine that the rolling friction force is much smaller than the force required to move the top plate over the bottom plate without the rolling element.

The theoretical considerations become slightly more complicated in the case of a rolling bearing. The rolling element (roller or ball) rolls on the inner and outer race – the bottom and top plates of Fig. 3.17 are transformed into two concentric rings (Fig. 3.18). The rolling element of the rolling bearing with a diameter d_k rolls on the inner race. After expansion, this race can be used to calculate the length of this rolling element's circumference:

$$l_k = \pi \cdot d_k \tag{3.34}$$

Once l_k has been expanded on the inner race (diameter D_w), an arc with the length $A_{wo}A_{w2}$ can be plotted. At the same time, the same length of the circumference l_k can be plotted on the diameter of the outer race D_z,, plotting an arc with the length length $A_{zo}A_{z2}$ (Fig. 3.18). The centre of the rolling element during rolling moves by half the length of this arc, i.e., it circles an arc with the length $A_{oz1}A_{zo1/2}$. Hence, the rolling coefficient p_s can be determined, and expressed by the formula:

$$p_s = \frac{\sphericalangle 0A_{wo}A_{w2}}{\sphericalangle 0A_{oz1}A_{zo1/2}} \tag{3.35}$$

After substituting the angle values into the arc measure, the rated value of the rolling coefficient can be obtained [113, 129]:

$$p_{sN} = \frac{D_w}{2 \cdot \left(D_w + 2 \cdot d_k \right)} \tag{3.36}$$

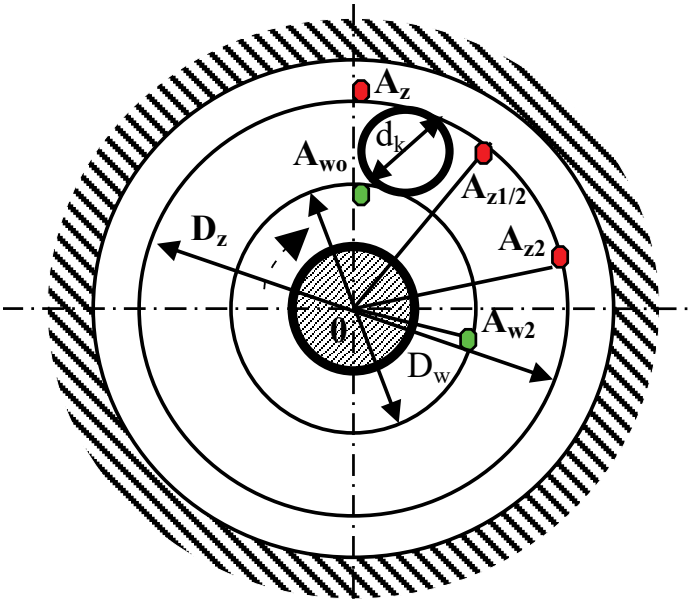

Fig. 3.18. Movement of the bearing cage relative to the inner race:
D_w – inner race diameter, D_z – outer race diameter, d_k – rolling element diameter

It can be noted that in the case of negligibly small rolling element diameters in relation to the inner race diameter (e.g., for needle roller bearings), this value tends towards 0.5. As the diameter of the rolling element increases relative to the inner race diameter, the value of this coefficient will decrease (Fig. 3.19). With an operational decrease of the rolling element diameters (due to abrasive wear), the rolling coefficient will increase (above the nominal value). Thus, decreasing rolling element diameters (due to abrasive processes) entails increasing rolling element angular velocities. The angular velocity of the cage-separator "pulled" by these elements also increases. This change will be more evident (relatively greater) for bearings with smaller inner race diameters, while this speed will be less pronounced (relatively less) for those with larger diameters.

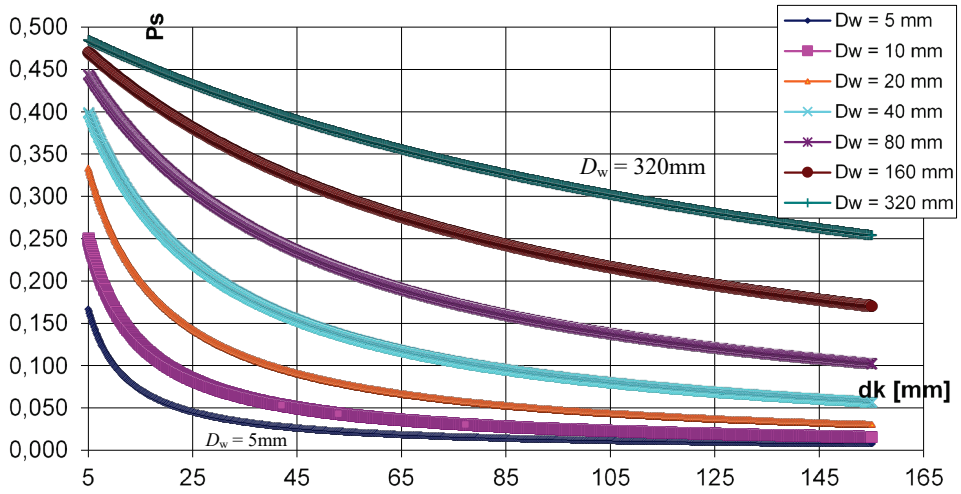

Fig. 3.19. Variation of the rolling coefficient rating p_{sN} as a function of changes to the rolling element diameter d_k for a given inner race diameter D_w

Any deviation of the real rolling coefficient p_s from the rated value p_{sN} (determined from the bearing design parameters in equation (3.36) indicates changes in the bearing. Angular relationships expressed by the formula (3.36) can become a simple and effective check of the rolling bearing fitness. This is because it is sufficient to mark both bearing rings (e.g., with a marker) with one common sign on the movable ring (usually the inner ring) and the bearing cage (Fig. 3.20). When rotating the movable ring (e.g., generator rotor) of the unit, observe the relative movement of the mark on the cage with respect to the mark on the movable ring. When the movable ring is fully rotated, the cage of the working bearing should complete a fraction of the full angle determined by the equation (3.36). A more accurate measurement can be obtained by rotating the movable race until the cage completes one revolution, in which case the angle circled by the movable race should complete a number of revolutions equal to the reciprocal of the value determined by the formula (3.36). Table 2 lists the parameters helpful in testing certain aviation bearings using this method. If the moveable race angle of rotation is greater than $360°\cdot 1/p_s$, the bearing has significant radial clearance and the rolling elements in certain angular sectors lose mechanical contact with the race. If, on the other hand, the angle was too small, this could indicate that the rotational movement of the rolling elements is blocked due to, e.g., contamination in certain angular sectors.

Table 2

Dressing angle for selected aircraft bearing sizes

No.	D_w	d_k	p_{sN}	$1/p_{sN}$	$1/p_{sN}$	Complementary angle
-	[mm]	[mm]	-	-	[°]	[°]
1	5	5	0.167	6.0	2160	0
2	30	5	0.375	2.7	960	240
3	70	10	0.389	2.6	926	206
4	360	10	0.474	2.1	760	40

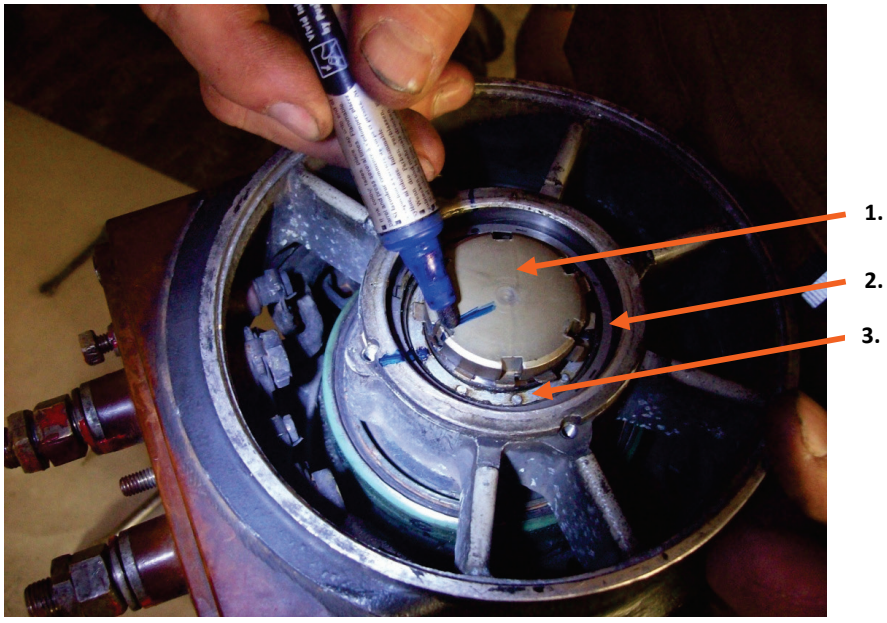

Fig. 3.20. Applying the inspection mark to the inner ring and the cage of an aircraft generator rolling bearing: 1 – bearing journal, 2 – immobile bearing race, 3 – bearing cage

3.2.1.2. Slide and rolling coefficient. Their significance for the rolling bearing classification criterion

The method of checking the bearing condition shown in Fig. 3.20 and described at the end of subsection 3.2.1.1 can serve as a preliminary, simple and in-

expensive method. This is possible when applying the FAM-C and FDM-A methods, where similar observations are conducted during normal bearing operation (i.e., during operation of a monitored propulsion unit), at different rated speeds and different load levels of the propulsion unit. A change in the rotational speed of the bearing shaft is of critical importance for the motion dynamics phenomena taking place within the rolling bearing, mainly due to the change in the hydromechanical forces acting on the rolling elements of the bearing. This includes the properties of the so-called "oil film"[2] [55, 179, 180, 198] that forms between the rolling elements and the rolling bearing races. For an "ideal" bearing in the FAM-C and FDM-A methods, the characteristic set will be a "narrowband" set with a kinematic frequency value equal to the product of the number of rolling elements, the bearing shaft angular velocity, i.e., the associated moving race (relative to the stationary race), and the rated rolling coefficient. If, due to the resistance forces and moment, e.g., caused by bearing contamination, the rotational movement of rolling elements is blocked, e.g., due to contamination in certain angular sectors, then the characteristic set of this bearing shifts towards higher values along the axis of abscissae 0-f_p. The instantaneous frequency waveform (as a function of time), in turn, shows oscillations of the instantaneous frequency changes with a lower period T. On the other hand, when the bearing exhibits significant radial clearance, the rolling elements lose mechanical contact with the race in certain angular sectors. In such situation, the characteristic set of this bearing will shift towards lower values on the 0-f_p axis [114, 122, 123, 129, 136].

Figure 3.21 shows crescent-shaped characteristic sets with raised edges. They have a significant bandwidth (f_{pmax}–f_{pmin}). The shapes and proportions result from observations of real sets in mechanical propulsion units. The bandwidth results from the unevenness of the rolling coefficient of individual rolling elements.

[2] According to [179], p. 18, "...The different behaviour of the oil layer, called the oil film, in the area of high pressures occurring in concentrated contact (e.g., in rolling bearings, gear drives) was pointed out as early as 1914 by Martin (UK) and Gümbel (Germany). However, the foundations of the elastohydrodynamic (EHD) lubrication model were not laid until 1949 by Grubin (USSR) based on Ertel's research. He demonstrated that the change in oil viscosity under high pressure could increase the load-bearing capacity of the oil film by up to twice the value provided by conventional hydromechanical lubrication...".

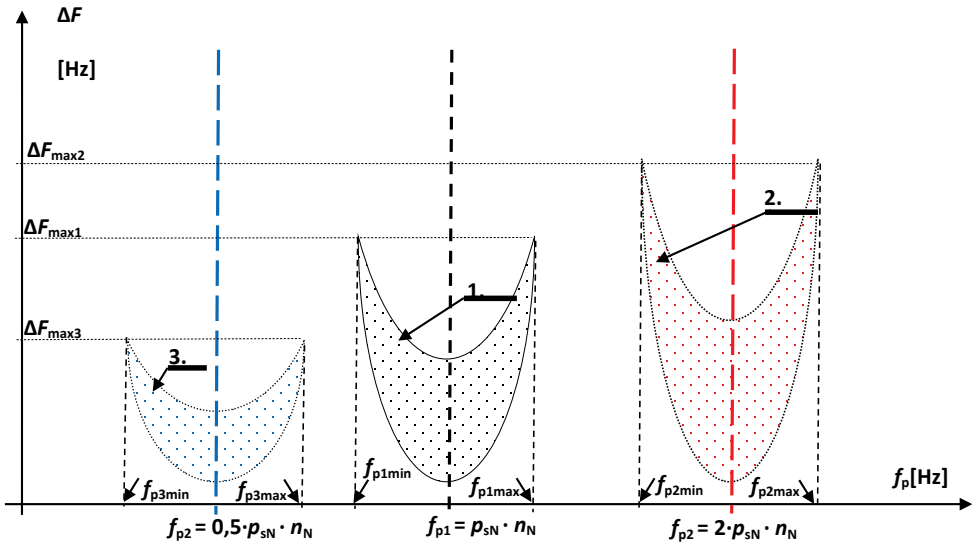

Fig. 3.21. Movement of characteristic sets at different rolling element rolling coefficient average values: 1 – "ideal" bearing $p_{ssr} = p_{sN}$, 2 – bearing with increased total rolling resistance $p_{ssr2} \approx 2 \cdot p_{sN}$, 3 – bearing with increased radial clearance $p_{ssr3} \approx 0{,}5 \cdot p_{sN}$

The rolling coefficient value is determined based on the quotient of a given rolling bearing characteristic set kinematic frequency and the product of the rated rotational speed and the number of rolling elements (up to the frequency of the locked bearing):

$$p_{ssr} = \frac{f_p}{n \cdot N} \tag{3.37}$$

where:
f_p – kinematic frequency of a given rolling bearing characteristic set, n – rated angular velocity in [rps], N – number of rolling elements in a given bearing.

In the extreme case of a blocked cage (no rolling elements surrounding each other on the race), the upper frequency will have the value of:

$$f_{\text{pmaxmax}} = n \cdot N \tag{3.37a}$$

Whereas another extreme case is the lack of contact between the rolling elements and the race, i.e., $f_{\text{pminmin}} \approx 0$.

3.2.2. Misalignment and miscylindricity of shaft bearing supports

3.2.2.1. Misalignment of shaft bearing supports

Misalignment of bearing supports involves an offset of the centre of symmetry of the central bearing relative to the line joining the centres of symmetry of the front and rear bearings. If the centre of symmetry of the central bearing is shifted downwards (towards the ground acceleration vector for an aircraft in the "take-off" position) with respect to the said line, there is a negative misalignment (Fig. 3.22), if upwards – a positive misalignment [44, 113, 114, 129, 133].

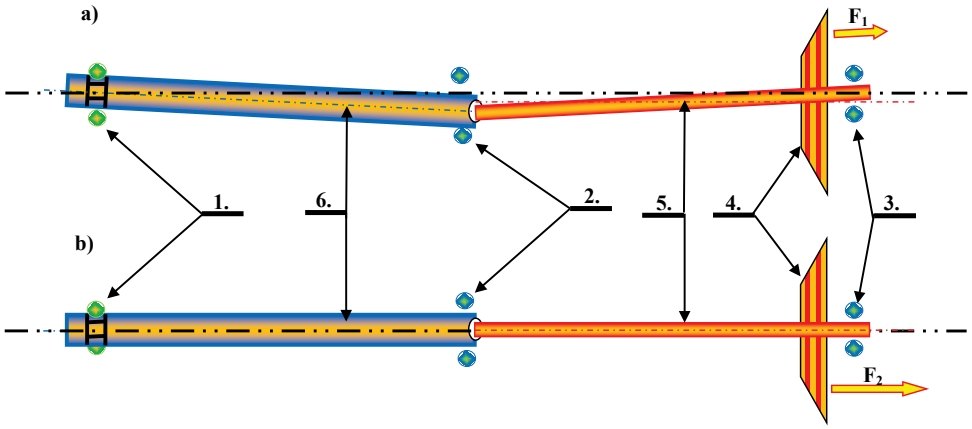

Fig. 3.22. Kinematic overview diagram for negative misalignment of shaft supports: a) "low" rotational speed, b) "high" rotational speed, 1 – front support thrust bearing, 2 – middle support bearing, 3 – rear support bearing, 4 – gas turbine, 5 – gas turbine shaft, 6 – compressor shaft, F_1 – turbine reactive force at "low" rotational speed, F_2 – turbine reactive force at "high" rotational speed

In the case of negative misalignments at low rated speeds, the central bearing is moderately loaded (Fig. 3.22.a). Under the influence of the compressor mass (its centre of mass is geometrically close to the geometric centre of the central bearing journal), part of the gravitational force is transferred through the spline of a splined connection (the connection point between the turbine shaft and the compressor shaft). As the rated speed increases, the longitudinal force from the turbine increases, causing the connection between two shaft parts (turbine shaft and compressor shaft) to stretch, thus lifting the central bearing journal upwards (Fig. 3.22.b). This results in an optimally uniform gap between the rolling elements and races at the rated speed – such rolling conditions are advantageous. The rolling ratio

characteristic as a function of the rated rotational speed is then used to derive the local minimum (Fig. 3.23).

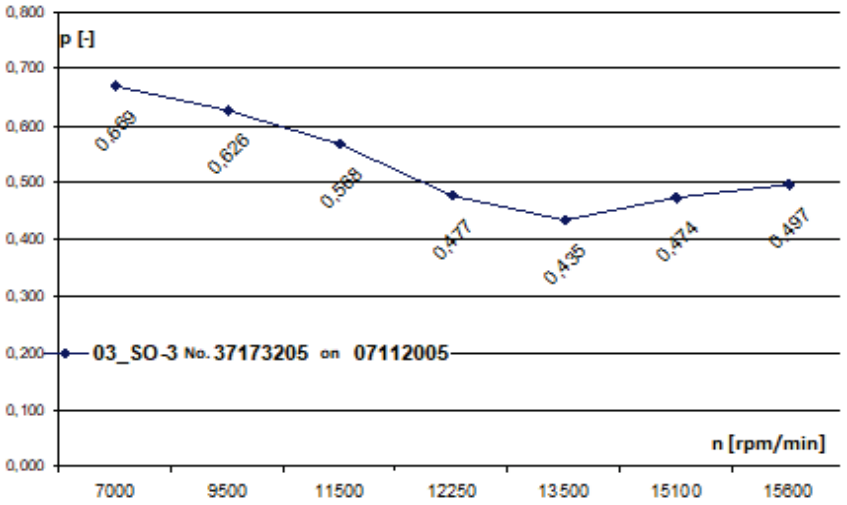

Fig. 3.23. Changes in the rolling coefficient of the SO-3 engine central bearing with a local minimum indicating misalignment

3.2.2.2. Miscylindricity of shaft bearing support seats

Walls of the cylindrical seats of all three bearings of a given engine being parallel to its main longitudinal axis of symmetry is important for the correct operation of shaft bearings (Fig. 3.24). Sometimes both parts of the engine body (Fig. 3.24, elements 1 and 9) have their bearing seats ground individually – the seat in the compressor body (element 4) and the seats in the compressor body (elements 8 and 10) separately. A spacer is fitted at a later stage of the assembly process (Fig. 3.24, item 7). This is usually previously machined by an angle grinder depending on the outcomes of measuring the coaxiality of the symmetry centres of three bearing seats. Therefore, once the entire engine is assembled, there is a danger of the central bearing symmetry axis misaligned relative the rear bearing symmetry axis. When the bearings are pressed in with a hydraulic press, their actual axis of symmetry is guided by the cylindrical surfaces of the bearing seats. Once a spacer has been selected (between the compressor body and the turbine body), these bearings are pressed in, and the two parts of the body are bolted together. The most favourable solution would be to grind all three seats at one mounting position of both body parts with the spacer (item 8) [114, 133]. If this is not possible, due to the existing machinery, the current technology can be maintained as a substitute, albeit with

certain modifications. The baseline in this case should not be the bearing seat centres of symmetry, but the lines (so-called "forming lines") of bearing seat cylindrical surfaces (Fig. 3.24.a and 3.24.b). Both parts of the engine body should be assembled according to these lines, and then openings for fitted bolts (with a diameter that closely matches the opening diameter) should be drilled (reamed) in the flange of both body parts.

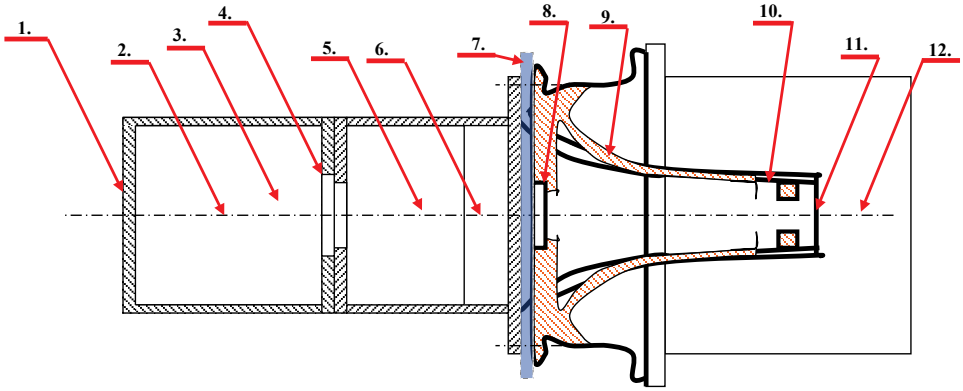

Fig. 3.24. Cross-section of an SO-3 type single-flow, single-shaft engine with control rollers prepared for mechanical measurement of bearing seat concentricity: 1 – turbine body; 2 – external control mark of control roller No. 1; 3 – inspection roller No. 1; 4 – rear bearing seat; 5 – internal inspection mark of inspection roller No. 1; 6 – internal inspection mark of inspection roller No. 2; 7 – spacer between the compressor body and the turbine body; 8 – central bearing seat; 9 – compressor body; 10 – rear bearing seat; 11 – inspection roller No. 2; 12 – external inspection mark of inspection roller No. 2

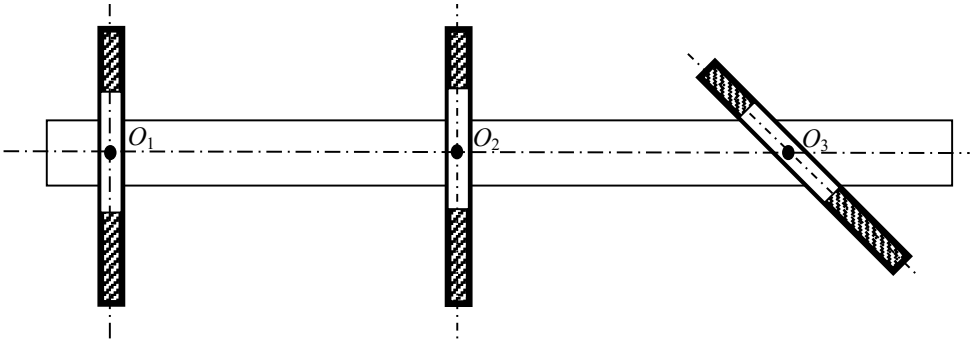

Fig. 3.24a. Three bearing seats with the centres of symmetry marked according to the typical measurements conducted by a repair shop, but with skew bearing seat 3 forming a cylindrical surface

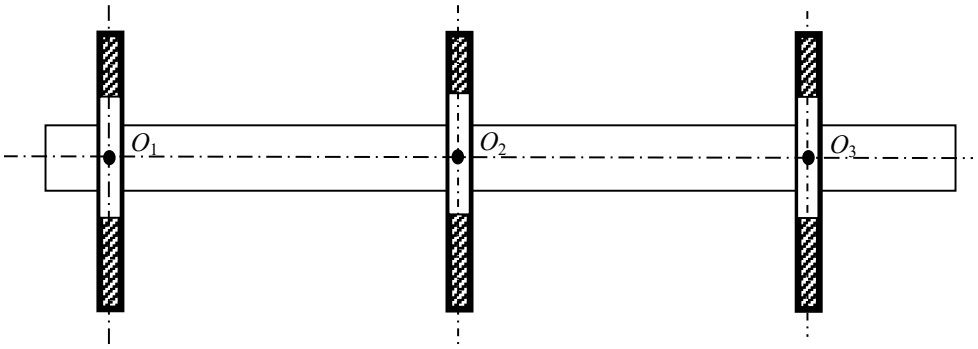

Fig. 3.24.b. Three bearing seats with the centres of symmetry marked according to the typical measurements conducted by a repair shop, without skew: O_1 – centre of symmetry of the front bearing seat (front support thrust bearing), O_2 – centre of symmetry of the middle bearing seat (middle support bearing), O_3 – centre of symmetry of the rear bearing seat (rear support bearing)

3.2.3. Rolling bearing spacer-cage falling onto the inner race

As noted in subsection 3.2.1, an "ideal" rolling bearing is characterised by the rolling of its rolling elements on the inner and outer race without slide. The rolling elements drag the separator cage (Fig. 3.25). The ratio of cage angular velocity quotient to the supported shaft journal speed is represented by the coefficient p_{sN} described by the formula (3.36). Table 2 lists p_{sN} values for various rolling bearing geometrical dimensions. The range of these values is p_{sN} = 0.167÷0.474 [114, 133]. Thus, cage-separator angular velocity is significantly lower than the supported shaft journal angular velocity (representing 0.167÷0.474 of its value). The situation changes when the cage falls onto the inner race, e.g., as a result of an increase (through abrasive wear) in the size of the separator windows (Fig. 3.26). The cage then starts to rotate faster at a speed close to that of the shaft bearing journal. After dropping down, a characteristic local maximum appears on the characteristic curve for the dependence of the rolling ratio on the rated speed (Fig. 3.27) [114, 136]. In comparison, in a properly operating bearing (without the cage-separator dropping down on the inner race), the relationship is monotonically descending (Fig. 3.26). After dropping down, the cage-separator rubs characteristic marks on the bearing inner race (Fig. 3.29, detail 2). At the same time, the cage-separator clamping rings also bear traces of rubbing against the race in question (Fig. 3.30). After descending, the cage-separator separating elements usually bear grinding marks – traces of rubbing against the bent orifice of the rolling bearing outer race (Fig. 3.31, detail 2).

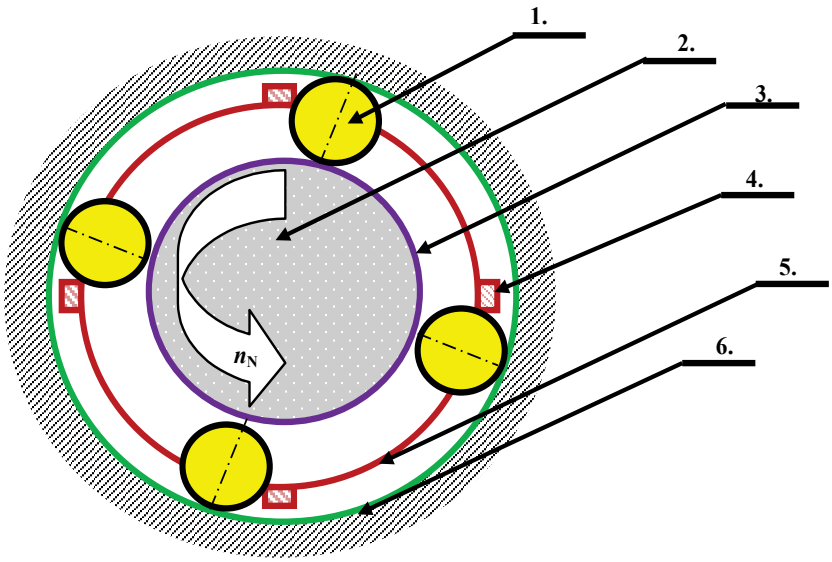

Fig. 3.25. Cooperation of a bearing at normal rolling of rolling elements between races – rolling elements drag the bearing cage with their perimeter: 1 – rolling element, 2 – bearing journal (arrow indicates its rotation direction), 3 – bearing inner race, 4 – cage separator, 5 – cage retaining ring, 6 – bearing outer race (pressed into the propulsion unit housing)

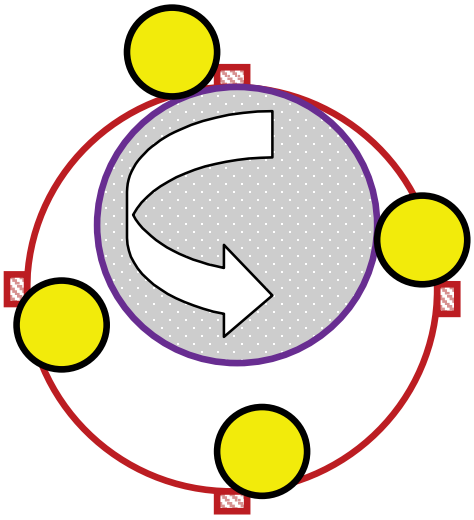

Fig. 3.26. Cooperation of rolling bearing elements after cage drops down – the cage achieves increased speed and drives rolling elements through secondary impact

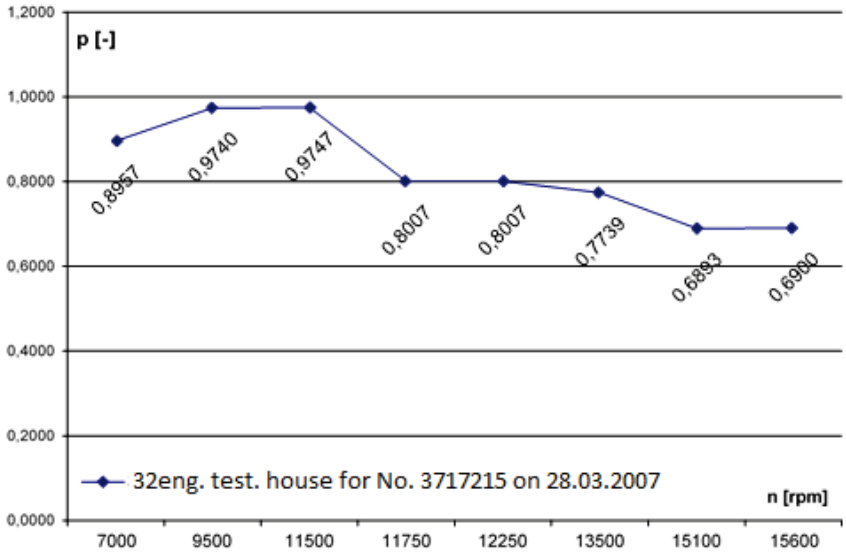

Fig. 3.27. Rolling coefficient changes (as a function of speed) in the central bearing of an SO-3 engine with a local maximum indicating cage dropping on the inner race

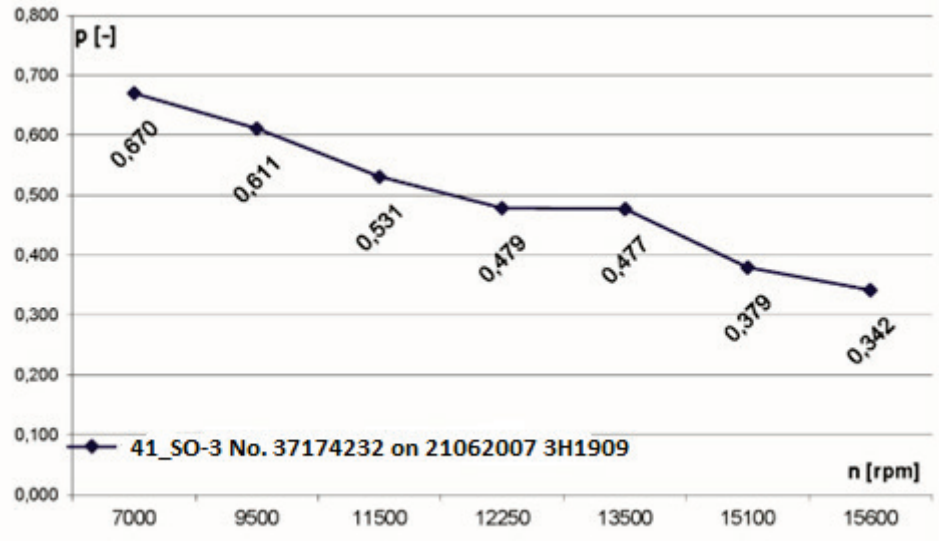

Fig. 3.28. Rolling coefficient changes (as a function of speed) in the central bearing of a correctly operating SO-3 engine

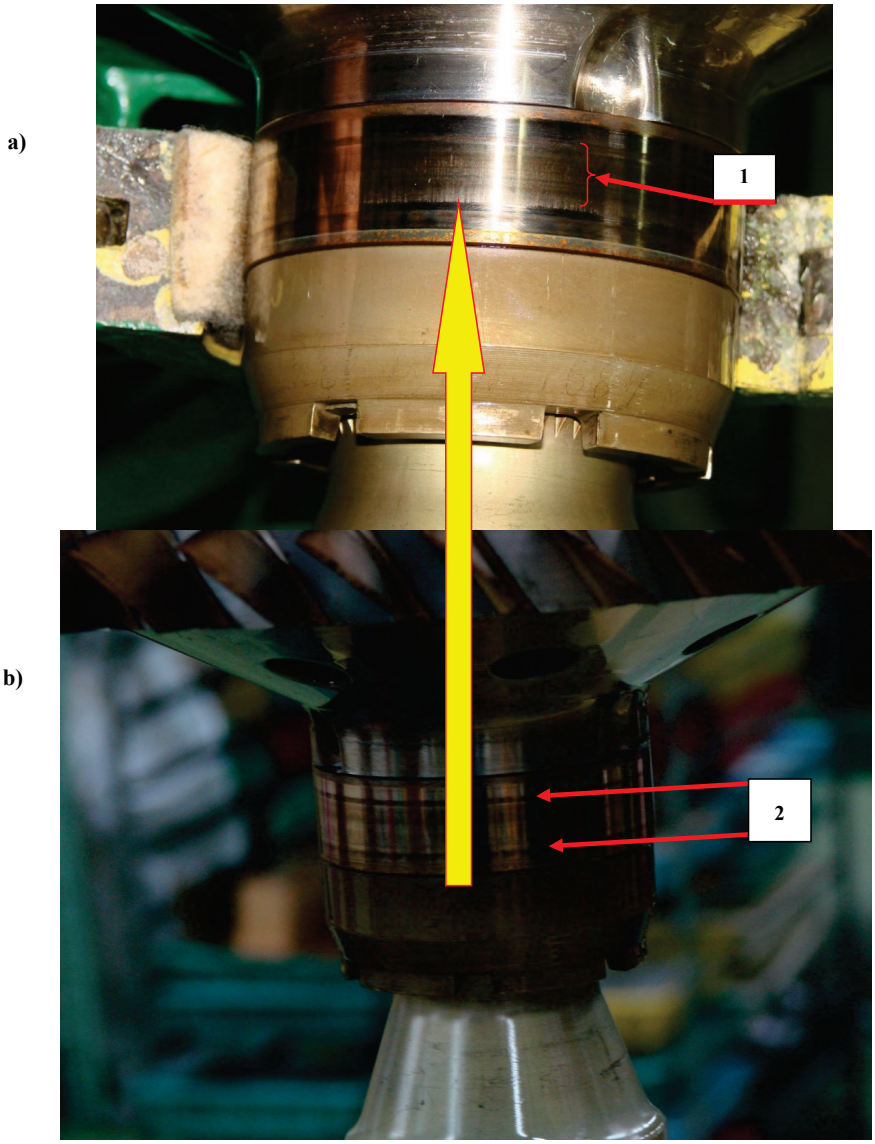

Fig. 3.29. Central bearing inner race: a) close-up: central bearing inner ring with visible ridging traces, b) overview: 1 – ridging traces (rippling of the inner race surface), 2 – race "grinding" traces after the cage has dropped down

The fastening rings of the centre bearing separator bear traces of rubbing against the inner race (Fig. 3.30, detail 1) and the outer race orifice (Fig. 3.31, detail 2). Moreover, the central bearing separator bears traces of significant circumferential forces – the separator windows show evidence of cage-separator material

flash where the cage window edges contact the rolling elements – in some cases, cage-separator material flash is visible in these areas (Fig. 3.32, detail 2). Separator windows are enlarged. All central bearing shafts (due to the enlarged windows) spill out when dismantled.

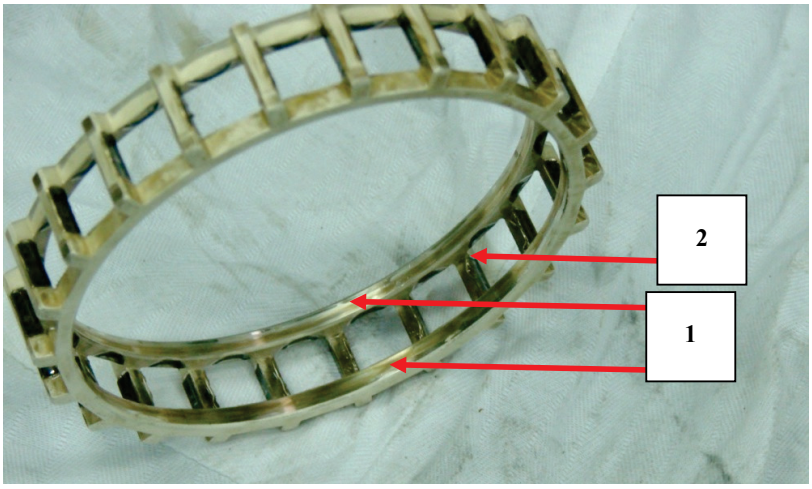

Fig. 3.30. Central bearing cage – oblique view – with traces of rubbing against the journal: 1 – traces of rubbing clamping rings, 2 – grinding traces on separating elements

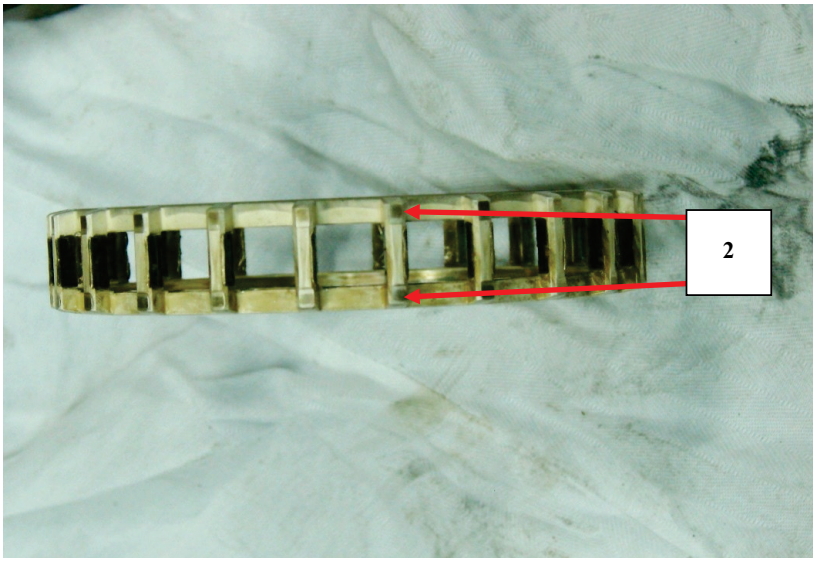

Fig. 3.31. Central bearing cage – vertical projection – with traces of rubbing against the bearing inner race orifice: 2 – grinding traces on separating elements

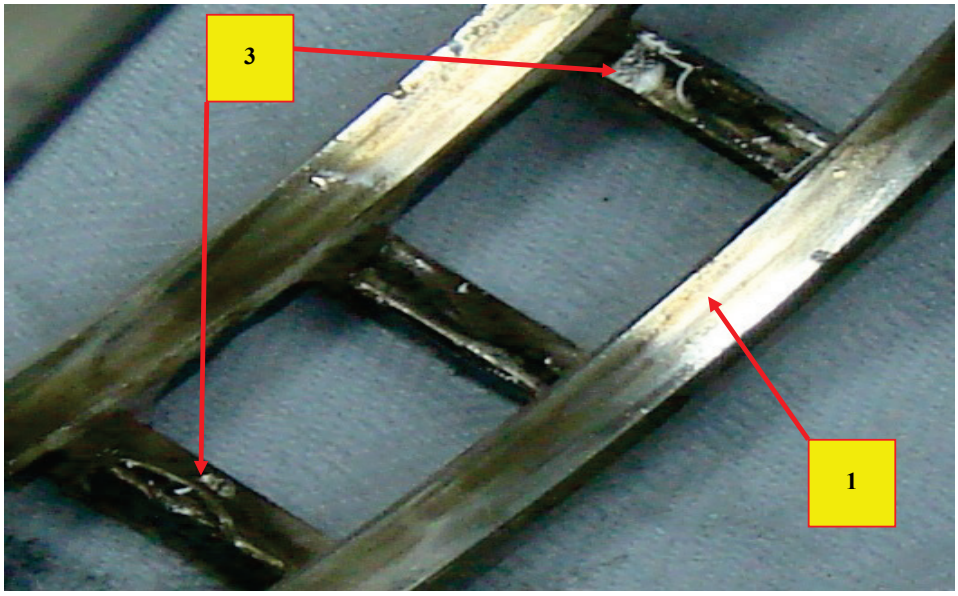

Fig. 3.32. Central bearing cage – close-up: 1 – rubbing marks on the cage perimeter, 3 – flash marks on the edge of the cage separating elements in contact with rolling elements

3.2.4. Rolling bearing resonance and its reflection in the FDM-A characteristic set shape

Resonant states in bearings can have various causes, which include errors in the assembly geometry of bearing supports (deviations in the geometry of fixing rolling bearing in a seat or on a journal, deviation in the geometry of the journal or seat) or inadequate storage, especially in the case of a complete machine, e.g., an engine (lack of periodic shunting redressing of rolling elements) [15, 47, 73, 129, 160, 169, 176, 179, 237, 244]. This leads to a formation of so-called "false Brinell imprints" on the perimeter of the race, which in later operation, become "pools of attraction" [5] for rolling elements. The author believes that aeronautical rolling bearings in the Polish Air Force are correctly stored and assembled, while "false Brinell imprints" are rather more likely caused by strong clamping of the rolling elements onto the outer race by the compressor journal induced by phenomena described in the previous chapter. The primary author of this tract has repeatedly participated in the disassembly of bearings wherein the mechanical resonance condition of the rolling bearings was previously observed (using the FDM-A method) during the operation of the aircraft engine. After the disassembly, the existence of "false Brinell imprints" on the outer race was usually found. The number of these

imprints was equal to the number of rolling elements of the rolling bearing in question. This number does not coincide with the product of the number of rolling elements N and the rolling coefficient p_{sN} of a normally operating rolling bearing. (Apparently, the number of imprints on the race should equal the product of the number of rolling elements and the rolling coefficient). Because, in reality, the number of imprints is equal to the number of rolling elements of the bearing in question, the author believes that prior to rolling elements achieving a state of resonance, the cage angular velocity must synchronise with the journal angular velocity. For this to occur, there must first be an increase in the size of the cage windows (due to sliding friction between the rolling elements and the edge of the cage window). The cage then drops down. This is confirmed by observation through the FAM-C and FDM-A methods [123, 129, 136, 147]:

- prior to the resonance condition occurring, there is a systematic increase in the value of the slow pulsation component, i.e., the envelope, on the waveform $f_i = f(t)$ of the AC channel (Fig. 3.8) for all rotational speeds, which indicates an increase in the circumferential backlash of the bearing node,
- symptoms of cage dropping onto the inner race appear – a local positive extreme (local maximum) appears on the rolling characteristic $p_s = f(n)$ (obtained from the DC measuring channel) – Fig. 3.27.

As soon as the cage drops down, it ceases to be driven by rolling elements (driven by bearing races under "normal" conditions) and is then driven directly by the inner race. Consequently, the cage increases its angular velocity and begins to drive the rolling elements itself (Fig. 3.26) Therefore, after the cage drops down onto the inner race, its speed increases from:

$$\omega_k = p_s \cdot \omega_{cz} \tag{3.38}$$

where:
ω_k – cage rotational speed, ω_{cz} – journal angular velocity;

to the pivot speed, taking into account the ratio of the friction gear formed, assuming slide absence, which can be expressed by the formula:

$$\omega_k = \omega_{cz} \cdot D_w/D_k \tag{3.39}$$

where:
D_k – inner cage diameter.

The value of D_k k is, in practice, a few percent higher than D_w, hence, the cage angular velocity is also a few percent lower than that of the journal. However, due

to the circumferential-elastic forces of the cage and the impact of the rolling elements rebounding between the cage and the inner race, the cage can reach the angular velocity of the journal. Rolling element motion in a state of resonance is radial. If, for any reason, the cage speed decreases below the journal speed, the rolling element will hit the cage window and increase its angular velocity. This is followed by a synchronisation of the cage angular velocity and the journal angular velocity. Of course, the phenomenon of synchronization between the cage angular velocity and the journal angular velocity also works in the other direction – if cage velocity exceeds journal velocity, a vibrating rolling element will hit the counter-rotating cage window edge and decelerate [123, 129].

The above gives rise to the question that may arise as to why the rolling elements gouge and deepen the "false Brinell imprints" at well-defined locations during bearing radial resonance? The primary author believes that rolling elements stochastically falling into hollows in the outer race lose a part of their energy, which results in a standardization of the angular velocity. If a rolling element loses too much energy within a "false Brinell imprint", it will be unable to rebound from the outer raceway quickly enough and will be dragged along the outer race by the "approaching" cage element. It will thus be forced through rolling between the raceways, to increase its energy. Therefore, the rolling element will obtain a higher rotational speed. If – inversely – a rolling element has an excessive rotational energy, then instead of rebounding from the "false Brinell imprint" straight away, it rolls over the race. Then the approaching cage separating element hits the rolling element, slowing down its speed. The above description of rolling element behaviour during resonance is the author's supposition – its confirmation requires a lot of experimental tests and analysis. However, it is a fact that "false Brinell imprints" (Fig. 3.34) [123, 136] have been identified on damaged bearings with excessive radial clearances during disassembly. According to source literature [15, 73, 176, 197], these imprints unequivocally indicate internal radial resonance of the rolling bearing. At the same time, the author observed in exactly the same bearings (during the operation of a turbine engine), an increasing relative height of characteristic sets obtained through the FDM-A method (relative characteristic set height – quotient of the characteristic set height $A = \left| \{\Delta F_i\}_{max} \right| + \left| \{\Delta F_i\}_{min} \right|$ to its width, i.e., to the width of the frequency band occupied by this characteristic set $\Delta f_{pj} = f_{pmaxj} - f_{pminj}$) [100, 101, 123, 129].

The quality factor of characteristic sets also increased:

$$Q = f_{oj} / \Delta f_{poj} \tag{3.40}$$

where:
f_{oj} – "carrier" frequency of a given characteristic set ($f_o \approx p_s \cdot f_N$) of bearing No. j,
Δf_{poj} – bandwidth of a characteristic set of bearing No. j.

In addition, the author observed, as the resonance states deepened, the separation (uncoupling) of the characteristic sets. In the course of further operation, these sets decomposed vertically and horizontally into separate subsets (Fig. 3.33) [100, 101, 123, 129]. These sets had a high quality factor Q > 10. In comparison, the characteristic sets of a bearing without resonance merge (Figs. 3.40 and 3.41) and exhibit a low quality factor $Q < 10$. When the bearing is operated with such a high quality factor, "false Brinell imprints" occur on the races. If the operation under this condition is prolonged, this may lead to a number of irreversible phenomena that potentially pose a safety hazard:

- breaking out of rolling bearing cage separating elements;
- excessive increase in radial clearances (resulting from intensive abrasive wear of rolling bearing and race surfaces) – possible shifting of the rotor assembly axis of symmetry relative to the body axis of symmetry – in extreme cases, also turbine or compressor blades rubbing[3] against the diffuser;
- spontaneous vibrations of the power transmission system felt by the onboard personnel (however, often not detected by the regular onboard vibration sensors) [7, 95] in the form of airframe vibrations;
- excessive increase in oil system swarf content;
- lost fit (intense sliding) between the bearing inner ring and journal.

[3] The phenomenon of the rotor assembly rubbing against the engine body mounted on the TS-11 aircraft was observed by the primary author after 60 h of bearing node operation with a quality factor (averaged from Q values for all rotational speeds) $Q>11$ over time Θ.

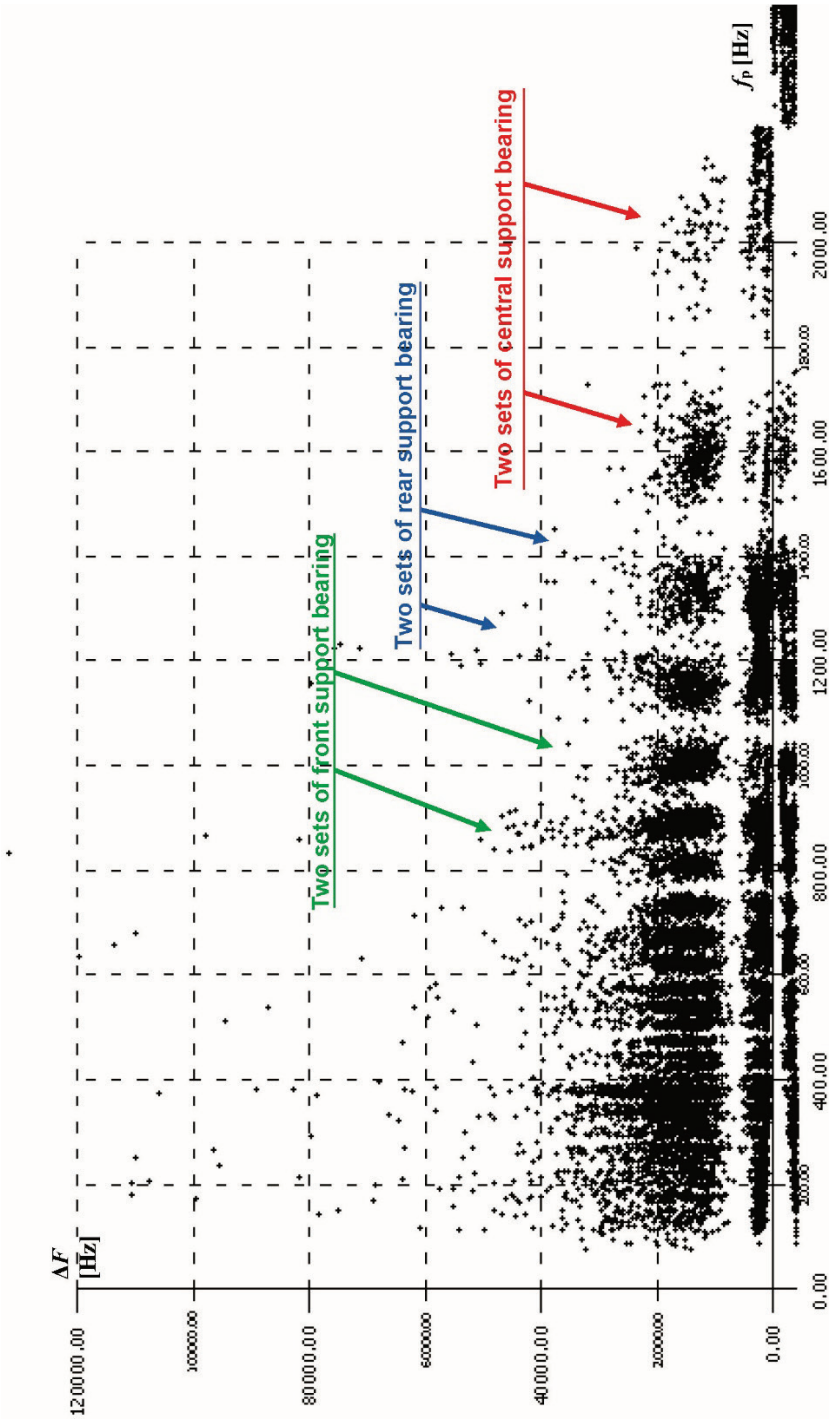

Fig. 3.33. Characteristic sets for resonant bearings

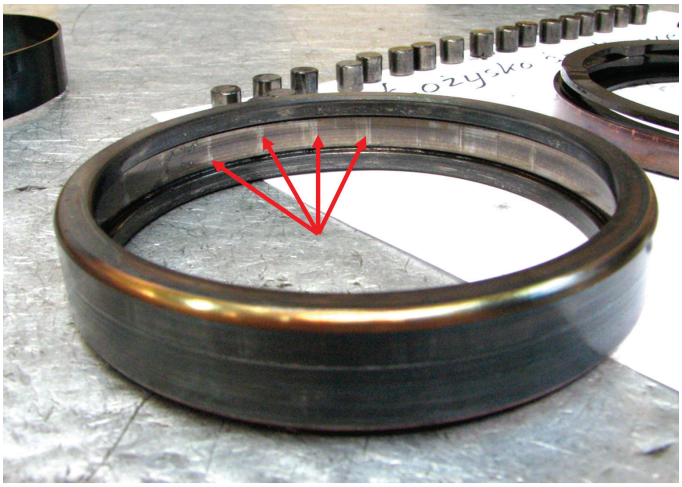

Fig. 3.34. "False Brinell imprints" (marked by arrows) on the race of a bearing under prolonged resonance

3.2.5. Condition arising from an excessively tightly clamped rolling bearing and its reflection in the shape of characteristic sets

According to source literature [18, 119, 176, 179, 261, 269, 291], a too-tight fit of the bearing on the journal or in the housing can remove bearing radial clearance and even induce pre-clamping of rolling elements. This significantly increases rolling resistance, especially at low loads.

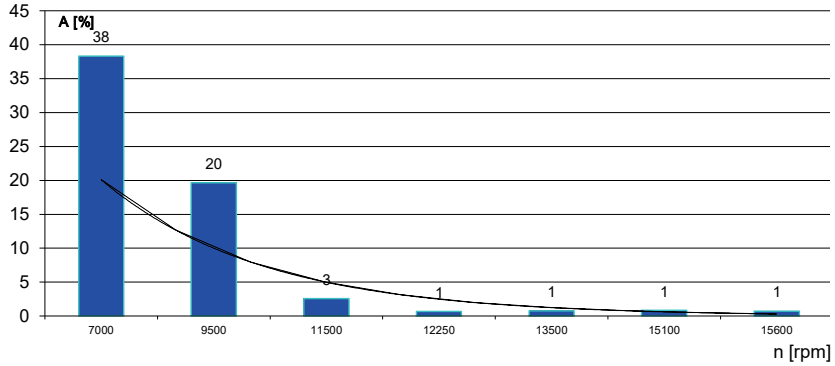

Fig. 3.35. Characterized height of characteristic sets of a correctly seated rolling bearing as a function of shaft rated speed

An analysis of the bearing support monitoring data provided by the FDM-A and FAM-C methods, as well as source literature data [15, 73, 114, 136, 244, 272]

enabled a conclusion that the longest operation of the bearing node in aviation turbine engines is ensured by rolling bearings with normative (according to the TR for a given engine) radial clearances. Their combined resistance characteristic (the height of the characteristic sets obtained by the FDM-A method), however, decreases as the rated rotational speed increases (Fig. 3.35).

The normative clearances between the rolling element and the race allows lubricating oil to flow through this clearance. As the rated speed increases, the oil increases its hydromechanical load-carrying capacity [148, 158, 179, 180, 198, 261], which significantly improves the operating conditions of the bearing, namely, it mitigates the impacts between the rolling element and race rough sections, enhances cooling and increases load-carrying capacity. However, excessive radial clearance (above the value shown in the TR) or an increase in the bearing lubrication system oil pump capacity leads to heightened motion resistance. The so-called "fording resistance" grows due to an increase in viscous friction – this results in a flattening of the aforementioned characteristic [129, 176], shown in Fig. 3.35.

In the case of a bearing with a correct (TR-compliant) value of radial clearances, the characteristic of the rolling coefficient p_s (quotient of cage angular velocity and journal angular velocity) as a function of rated rotational speed n assumes an exponential shape monotonically decreasing due to an increase in the action of hydromechanical forces at increasing rated rotational speed (Fig. 3.36). The greater the radial clearance values, the smaller the p_s values.

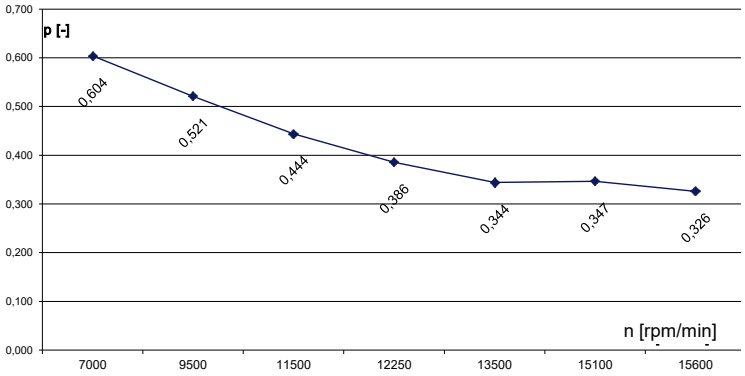

Fig. 3.36. Characterized rolling coefficient of a correctly seated rolling bearing as a function of shaft rated speed

An "ideal" bearing will have a rated rolling coefficient expressed by the formula (4.3) [113]. If the bearing is pressed too tightly onto the journal, inverse characteristics are usually observed:

– total resistance increases with increasing rated speed (Fig. 3.37),

– the rolling coefficient characteristic is not monotonically decreasing (Fig. 3.38) for higher rotational speeds (Fig. 3.38, n = 15,600 rpm), and a monotonically increasing characteristic is often manifested instead.

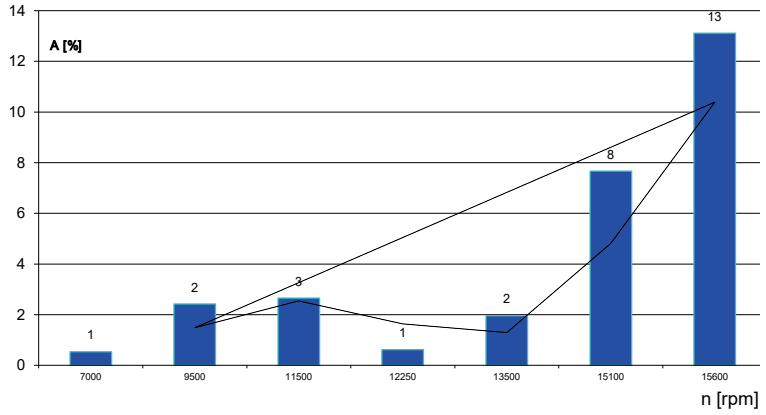

Fig. 3.37. Characteristic set height of a rolling bearing seated on a journal with excessive pressure as a function of shaft speed

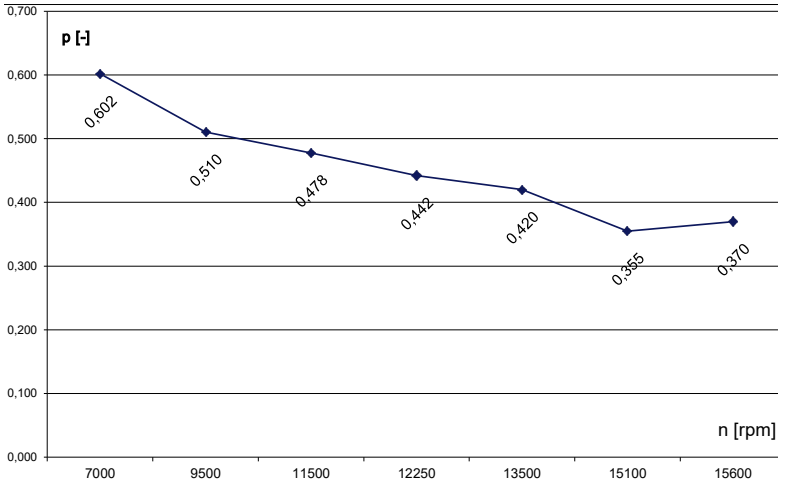

Fig. 3.38. Rolling coefficient characteristic of a rolling bearing seated on a journal with excessive pressure as a function of shaft speed

In such a situation, the absolute rolling coefficient for lower rotational speeds is:

$$p_s > p_N \geq 1.0 \tag{3.41}$$

A rolling coefficient p_s above unity would apparently make no mathematical and physical sense. In practice, such high rolling coefficient values are sometimes observed [114, 136], and may indicate:

- a mechanical defect with regard to the races, e.g., surface rippling or material decrements,
- deviation from the circular shape of certain rolling elements,
- blocking of rolling elements in cage windows (rolling element dressing failure) and a step-wise friction force changes in stationary rolling elements on the race due to adhesive forces.

Friction of unlubricated surfaces and under boundary lubrication conditions, entails a step-wise change of the friction force [4] [165, 172, 215, 269, 291]. Such phenomena have been observed more than once using the FAM-C method for highly clamped rolling bearings in some aircraft engines [114, 119, 129, 136]. Observations made by the author in an engine test house show that when a bearing journal is coated with an additional chromium layer, which increases joint clamping, the average rolling coefficient value (averaged for all levels set during the engine test) of p_{sr} increases significantly [266]. The spread in rolling coefficient values calculated for individual tests with the same rotational speed also increase, which will be further determined by the $p_{s\max\max}/p_{s\min\min}$ coefficient.

Mean rolling coefficient value average from all rated speed values [119, 129] can be derived through:

$$p_{śr} = (p_1 + p_2 + p_2 + ... + p_{\max}) / k \tag{3.42}$$

where:

$p_1, p_2, p_2, ..., p_{\max}$ – successive rolling coefficients for subsequent tested turbojet engine main shaft rated speeds ($n_{\min}, n_2, n_2, ..., n_{\max}$), k – number of tests.

For $n = n_{\min}$ ($n = n_1$), rolling coefficient value $p>1$, while near $n = n_{\max}$, the characteristics became monotonically increasing. In the situation described above, due to the relatively small layer of technical chromium applied onto the journal, rolling coefficient values (p_{rr}) decreased after several hours of turbojet engine operation, and the characteristic $p = f(n)$ assumed a monotonically descending shape.

No other bearing observed by the author [119] exhibited such a smooth "alignment" of the characteristics. After running the engine for approximately 3 hours, the diagnosticians observed (through the FAM-C method) the appearance of significant backlash, manifested through increase in the height of the first harmonic (relative to the engine main shaft angular velocity) obtained from the measurement

[4] The lubricating oil is unable to separate mating surfaces when bearings are firmly clamped. This results in the occurrence of surface adhesion forces.

path of the three-phase generator. Significant stochastic changes were also observed in the bandwidth of the characteristic set for each rated speed of the turbojet engine main shaft, i.e., significant changes in the rolling coefficient during successive tests for a given rated speed. After a further 13 h of engine operation, the aviation personnel (during the ground test) identified strong vibrations within the airframe. The engine was disassembled and the bearing was verified. Significant race material loss and severe strains induced by the circularity of the rolling element surface shape with traces of softening on the rolling element surface (traces of "milling" and surface rippling) were found to have occurred, Fig. 3.39. According to source literature [18, 73, 129, 215, 244, 268, 281], this is the consequence of internal friction (plastic deformation due to rolling elements squeezing between the races) and increased external friction. There was also an exceptionally large diversification in shape between individual rolling elements (Fig. 3.39).

Four types of rolling rollers cylindrical surface shape types can be distinguished. They prove the considerable differentiation (resulting mainly from the initial variation in the rolling element diameters) of the tribological processes [119, 129, 268]:

1) with a strongly rippled cylindrical surface, with traces of "milling" and surface rippling, caused by excessive thermal energy release (Fig. 3.39),
2) with traces of pitting,
3) with traces of fretting,
4) one-sided tapered, smooth grinding.

If there is no backlash between rolling elements and races, the smallest differences in rolling element geometries start gaining importance– some (with larger diameters) experience a strong interaction of adhesive [56, 215, 244, 269] and micro-adhesion forces [291]. Despite this fact, the FDM-A method can quickly identify a bearing with excessive clamping and can thoroughly describe a number of parameters characterising this type of wear. Due to the aforementioned complex structure of tribological phenomena, there are strong internal vibrations, which include significant rolling coefficient variations between rolling elements. Therefore, it is possible to observe (using the FDM-A method) notable changes in the bandwidth of the characteristic set for such a firmly clamped bearing at individual rated speeds of the turbine engine main shaft.

The primary author has developed a coefficient for extreme stochastic changes $p_{s\mathrm{maxmax}}/p_{s\mathrm{minmin}}$ (also called [119, 129] the "rolling characteristics dynamic tilt coefficient"), that is expressed by the formula:

$$p_{s\mathrm{maxmax}}/p_{s\mathrm{minmin}} = \{\{p_{1i}\}_{i=1}^{i=k}/\{p_{1i}\}_{i=1}^{i=k}, \{p_{2i}\}_{i=1}^{i=k}/\{p_{2i}\}_{i=1}^{i=k}, \ldots, \{p_{1i}\}_{i=1}^{i=k}/\{p_{1i}\}_{i=1}^{i=k}\}_{\max} \tag{3.43}$$

where:

i – number of consecutive tests for a given rated speed, k – number of tests for a given main shaft rated speed – measurement practice shows that usually $k = 5$ tests are conducted for each main shaft rated speed set by an aircraft technician, p_{1i}, $p_{2,}$ ..., p_{max} – consecutive rolling coefficients for consecutive rated speeds.

It was found that in the case of a bearing with excessive press, $p_{smax\text{-}max}/p_{sminmin} > 2$, while in the case of correctly embedded bearings $p_{smaxmax}/p_{sminmin} = 1{,}1 \div 2{,}0$.

Fig. 3.39. Rolling element of a bearing with excessive clamp and traces of "milling" and surface rippling caused by excessive thermal energy release

3.2.6. Condition of excessive internal passive rolling bearing anti-torques and its reflection in the shapes of characteristic sets

A systematic increase in the individual bearing characteristic set height within a turbojet engine group can be noted when observing turbine engine bearings using FDM-A and FAM-C methods – the characteristic set height in factory-new bearings (Fig. 3.40) ranges mostly from 30 kHz to 60 kHz high, and falls in the range of 3000 kHz to 4000 kHz (3÷4 MHz) in the case of highly corroded or contaminated bearings (Fig. 3.41). Engine inspection disassembly operations have shown significant corrosion pitting on the surface of rolling elements and on bearing covers [129, 136]. Signs of overheating (tarnish colours) or blue-coloured micro-adhesion [291] are also common.

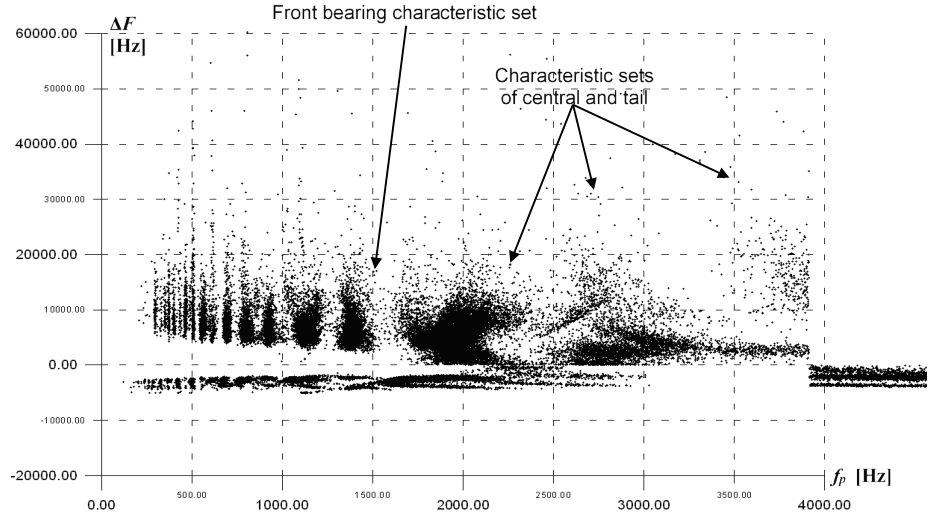

Fig. 3.40. Characteristic sets of turbine engine No. 15 prior to long-term shutdowns

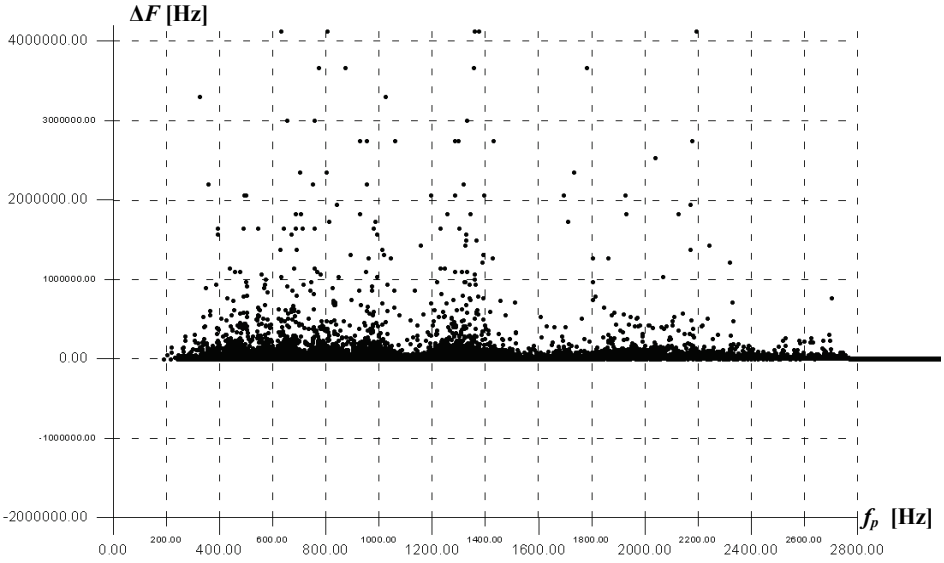

Fig. 3.41. Characteristic sets of turbine engine No. 215 after a 7-month shutdown without maintenance

In extreme cases of bearing node overheating, the journal undergoes secondary softening (Fig. 3.42) due to a significant reduction in bending strength, followed by increased unbalance of the engine rotor assembly leading to its failure.

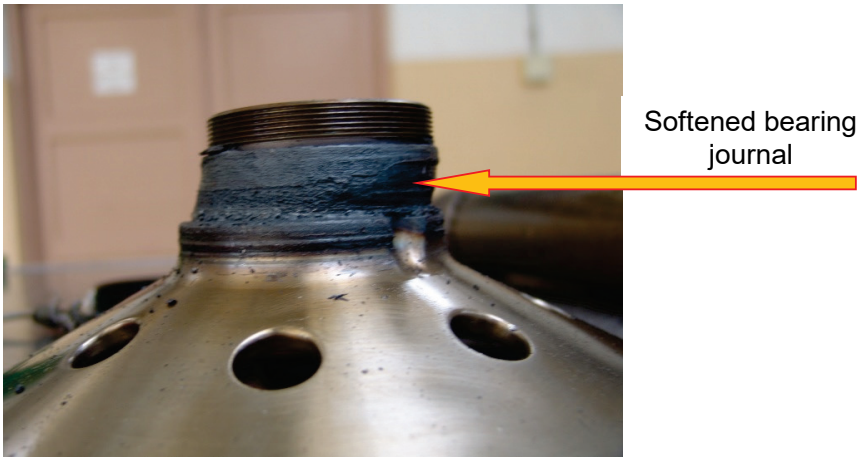

Fig. 3.42. Softened bearing journal

3.2.7. Spacer sleeve fracture

In the case of housings made of light alloys and non-metallic materials, it is advisable to use spacer sleeves made of steel or cast iron, press-fitted into the seats of these housings [73, 74]. They improve the tolerance of bearing supports to bearing skewing and facilitate the assembly process. However, their fracture results in mechanical unbalance of the rotor assembly borne by this support.

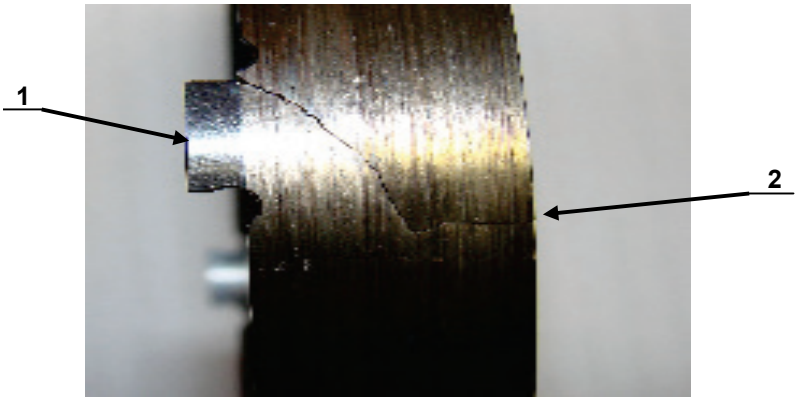

Fig. 3.43. Cracked sleeve fixing the rolling bearing outer race to the turbine engine body: 1 – sleeve rotation limiter, 2 – sleeve fracture location

During testing of the SO-3W engine No. 48170308 [266], the compressor journal was damaged, undercutting half of its thickness. This resulted in a strong

motion of the central bearing journal eccentric, and, probably, its enhanced action on the sleeve through the bearing outer ring. After the engine had been running for several hours, an inspection disassembly was conducted. A fracture of the central bearing bushing was identified (Fig. 3.43). In consequence, the results of measurements taken using the FAM-C method were analysed.

Analysis of previously taken measurements demonstrated that there was a reduction in the characteristic set height for the **first AC harmonic** of the engine main shaft rated speed to A_o = 1.7 Hz after the fracture of the central bearing sleeve. The nature of the "resultant eccentricity *a*" parameter changed – a clear "resonance boost" can be seen, i.e., a significant increase in the characteristic set height at n_5 = 15,100 rpm, i.e., the shape of the characteristic changed from "bath-like" to "resonant" (Fig. 3.44).

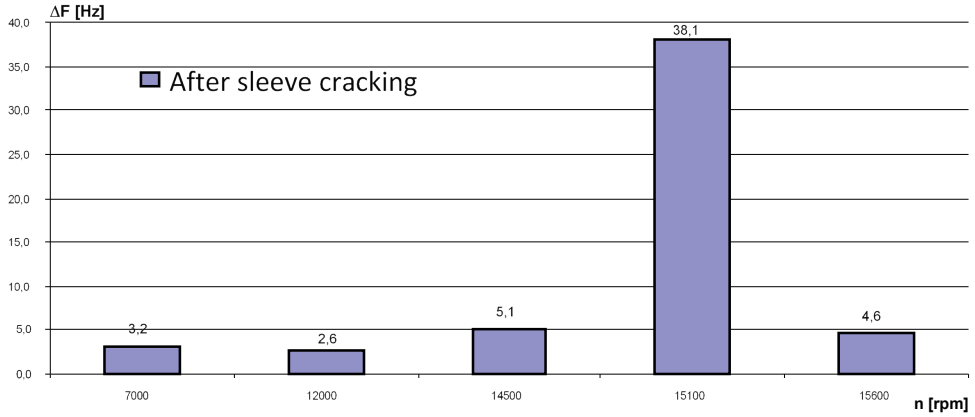

Fig. 3.44. First sub-harmonic characteristic set height after the fracture of the sleeve fixing the rolling bearing inner race to the turbine engine body

First sub-harmonic of the engine main shaft rated speed:

a) during tests conducted in the WZL-3 engine test house, the value of the amplitude of the engine main shaft rated speed first sub-harmonic remained approximately constant – its value averaged based on all rated rotational speeds was $A_{0,5}$ = 31.4 Hz, while the diagram of AC channel characteristic set height changes depending on rotational speed was monotonically increasing,

b) after fracture of the central bearing sleeve, the characteristic set height for the fundamental harmonic decreased to (averaged over all rated rotational speeds) $A_{0,5}$ = 3.8 Hz. The distribution of the characteristic set height for individual rated speeds changed – a clear "resonance boost" can be observed for n = 15,100 rpm (analogous to the first harmonic) (Fig. 3.45).

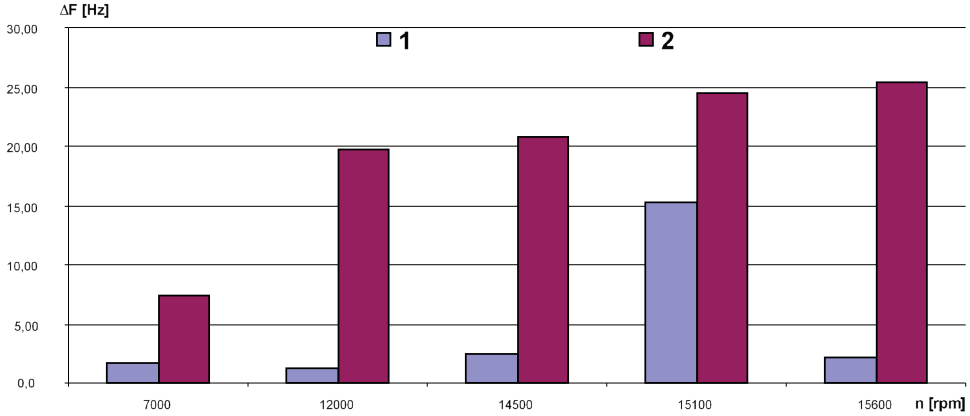

Fig. 3.45. Changes in the first harmonic characteristic set heights after the fracture of the sleeve fixing the rolling bearing inner race to the turbine engine body: 1 – after sleeve fracture, 2 – before sleeve fracture

3.3. Selected mechanical defects manifested by stochastic quasi-pulsed motion dynamics phenomena

The authors previously discussed FAM-C and FDM-A representations of mechanical defects that can be defined in classical Fourier-decomposition terminology as angular velocity modulations characteristic of the continuous analogue spectrum. These are divided into narrowband (subsection 3.1) and broadband (subsection 3.2). This section will discuss the FAM-C and FDM-A representations of mechanical defects generating short angular velocity pulses. These pulses are usually not periodic – their generation timing depends on numerous, often random, phenomena. In theory, a pulse, e.g., a quasi-rectangular pulse, can also be decomposed into set of Fourier series harmonic components [231, 270, 304, 306]. However, the decomposition of such a pulse has specific features that are completely different from the continuous analogue spectrum signal decomposition reviewed in subsection 3.2. Highlighting the subsection on quasi-impulse phenomena is also important from the perspective of mechanics, dynamics of motion and material strength. Local force peaks occur in the case of pulse phenomena of motion dynamics. They cause, among other issues, dynamic surpluses of considerable magnitude, directly leading to fracture or twisting of components. Such actions have a very negative effect on, e.g., rolling bearings [73]. Rolling bearings can also be the source of such angular velocity pulses [244]. It is commonly stated in the source literature on motion dynamics that such phenomena are difficult to monitor, since the available

monitoring methods detect them just before a propulsion unit fails, at best. In aviation, such a failure can entail a flight safety hazard or even a crash.

3.3.1. Spontaneous decoupling of one-way couplings

The design of one-way coupling (Fig. 3.47) enables transmitting power only in one rotational direction [18, 192, 193, 261]. However, if a race surface of a one-way coupling fails (Fig. 3.46), decoupling can follow and dynamic excesses can be created within the transmission system [80, 81, 83, 84, 94, 168]. In many a case, the cause lies in a poorly designed one-way coupling cage pitch. As the wear level of one-way coupling increases, the characteristic set height in the band f_p 0.6÷30 Hz also increases [81, 83, 84, 129, 168], Fig. 3.48.

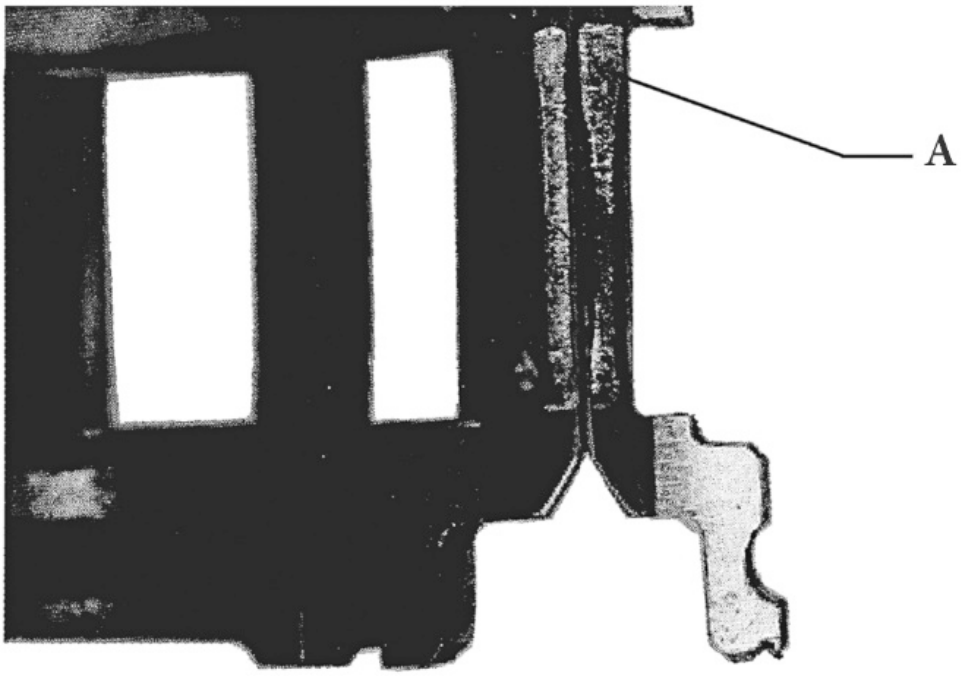

Fig. 3.46. Cage-separator from a worn-out one-way coupling: A – wear mark on the window surface

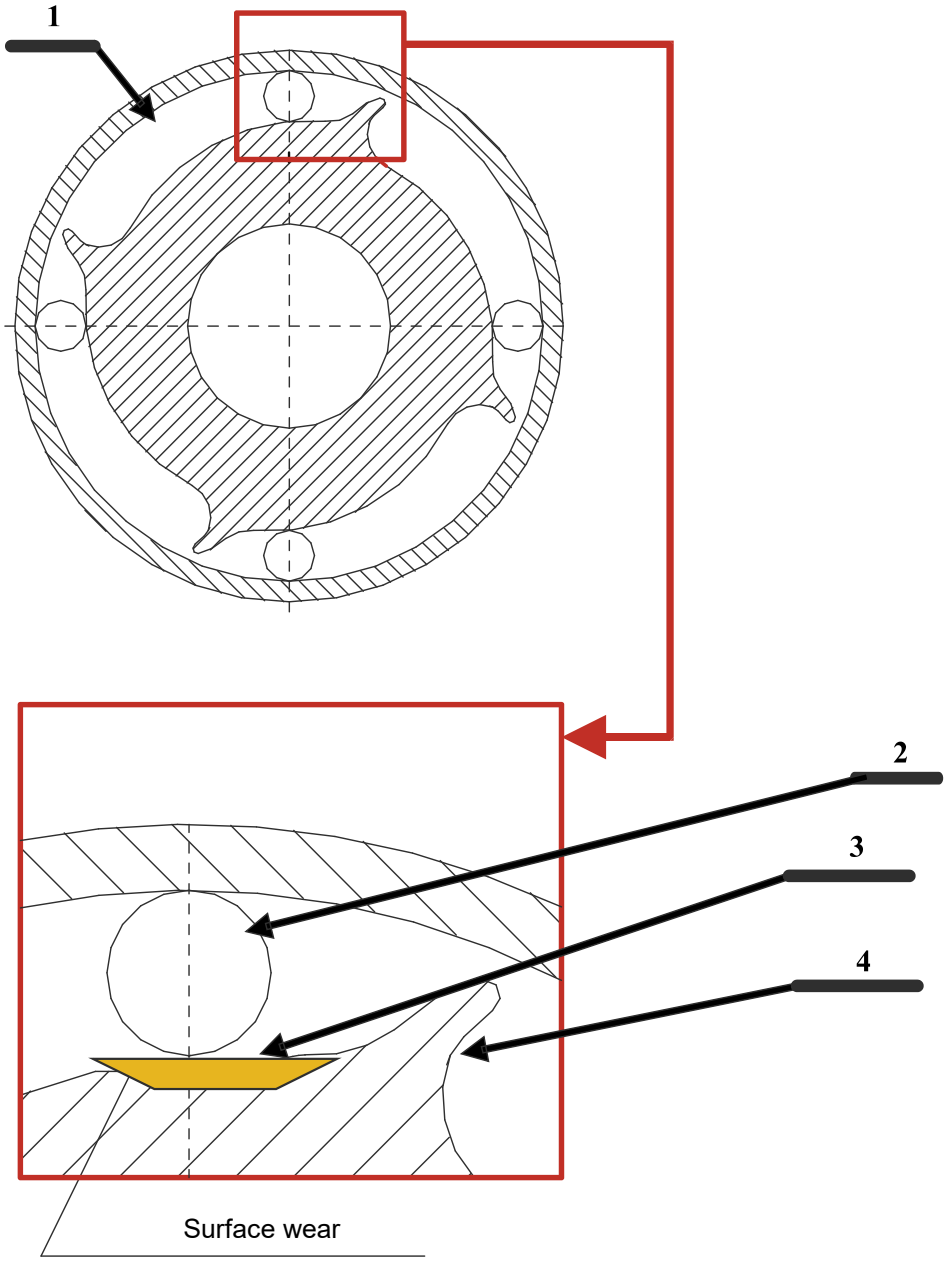

Fig. 3.47. One-way coupling – overview diagram: 1 – outer ring (with inner race), 2 – rolling element, 3 – inner race flaking, 4 – cage-separator

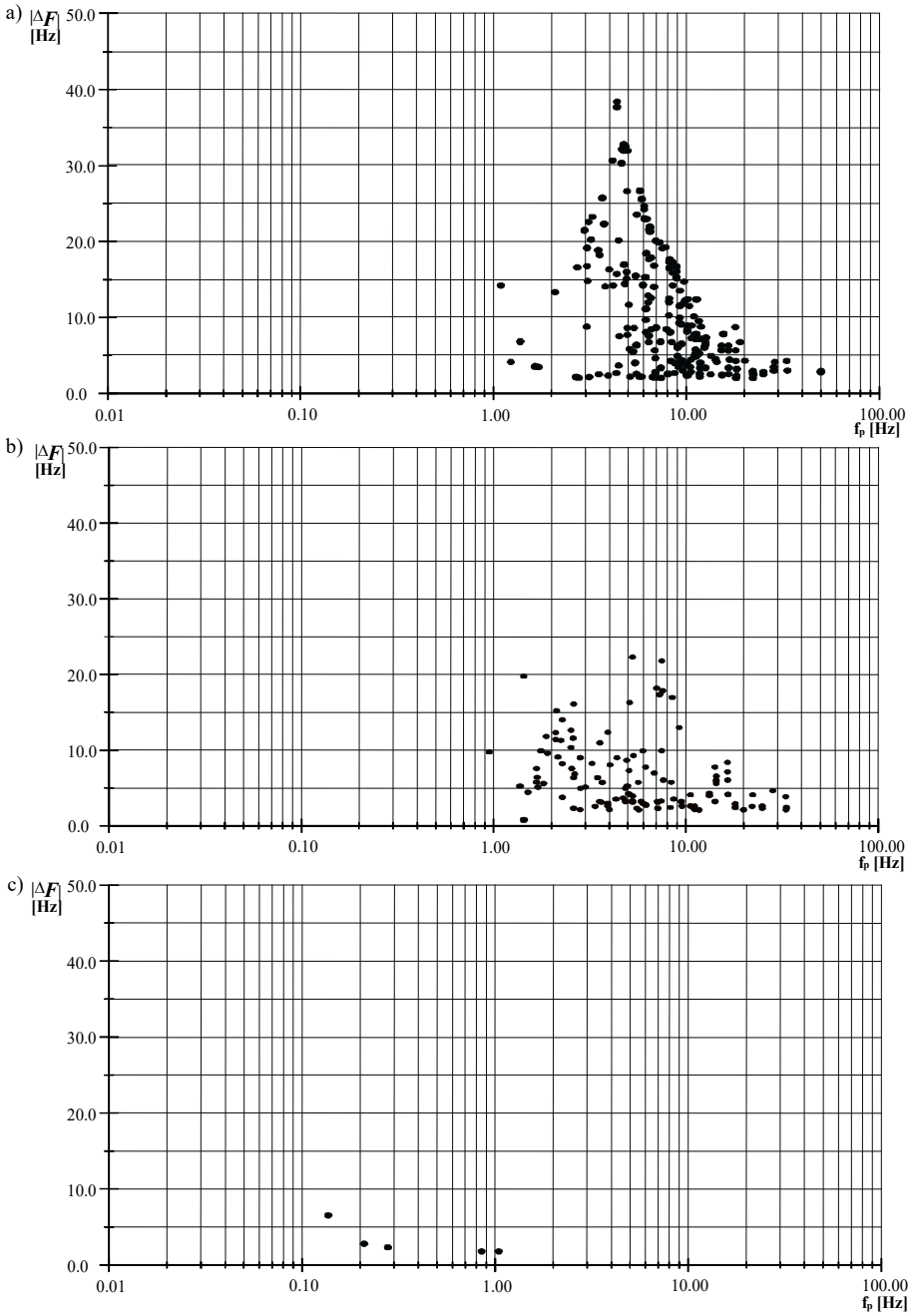

Fig. 3.48. Set of characteristic points for a KSA-2 gearbox with a worn-out one-way coupling: a) high wear, b) medium wear, c) brand-new

3.3.2. Air lock phenomena within the rotational speed controller hydraulic systems

The nature of the shaft rupture upon burst pressure changes in the hydraulic controller block as a result of hydraulic system air blockage is completely different to the aforementioned. In one instance, a generator drive shaft fracture surface was seen warped. The fracture plane of this drive shaft had evident metal grains indicating a relatively slow process of shaft twisting [83, 96, 104, 105].

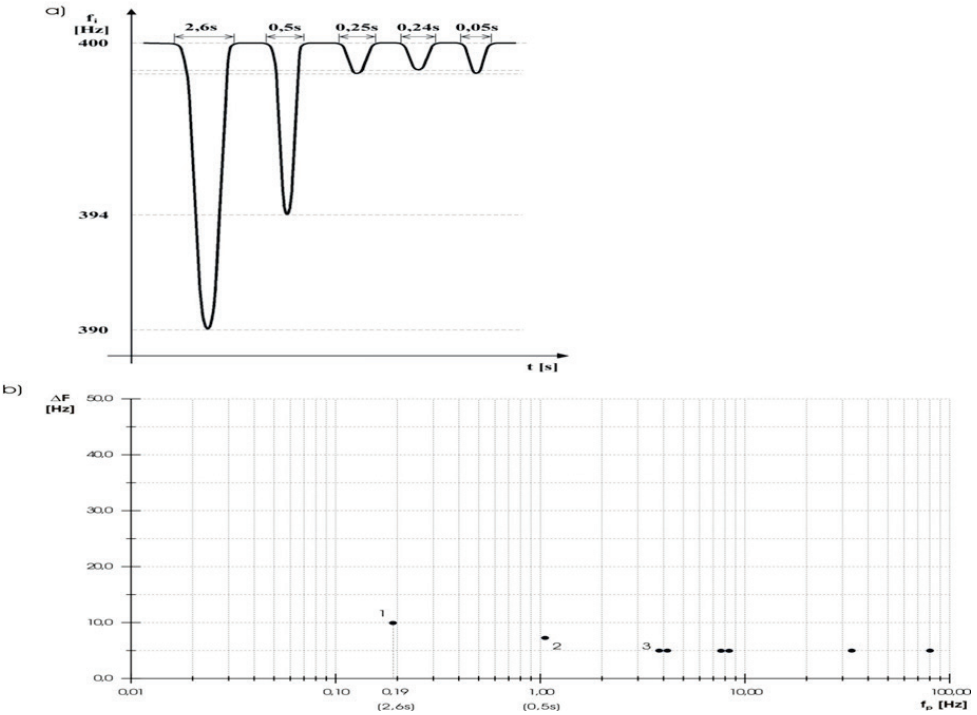

Fig. 3.49. Images related to hydronic system air-blockage: a) instantaneous frequency variation waveform $f_i = f(t)$ with visible fading pulses, b) characteristic set $\Delta F = f(f_p)$

The instantaneous frequency change waveform of this example is shown in Fig. 3.49. This waveform includes fading, unimodal decelerations in the form of fading pulses with systematically changing amplitude and decreasing duration (Fig. 3.49 – successive fading pulse duration values: 2.6 s, 0.5 s, 0.25 s, 0.24 s, 0.05 s) of the instantaneous frequency waveform (reflecting changes in angular velocity)). The duration and repetition time in this case is much longer than the period of the oscillatory vibrations associated with one-way coupling rupturing. Hence, based on

the knowledge on aeronautical hydraulics, it was concluded that shaft twisting was caused by the air blockage of the hydraulic stabiliser block [80, 83, 94, 127, 141, 183, 187, 236].

3.3.3. Breaking out of rolling bearing separation elements and cracking of the spacer-cage perimeter

Long-term operation of a rolling bearing in a resonant state with a quality factor (calculated from FAM-C characteristic sets) Q >11 involves, among other notions, strong impacts of the rolling elements against the cage window edges [73, 123, 176]. These forces can cause the cage separating elements to break out[5]. In the case of the FAM-C method, such breakouts are represented as spike pulse bundles (Fig. 3.50). Here, the number of pulses in the bundle is equal to the number of cage separating elements broken out. Such separating elements breakout can even lead to a rupture of the cage circuit (3.51).

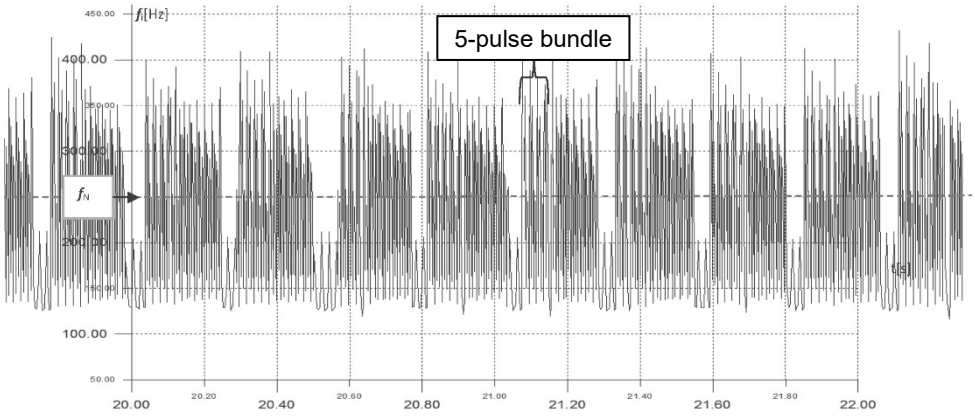

Fig. 3.50. Instantaneous frequency waveform $f_i = f(t)$ of the three-phase FAM-C measuring channel for a turbojet engine, the bearing of which had five separating elements broken out – pulse "bundles" (5-element family of spike pulses) are visible

It can be seen in Fig. 3.50 that the bundles of five spike pulses are systematically repeating (every single journal rotation). Before the breakout of the separating elements, these pulses were absent – the waveform oscillated with a pulsation amplitude of about 10% at a level of approx. $f_{śr} = f_N$. Here: n = 7000 rpm, i.e.,

[5] [73], p. 53 "Until recently, the influence of the quality – shape-dimensional accuracy – of the cages on bearing reliability has been underestimated. It is known, however, that substantial mass forces of the rotating rolling parts are released at high bearing speeds, rapid accelerations and vibrations..."

f_N = 167 Hz). Therefore, it can be concluded that the FAM-C method is sensitive to the breakout of the rolling bearing separating elements.

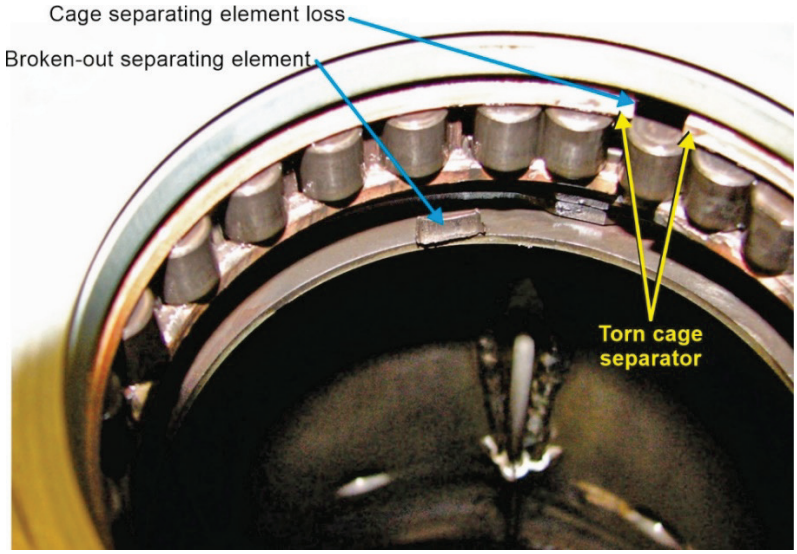

Fig. 3.51. Rolling bearing with a burst cage and broken out five separating elements

3.3.4. Breaking out of a transmission gear tooth

There are many source literature publications on the toothed gear wear theory [11, 61, 95, 140, 152, 158, 208-211, 218, 307]. The authors pointed out the cascade nature of the phenomena leading to tooth fracture in a gear wheel and the considerable rate of the destructive process, which hinders available monitoring systems in signalling the danger in advance. It seems obvious that in order to identify the hazard of tooth breakage, it is necessary to systematically and reliably monitor the process of increasing inter-tooth backlash during tooth meshing. Subsection 3.1.4 discusses the possibility of FDM-A monitoring. An increase in radial clearances below 10% of the modular pitch in some AC generators-transducers can be clearly distinguished in the instantaneous frequency waveform. This is confirmed both by the primary author's measurements [95, 99, 108, 126, 127, 129] and by theoretical calculations confirming that the Kotielnikov-Shannon condition is fulfilled.

Measurements made with DC generator-transducers with a significant number of slots can enable the observation of backlash increased by as little as 10 per cent of the pitch. The application of the FDM-A method enables prematurely interrupting the destruction process and protecting the monitored propulsion unit against gear wheel breakage. While the case of using DC generators for this purpose has

been closed, the question of how to monitor such wear if only AC generators are connected to the tested propulsion unit arises. In theoretical terms (using the Kotielnikov-Shannon theorem), no AC alternator-generator can even "see" wear on a contact area of 20% of the modular pitch [127]. Nevertheless, practical applications of FAM-C testing on real objects show that this is possible [127, 129]. Evidence is provided by the instantaneous frequency waveform (based on sub-structure voltage) from the GT-40PCz6 AC generator of a Mi-24 helicopter, where the inter-teeth backlash irregularities of the unit gearbox were observed in pulsed form (Fig. 3.52).

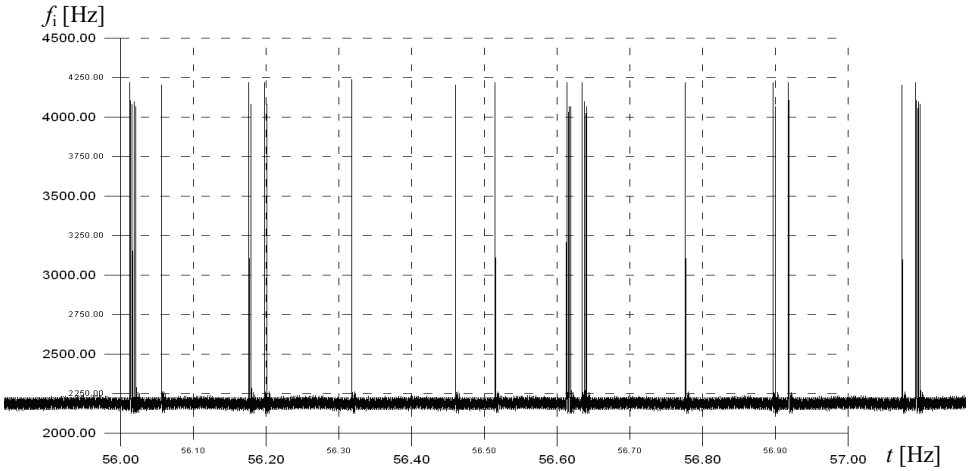

Fig. 3.52. The waveform $f_i = f(t)$ of the AC measuring channel in the case of excessive meshing backlash in a gear wheel pair of a worn-out gearbox of a Mi-24 helicopter generator – visible single spike pulses

This is rather a spike pulse indication (it is difficult to talk about precise calculation of the backlash magnitude in this case), but this is already sufficient for a diagnostician – it can be an important warning for the operators. So how is it possible that this valuable warning signal is visible? This is due to the natural synchronisation of the tested signal (observed primary spectrum of the gear pair) with the subcarrier frequency. Even if the passage through a magnetically neutral generator-transducer line (Figs. 2.2÷2.4) does not "fit" the actual angular velocity section just after the kinematic link is established, it is statistically possible (on average) further on (during subsequent rotations), due to the backlash of the kinematic links located between the gear pair under test and the generator-transducer rotor. This issue was already partially discussed in [129], in the chapter on the metrological characteristics of the FAM-C and FDM-A methods. The author will expand on this problem in Chapter 4.

At the same time, it should be noted that some time after the FAM-C system sends signals in the form of spike pulses (Fig. 3.52), a dynamic rupture of several teeth in one of the gears can occur (Fig. 3.53). This generally leads to severe damage to the helicopter [7, 95].

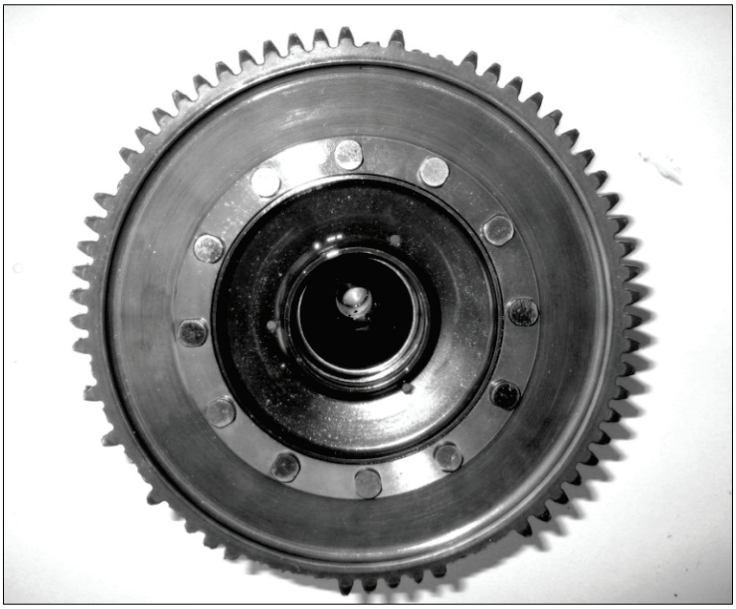

Fig. 3.53. Damaged gear wheel in the gearbox of a Mi-24 helicopter

3.3.5. Broken clamp fit between the rolling bearing ring and shaft or bearing seat

According to source literature [18, 73, 176, 244], rolling bearings are mounted using the interference-fit method with a journal, as only this method guarantees correct long-term operation. If the interference fit breaks, considerable amounts of heat can be generated. This is because a slide bearing is then created between the inner ring and the rotor shaft journal. Frequent and prolonged ruptures can cause a cascade of thermo-mechanical phenomena, which can ultimately lead to journal failure or even destruction of the propulsion unit. A quantifiable assessment of the magnitude and intensity of such phenomena is therefore important for operational safety, in relation to aircraft propulsion units, in particular.

A fading pulse appears when the clamping mechanical fits between the bearing inner ring and the journal (shaft) or the outer ring and the bearing seat are broken [18, 129, 176, 269]. This results in a sliding displacement of both surfaces, which can be converted into an angular measure (“rupture angle”) (Table 3).

Table 3

Fade pulses for the SO/SO-3W engine obtained from the circuit of the GSR-ST-6000WT onboard DC generator

Rotational speed n	Min. rupture angle	Max. rupture angle	Avg. rupture angle	Min. rupture frequency	Max. rupture frequency	Avg. rupture frequency	Min. quotient	Max. quotient	Avg. quotient
	$\Delta\varphi_{min}$	$\Delta\varphi_{max}$	$\Delta\varphi_{śr}$	Δn_{min}	Δn_{max}	$\Delta n_{śr}$	$\Delta\varphi_{min}/\Delta n_{min}$	$\Delta\varphi_{max}/\Delta n_{max}$	$\Delta\varphi_{śr}/\Delta n_{śr}$
rpm	o	o	o	rev.	rev.	rev.	°/rev.	°/rev.	°/rev.
7000	4	257	50	0	11	3	15.71	24.45	19.74
9500	12	219	79	0	27	5	26.20	8.14	16.52
11500	21	256	93	1	20	5	40.75	12.72	18.24
11750	15	391	87	0	10	3	56.06	39.93	27.89
12250	22	231	82	1	14	5	36.67	16.17	18.13
13500	25	239	101	0	14	5	64.72	17.71	20.40
15100	40	324	146	1	21	4	39.33	15.17	34.95
15600	29	777	134	1	3640	168	44.02	0.21	0.80
aver-age	21	**337**	**96**	1	470	25	40.43	16.81	**19.58**

The value of the rupture angle can be represented as a function of rotational speed (Fig. 3.54). Rupture frequency is as important as the value of the rupture angle (Fig. 3.55). These values are determined based on the parameters obtained from the instantaneous frequency waveform as a function of time $f_i = f(t)$ (Fig. 3.56).

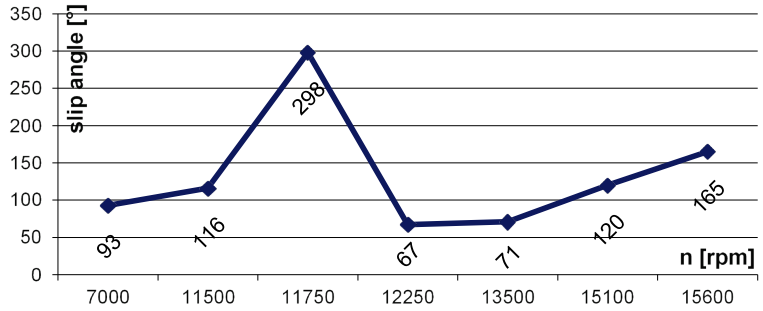

Fig. 3.54. Examples of changes in the rupture angle of the fit (interference fit) between a journal and a rolling bearing inner ring

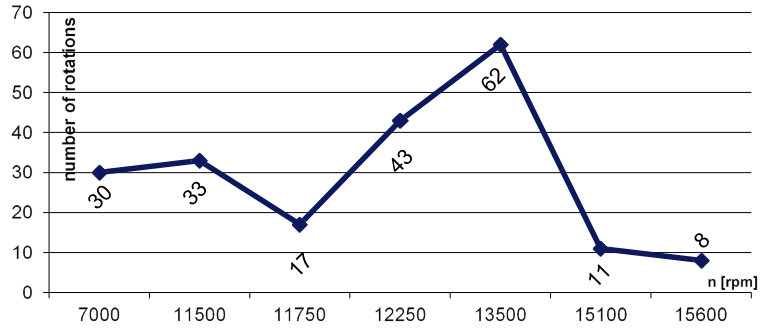

Fig. 3.55. Sample frequencies of ruptured fit (interference fit) between a journal and a rolling bearing inner ring

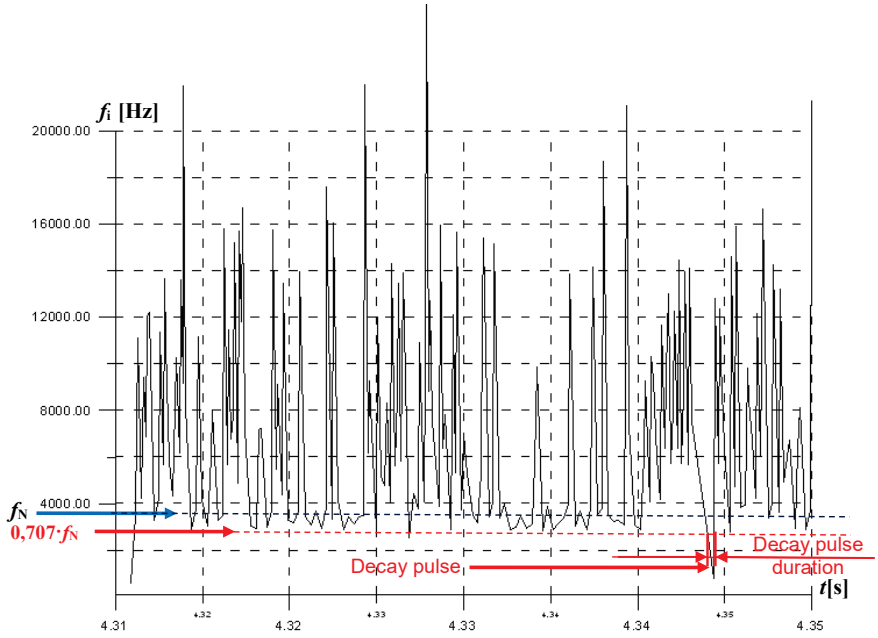

Fig. 3.56. Instantaneous frequency change waveform $f_i = f(t)$ for a DC generator pulsation example: f_N – DC generator slot pulsation rated frequency value (level)

The primary author believes that an unacceptable rupture frequency (defined as the quotient of the max. rupture angle and the rupture frequency arithmetic mean) can be considered to be 60°/rev. [114, 136]. In such situations, upon exceeding this level, and dismantling the bearing off the journal, canker on the journal surface was often identified (Fig. 3.57). Further operation of the journal after exceeding this value may lead to increased concentration of released heat between the inner ring surface and the journal, resulting in the formation of a slide bearing.

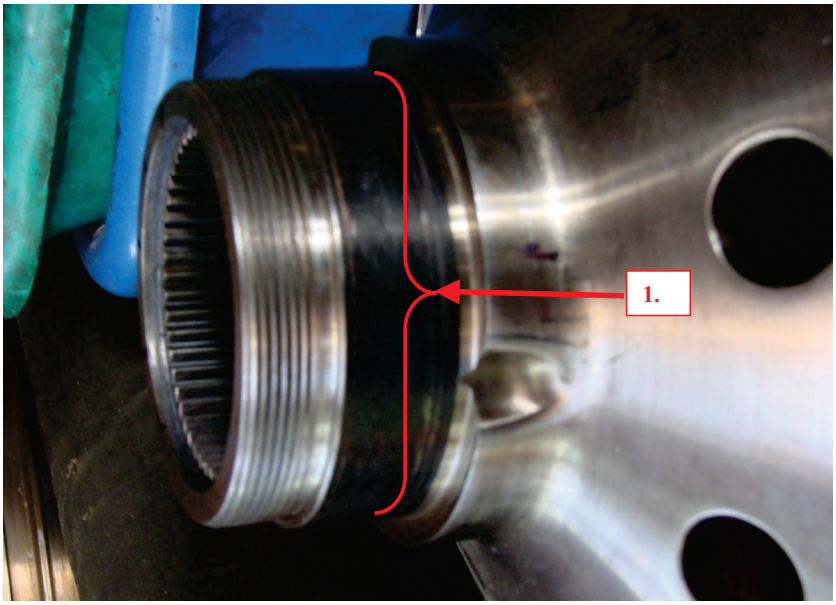

Fig. 3.57. Single-shaft turbo-jet engine bearing journal after prolonged key fit between a rolling bearing inner ring and a journal: 1 – trace (canker) on the journal surface after fit (interference fit) rupture and removal of the rolling bearing inner ring

3.4. The role of a mechanical failure catalogue in propulsion unit diagnosis

Chapter 3 "Relationships between individual defects of mechanical propulsion unit kinematic pairs with FAM-C and FDM-A imaging" involved the creation of a basic set of benchmarks-models. This enables attempting an analysis of the technical condition exhibited by individual kinematic pairs in the monitored propulsion unit. Based on the comparison of certain characteristics and parameters obtained with the use of the FAM-C method, it will be possible to assess the technical condition of individual kinematic pairs in the monitored propulsion unit. The aforementioned measurements are characterised by various errors, both methodological and instrumentation-related. Familiarity with them, their depth and structural versatility can greatly enhance the reliability of these prototype methods in the monitoring of mechanical propulsion units. Therefore, the next chapter will focus on aspects related to diagnostic measurement technology and metrology.

4

METROLOGICAL PROPERTIES OF THE FAM-C AND FDM-A METHODS

4.1. Overall metrological structure of the FAM-C and FDM-A methods

This chapter expands on the concept of metrological structure to include all activities associated with error assessment, starting from measurement and ending with determination of a diagnostic decision (Fig. 4.1). The multifaceted approach to diagnostics enables estimating the risk of generating an incorrect diagnostic evaluation. Indeed, even the original diagnostic signal in the form of angular velocity modulations by faulty kinematic pairs within the propulsion unit under test is exposed to certain distortion and sometimes even attenuation due to mutual interference. Moreover, the propulsion unit's integral generator-transducer behaves like a band-pass filter and, therefore, also, sort of, distorts or masks some wear-related phenomena.

The first step in creating an appropriate diagnosis is to standardise the generator output voltage signal in terms of processing in a counter card. A so-called "diagnostic attachment" is used for standardization purposes. This enables generating a series of pulses (TTL standard) starting and ending the time increment counting process. Therefore, measuring the duration of rotor groove passage under the generator-transducer pole piece or the turbine engine compressor blade passage under the CRL electromagnetic sensor (or under the current sensor) requires replacing an actual analogue signal from the TTM sensor, with the standardised signal that is required by the precise time increment measurement path [303]. This pulse can be

referred to as a "working gate pulse", since in the course of further processing, it "gates" the time base pulses of the counter card.

Herein, numerous time increment offset errors come about due to the nature of their electronic preparation. The generated gate pulse does not arise exactly where $u(t)$ passes - where the generator-transducer output voltage passes the zero level. There is a delay in the generation of this pulse at this point. The delay time depends on the $u(t)$ waveform edge steepness. The greater the edge steepness, the faster the gating pulse formation and generation. The gate pulse generation circuit is a differential one. Therefore, the $u(t)$ signal should be subject to amplitude standardisation. Initial amplitude standardisation is achieved through the action of the onboard generator voltage regulator. These regulators are characterised by considerable inertia manifested by a significant time constant; electronic $\tau = 20 \div 40$ ms, carbon $\tau = 40 \div 80$ ms. Given that the AC voltage waveform fluctuation period (for a typical onboard AC grid) is $T_{AC} = 2.5$ ms, while that for a DC channel (pulsation component) is $T_{DC} = 0.2 \div 0.4$ ms, the electromechanical stabilisation of the voltage amplitude level is far from sufficient, especially for the DC channel. Therefore, the signal standardization block (the "electronic attachment") of the FDM-A measurement system contains an analogue amplifier. In the case of a DC measurement channel, the generator-transducer output voltage groove pulsation component $u(t)$ usually takes values in the range of $U = 0.1 \div 2.1$ V.

FDM-A measurement systems use $K \cong 20$ amplification and achieve saturation at an output voltage level of $U = \pm 12$ V. Reducing the phase gate pulse formation system phase error requires attempts at developing an automatic gain control (AGC) system with a delay time $\tau < 0.5 \cdot T_N$. Such a relationship would satisfy the Kotielnikov-Shannon condition of a measurement system recognizing a tracked diagnostic process. This AGC chain would be employed to control the gain value K of the measurement system amplifier throughout the DC channel, inversely proportional to the input voltage value.

Pulse bundles accumulated in the counter board buffer are sent to the hard drive, where measurement files are created ["pom" extension]. Sets of such files are processed into two forms: a) waveforms $f_i = f(t)$ and b) characteristic sets $\Delta F = f(f_p)$. Characteristic set parameters $\Delta F = f(f_p)$ allow calculation of the parameters representing tested propulsion unit component defects, as they display the image of extreme fluctuation amplitudes (angular velocity) that are associated with individual defects. Moreover, band limits f_p of individual sets and their heights ΔF are determined for each characteristic set, while numerous parameters, such as the amplitude depth coefficient, relative total pulsation value, spike pulse amplitude, decay pulse amplitude, etc. are determined for the waveforms $f_i = f(t)$.

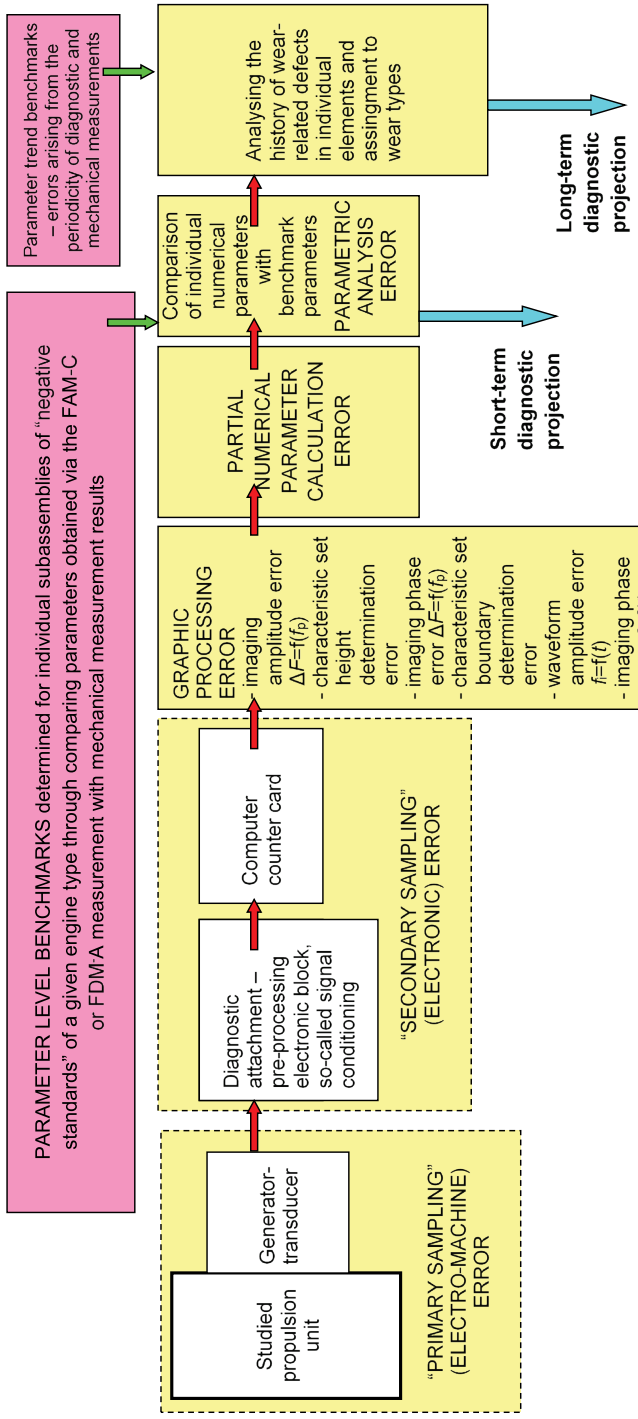

Fig. 4.1. Block diagram of the FAM-C and FDM-A method metrological structure

These parameters reveal the fluctuations (angular velocity) dynamics that are associated with individual defects, The parameters determined through graphical processing are then subjected to further arithmetic and statistical processing. As an outcome, partial numerical parameters are determined that reflect the specific mechanical characteristics of individual components.

These parameters have their equivalents in the form of parameter level benchmark arrays. Comparing the value of a numerical parameter with a qualification table for that parameter enables qualifying it at one of the wear levels. There are usually several or even more than a dozen of such parameters – hence the need to determine the weighting factors in advance [99, 114, 122, 129, 136]. A short-term diagnostic forecast of the tested propulsion unit covering 12÷50 h of flight can be presented upon completing the analysis. A long-term forecast requires a much greater observation period. The primary author recommends observations throughout the entire period between the overhauls of a given propulsion unit to facilitate verification of the results within each subsequent overhaul process.

Such a process can only be initiated after a number of subsequent diagnostic tests involving a given propulsion unit, wherein the trends of changes in individual parameters can be initially observed and determined. In other words, an analysis to determine the wear development of individual components of the tested propulsion unit is necessary. At the same time, the type of wear trend must be assigned to the component being monitored. Therefore, wear trend type patterns shall be developed before such diagnostic tests. These parameter trend patterns should be defined for each wear model in advance. They are developed based on long-term diagnostic observations (FAM-C or FDM-A) supported by periodic mechanical verifications.

These verifications often entail partial disassembly of the tested propulsion unit scaling-up, but enable "scaling up" the FAM-C and FDM-A observations and matching diagnostic coefficients to the parameters obtained from diagnostic measurements. Developing a long-term diagnostic projection is possible by comparing the trend of changes in the parameters of a given component with a tested propulsion unit with the trend pattern for that component under a previously recognised wear model type.

Chapter 6 will emphasize the periodicity of changes in the type of tribological wear models of a turbojet engine bearing node. Wear model type changes can be described in the form of quasi-sinusoidal parameter changes. Quasi-sinusoidal change frequency increases along with the operation time of the tested propulsion unit (the processes of transforming one model type into another are accelerated). FAM-C and FDM-A method engine testing frequency should match the dynamics of this long-term process – as the design ageing process progresses, the testing intervals should shorten. The intervals between successive tests should be more than

two times shorter than the period of quasi-sinusoidal changes in the type of tribological wear model (according to the Kotielnikov-Shannon law). Otherwise, significant errors in long-term predictions should be expected (Fig. 4.1).

Measurement sampling method structural analysis

The FAM-C and FDM-A diagnostic methods successively employ two types of sampling:

a) primary sampling, which can also be called "electromechanical sampling" – implemented by a generator-transducer coupled to the tested propulsion unit,
b) secondary sampling – implemented by a comparator circuit (which detects zero-level crossings), a gating circuit and a counting circuit with a time base clock.

Throughout primary sampling, a diagnostician has no influence on the error rate (has no current control over the error rate during the diagnostic measurement), but should calculate and take it into account when assessing the measurement error. The phenomena impacting error formation arise, as it were, naturally, through the interweaving of the following phenomena:

a) those related to the angular motion dynamics of propulsion unit components,
b) electromechanical conversion of generator rotor angular motion into generator output voltage angular modulations.

Therefore, any errors of the FAM-C or FDM-A methods related to these phenomena depend on the interrelationship between the structural parameters of the tested propulsion unit and the structural parameters of the generator-transducer.

However, primary sampling sensitivity and measurement accuracy can be tuned prior to measurement by appropriately configuring the measurement structures. Single- and multi-phase measurement can be applied to this end. It is also possible to employ more than just generator-transducer output voltage, namely, the output voltage of its sub-exciter. Synchronous and simultaneous measurement from multiple onboard generator-transducers is also possible [313]. From the perspective of measurement systematics [129], this is already a secondary sampling-related issue. The error, sensitivity threshold and resolution of a method can be affected by the changing frequency of the time base clock - and can be impacted throughout secondary sampling. Typically, commercially available counter cards enable broad changes to the time base clock frequency. Experience gained through method deployment shows that appropriately selecting the time base

clock frequency and counting method enables achieving optimum diagnostic sensitivity for a given kinematic link.

4.2. Primary sampling – electromechanical

4.2.1. Primary sampling not taking mechanical transmission backlash into account

As mentioned in [129], subsection 1.2 (FAM-C method description), the SEM induced in the windings reaches an instantaneous value equal to zero for the angular position corresponding to the coil on the rotor reaching the neutral magnetic axis between stator pole pieces. Assuming a rigid connection between the generator rotor and the propulsion unit under study, the idea of generator rotor instantaneous angular velocity changes being represented by output voltage frequency is explained there. Since the generator rotor is, so to speak, a summation node of tested propulsion unit individual kinematic link harmonic fluctuations, generator output voltage frequency modulation will be a discrete image of faulty kinematic pair angular velocity modulations. As suggested by numerous source-literature materials [29, 39, 40, 303], the Kotielnikov-Shannon condition (defined by equation (2.1)) can be relaxed in relation to diagnostic signal synchronous processing, however, without specifying strict dependencies. According to the primary author, this condition can be reduced to the following form:

$$\Delta t_N < \Delta t_{od} \tag{4.1}$$

(4.1) indicates that monitoring the angular velocity fluctuations of the faulty j kinematic pair with frequency f_p requires selecting a generator generating rated frequency f_N, defined by the relation:

$$f_{\mathrm{N}} > f_{\mathrm{pj}} \tag{4.2}$$

It should be noted that this is a condition for the distinguishability of a given harmonic mechanical fluctuation to a synchronous measurement – the determination of its frequency – and not to the exact measurement of its phase and amplitude values.

Figure 4.2 can be employed to illustrate the latter statement. An ideal representation of the changes in mechanical fluctuations is shown herein in the form of a reference waveform $f_{\mathrm{iwz}}(t)$. At the same time, two waveforms synchronised

with $f_{iwz}(t)$ are shown against it, reflecting the primary (electromechanical) sampling: $f_i'(t)$ and $f_i''(t)$. The $f_i'(t)$ and $f_i''(t)$ waveforms are represented by sets of points:

a) $f_i'(t) = \{1', 2', 3', 4', 5', ...\}$,

b) $f_i''(t) = \{1'', 2'', 3'', 4'', 5'', ...\}$.

The $f_i'(t)$ and $f_i''(t)$ waveforms have different phase shifts with respect to the reference waveform $f_{iwz}(t)$:

a) $f_i'(t)$ phase shift angle of approx. 30°,

b) $f_i''(t)$ phase shift angle of approx. 60°.

At the same time, it can be noted that the frequency of the $ff_i'(t)$ and $f_i''(t)$ waveforms is equal to the frequency of the $f_{iwz}(t)$ waveform. Therefore, the least favourable condition for synchronous sampling occurs, e.g., *aliasing* [29, 39, 40, 77, 303]:

$$f_N = f_p \tag{4.3}$$

Instantaneous frequency amplitude deviations from the reference level (Fig. 2.1) can be seen:

a) $f_i'(t)$: $\{\Delta F_{11}', \Delta F_{12}', \Delta F_{21}', \Delta F_{22}', \Delta F_{31}', ...\}$,

b) $f_i''(t)$: $\{\Delta F_{11}'', \Delta F_{12}'', \Delta F_{21}'', \Delta F_{22}'', \Delta F_{31}'', ...\}$.

Thus, as the phase shift angle of the signal $u(t)$ increases in the range of (0, 90°), the magnitudes of amplitude deviations ΔF increase and, thus, the instantaneous frequency amplitude error decreases with respect to the reference waveform. The first arising conclusion is that when using the FAM-C or FDM-A methods, it may sometimes be reasonable to change the angle between the generator-transducer shaft and the drive seat, e.g., by rotating the generator shaft by one spline pitch. Satisfying the condition (4.2) enables achieving a significant change in the value of a given harmonic amplitude error. This also enables drawing a second conclusion that not only does aliasing not arise for condition (4.2), but there is a natural stepwise change in the phase shift angle for each successive period of the waveform. In relation to $\Delta F = f(f_p)$ imaging, this means that characteristic set heights will exhibit a relatively small error. In such a case, the zero error would arise if at least one point reached a phase shift value of $90° \pm n \cdot 180°$ during the measurement. The quotient of the nominal frequency f_N and the angular velocity fluctuations frequency of a faulty kinematic pair with a frequency f_p can, therefore be called the k_r multiplication factor – i.e., [114, 129, 136]:

$$k_r = \frac{f_N}{f_p} \tag{4.4}$$

It can also be defined as the quotient of the tested kinematic link observed angular velocity modulation waveform period rated value (T_p) and the generator output voltage waveform period (T_{NG}), which can be described by the formula:

$$k_r = \frac{T_p}{T_{NG}} \tag{4.5}$$

At the same time, the multiplication factor can be calculated based on design data as the product of the:

a) harmonic number h of the given kinematic link angular velocity rated value,
b) mechanical ratio between the generator shaft and the kinematic link to be diagnosed (the greater the generator rotor rated angular velocity in relation to the given kinematic link angular velocity, the greater the multiplication factor k_r),
c) number of phases (1 or 3),
d) number of pole pairs (for an AC generator) or number of rotor slots (for a DC generator),
e) system for measuring generator output voltage time increments:
   – half-period – value 2,
   – full-period – value 1.

The $\omega_2 = f(t)$ waveforms are characterised by a significant number of quasi-continuous locations in the case of many propulsion systems. Therefore, laboratory measurements should mimic them – a sawtooth waveform was first chosen as baseline [114, 116, 136] – it was originally supposed to mimic the variability of instantaneous frequency waveform dynamic change processes observed for marine compression-ignition engines.

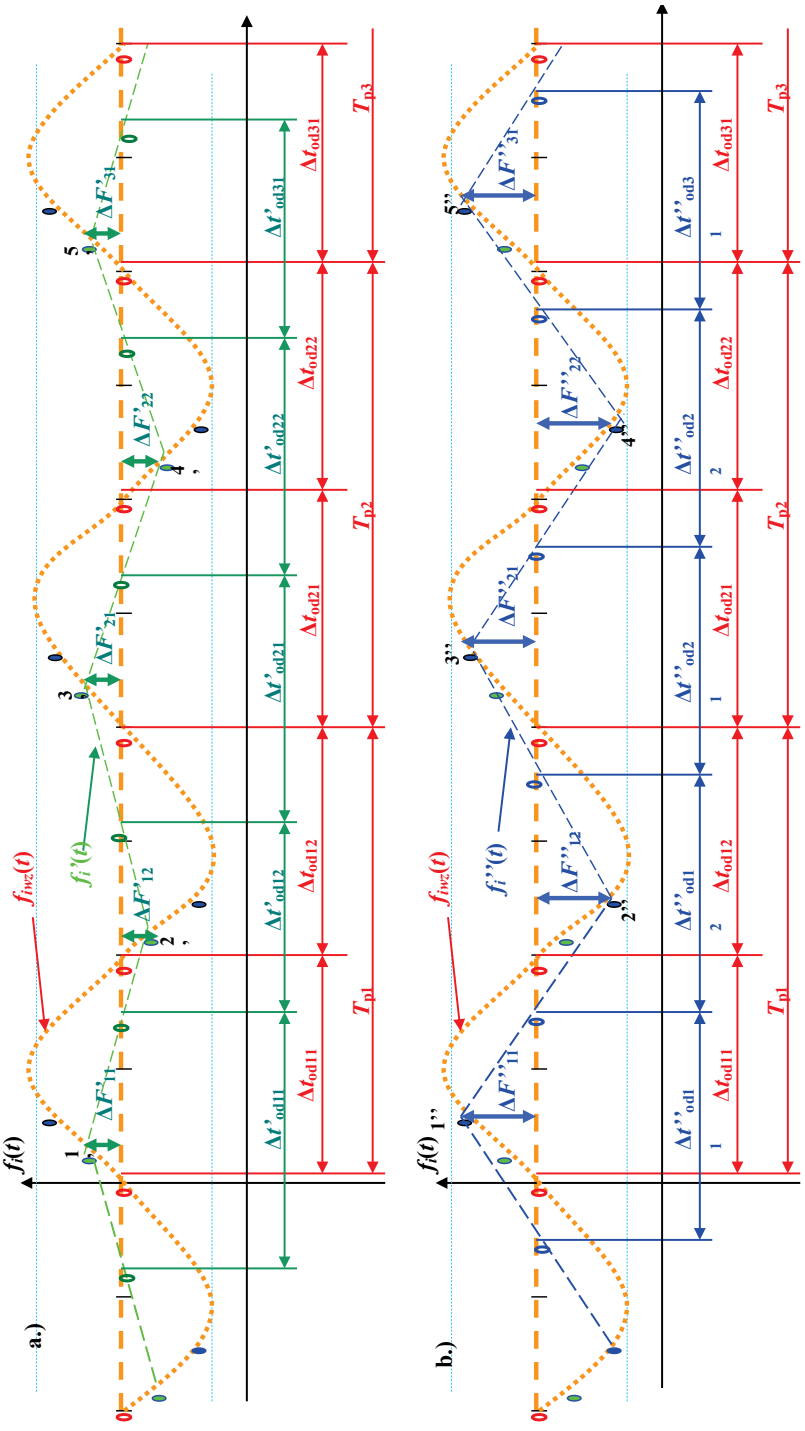

Fig. 4.2. Changes in the characteristic parameters of the generator output voltage frequency modulation depending on the frequency and phase relationship between the mechanical fluctuation waveform frequency and the given generator-transducer rated frequency

This waveform was obtained using the Rhode & Schwartz AGFU function generator in a configuration as in Fig. 4.3 (in the discussed case of representing an AC generator signal, the DC component voltage implemented with the TSX3510 power supply was set to zero). The generated voltage waveform amplitude $u = f(t)$ was constant at U_{pp} = 10 V (U rms = 3.54 V). Voltage waveform – sinusoidal, frequency-modulated. Carrier waveform frequency $F_N = F_1$ = 400 Hz. However, a level of 100 Hz or 200 Hz was also applied for lower values of the k_r-factor due to instrumentation limitations of the function generator. Moreover, the modulating frequency F_2 was changed (frequency modulation was implemented) to a sawtooth shape (linearly ascending function followed by a rapid descent). The period of the sawtooth variation T_2 ($T_2 = f(1/F_2)$) was chosen so that its quotient value k_r multiplication factor) to the carrier wave period T_1 ($T_1 = f(1/F_1)$ assumed certain values. In addition, the k_r value was switched from 3 to 50, with a step of 0.1.

Changes in the time increments for such a modulated voltage signal were counted using typical FAM-C method instrumentation. Resultant waveforms $f_i = f(t)$ were then compared with the reference sawtooth waveform (Fig. 4.4). The phase and amplitude errors were determined this way. Total errors of the amplitude $\delta_A = f(k)$ are shown in Fig. 4.4, and phase errors $\delta_\varphi = f(k)$ in Fig. 4.5. Fig. 4.4 demonstrated the simulated generator-transducer output voltage waveform. This is actually the output voltage waveform from the Rhode & Schwartz generator (Fig. 4.4, red sine wave). This waveform is frequency-modulated (U_{max} = const, f_i = var) according to programmed variations shown as a sawtooth waveform (blue line). At the same time, this is the reference waveform for frequency modulation changes. The $f_i = f(t)$ "waveform" obtained from the FAM-C measurement is compared to it. This "waveform", as stated previously (at the beginning of this monograph), is in fact a set of points (Fig. 4.4, dark blue coloured points). This set is linearised by connecting adjacent points with segments. The interpreted $f_i = f(t)$ "waveform" is then compared to the reference waveform (here: a sawtooth). As absolute amplitude error value and phase error are subsequently determined for each sawtooth period (Fig. 4.4), by dividing the absolute (either amplitude or phase) error value by the reference value, the relative amplitude (Fig, 4.5) or phase (Fig. 4.6) error value is obtained.

As mentioned earlier, a series of measurements are taken at the carrier wave frequency (Table 4, parameter F1) for the next value sawtooth period waveform (Table 5, column "Tsinus period duration"). Therefore, the value of the multiplication factor k_r is – according to the definition provided at the beginning of the monograph – the quotient of these quantities (Table 4, value of the period factor in the column "multiplication factor k"). This enables plotting the empirical dependence of the relative errors ($\delta_A = f(k_r)$ for amplitude, $\delta_\varphi = f(k_r)$ for phase) depending on the multiplication factor.

Table 4

Preset parameters (on a function generator) of instantaneous frequency sawtooth waveforms $f_i = f(t)$

lp	Output voltage frequency	Period duration		Period multiplicity factor	Upper frequency	Period duration	Modulating wave frequency
-	F1	T nośnej		k	F2	Tsinus	Fsinus
-	Hz	ms		-	Hz	ms	Hz
1	100	10		1,1	110	11,00	90,91
2	100	10		1,2	110	12,00	83,33
3	100	10		1,3	110	13,00	76,92
4	100	10		1,4	110	14,00	71,43
5	100	10		1,5	110	15,00	66,67
6	100	10		1,6	110	16,00	62,50
7	100	10		1,7	110	17,00	58,82
8	100	10		1,8	110	18,00	55,56
9	100	10		1,9	110	19,00	52,63
10	100	10		2	110	20,00	50,00
11	100	10		2,1	110	21,00	47,62
12	100	10		2,2	110	22,00	45,45
13	100	10		2,3	110	23,00	43,48
14	100	10	0	2,4	110	24,00	41,67
15	100	10	0	2,5	110	25,00	40,00
16	100	10	0	2,6	110	26,00	38,46
17	100	10	0	2,7	110	27,00	37,04
18	100	10	0	2,8	110	28,00	35,71
19	200	10	0	2,9	220	29,00	34,48
20	200	10	0	3	220	30,00	33,33
21	200	10	0	3,1	220	31,00	32,26
22	200	10	0	3,2	220	32,00	31,25
23	200	10	0	3,3	220	33,00	30,30
24	200	10	0	3,4	220	34,00	29,41
25	200	10	0	3,5	220	35,00	28,57
26	200	10	0	3,6	220	36,00	27,78
27	200	10	0	3,7	220	37,00	27,03
28	200	10	0	3,8	220	38,00	26,32
29	200	10	0	3,9	220	39,00	25,64
30	200	10	0	4	220	40,00	25,00
31	200	10	0	4,1	220	41,00	24,39
32	200	10	0	4,2	220	42,00	23,81
33	200	10	0	4,3	220	43,00	23,26
34	200	10	0	4,4	220	44,00	22,73
35	200	10	0	4,5	220	45,00	22,22
36	200	10	0	4,6	220	46,00	21,74
37	200	10	0	4,7	220	47,00	21,28
38	200	10	0	4,8	220	48,00	20,83
39	200	10	0	4,9	220	49,00	20,41
40	200	10	0	5	220	50,00	20,00
41	200	10	0	5,1	220	51,00	19,61
42	200	10	0	5,2	220	52,00	19,23
43	200	10	0	5,3	220	53,00	18,87
44	200	10	0	5,4	220	54,00	18,52
45	200	10	0	5,5	220	55,00	18,18
46	200	10	0	5,6	220	56,00	17,86
47	200	10	0	5,7	220	57,00	17,54
48	200	10	0	5,8	220	58,00	17,24
49	200	10	0	5,9	220	59,00	16,95

It is evident that the amplitude error decreases along with increasing period multiplication factor k_r: for $k_r = 3$, $\delta_A = 32\%$; for $k_r = 7$, $\delta_A 7\%$, and then slowly tends towards saturation: for $k_r = 27$, $\delta_A = 1.26\%$; for $k_r = 50$, $\delta_A = 1.24\%$. The phase error changes in a similar way: for $k_r = 3$, $\delta_\varphi = 33\%$; for $k_r = 7$, $\delta_\varphi = 8\%$. Since the error $\delta < 10\%$ can be considered tentatively satisfactory, it can therefore be assumed that, for a multiplication factor $k_r \geq 7$, there is a reliable speed variation representation for a given kinematic pair with a given mechanical defect. In fact, primary sampling within the FAM-C method is naturally synchronised with the observed waveform. This makes the amplitude and phase errors much smaller, especially in the case of increasing the angular velocity of the observed kinematic pair, where the number of "samples" ("primary sampling") also increases proportionally to increasing velocity.

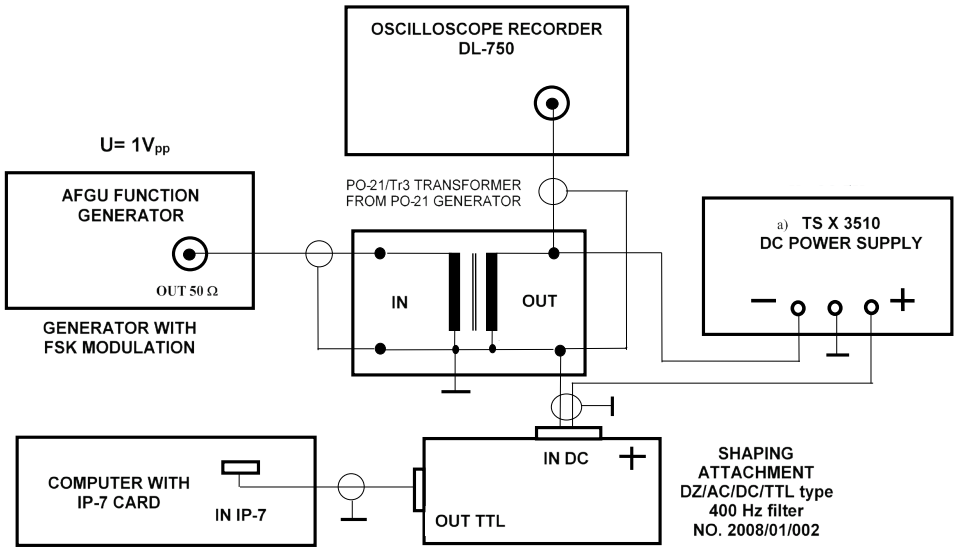

Fig. 4.3. Diagram of a bench mimicking the mechanical propulsion unit angular velocity modulation phenomena and its reflection in the FAM-C representation of an AC onboard DC generator voltage frequency modulation, enabling diagnostic system calibration

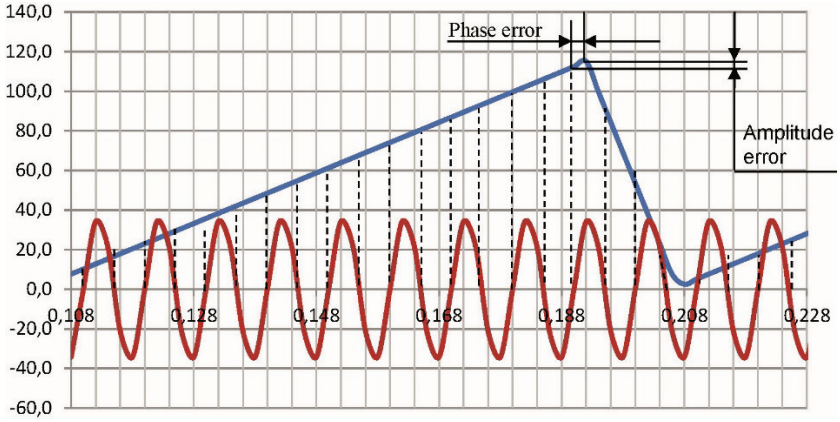

Fig. 4.4. Determination of the amplitude error and phase errors for a sawtooth modulating waveform – overview drawing of single-phase, half-periodic primary sampling $k_r = 20$

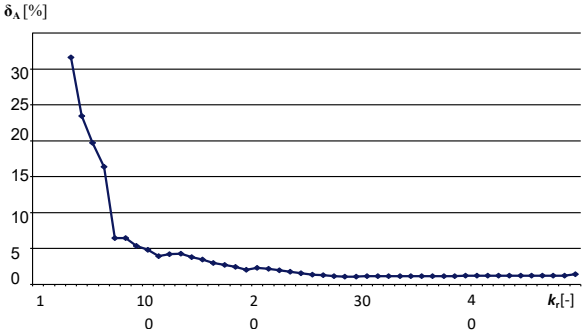

Fig. 4.5. Relative changes in the amplitude error for a sawtooth waveform as a function of changes in the k_r multiplication factor

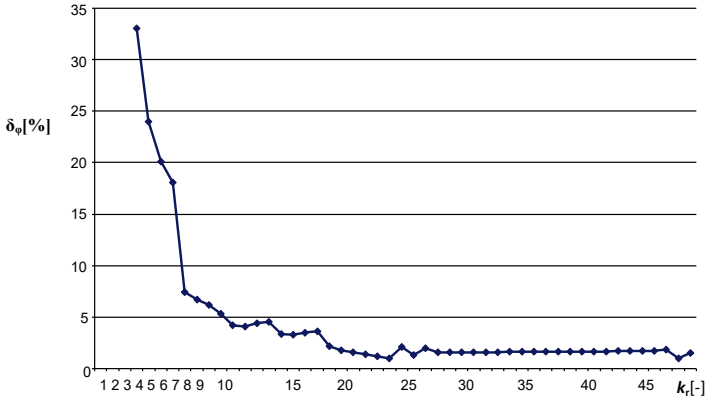

Fig. 4.6. Relative changes in the phase error for a sawtooth waveform as a function of changes in the k_r multiplication factor

The considerations above enable a conclusion that if the multiplication factor value is chosen from a range of real numbers, e.g., from 1 to 2, i.e., $k_r = (1; 2)$, then it would be most advantageous in terms of minimising the "primary sampling" representation amplitude error, if the number characteristic is 1 and the mantissa has the smallest possible value, while systematically increasing the measurement duration.

4.2.2. Primary sampling taking mechanical transmission backlash into account

Each propulsion unit is a composite of a number of subcomponents. According to the theory of machine dynamics [209, 314], the elements (kinematic pairs) of an operating unloaded mechanical unit with a quasi-stable speed exhibit significantly more individual features (natural vibrations, vibrations within local clearances) than under significant (relative to the propulsion unit rated power) load torque or a dynamic increase of this torque. Under such conditions, in the course of rotary motion, the kinematic links of a monitored propulsion unit execute oscillatory movements within the backlash with respect to the neighbouring elements in the kinematic chain. The backlash means that the generator-transducer is not accurately (rigidly) synchronised with the diagnosed link – synchronisation undergoes certain additional modulations (phase tremors[1]). This reduces leasing-related errors. This is reminiscent of the concept of eliminating the device "stagnation error", applied in the theory and practice of studying aviation equipment. Most commonly, this concept is related to friction non-linearity or non-linearity associated fluid surface tension. A similar situation is also experienced in the case of laser gyroscopes. Therefore, mechanical vibrations are often introduced in these devices to force continuous motion (angular oscillation) in such elements.

In the case of FAM-C and FDM-A measurements, there is a similar phenomenon – a natural elimination of the aliasing phenomenon [29, 77] arises due to the oscillatory movements of the tested propulsion unit mechanical elements. The kinematic chain of a propulsion unit experiences an oscillatory change in the mapping errors of the deviation amplitudes ΔF in the course of oscillatory angular movements. Herein, the greater the angular velocity oscillation amplitude associated with the backlash, the smaller the instantaneous frequency modulation error (for $\Delta F = f(f_p)$ imaging) will be in relation to the angular velocity oscillation amplitude of individual kinematic pairs in the tested propulsion unit. Thus, the characteristic set heights determined by a diagnostician will exhibit a reduced error [129]. At the same time, when the backlash of a given propulsion unit increases, the phenomena

[1] According to the author, the described phase jitter caused by backlash is the analogue of sampling pulse jitter in signal theory [303, 307].

of establishing kinematic bonds on the contact planes of gears may be less frequent. The characteristic sets $\Delta F = f(f_p)$ will then be less frequent (rarer) and, therefore, when testing machine assemblies with significant backlash, it would be advantageous to extend the diagnostic measurement duration. As an outcome, the probability of mapping extreme fluctuation amplitudes for all kinematic pairs visible for a given generator-transducer of the monitored mechanical propulsion unit, subsequently, will be increased.

4.2.3. Primary sampling for multi-phase measurement systems

The concept of multiphase sampling involves "applying" the zero-crossing points of all phases simultaneously on the time axis (Fig. 4.7). So far, the primary author of this tract has employed this measurement method for three-phase generators [129]. Thus, three times as many zero-level crossings are obtained per unit of time as in the case of a single-phase measurement. In practical terms, the voltage induction phenomenon remains unchanged – the tester does not affect three-phase generator-transducer output voltage phase shifts. This is an issue that arises upon detecting an output signal in the so-called "electronic attachment".

To provide suitable diagnostics, all three measuring chains must have very carefully matched (symmetrical) parameters related to the initial phase shift. Therefore, all three input chains must exhibit electrical resistance, inductance and replacement capacitance parameters as close to each other as possible.

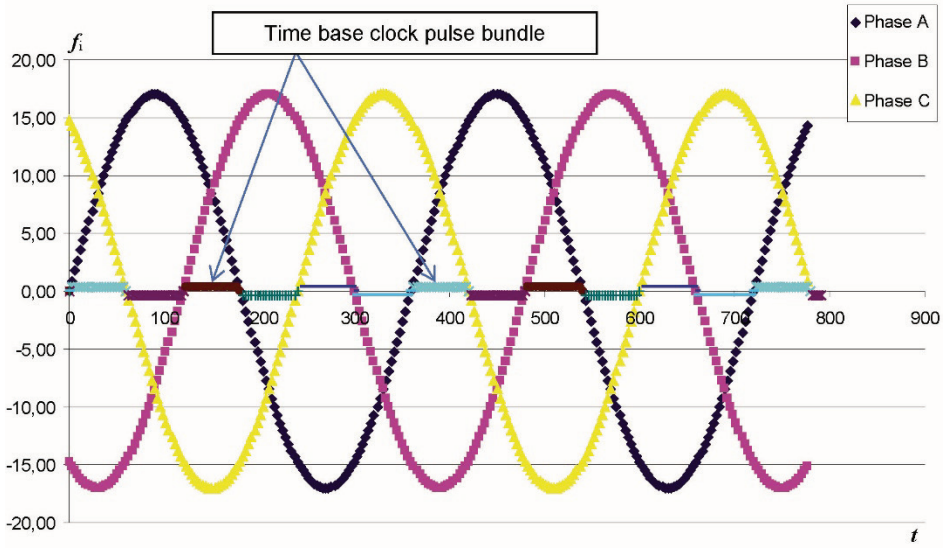

Fig. 4.7. Three-phase waveform and the method of counting time between zero-level crossings

It is planned to implement instantaneous frequency measurements from five-phase systems in the future (in addition to three-phase measurements) – via simultaneous acquisition of the signal from two different generator-transducers: a DC generator and from three phases of a three-phase generator [313]. This would enable (in addition to the existing individual kinematic pair imaging) to track torsional vibration processes within a mechanical system (in transmission) between the socket powering the DC generator and the socket powering the three-phase AC generator [313]. Projects to run a six-phase system – simultaneous three-phase measurement from two three-phase alternators powered from the same transmission box (e.g., Mi-24 helicopter) are also under consideration. It is also possible to conduct 9-phase measurements (three-phase generators: 2 three-phase electric generators and one tach generator) and 12-phase measurements (three-phase generators: 2 electrically powered and 2 tach generators). They will enable active control of the structural bandwidth associated with the monitoring of a given mechanical propulsion unit. Furthermore, the phase-shifting capabilities of a FAM-C measurement system will make possible the directing of the optimum resolution of the measurement system to the mechanical nodes of interest to a diagnostician. It will thus be possible to achieve an optimally advantageous (in terms of diagnostic resolution) k_r multiplication factor value. The elastic vibration processes (torsional vibrations) of the mechanical components located between the powering sockets of individual generators will be additional tracked simultaneously.

4.3. TTM secondary sampling

4.3.1. General issues associated with secondary sampling within the FAM-C and FDM-A methods

With the development of digital technology in the 1980s, TTMs (for the determination of propulsion unit turbine blade natural vibration and turbojet engine compressor natural vibrations) began to be applied with digital measurement [273-275, 278, 279, 282, 301]. A similar measurement implementation method is also applied by quasi-phase torque meter systems, which test torsional angles of an additional shaft placed between a mechanical power source and an energy consumer [68, 201, 202, 206, 256, 295-297]. TTM does not require an extensive measurement chain, and the synchronous signal discretisation method guarantees low measurement data volume (relative to the tensometric method) and the rapid result analysis (with a delay of up to 0.1 second) required by critical component monitoring systems [278, 301-303].

In the case of FAM-C and FDM-A methods, similarly to TTM, secondary sampling is executed by a comparison circuit in the so-called "electronic attachment" (electronic circuit for signal conditioning) and the time base clock of the counter board. This is the classical sampling method described in numerous TTM studies. In turn, radio altimeter and pulsed rangefinder signal return duration is measured in radioengineering in a similar way [164], whereas the electrical engineering community has conducted studies on sampling via an analogue waveform, e.g., the generator voltage, and possibly digitally reproducing its amplitude.

Numerous error parameters are considered in such a case. They include reconstructed signal shape error, radio interference error, etc. In the FAM-C and FDM-A methods, the object of interest is not the generator voltage amplitude change waveform, but its frequency, or more precisely, the changes in the time increments between successive generator-transducer winding positions within the magnetically neutral stator zone. Reflecting the history of these successive positions allows a secondary digital reconstruction of angular velocity change waveform for individual kinematic links of the tested propulsion unit.

Due to the specific nature of input signal acquisition and processing (generator voltage waveform) into an instantaneous frequency waveform, the electronic signal processing methods applied used should be discussed at this point – this will enable explaining system and instrumentation errors made during secondary sampling.

4.3.2. Signal conditioning system – error analysis

The signal conditioning circuit is the first block of an FAM-C measurement system. It is tasked with receiving the generator-transducer output voltage analogue signal (Fig. 4.8) and prepare it according to the TTL standard. As previously described, the generator-transducer signal contains valuable diagnostic information on the technical condition of individual mechanical propulsion unit kinematic pairs encoded within the frequency modulation of this waveform. Angular velocity frequency modulations of the propulsion unit under test constitute primary diagnostic signals. They lead to generator-transducer output voltage rated frequency modulations. Depending on the quotient of the rated frequency and the primary diagnostic signal frequency, the observation resolution of individual kinematic pairs directly and proportionally changes. A diagnostician is able to control the resolution by modifying the measurement system phase structure configuration. Changing the configuration requires parallel operation of the same number of measurement chains as the number of phases.

The received (input) generator-transducer voltage analogue signal is prepared in the conditioning block so as to be converted into digital form. For this purpose, the received voltage signal is amplified, and truncated symmetrically (top and bottom) at

a certain voltage level. The output signal is the gate pulses generated upon the crossing of the generator-transducer output voltage signal through the zero level. This creates a set of pulses wherein the diagnostic information is encoded in the time intervals between these pulses. A pulse sequence (Dirac quasi-pulses) $\delta_i(1)$ is thus generated at the output. The information carrier is the time interval between consecutive pulses – the sequence $\{\Delta t_i\}$. The number of elements of this sequence is equal to the quotient of the measurement observation time θ and the value of the input frequency f_{we}.

According to source literature [265, 294], the pulse-formation system exhibits a certain operating threshold and delay, causing a time increment error Δt_i. This error depends on the steepness of the input waveform voltage increment and decreases with increasing steepness. This steepness depends on the gain value in the signal conditioning system and on the generator-transducer voltage signal peak value, i.e., the signal conditioning system input signal. The time gain error Δt_i is significantly influenced by the distortion of the generator-transducer voltage waveform signal $u(t)$ near the zero crossing.

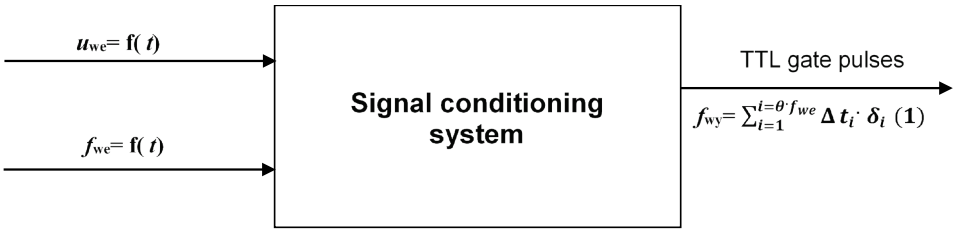

Fig. 4.8. A three-piece signal conditioning system

4.3.3. The role of a meter sheet and its interaction with a computer within a FAM-C and FDM-A measurement system

Measurement counter cards enable the measurement of pulse duration in the TTL standard. These cards are equipped with one or more independent measurement counters. In his study, the primary author employs two-byte, 16-bit card counters, which have the ability to store a maximum value of $2^{16} = 65535$ [290] items of information. The highest measurement accuracy of a counter card can be obtained when the pulse counter value is close to the counter capacity. Thus, a counter card with a higher time base clock frequency is able to measure the mechanical fluctuation frequencies with a higher minimum frequency threshold f_p than a card with a lower frequency.

In AC measurement chains (FAM-C), frequency modulation measurement is often used with two-wave (half-period) counting, Fig. 4.9. This requires two measurement chains (Fig. 4.10) on the counter card, and the two chains must exhibit

phase shift values as close to each other as possible. The correctness of the operation is usually verified by applying a generator-transducer voltage (Fig. 4.9, red sine wave) with the frequency varying according to a rectangular frequency waveform with a filling factor of 50%. This rectangular frequency waveform simulates the angular velocity frequency modulation of a given mechanical propulsion unit's kinematic link. At the same time, this rectangular frequency waveform reflects the shape of the signal controlling the function generator frequency change (Fig. 4.3). As mentioned, an FM modulation is produced at the output of the function generator directly proportionally to this rectangular waveform.

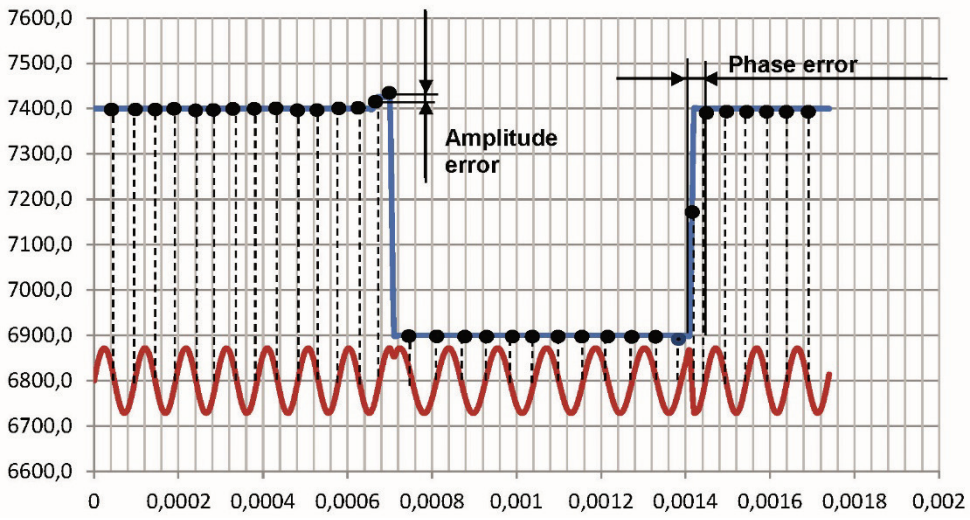

Fig. 4.9. Determination of the amplitude error and phase errors for a rectangular modulating waveform with a 50% infill ratio – overview of single-phase, half-periodic primary sampling $k_r = 27$

The measurement system (Fig. 4.10) measures time increments between zero level crossings. Next, a discrete instantaneous frequency waveform as a function of time is determined (Fig. 4.9, black dots). Now, comparing the reference signal phase (Fig. 4.9, blue solid line) with this waveform's discrete reflection phase (black dots) enables determining the phase error. The amplitude deviations for the curve routed between the set of black spots and the reference rectangular waveform can be tracked in a similar manner. This allows determining the amplitude and phase error of individual FAM-C and FDM-A measurement units (Fig. 4.9). The actual frequency waveform signal obtained from the function generator is shown in Fig. 4.11. An example set of amplitude and phase error parameters for a genuine DC channel system (FDM-A method) prepared for testing an SO-3 engine is listed in Table 5.

Table 5

Values of the FSK frequency modulation rectangular wave, set on the function generator to simulate the DC generator pulsation component frequency modulation changes caused by SO3/3W engine rotor supports at 1/10 of the process frequency for *n* = 7000 rpm and 15 600 rpm – preset values

Rotational speed main shaft power turbine (rpm)	Diag-nostic class	Preset values						
		$F_1 = F_{min}$	$F_2 = F_{max}$	t_1	t_2	Name of set	A	fp
		Hz	Hz	ms	ms	-	Hz	Hz
7000	O	3201	3151	2.435	2.435	1OGS	50	205
	A	3216	3136	2.435	2.435	1AGS	80	205
	B	3276	3076	2.435	2.435	1BGS	200	205
	C	3376	2976	2.435	2.435	1CGS	400	205
	D	4076	2276	2.435	2.435	1DGS	1800	205
	E	4426	1926	2.435	2.435	1EGS	2500	205
15600	O	7103	7053	1.945	1.945	7OGS	50	257
	A	7118	7038	1.945	1.945	7AGS	80	257
	B	7178	6978	1.945	1.945	7BGS	200	257
	C	7278	6878	1.945	1.945	7CGS	400	257
	D	7978	6178	1.945	1.945	7DGS	1800	257
	E	8328	5828	1.945	1.945	7EGS	2500	257

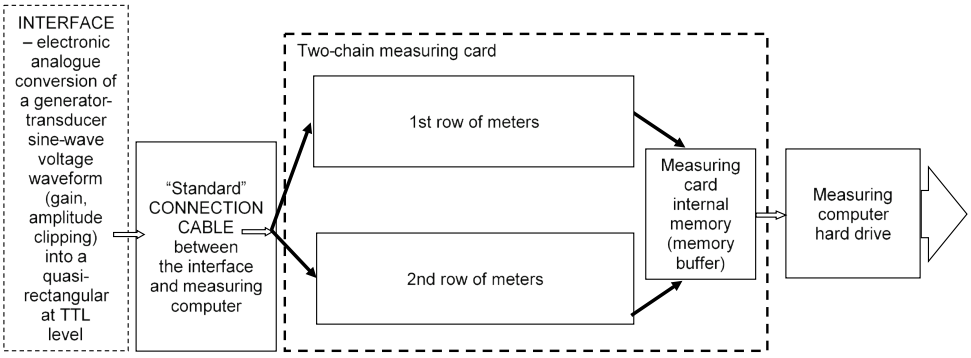

Fig. 4.10. Universal general block diagram of sub-assemblies housed in a measuring computer adapted to the FAM-C and FDM-A methods, showing the tested sub-assemblies for a bi-polar zero-crossing counting system

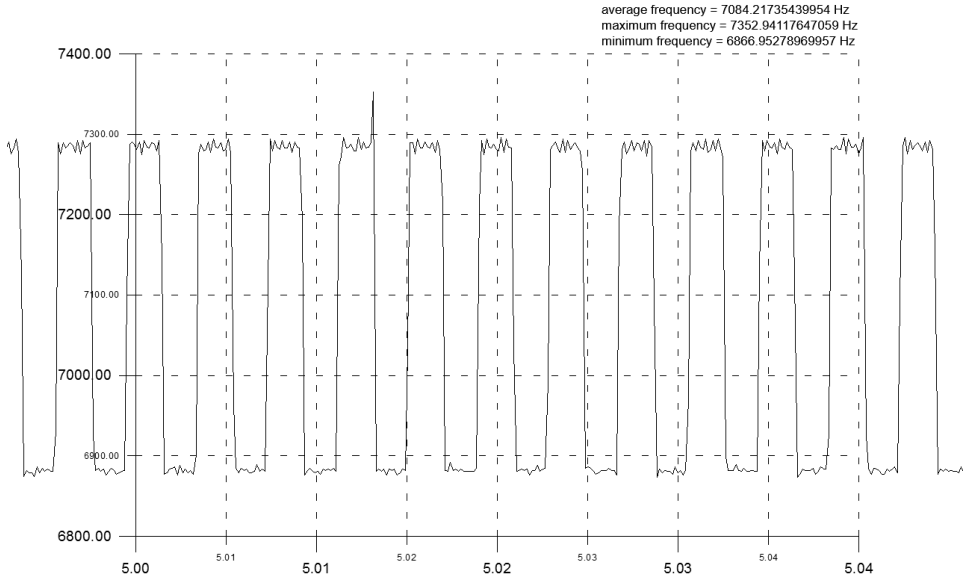

Fig. 4.11. Instantaneous frequency waveform for frequency modulations in the form of a rectangular waveform during a performance check of the FDM-A system under laboratory conditions

4.3.4. Selected issues from the theory and practice of the frequency measurement technique

Digital measuring instruments can be divided, in terms of their measurement structure [231, 265], into:

- granular, i.e., discrete,
- analogue.

Two digital frequency measurement methods are applied [76, 259, 265]. The first, so-called "direct", involves counting pulses generated from the measured frequency waveform f_x over a standard time interval T_p. The second involves measuring the T_x period (instead of frequency f_x). This method, called "indirect", is also employed (during secondary sampling) in the FAM-C and FDM-A measuring instrumentation.

The direct method relative error, following [265], is:

$$\frac{\Delta f_{\mathrm{x}}}{f_{\mathrm{x}}} = \frac{1}{n} + \frac{\Delta T_p}{T_p} = \frac{1}{f_{\mathrm{x}} T_p} + \frac{\Delta f_{\mathrm{w}}}{f_{\mathrm{w}}} \tag{4.6}$$

The first error component, characteristic of the direct method, decreases along with increasing measured frequency f_w and extending reference measurement duration T_p. In the case of rapid measured frequency changes, the measurement duration must not be too long, since the frequency meter counts the number of crossings through zero during the measurement. If it is, the counter may fill up.

The indirect method is employed to measure lower frequencies, for which the direct method accuracy is decreasing. Thus, obtaining the value of an unknown frequency f_x entered at the input of the instrument requires calculating this frequency as the inverse of the period T_x. The period measurement error is:

$$\frac{\Delta T_{\mathrm{x}}}{T_{\mathrm{x}}} = \frac{1}{n} + \frac{\Delta T_b}{T_b} = \frac{f_{\mathrm{x}}}{f_{\mathrm{w}} k} + \frac{\Delta f_{\mathrm{w}}}{f_{\mathrm{w}}} + \frac{1}{k S_1 T_x} \tag{4.7}$$

Unfortunately, it is difficult to set the trigger levels precisely close to zero, where a minimum phase shift angle measurement error is ensured. When the input voltage is amplified, however, the error value decreases – it will be inversely proportional to the amplification magnitude. Therefore, the structure of the FDM-A instrumentation (DC electronic attachment) contains a voltage amplifier. The DC generator-transducer generates a DC pulsation component with a relatively low amplitude value of $U_{pp} = 0.2 \div 2.1$ V. For comparison, an aviation AC generator-transducer generates an AC inter-phase voltage with a relatively high amplitude value of $U_{\mathrm{RMS}} = 200$ V, or $U_{pp} = 560$ V. In order to "level the chances", the pulsation component signal for the DC generator-transducer should be highly amplified.

The time increment measurement method error is random. It can be reduced if there is a possibility to repeat the measurement of the same value ("observations" of the same dynamic process) k times under identical conditions. The method error associated with a single measurement can, however, be reduced by using two parallel measurement systems, each with a different generator frequency: the first – the "main" with a longer pulse repetition period T_{w1}, the second with a pulse repetition period T_{w2}. The result of the time increment measurement can be determined from the equation:

$$T_{\mathrm{x}} = n_1 \cdot T_{\mathrm{w1}} + n_2 \cdot (T_{\mathrm{w1}} - T_{\mathrm{w2}}) \tag{4.8}$$

where:
n_1 – number of crossings through zero for the measurement system using a generator with the longer pulse repetition period T_{w1}; n_2 – number of crossings through zero for the measurement system using a generator with the shorter pulse repetition period T_{w2}.

In practice, this method is applied in the case of FAM-C measurements with two measurement systems exhibiting a minor difference in internal clock frequency simultaneously used for measurements from the same generator-transducer. The effects are only taken into account when analysing the parameters of the characteristic sets, where the imaging parameters from both measurement chains are averaged. However, it is also technically possible to synchronise the two measurement chains to conduct the averaging at the stage of creating the pulse bundle sets.

4.3.5. The possibilities of synchronizing the measurement chains of two different generator-transducers

Section 4.2.3 discussed the possibilities for synchronous multiphase measurement of several different AC generator-transducers. Meanwhile, practical and theoretical premises can demonstrate that an AC generator can operate synchronously with a DC generator – indeed, the FAM-C and FDM-A methods are mutually complementary [114, 136, 313]. The simultaneous application of both generator types, DC and AC, should result in a significant increase in the certainty of diagnostic data obtained, contributing to diagnosis reliability. By synchronising the process of acquiring and analysing results from several generators (measurement chains composed of different generator types) (Fig. 4.12), it is possible to analyse numerous additional issues, such as determining the level of torsional stress of power transmission elements and bearing wear.

This monograph expands the research concentrating on this issue. The study was conducted in the form of both mathematical considerations and physical tests [313]. Each of the measurement chains generates voltage waveform components of a completely different shape (Fig. 4.13). These variations result from the different manner of voltage formation:

- in an AC generator, where only the quasi-sinusoidal AC component is induced (no DC component),
- in a commutator DC generator, where the first formation stage is similar to that in an AC device, but is then electromechanically rectified by the commutator, resulting in two components, namely, a DC voltage component (with a value of 28 V) and an AC component with a rms amplitude of 0.1÷2.1 V [215]. The shape of the alternating component resembles a combination of inverted semi-sinusoids (Fig. 4.13, detail 2).

The instantaneous frequency measurement is also different in each method:

- AC channel (in the FAM-C method) – three-phase and half-period measurement,
- DC channel (in the FDM-A method) – full-period measurement.

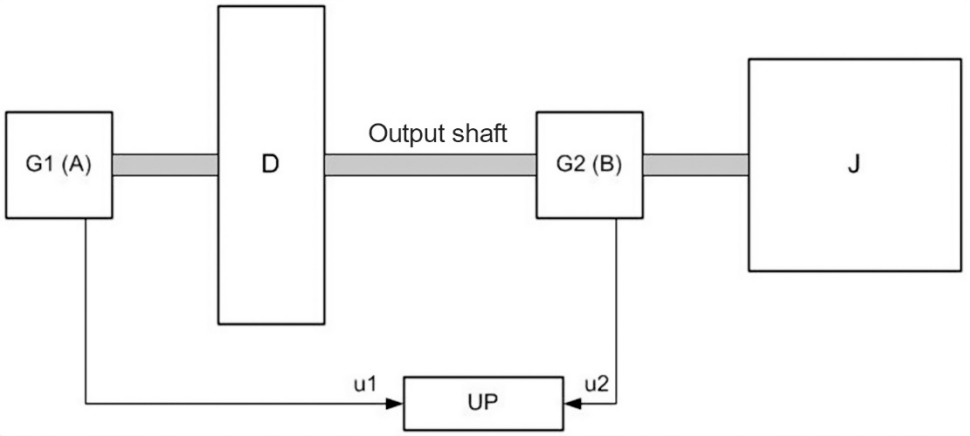

Fig. 4.12. Block diagram of transmission shaft torsion angle measurement using voltage frequency modulation of two different generators: G1, G2 – generators, D – propulsion engine, UP – measurement system, u1, u2 – generator output voltage (G1, G2), motor mechanical load (e.g., helicopter main gearbox including a propeller)

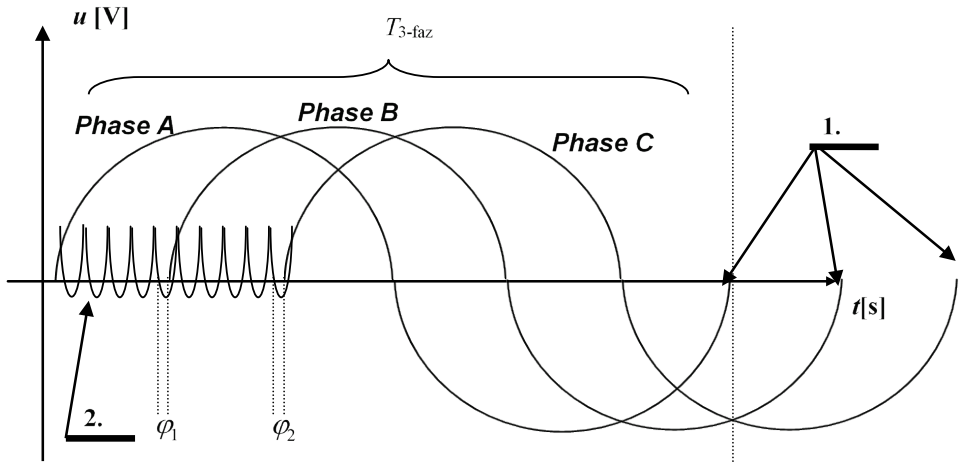

Fig. 4.13. Voltage waveforms from two different generators employed to measure the shaft torsion angle: 1 – three-phase AC generator output voltage (phases: A, B, C), 2 – commutator DC generator output voltage pulsation component

In addition, each of these generators has a different measurement method – the three-phase generator utilizes a half-period and a three-phase counting method, while the commutator DC generator employs a full-period single-phase counting method (Figs. 4.14 and 4.15).

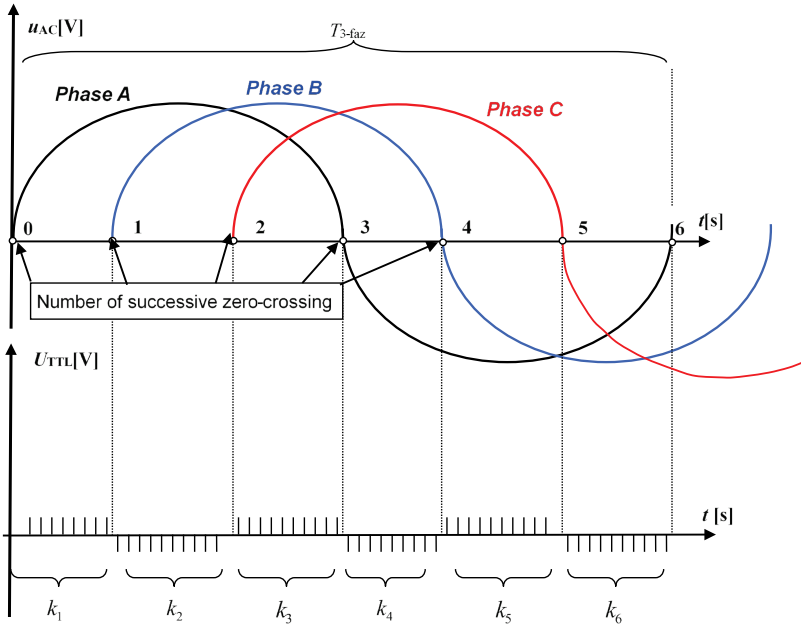

Fig. 4.14. Method of counting zero-level crossings for a three-phase AC generator: u_{AC} – three-phase generator-transducer individual phase voltage waveform in the FAM-C method, $k_1, k_2, k_3, k_4, k_5, k_6$ number of pulses for the next successive computation exposure (UTTL), respectively

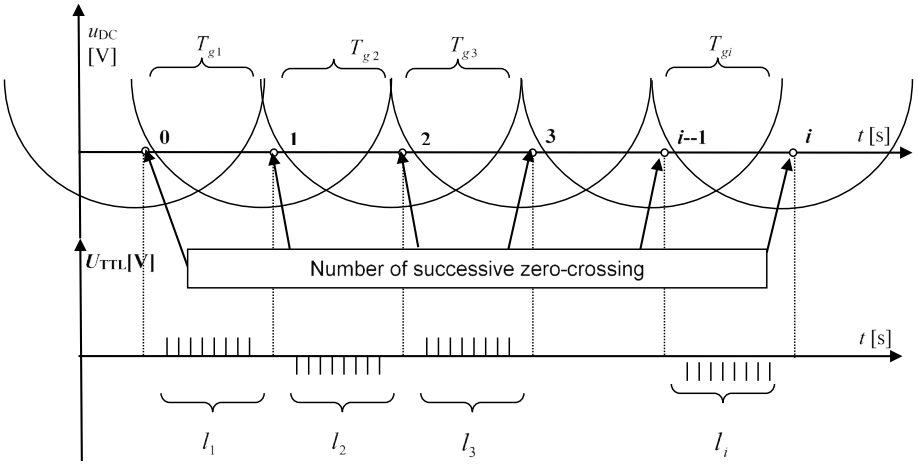

Fig. 4.15. Method of counting zero-level crossings for a commutator DC generator: u_{DC} – three-phase generator-transducer individual phase voltage waveform in the FDM-C method, $l_1, l_2, l_3, l_4, l_5, l_6$ number of pulses for the next successive computation exposure (UTTL), respectively

The counter card time base generator frequencies are also different. For example, in the course of diagnostic measurements of the SO-3 engine, the author used:

- an IP-7 counter card with a time base frequency of $f_{zg} = f_s = 32$ MHz in the DC circuit (for a DC generator),
- a PCL-830 counter card with a time base frequency (of the counter card's internal generator) of $f_{z\text{-}3faz} = f_s = 1$ MHz in the AC circuit (for a three-phase AC generator).

This means that for one pulse generated through the FAM-C method, there are 32 pulses generated through the FDM-A method. Therefore, the time needed to generate one period of the output voltage waveform T_{3faz} (Fig. 4.14) for a 3-phase AC generator with two-pulse measurement (using a two-track counter card with a time base generator $f_{z\text{-}3faz} = f_s = 1$MHz) is:

$$t_{z1-3\,faz} = \frac{\sum_{i=1}^{6} k_1}{1000000} = \frac{\sum_{i=1}^{m} k_i}{f_{z-3\,faz}} \text{ [s]} \tag{4.9}$$

The number 6 comes from the fact that, for the SO-3/3W engine measurement system, there is one half-period of the three-phase AC generator for every six periods of the DC generator pulsation component voltage waveform.

In turn, the time of one period T_{z1g} (Fig. 4.13) for the DC generator can be determined:

$$T_{z1g} = \frac{l_i}{32000000} = \frac{l_i}{f_{zg}} \text{ [s]} \tag{4.10}$$

Thus, when analysing a simultaneous measurement of signals from both generators (Fig. 4.11), the principle of coupled "families"[2] [313], the periods and half-periods of which are selected based on the least common multiple (LCM) principle, must be applied. Let us assume that for a DC generator, this will be $l = \{l_1, l_2, \ldots, l_i, \ldots l_n\}$, and for a three-phase AC generator $k = \{k_1, k_2, \ldots, k_i, \ldots, k_m\}$.

In the future, it will be possible to apply this theory to analyse the measurement of the shaft torsion angle between two generators. Monitoring the dynamics of the torsion angle in such a shaft [313] and calculating the amplitude value of this angle will also be possible:

[2] Each "family" is selected in the form of a certain number of half-periods of the AC generator voltage waveform and DC generator output voltage pulsation component waveform periods.

$$\phi_1 \approx \frac{(f_{z-3\,faz\max} k_1 - f_{zg\min} \sum_{i=1}^{n} l_i)}{f_{z-3\,faz\max} \sum_{i=1}^{6} k_i} 2\pi \tag{4.11}$$

where:

$f_{z\text{-}3fazmax}$ – maximum frequency of the time base applied onto measurement system counter cards for AC generator measuring chain, f_{zgmin} – minimum frequency of the time base applied onto the measurement system counter cards for the commutator DC generator measuring circuit, l_i – number of consecutive (i-) pulse bundles generated between consecutive crossings of the commutator DC generator pulsation component through the zero level, k_i – number of consecutive (i-) pulse bundles generated between successive crossings of the AC generator's three-phase output voltage through the zero level, n – number of pulse bundles received in the DC measuring chain, m – number of pulse bundles received in the AC measuring chain.

A comparison of individual shaft torsion angles enables determining its torsion dynamics and drawing appropriate conclusions. It will be possible to prepare the mathematical apparatus for other mechanical phenomena, e.g., monitoring the combined loosening of different aircraft propulsion units with many different onboard generators.

4.3.6. Impact of generator-transducer voltage signal interference on the secondary sampling error

Preliminary description of the physics behind the impact of interference on FAM-C and FDM-A measurement errors

The operation of the FAM-C method is based on applying frequency and phase modulation parameters, which, according to the signal theory, should provide high noise immunity. In the FAM-C method, the instantaneous frequency is calculated using an indirect method – by calculating the time increments between successive zero-level crossings. At this point (near the zero crossing), the voltage change gradient is the highest, therefore, the resistance to high-frequency interference is also the highest [67, 270, 304-306].

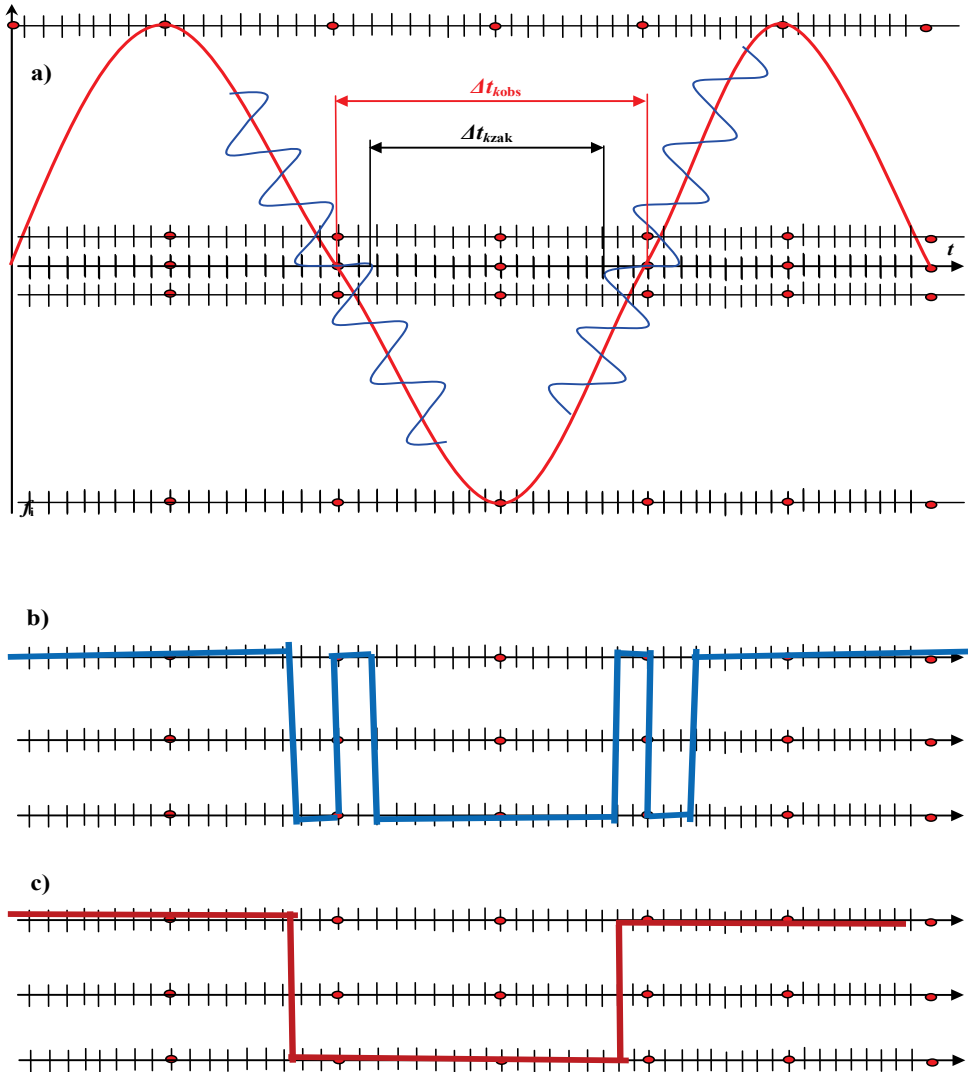

Fig. 4.16. Interaction between a waveform with high frequency interference:
a) observed waveform with an interfering waveform having higher frequency:
Δt_{kobs} – time increment of the observed signal without interference, Δt_{kzak} – time increment of the resultant signal: observed signal with superimposed interference, b) comparator response without hysteresis, c) comparator response with hysteresis

Nevertheless, the influence of interference on the results does exist[3]. This is mentioned in many source literature positions, e.g., [270, 304÷306], wherein it is mathematically proven that when the observed voltage waveform signal is "contaminated":

$$u_{\text{obs}} = f(t) = U_{\text{obs}} \cdot \sin(2\pi f_{obs} t) \tag{4.12}$$

the interfering signal:

$$u_{\text{zak}} = f(t) = U_{\text{zak}} \cdot \sin(2\pi f_{zak} t) \tag{4.13}$$

overlaps, and time increments between successive crossings through the zero-level decrease statistically on average. This will result in an apparent increase in the frequency calculated this way [304] (Fig. 4.16). Thus, a waveform composed of both signals (interfering and observed) may have a time increment between successive k- crossings through the zero level $\Delta t_{k\text{zak}}$ that is smaller than for an undisturbed signal (Δt_k). These relationships can be described, following [304, 305], in the form of the formulae:

a) observed signal time increment without interference:

$$\Delta t_{kobs} = \frac{1}{2 \cdot f_{obs}} \tag{4.14}$$

b) resultant signal time increment: signal observed with interference applied:

$$\Delta t_{kzak} = \Delta t_{kobs} - 2 \cdot U_{\text{zak}} \left[1 - u_{\text{obs}}'(t_{\text{k}})\right] \tag{4.15}$$

After substituting the formulae (4.12) and (4.14) to (4.15), one can obtain:

$$\Delta t_{kzak} = \frac{1}{2 \cdot f_{obs}} - 4 \cdot U_{\text{zak}} U_{\text{obs}} \pi f_{obs} \cdot \cos.(2\pi f_{obs} t_{\text{k}}) \tag{4.16}$$

Due to a diagnostic process involving the use of, among others, the output signal from a three-phase tach generator, it is also required to employ a three-phase reference source in the form of a frequency-modulated three-phase calibrator. The

[3] [161], p. 165, "We do not actually measure the time intervals between "pulses", but rather the time intervals between moments when output waveforms exceed certain predetermined voltage levels (thresholds) ...".

entire calibration process is designed to evaluate and quantify the metrological errors of measurement structures in individual FAM-C measurement sets. Calibrations involve applying calibrated variations and distortions of the three-phase voltage to the input of a tested FDM-A measurement system:

1) output voltage carrier frequency,
2) voltage rms value,
3) phase voltage asymmetry,
4) amplitude coefficient values,
5) total harmonic content,
6) individual harmonics,
7) voltage constant component,
8) phase angle changes between individual voltage phase vectors,
9) amplitude modulation depth.

It is therefore necessary to start with conducting tests on a real object or conduct a theoretical analysis. The value of the output voltage carrier frequency of a D-10/2 tach generator is a result of several design features, such as the 4:1[4] reduction ratio [129, 312] of the tach generator shaft speed relative to the main shaft angular velocity (Table 6). The rms values of the voltage obtained from measurements on the SO-3/3W engines are summarised in Tables 7 and 8.

Table 6

D-10/2 tach generator frequency parameter measurement

SO-3 engine main shaft rated speed number	SO-3 engine main shaft	SO-3 engine main shaft	D-10/2 generator shaft	D-10/2 generator shaft
-	*n*	*n*	*n*	*n*
-	rpm	Hz	rpm	Hz
1	7000	116.7	1750	29.2
2	9500	158.3	2375	39.6
3	11500	191.7	2875	47.9
4	12250	204.2	3063	51.0
5	13500	225.0	3375	56.3
6	15100	251.7	3775	62.9
7	15600	260.0	3900	65.0

[4] This is the ratio (4:1) in the TS-11 Iskra propulsion unit between the main shaft of the SO-3/3W engine and the shaft of the D-2/10 tach generator [312].

Unfortunately, no measurements of the tach generator output signal distortion have so far been conducted during diagnostic measurements at airfields. In the course of this study, it was therefore necessary to take these measurements under laboratory conditions. A propulsion unit was constructed for this purpose. A three-phase waveform with a significant deviation in shape from the sine wave was obtained at the generator output [114].

Significant values of distortion parameters were found, as well as numerous cases of exceeded distortion level relative to normative values:

- amplitude depth factor $p = 1.06 \div 1.95\%$, according to standard: $p<1\%$,
- amplitude factor $k_a = 1.5 \div 1.69$, according to the standard: $k_a = 1.26 \div 1.56$ – the vertices become elongated relative to the sinusoid and start resembling the shape of a triangle (for a triangle: $k_a = 1.73$),
- voltage asymmetry ranging from 1.02% to 6.7% – according to standard: 1.5%,
- total harmonic content $m = 10.5 \div 10.8\%$, according to standard: $m < 8\%$,
- highest harmonic $h_{11} = 7.4\%$, according to standard: $h_{max} < 5\%$.

These values improved when the speed of the "engine main shaft" was increased to $n_N = 15{,}600$ rpm, i.e., for s tach generator shaft: $n_{D10} = 3{,}900$ rpm, however, they still exceeded the normative requirements.

Table 7

D-10/2 tach generator output voltage measurements, tests No. 54, 69 and 88

Speed number	Main shaft	SO-3 No. 37173205TS-11 No. 3H1405			SO-3 No. 37173205TS-11 No. 3H1405			SO-3 No. 37173205TS-11 No. 3H1405		
		test No. 54, 8/11/2007			test No. 69, 30/6/2008			test No. 88, 28/4/2009		
-	n	U_{AB}	U_{BC}	U_{AB}	U_{BC}	U_{CA}	U_{CA}	U_{AB}	U_{BC}	U_{CA}
-	rpm	V	V	V	V	V	V	V	V	V
1	7000	12.73	12.53	12.73	-	-	-	11.05	11.25	11.22
2	9500	16.61	16.31	16.58	15.95	16.20	16.22	13.70	13.90	14.23
3	11500	18.97	18.48	18.75	18.94	19.26	19.30	16.50	16.80	16.77
4	12250	20.09	19.67	19.91	20.00	20.35	20.37	17.70	18.12	18.04
5	13500	21.8	21.4	21.7	21.67	22.05	22.13	19.10	19.51	19.43
6	15100	23.73	23.2	23.6	23.75	23.17	24.32	20.91	21.02	21.30
7	15600	24.17	23.67	24.07	24.4	24.85	24.95	21.80	21.40	21.8

Table 8

D-10/2 tach generator output voltage measurements, tests No. 52, 86 and 87

Speed number	Main shaft	SO-3 37174238 TS-11 No. 3H1611			SO-3 No. 37176110 TS-11 No. 3H1712			SO-3W 48172110 TS-11 No. 3H1630		
		test No. 52, 16/10/2007			test No. 87, 28/4/2009			test No. 86, 28/4/2009		
-	n	U_{AB}	U_{BC}	U_{CA}	U_{AB}	U_{BC}	U_{CA}	U_{AB}	U_{BC}	U_{CA}
-	rpm	V	V	V	V	V	V	V	V	V
1	7000	11.9	12.0	11.8	11.07	11.32	11.24	11.17	11.17	11.17
2	9500	16.3	16.6	16.4	14.64	15.07	14.82	14.89	14.89	14.89
3	11500	19.1	19.7	19.4	17.30	17.78	17.63	17.28	17.28	17.28
4	12250	20.3	20.6	20.4	18.03	18.54	18.38	18.44	18.44	18.44
5	13500	21.6	21.9	21.8	19.54	20.09	19.95	20.15	20.15	20.15
6	15100	23.5	23.9	23.6	21.29	21.96	21.70	21.91	21.91	21.91
7	15600	24.0	24.5	24.2	22.07	22.36	22.11	22.37	22.37	22.37

4.3.7. Possible applications of quadrature modulation in the FAM-C and FDM-A methods

Digital signal transmission involves using so-called "quadrature amplitude modulation" (QAM), proposed in 1960 [67, 155, 200, 239, 246]. In essence, quadrature modulation is a type of modulation without a carrier wave in two independent channels. It is based on a trigonometric property of the sine and cosine signals being orthogonal. Therefore, if the phase of two different signals with the same carrier frequency value is shifted by 90°, it will be possible to transmit and detect two different signals with the same carrier frequency independently and without interfering with each other, owing to the use of "coherent" ("synchronous") demodulation[5]. In the case of the FDM-A and FAM-C methods, a double (duplicated) measurement system with an initial relative output voltage phase shift by 90° can be applied for each generator. This will enable observing mechanical signals from two different resonators or mechanical modulators with a similar rated frequency and

[5] Source literature [67, 155, 200, 246] refers to one of them as synphase "I", and to the other as quadrature "Q".

a similar modulation bandwidth. This is entirely possible because the two mechanical resonators usually do not exhibit "perfectly equal" rated frequencies, i.e., LF carriers ($\omega_{N1} \neq \omega_{N2}$). Therefore, once the original diagnostic signals are converted by the generator-transducer into the HF signal band, these relationships will be preserved.

The HF signal is subsequently transferred via the onboard electrical grid (HF signal propagation medium) to its various components, including different terminals. The FAM-C or FDM-A measurement systems are usually connected to these elements. An HF signal subjected to detection by such a system returns to the low-frequency band. The frequency spectrum of each kinematic pair is analysed. If the detection system has a structure similar to that shown in Fig. 4.17, new possibilities for analysing such a frequency spectrum arise. Such a system resembles a coherent decoder system employed in telecommunications (in cellular telephony) to reproduce two different LF signals transmitted in the same HF band. In the case of the system presented in Fig. 4.17, two HF frequency spectra are obtained in each detection channel based on the HF signal by means of reciprocal transformation. Due to the phase shift on the input transformer, time increments (FAM-C secondary sampling) for each of these spectra are counted in a different order. Therefore, the first resonator will be favoured in one channel and the second resonator in the other. However, if both resonators have "perfectly equal"[6] carrier frequencies, there still remains the issue of carrier frequency periodic shifting due to the stochastic or periodic loss of kinematic link with the main power source (primary carrier wave) resulting from, e.g., gear backlash.

Notwithstanding the above, a 90° phase shift is also a shift in the observation time. This effect increases the probability of "capturing" short-lived fast fluctuations of the primary diagnostic signal. In practice, this means shifting the upper limit of the FAM-C and FDM-A method visibility window towards higher frequencies.

So far, the FDM-A and FAM-C methods have involved simultaneous observation of all processes on one coordinate system, and overlapping characteristic sets were obtained for mechanical vibration sources (resonators) with similar eigenfrequencies. Calculating their parameters (e.g., the heights and limits of occupied individual characteristic set bands) was sometimes very burdensome and even impossible, especially in the case of resonators or mechanical modulators with dynamically varying limits of the occupied band or amplitude values seen in the course of the test. The author believes that applying coherent demodulation (QAM)

[6] "Perfectly equal" frequencies are considered as frequencies so close that, after primary sampling (electromechanical sampling in a generator-transducer), secondary sampling at a given time base frequency is (on average statistically) unable to detect them.

[67, 100-101, 155, 220, 228, 306] will enable separating such characteristic sets of mechanical vibration sources. This would require using two twin measurement circuits in the DC generator signal measurement chain. As an outcome, generator-observer counter-phase output voltage signal would be sent to the input of both these systems.

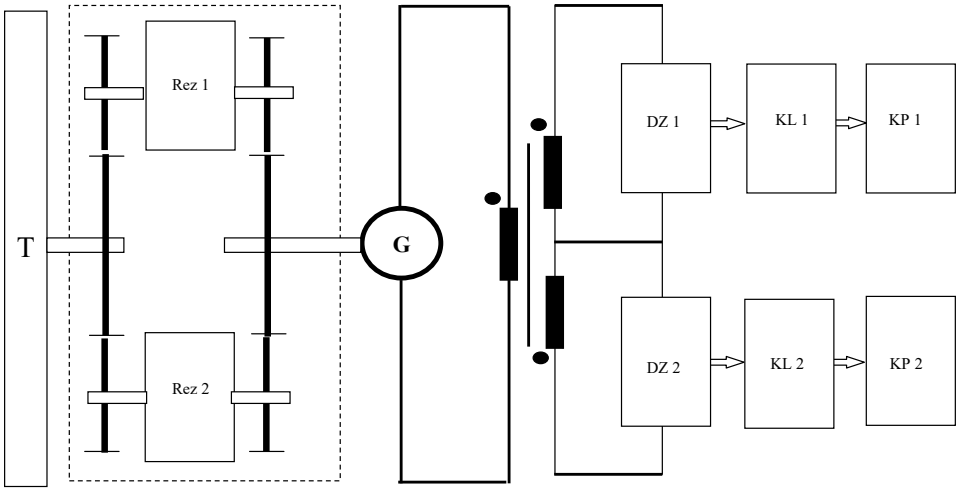

Fig. 4.17. Quadrature modulation system in the FAM-C method: T – primary source of mechanical power (e.g., gas turbine), Rez 1 – mechanical resonator No. 1, Rez 2 – mechanical resonator No. 2, G – generator-transducer, DZ – zero detector (electronic attachment, i.e., signal conditioning block) No. 1, DZ 2 – zero detector No. 2, KL 1 – counter card (timer) No. 1, KL 2 – counter card No. 2, KP 1 – measuring computer No. 1, KP 2 – measuring computer No. 2

4.4. Significance of FAM-C and FDM-A method metrological properties in verifying study hypothesis – summary

In this chapter, the primary author included his knowledge of FAM-C and FDM-A metrological properties. The main focus was on the measurement system and the errors associated with it. In particular, a thorough analysis covered the issues associated with converting the generator-transducer voltage analogue signal into a digital signal in a FAM-C or FDM-A measurement system [100, 104, 105, 127, 129].

Subsection 4.2.3 dealt primarily with the errors of primary sampling implemented by the generator-transducer, and highlighted the phase multiplication control of the FAM-C measurement systems. This control is not implemented by the generator-transducer, but by changing the structure of the electronic measurement system. Changes in phase multiplication result in significant changes in method sensitivity and error rate.

In turn, subsection 4.3.5 presented the concept of increasing the propulsion unit diagnosis resolution by simultaneously employing several different generator-transducers. The error relationships resulting from the time base generator error are relevant, i.e., the change in frequency f_s of the counter card (as discussed in subsection 4.3.4), due to the instability of this frequency and the stochastic phase relationships between the pulses (f_s) and the locations of zero-level crossings of the generator-transducer voltage waveform. In addition to errors resulting from changes in the phase structure of the measurement system (subsections 4.2.3 and 4.3.5) and errors due to time base clock instability and phase relations between pulses of this clock and the observed signal from the generator-transducer (subsection 4.3.4), there is also the impact of amplitude interference on the measurement error (subsection 4.3.6). In general, the contribution of amplitude interference broadens the signal spectral bandwidth and increases the value of limiting frequencies.

The metrological issues associated with the operation of a generator-transducer (which executes electro-mechanical primary sampling) and with measuring the time increment (secondary electronic sampling) were also discussed. Numerous courses of action required to reduced measurement errors and improve the reliability of diagnosing a tested propulsion unit were determined. The idea of applying quadrature modulation modified by the author is noteworthy. The implementation of this idea requires twice as many measurement chains, but will enable separating some characteristic sets associated with kinematic links exhibiting similar rated angular velocities.

The metrological description of the method included in this chapter contains a set of benchmarks for the relationship models between the propulsion unit kinematic pair defects associated with FAM-C and FDM-A imaging. The set of these benchmarks is essential in the process of verifying the hypothesis from subsection 2.3 on the properties of generator-transducers as a comprehensive source of information in the surveillance of mechanical propulsion units. A partial explanation of the veracity of this conjecture is included in Chapter 3 (based on physical tests, including mechanical measurements and mathematical analyses) in relation to model benchmarks for individual types of wear and damage of single kinematic pairs in the tested propulsion unit. However, the scope of the considerations in Chapter 3 was limited to the diagnosis of individual kinematic pairs. In practice, the manager (owner) of propulsion units is interested in a comprehensive and

complex simultaneous diagnosis of many kinematic pairs, and not only of single and isolated components. Such a comprehensive diagnosis entails dealing with numerous issues associated with the practical analysis of complex and often highly elaborate real mechanical propulsion units. This issue is to be reviewed in the next chapter. In Chapter 5, a discussion will be found of the evidence supporting the veracity of the formulated hypothesis on the possible simultaneous monitoring of multiple kinematic links through controlling the summed observability window of the FAM-C and FDM-A multicircuit measurement structure.

5

APPLICATION OF THE FAM-C AND FDM-A METHODS WITHIN THE TECHNICAL OBJECT MONITORING PROCESS

5.1. Scope of FAM-C and FDM-A method implementation in relation to actual objects

The FAM-C method has been applied by the primary author and his team since 1991. Its first use was to determine the reasons for shaft detachment in the generators of LUZES-V mobile power supply equipment [191]. The identified cause was a too-slow turbine engine speed controller. Upon a stepwise generator load drop from 160% S_{Ne} to 10% S_{Ne}[1], its response was too slow. This resulted in specific correlations between the generator rotor engine shaft fluctuations and the inappropriate action of the dynamically slow speed controller that resulted in torsional vibrations with an increasing amplitude, followed by accelerated fatigue wear [194]. The used turbine engines from obsolete helicopters probably exhibited increased (significant) circumferential backlash at the splines between the free turbine connections and the TUN-75/R reducer, within the reducer gears, and at the splined connection between drive sleeve and the alternator. The combined

[1] S_{Ne} – rated generator power – in the case in question (GT-40 aircraft generator), the change in electrical load ranged from 64 kW to 4 kW. This generator was powered by a GTD-350 turboprop engine (removed from a Mi-2 helicopter) with a power of 350 HP, i.e., S_{Nm} = 455 kW. Therefore, the turbine engine shaft load change ranged from 14%, to 9% S_{Nm}.

backlash during fluctuations associated with load changes enabled decelerating the elements of the transmission chain between the turbine and generator rotor. Upon establishing the kinematic bond (after circumferential backlash is selected), there was a rapid acceleration in the angular velocity. This acceleration was counteracted by forces induced by the transmission chain moments of inertia. This led to significant torsional moments. After some time, the elastic forces caused a "twisting" in the other direction. The consequence was a transmission chain shaft torsional angle oscillatory motion. The phenomena of shaft springing can be demonstrated in the form of an electrical equivalent system, wherein the elastic properties can be represented as inductance, while circumferential backlash and moments of inertia can be seen as capacitance, and the frictional forces and viscous damping moments noted as active resistance. The equivalent system has a well-defined resonant frequency. If the attenuation within the system (as active resistance) is insufficient, electrical circuit overheating and even failure can occur during resonant oscillations.

A question comes to mind at this point – why did Mi-2 helicopters not experience resonant failures of their generator shafts? The answer is straightforward. The main reason is the mechanical coupling between their propulsion units and their main rotors. This moment of inertia of this rotor relative to the moment of inertia of other transmission chain elements is so high that it shifts the resonant frequency value towards extreme lows, far below the generator shaft frequency.

It was then employed to diagnose method one-way couplings in MiG-29 aircraft [80, 81, 83-86, 97, 129], wherein, primarily due to the incorrect operation of one-way couplings, certain engines also experienced dynamic twisting of their generator shafts [81, 84-87, 93, 94]. Based on these experiences, the first prototype semi-automatic pocket tester was developed in 1994. The SD-KSA system for diagnosing one-way couplings and hydraulic controller blocks of MiG-29 aircraft was implemented in 2001 [80, 97, 129].

For several years the FAM-C method has been employed to locate and determine the skew angle β and eccentricity a values of splined connections [129]. This enables detecting angle β change in the order of $0.1 \div 0.2^{o}$ [90, 104, 105, 124, 127, 131]. Splined connection skew is one of the more dangerous consequences of assembly defects. Point displacement of the spline edge interface area is experienced in this case. This causes heat to accumulate (due to sliding friction) and local contact stresses in the centre of the splines to appear. This leads to significant surface material loss [35, 41-43, 247]. $\beta = 1.5^{o}$ skew of the SGO-8 generator splined shaft results in a characteristic "barrel-shaped" material loss of the splines after 800 h of operation (according to experiments conducted under the author's direction that involved the LUZES-II propulsion unit). The effects are known to be much more dangerous – interrupted operation of the units, and even the entire gearbox. As

known, the gearbox transmits mechanical energy to, e.g., the hydraulic pump. And hydraulic pressure is essential for proper control over a modern aircraft, since otherwise it becomes uncontrollable or experiences mushing, which is often followed by a crash.

The FAM-C method was also applied to execute a series of tests covering electromechanical transducers [112, 115, 117, 129]. These involved controlled infliction of various faults, such as parallel rotor misalignment, skew and commutator brush suspension. In such investigation, analytical and partially practical work was undertaken regarding the application of transducer run-up for diagnostic purposes. At the time, the FDM-A approach started to be employed upon changing DC electrical engine operation from engine-based to generator-based. This enabled diagnosis of the state of transducer bearings.

Due to such successful application, testing of steady-state electromechanical transducers using the FAM-C method has become a permanent element of test programmes associated with extending military aircraft inter-overhaul service life.

For several years now, since the catastrophic rupture of the central bearing journal in the SO-3 engine of a TS-11 Iskra aircraft, the primary author of this tract has intensively studied the application of FAM-C and FDM-A methods to diagnose the technical condition of single-shaft engine bearing supports [113, 121, 129]. At the same time, as it were by the way, the author had to theoretically and practically delve into the numerous rolling bearing wear-related issues. The observations made with regard to these processes ongoing in engines diagnosed using the FAM-C and FDM-A methods are also included in this chapter.

Based on a trial-and-error method, the author selected numerous parameters obtained from onboard generator output voltages and grouped them in tables. Five diagnostic classes (levels) were developed: A – normal wear condition, B – increased wear condition, C – average wear condition, D – significant wear condition, E – very high wear condition. After reaching level E, in accordance with the recommendations, the engine is to be decommissioned from flights and usually subjected to a joint disassembly, combined with mechanical measurements.

Building upon the aforementioned observations, the author also developed a series of tribological wear models (4 basic types). Each model has different leading parameters and different inter-relations. Furthermore, it became apparent that after long-term observations using with the FAM-C and FDM-A methods that the tribological wear model undergoes changes throughout the service life due to wear-related processes.

In 2007, the author, located a damaged main rotor main bearing in the WR-24 reduction gear of a Mi-24 helicopter [7, 95, 98]. This was the first time that a kinematic link outside the direct power stream was diagnosed through FAM-C and FDM-A. All this because previously only the kinematic links between a mechanical

energy source (usually a gas turbine) and a generator-transducer had been diagnosed. Analytical and research work has also been commenced that focuses upon the possibility of diagnosing an entire helicopter transmission system designed by Mila and operated by the Polish Armed Forces, the Mi-24 in particular. The equity of these interests has been proven by a case of severe[2] helicopter failure (January 2011) [95]. The Air Accident Investigation Commission of the Ministry of Defence (including, among others, the author) identified damage within the transmission system power unit gearbox. Other measurement and diagnostic tests in Afghanistan identified a damaged swash plate bearing on one Mi-17 helicopter [98], while increased circumferential backlash of the synchroniser-actuator was indicated in another.

Numerous implementations of the FAM-C and FDM-A methods in relation to diagnostic measurements that involved the use of measurement-based systems have enabled presenting long- and short-term projections for specific propulsion units. It was found that the FAM-C and FDM-A parametric imaging methods (just like other TTM methods) can be relatively easily automated, diagnostic testers for certain propulsion units were developed under the guidance of the author.

5.2. Diagnostic systems and semi-automatic diagnostic testers for assessing the technical condition of aviation propulsion units

As mentioned in the introduction, the FAM-C and FDM-A methods synchronously process the diagnostic signal (angular velocity fluctuations in individual kinematic pairs of a tested propulsion unit) into a discrete-frequency system of characteristic sets. Such characteristic sets can be easily transposed into an electronic signalling system, and each of the characteristic sets reflects the dynamics of a different kinetic pair. Moreover, the position on the abscissa axis indicates the rated velocity of a given kinetic pair, which greatly simplifies their identification issues. Usually, at least several such sets can be observed simultaneously.

[2] Severe aircraft damage – damage resulting in the withdrawal of the entire aircraft structure from operation, caused by the extent of damage to the airframe.

5.2.1. SD-KSA diagnostic system and DIA-KSA-CM diagnostic tester for the propulsion unit of a MiG-29 aircraft

5.2.1.1. Technical description and operation of the DIA-KSA-CM diagnostic tester

Tester purpose

The DIA-KSA-CM diagnostic tester (similarly to the DIA-KSA-C prototype) is employed to determine the degree of wear of one-way couplings in KS2-A gearboxes and GP-21-3PS generator hydraulic blocks in MiG-29 aircraft. It is also used to conduct single-phase measurement of the frequency modulation of the GŻ-30 onboard power generator output voltage [80, 81, 83, 84, 87, 129]. The tester is distinguished by its ergonomics and simple operation – even with winter gloves on (Fig. 5.2). The initial test result (measurement of individual characteristic set heights) is displayed after a one-minute test. At this stage, the tester acts as a digital measuring instrument.

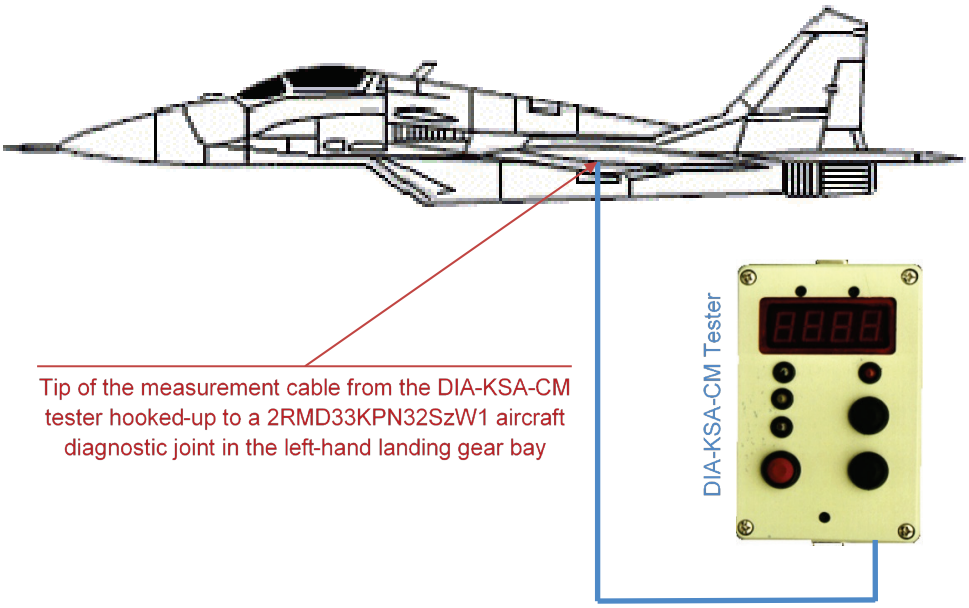

Fig. 5.1. Manner of connecting the DIA-KSA-CM diagnostic tester to a Mi-G29 aircraft

Fig. 5.2. Operation of the DIA-KSA-CM diagnostic tester during a test at an airfield

Test result application

After every 50÷100 measurements, the tester should be hooked up to the squadron data base (pursuant to the "Technical description, operation and maintenance manual of the SD-KSA system for diagnosing one-way couplings and hydraulic controller blocks of MiG-29 aircraft", Warsaw 2000) to transfer the information contained in the internal memory to the EbD-KSA squadron data base. The internal storage capacity of the diagnostic tester is 100 entries. To facilitate monitoring the internal memory filling, upon completing 50 tests, after powering up (prior to the next test), the screen will display double lines (= = = =**),** and after 75 tests – triple lines **(**≡≡≡≡). It will also display a "FULL" message after 100 tests. These markers disappear after copying the information saved in the internal memory of the tester to the squadron's database system.

5.2.1.2. Description of the SD-KSA diagnostic system

Purpose of the SD-KSA system

The SD-KSA diagnostic system is intended for diagnosing one-way couplings and hydraulic controller blocks of a MiG-29 aircraft based on data from DIA-KSA-CM diagnostic testers (themselves being an integral part of the system). The system is tasked with providing data to the aircraft technical personnel to enable predicting the occurrence of failure conditions associated with the aforementioned aircraft components (Fig. 5.3). The SD-KSA system enables collecting data for the "SAN" computer-aided aircraft reliability analysis system.

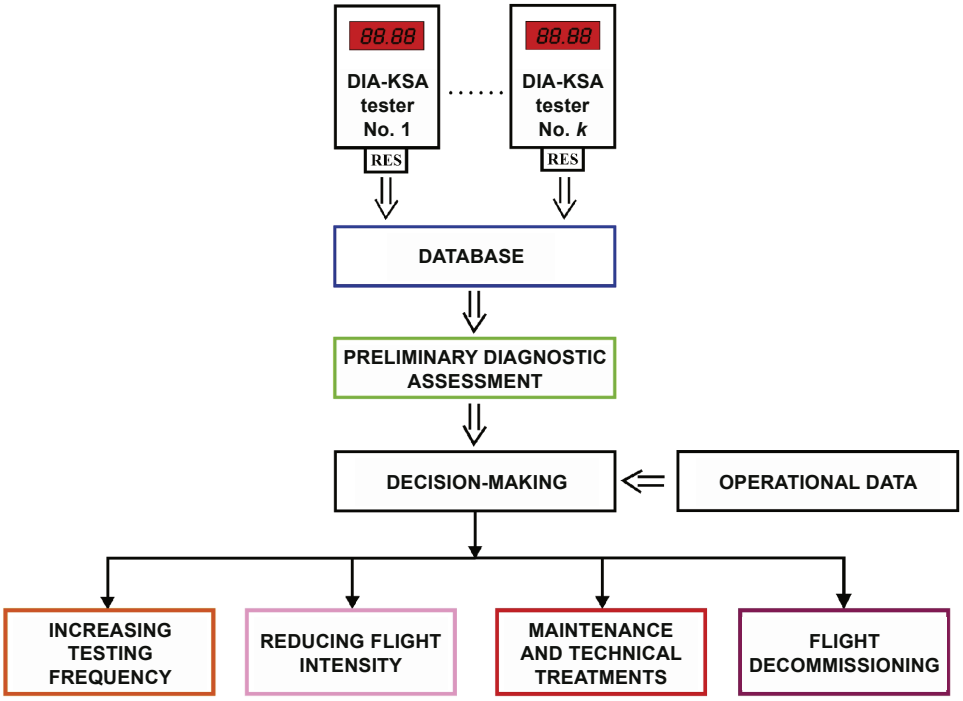

Fig. 5.3. SD-KSA diagnostic system

Design and operation of the SD-KSA system

The SD-KSA diagnostic system [80, 81, 83, 84, 125, 168] consists of four data acquisition and processing levels:

1) direct acquisition of data on the wear of the KSA-2 gearbox one-way couplings and the hydraulic block of the GP-21-3PS power unit in MiG-29 aircraft;
2) preliminary processing of data at the air squadron;

3) collective records of wear and tear of the aforementioned MiG-29 aircraft components in the engineering and aviation section of an air regiment;
4) making logistic and diagnostic decisions:
   - to increase testing frequency,
   - to decrease flight intensity,
   - maintenance and technical procedures, such as bleeding the GP-21-3PS block or ordering manual start-ups beginning with the left engine – by default, start-ups are conducted automatically, beginning with the right engine; after the right engine is started, the left engine is driven by gas-dynamic power, without loading the one-way coupling – hence, the right one-way coupling is protected, since a running engine transmits the starting torque to the other engine in a gas-dynamic manner, i.e., bypassing the one-way coupling,
   - to decommission from flights to release the damaged component for an overhaul.

The SD-KSA system contains two databases:
- EbD-KSA database at air squadron level,
- BD-KSA database at air regiment engineer level.

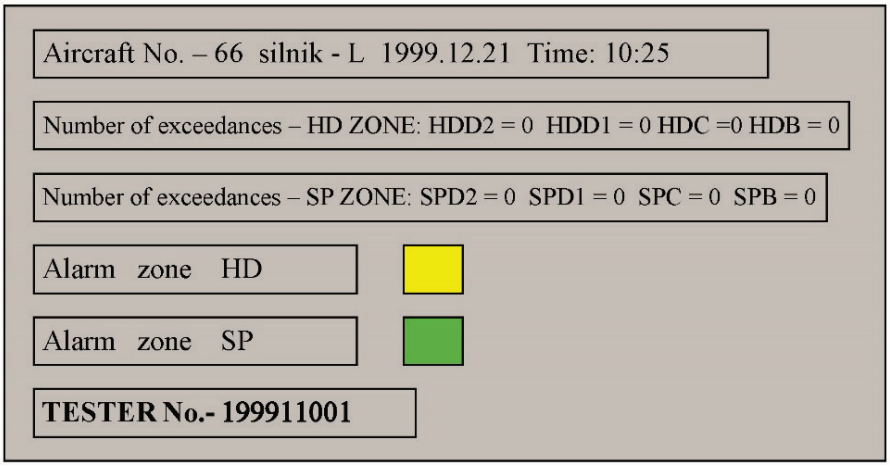

Fig. 5.4. Sample view of the edition window for all measurements previously conducted with the DIA-KSA-CM on an AC with determined exceeded values in individual zones

Wear trends within individual propulsion unit components are observed at squadron level as a function of flight hours, individually for each aircraft. This enables pre-developing maintenance and technical measures. The squadron engineer is thus able to react in the event of abnormal wear acceleration as a function of

flight hours (Figs. 5.4 and 5.5). Bar charts that comprehensively collate the parameters of all aircraft are preferred in the database at the air regiment engineer level. This allows to rapidly pre-determine the number of aircraft for flight planning purposes. Moreover, the wear information is transferred from level 3 (the regiment engineering and aviation section) to the SAN aircraft reliability analysis system, which is a centralized national database of military aircraft failures. Each level has specific equipment assigned to it. These are, respectively, for each data acquisition and processing level for a given MU, and are:

a) 2 to 4 complete DIA-KSA-CM testers;
b) 1 to 3 (depending on the organisational system of the military unit) squadron EbD-KSA databases installed on PCs;
c) 1 BD-KSA database installed on a PC.

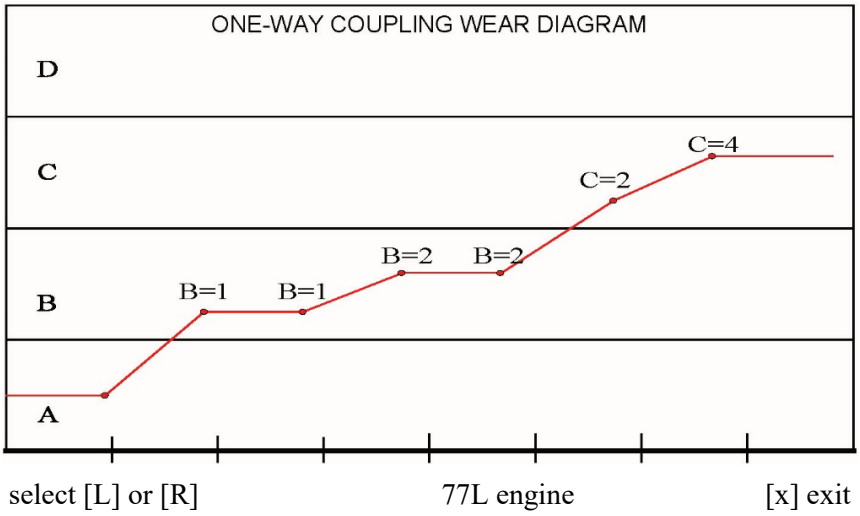

Fig. 5.5. Example of a one-way coupling wear chart in a squadron database

5.2.2. DIA-SO3 diagnostic tester for the propulsion unit of a TS-11 Iskra aircraft

5.2.2.1. Operation algorithm of a DIA-SO3 diagnostic tester

The tester has two measurement chains within its structure:

– DC current using the pulsation component of the TS-11 Iskra aircraft DC generator,
– AC current, using the tach generator voltage.

These measurement paths are analogue, just like in the classic FDM-A and FAM-C computer measurement systems. Thus, first the counting of the time base clock pulses between zero level crossings in both measuring paths takes place and the images $\Delta F = f(f_p)$ and $f_i = f(t)$ are automatically determined, without their external visualisation. Next, the 27 parameters are calculated in semi-automatic mode based on the information contained in these images. The tester will soon also offer logical functions that a diagnostician would so far implement based on his/her knowledge, and partially on intuition and experience [114]. The tester will only execute short-term predictions (up to 25 flight hours), as well as logical functions such as:

- tested engine bearing support wear type recognition,
- diagnostic classification – further operation proposal; the tester indicating an unacceptable level will require verification with the FAM-C and FDM-A computer diagnostic instrumentation.

It would be best if a separate tester is allocated to each engine starting from the first trial at the test house, through operation at an airfield, until the next overhaul. Such a proposal is based on the observation of long-term parameter changes throughout engine operation. Plenty of valuable parameter-related information is included in the measurement parameters obtained during the first hours of an engine's "service life". If it were possible to monitor engine parameters from the very moment of its production, both the wear model type recognition and diagnostic classification would be more reliable. In terms of the diagnostic process, the tester should implement the following steps:

a) measurement of successive time increments between consecutive crossings through the "zero" level within the AC and DC measurement channels for seven rated rotational speeds – development of pulse bundle sets corresponding to successive time increments; these sets are archived by the tester's internal memory;
b) measurement of the run-up time; its value should be archived;
c) wear model type recognition (Figs. 5.6÷5.9 and 5.11); model types should be displayed on the tester's control panel and archived in its internal memory;
d) development of a short-term forecast for the tested engine – comparison of parameters characteristic for a given diagnostic level with benchmark parameter levels; diagnostic levels are prompted on the tester's control panel by coloured LEDs (LEDs: continuously illuminated green, flashing green, continuous yellow, flashing yellow, continuous red, and flashing) (Fig. 5.12).

It is advisable for the tester to display subsequent instructions for an aircraft technician with briefly expressed names of the consecutive actions.

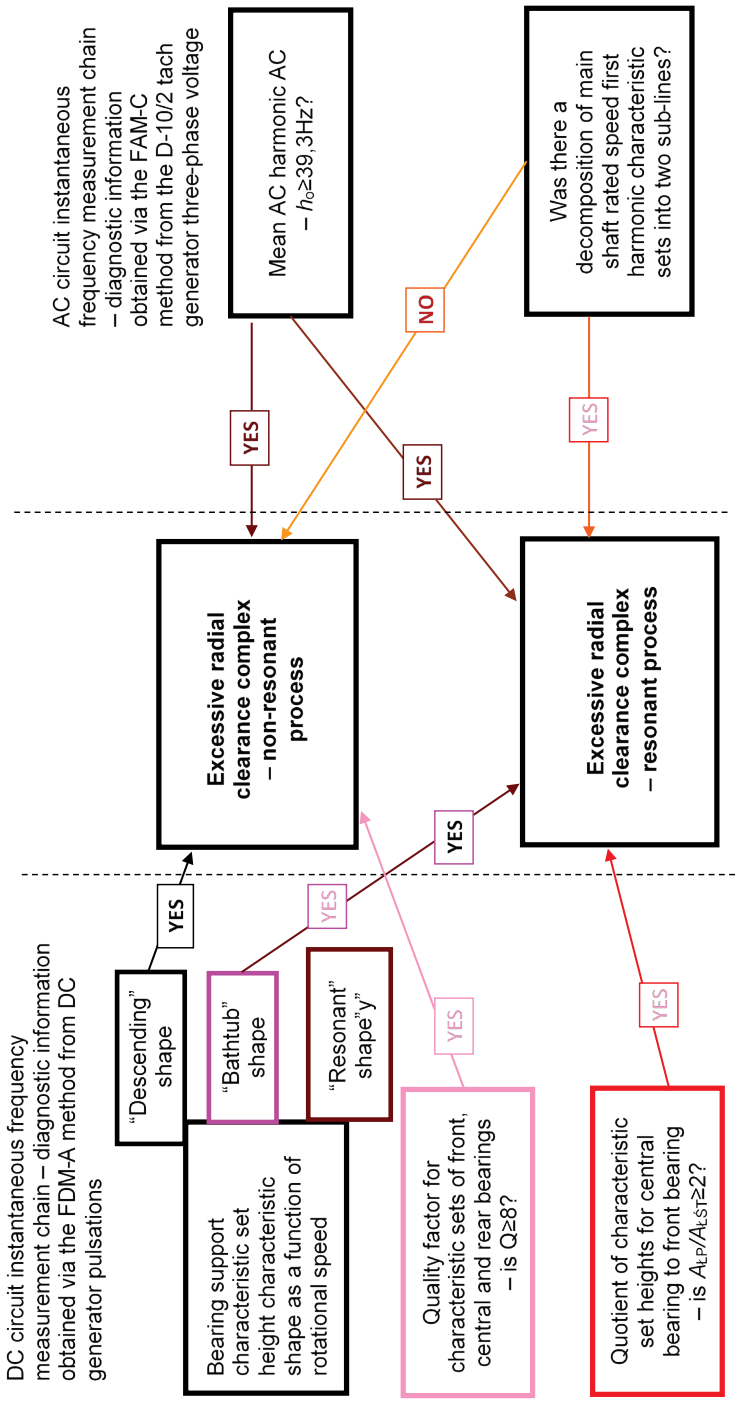

Fig. 5.6. Block diagram of a field tester for short-term diagnosis of SO-3/3W engine bearing supports – mechanical wear process type recognition function – part 1. Identification of an excessive radial clearance model

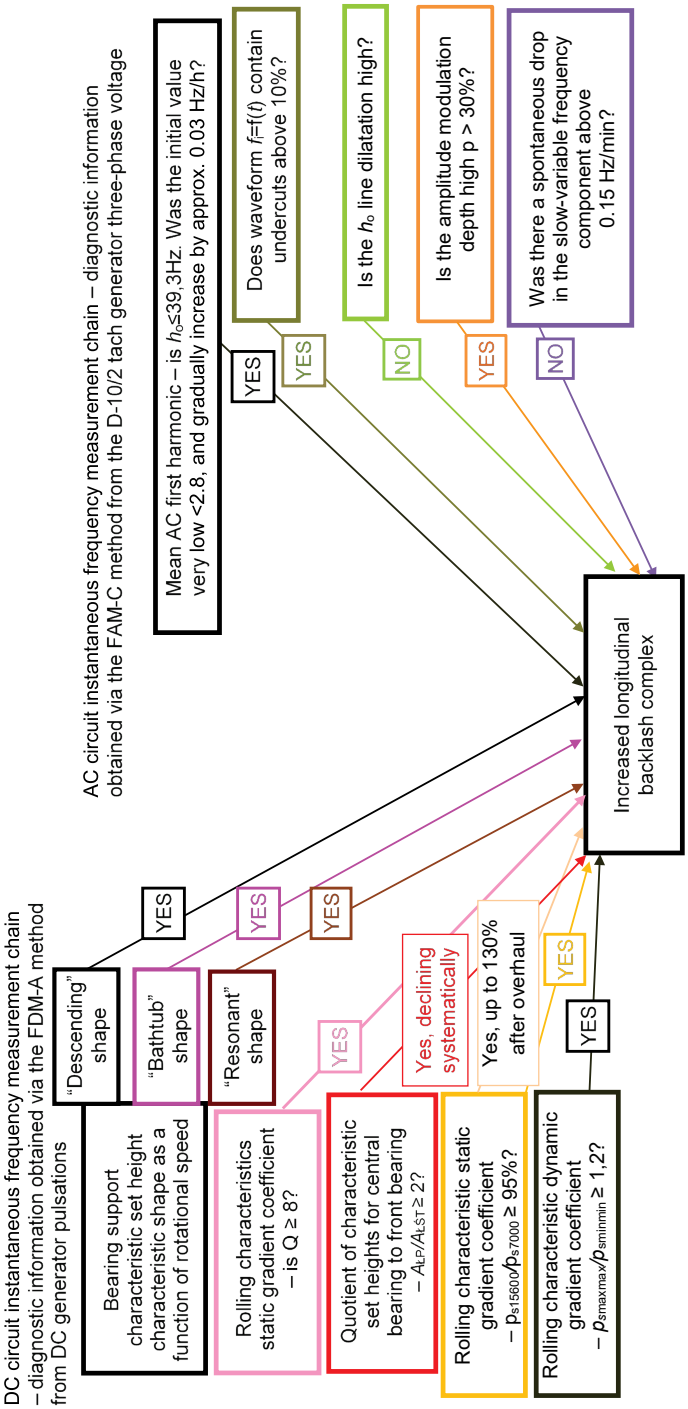

Fig. 5.7. Block diagram of a field tester for short-term diagnosis of SO-3/3W engine bearing supports – mechanical wear process type recognition function – part 2. Identification of an increased longitudinal clearance model

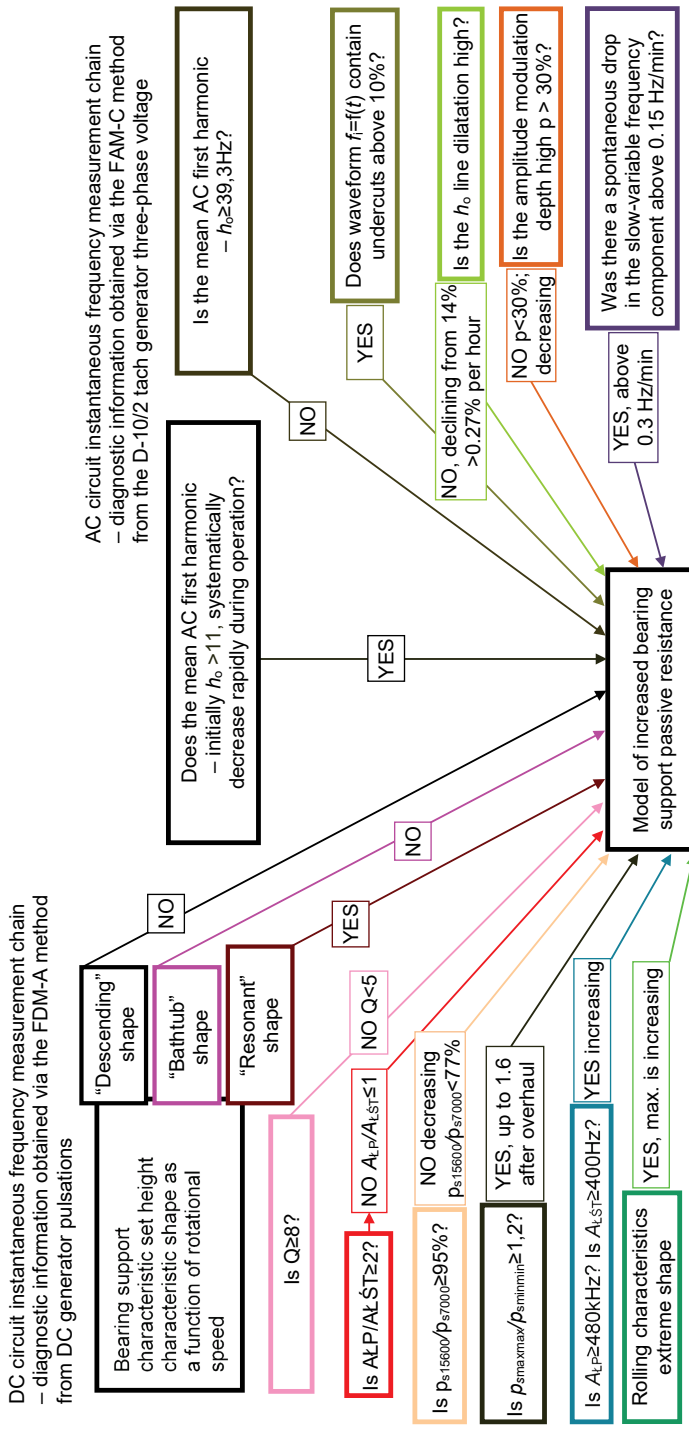

Fig. 5.8. Block diagram of a field tester for short-term diagnosis of SO-3/3W engine bearing supports – mechanical wear process type recognition function – part 3. Identification of an increased bearing support passive resistance model

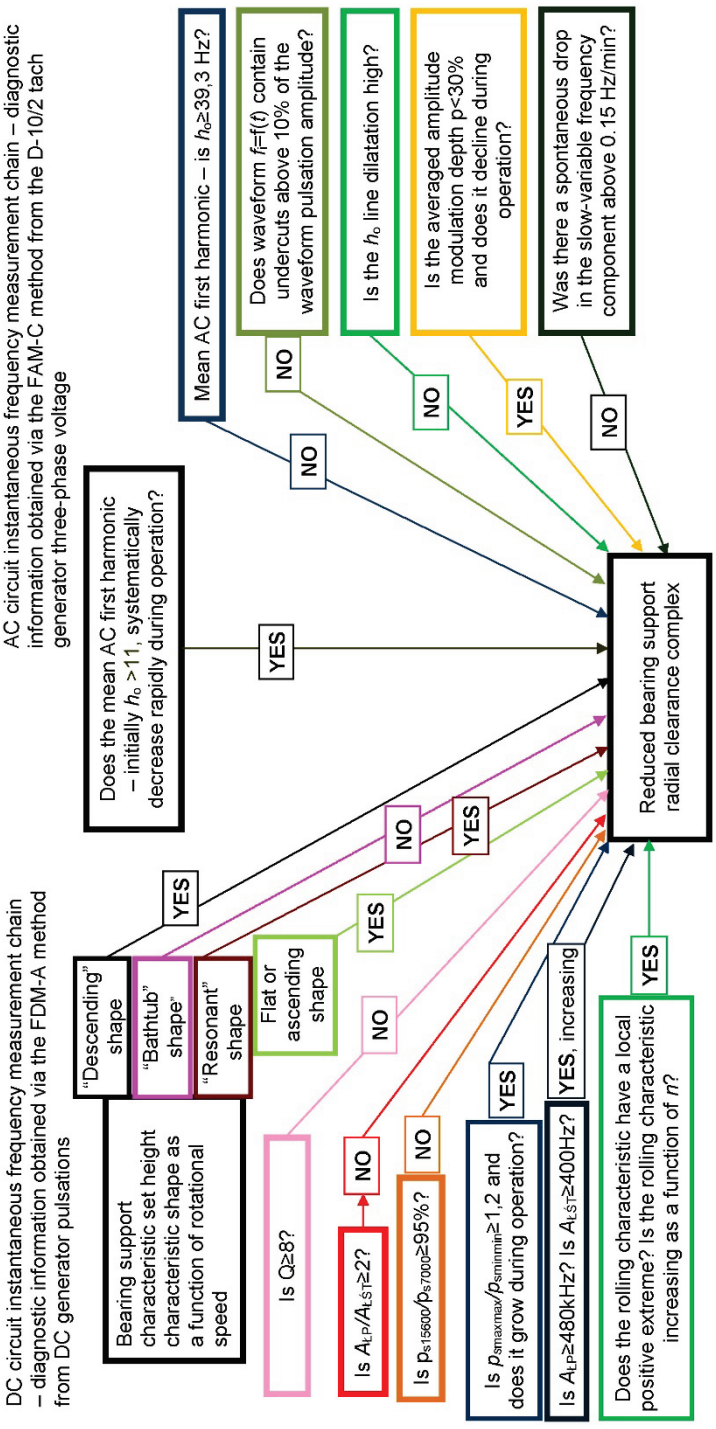

Fig. 5.9. Block diagram of a field tester for short-term diagnosis of SO-3/3W engine bearing supports – mechanical wear process type recognition function – part 4. Identification of a reduced bearing support radial clearance model

5.2.2.2. Tester tribological process recognition algorithm

The design of the tribological process recognition algorithm needed to automate the procedure of working out a diagnostic decision by a short-term tester is shown in Figs. 5.6÷5.9 [114]. Two parallel measurement chains were applied within a single device: the GSR-ST-6000WT DC generator chain and the track of the D-2/10 tach generator chain. The automatic processing of voltage signals is slightly different than the manual method without a diagnostic tester. However, new functional blocks introduce automatic wear model type recognition. Until recently, a diagnostician implemented this in the case of the classic laboratory and computer-aided testing form based on own operational experience. It is now executed by the tester (Fig. 5.11). To enable this, the criteria for recognising a tribological model had to be reduced to simple and unambiguous mathematical relationships [114]:

1. Model of excessive radial clearances with central bearing resonance

The properties of rolling bearings with excessive radial clearances and their mechanical resonance have been discussed in [15, 18, 73, 160, 176, 197, 244, 245, 216, 303]. Together with a group of colleagues, the author conducted original research in this area [114, 123, 129, 136]. These experiments allowed to parametrically capture the features of a bearing node model with excessive radial clearances via:

a) DC measuring channel characteristic set quality factor: limit value $Q \geq 8$ (unacceptable value $Q \geq 11.00$).
b) In the AC channel, the instantaneous frequency waveform as a function of time – the number of individual spike pulses in the $\Delta t = 2$ s time window with an amplitude above 200 Hz: limit value is 12 pulses, unacceptable value ≥ 24 pulses.
c) In the AC channel, the instantaneous frequency waveform as a function of time – the number of spike pulses with a repetition period (group) every single main shaft revolution, in the $\Delta t = 2$ s time window, with an amplitude above 200 Hz: limit value is 1 pulse, unacceptable value ≥2 pulses.
d) Averaged maximum duration of DC channel fade pulses (rupture angles) exceeding the limit value $\varphi_{max} \geq 235^{o}$ (unacceptable rupture angle $\varphi_{max} \geq 365^{o}$).
e) Value averaged from the quotient of the maximum duration of the DC channel fade pulses (rupture angles) and the number of revolutions between pulses $^{\Delta\varphi_{max}}/_{\Delta n} \geq 50^{o}$/rev (unacceptable value $^{\Delta\varphi_{max}}/_{\Delta n} \geq 60^{o}$/rev).

1a. Model of excessive radial clearances with central bearing resonance

a) Average value of the AC measurement chain first harmonic: limit value $h_o \geq 39.3$ Hz (unacceptable value $h_o \geq 52.4$).

b) Averaged maximum duration of DC channel fade pulses (rupture angles) exceeding the limit value $\varphi_{max} < 150^{o}$ (unacceptable rupture angle $\varphi_{max} \geq 365^{o}$).
c) Value averaged from the quotient of the maximum duration of the DC channel fade pulses (rupture angles) and the number of revolutions between pulses; limit value $^{\Delta\varphi_{max}}/_{\Delta n} < 30^{o}$/rev (unacceptable value $^{\Delta\varphi_{max}}/_{\Delta n} \geq 60^{o}$/rev).

2. Model of dynamic forces causing longitudinal motion of the engine rotor unit

a) After an overhaul, the values of the mechanical quality factor for all bearing supports reach a very high level of $Q \geq 13$, followed by a rapid decrease to $Q \geq 4$ within 20 h of engine operation, after which it steadily increases [273, 274]; upon reaching $Q \geq 11$ for all bearing supports or $Q \geq 13$ for any given bearing support, the engine must be decommissioned.
b) The value of the rolling characteristic static inclination coefficient is virtually always stable at a level of $^{p_s 15600}/_{p_{s7000}} \geq 95\%$ (unacceptable value for an engine under operation is $^{p_s 15600}/_{p_{s7000}} \geq 137\%$).
c) Deep undercuts on the slopes of significant depth (deviation from sine wave shape ranging from 10% to several percent).
d) The first harmonic amplitude after an overhaul increases steadily from a low of $h_o \geq 2.8$ by about 0.03 Hz/h; upon reaching $h_o \geq 52.4$ Hz, the engine should be decommissioned.
e) Averaged maximum duration of DC channel fade pulses (rupture angles) exceeding $\varphi_{max} \geq 150^{o}$ (unacceptable rupture angle $\varphi_{max} \geq 365^{o}$).
f) Value averaged from the quotient of the maximum duration of the DC channel fade pulses (rupture angles) and the number of revolutions between pulses $^{\Delta\varphi max}/_{\Delta n} \geq 30^{o}$//rev (unacceptable value $^{\Delta\varphi max}/_{\Delta n} \geq 60^{o}$/rev).

3. Model of increased passive resistance

a) Height of the front bearing DC channel characteristic set $\Delta F = f(f_p)$ after averaging: total front bearing $A_{śrŁP} \geq 480$Hz (unacceptable value $A_{śrŁP} \geq 2160$ kHz).
Height of the central and rear bearing DC channel characteristic set $\Delta F = f(f_p)$ after averaging: total front bearing resistance $A_{śrŚT} \geq 400$ (unacceptable value $A_{śrŚT} \geq 1800$ kHz).
b) Run-up duration reduced below $t_{dob} < 90$ s.
c) Spontaneous rotational speed deceleration – extreme change in the slow-variable component amplitude to the mean value $f_{śr}$ within the time window automatically implemented by the FAM-C method (2÷4 minutes) for $n = 7000$ rpm: $\Delta n_{w7000} \geq 1.4$ Hz (unacceptable value is $\Delta n_{w7000} \geq 3$ Hz).

d) Spontaneous rotational speed deceleration – extreme change in the slow-variable component amplitude to the mean value $f_{śrw}$ within the time window automatically implemented by the FAM-C method (2÷4 minutes) for n = 15600 rpm: $\Delta n_{w15600} \geq 0.3$ Hz (unacceptable value is $\Delta n_{w15600} \geq 0.6$ Hz).
e) Averaged maximum duration of DC channel fade pulses (rupture angles) exceeds $\varphi_{max} < 150^o$ (unacceptable rupture angle $\varphi_{max} \geq 365^o$).
f) Value averaged from the quotient of the maximum duration of the DC channel fade pulses (rupture angles) and the number of revolutions between pulses $^{\Delta\varphi max}/_{\Delta n} < 30^o$//rev (unacceptable value $^{\Delta\varphi max}/_{\Delta n} \geq 60^o$/rev).

4. Model of rolling elements clamped between races

a) Changes in the rolling coefficient mean value $p_{śr}$ for the maximum speed per flight hour $\delta_{ps15600} \leq -15\%$/h (unacceptable value $\delta_{ps15600} \leq -18\%$/h).
b) The rolling characteristic static inclination coefficient $^{p_{s15600}}/_{p_{s7000}} \geq 85\%$ (unacceptable value for an engine in operation $^{p_{s15600}}/_{p_{s7000}} \geq 107\%$; value is acceptable only during a controlled run-in period).
c) The rolling characteristic dynamic inclination coefficient $^{p_{smaxmax}}/_{p_{sminmin}} \geq 2$ (unacceptable value $^{p_{smaxmax}}/_{p_{sminmin}} \geq 3.0$).
d) Increasing "tip" of the rolling characteristic $p_s = f(n)$, i.e., $p_{s15600}/\ p_{s15100} > 100\%$ (usually observed after the first run-in period).
e) Averaged maximum duration of DC channel fade pulses (rupture angles) exceeds $\varphi max < 150^o$ (unacceptable rupture angle $\varphi max \geq 365^o$).
f) Value averaged from the quotient of the maximum duration of the DC channel fade pulses (rupture angles) and the number of revolutions between pulses $^{\Delta\varphi max}/_{\Delta n} < 30^o$//rev (unacceptable value $^{\Delta\varphi max}/_{\Delta n} \geq 60^o$/rev).

A diagnostic assessment of the SO-3/3W engine technical condition in terms of bearing support fitness is possible only upon a clear identification of the tribological model type. The increase of a given parameter (or rather a group of parameters) is of a totally different significance in the case of each wear model type. Therefore, displaying (one of the coloured LEDs) information on assigning a bearing support technical condition to one of the four diagnostic classes (A÷D) is possible only after the tribological process type is determined. Short-term safe operation forecast and preventive measure suggestions are also associated with the diagnostic class.

5.2.2.3. DIA-SO3 diagnostic tester structural description

In general, the tester is a compact and miniaturized version of the previously used computer-based FAM-C and FDM-A derived measurement apparatuses. It is employed to determine the current condition of bearing supports in SO-3/3W engines. Two measurement channels can be distinguished therein (Fig. 6.81÷114):

a) measurements in the DC channel - measurement of the GSR-ST-6000WT DC generator output voltage pulsation component FM parameters,
b) measurements in the AC channel - measurement of D-10/2 tach generator output voltage FM parameters.

Locations for hooking-up the tester measurement system to the electrical system of the TS-11 Iskra aircraft are presented in Fig. 5.10 and 5.13. Each of the measuring channels will consist of blocks proven and tested within the existing (laboratory and computer-aided) measuring set-up, such as:

a) input voltage signal standardisation block;
b) block for measuring the time increments between successive crossings of the input voltage waveform $u = f(t)$ through the reference level (successive period or half-period duration calculation block), Fig. 5.10;
c) image formation blocks:
   – instantaneous frequency waveform $f_i = f(t)$,
   – characteristic sets on plane $\Delta F = f(f_p)$;
d) blocks for calculating 27 measurable parameters based on images: $f_i = f(t)$, $\Delta F = f(f_p)$, Fig. 5.11;
e) blocks comparing measured values (27 quantifiable parameters) with limit levels – determination of the wear class for each parameter, Fig. 5.11;
f) diagnostic decision blocks, Fig. 5.11:
   – weighting function blocks,
   – wear model type classification determination block;
g) internal memory block – for storage of:
   – measurement data (“.pom.” extensions),
   – diagnostic process results;
h) luminous elements – indicators:
   – individual bearing support wear model type display, Fig. 5.12,
   – bearing support wear level indication, Fig. 5.12;
i) blocks of developing diagnostic forecast for a particular wear model – block of comparison of the parameters selected for a given model and the relations obtained based on measurements with benchmark levels and relationships, Fig. 5.11.

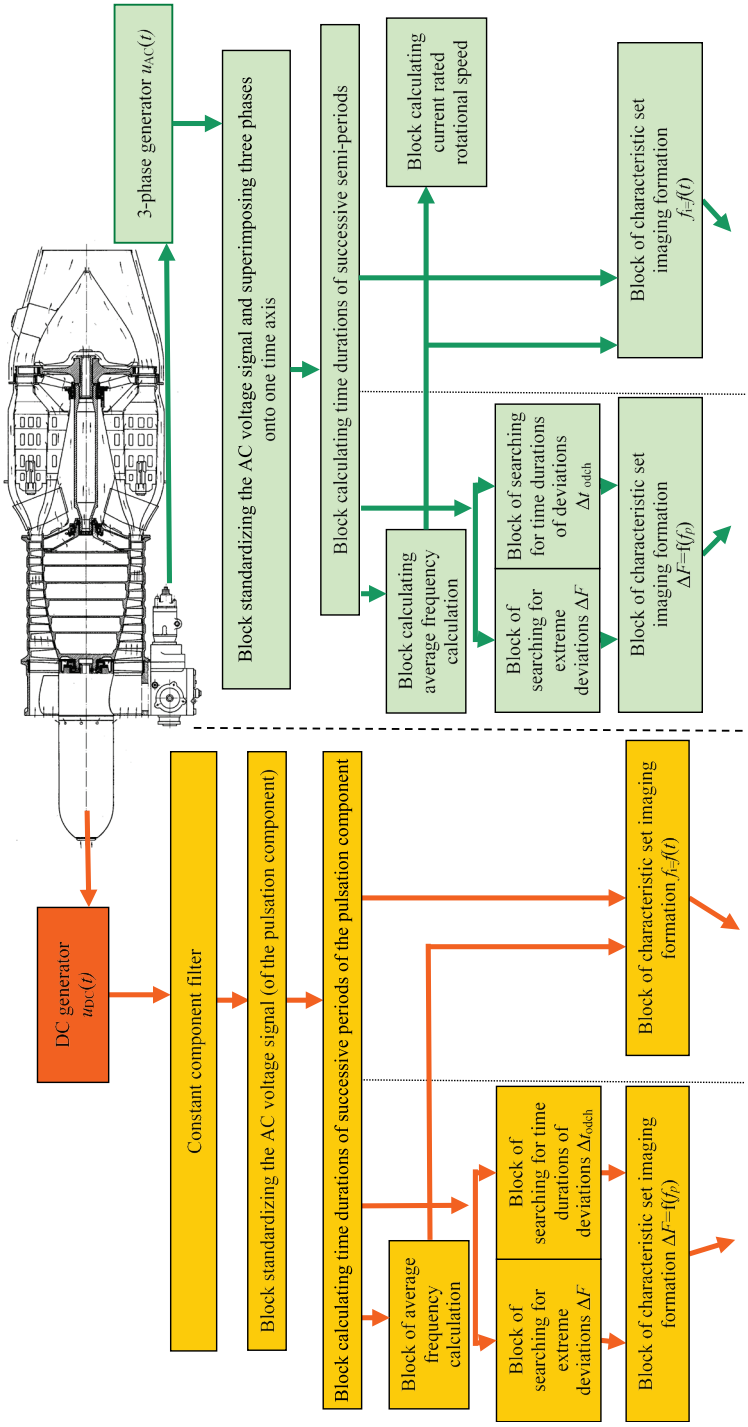

Fig. 5.10. Logic structure block diagram of a field tester for short-term diagnosis of SO-3/3W engine bearing supports – part. 1. Formation of characteristic sets and time waveforms

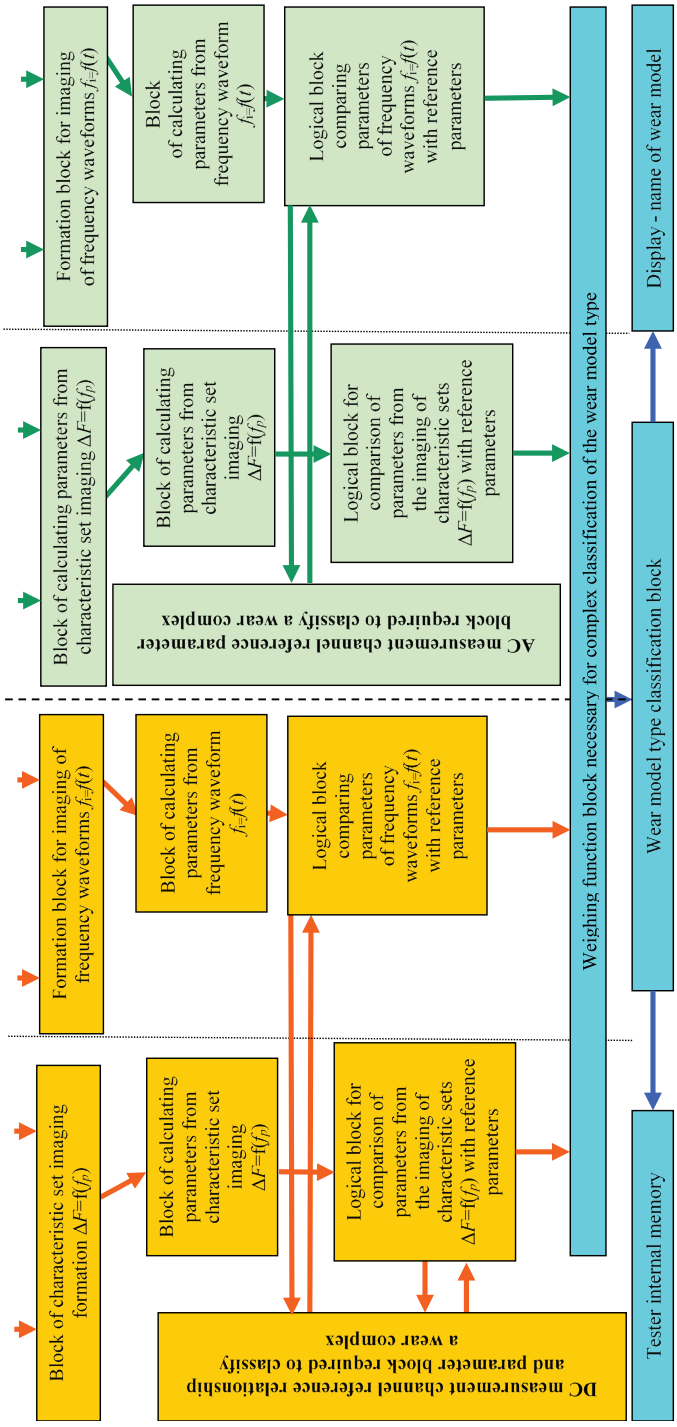

Fig. 5.11. Logic structure block diagram of a field tester for short-term diagnosis of SO-3/3W engine bearing supports – part. 2. Wear model type determination

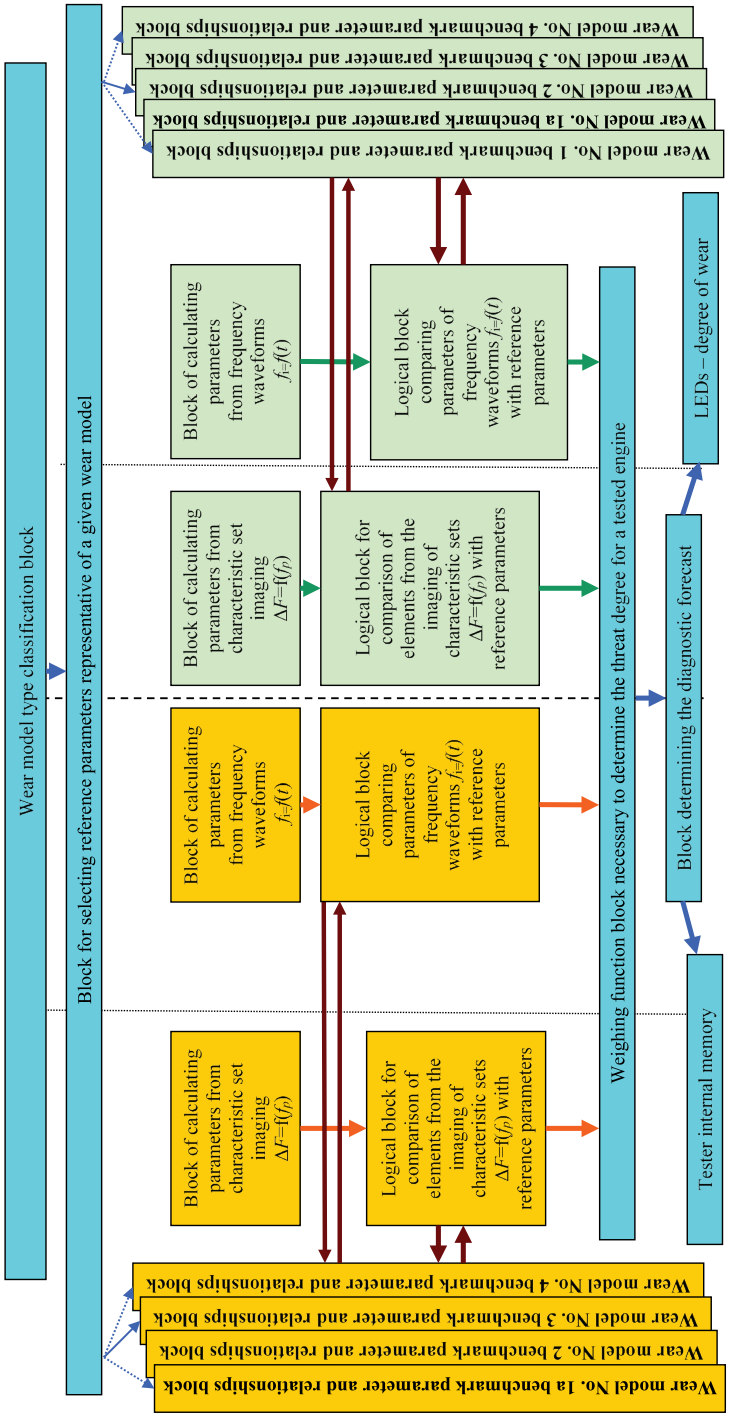

Fig. 5.12. Logic structure block diagram of a field tester for short-term diagnosis of SO-3/3W engine bearing supports – part. 3. Drawing up a diagnostic prediction

Fig. 5.13. TS-11 Iskra aircraft with a connected DIA-SO3 diagnostic tester: 1 – diagnostic tester DIA-SO3, 2 – 28V DC socket (nose cone part of the fuselage) – tie-in location for a DC measurement channel of the DIA-SO3 tester circuit, 2a – electrical cable connecting the 28V socket and the tester, 3 – tachometer connector (dashboard in the second cabin) – tie-in location of the AC measurement channel (three-phase) to the DIA-SO3 tester, 3a – electrical cable connecting the tachometer connector with the tester

5.3. Monitoring military aircraft propulsion units at airfields

5.3.1. Detecting a damaged bearing in the Mi-24 helicopter main rotor shaft using the FAM-C method

Fig. 5.14 shows the instantaneous frequency waveform for a properly operating rolling bearing, while Fig. 5.15 shows a defective one. That shown in Fig. 5.15 is that of a negative standard waveform of a WR-24 main transmission upper bearing. The displayed waveforms were obtained through measurements involving two Mi-24 helicopters [7, 95, 99]. Here, for the positive standard, 13 distinct fluctuations are apparent per four revolutions of the main engine can be seen on the positive benchmark. Therefore, according to [95], it is possible to calculate the current value of the rolling coefficient $p_s = 13/(4 \cdot 16) = 0.203$ (where the number of main transmission upper bearing rolling elements $N = 16$). Design data [7, 95, 98, 99] enable calculating the current rolling coefficient value (for an "ideal" bearing) $p_{sN} = 0.355$. Thus, the WR-24 main shaft upper bearing rotates lighter than an "ideal" bearing. This is probably due to the (positive) action of vibrations and hydro-mechanical forces generated by the lubricating oil film and the optimum backlash

level. This type of a relationship was encountered in certain bearings of the TS-11 Iskra aircraft engine supports [114, 136]. With regard to the negative standard, 51 oscillations are observed per four revolutions (approx. 1 s) of the main shaft. It is therefore possible to calculate the value of the current rolling coefficient $p_s = 51/(4 \cdot 16) = 0.799$. This is twice the rated value of the coefficient. The operation of such a bearing must be evaluated as being very extreme.

Additional information on the wear-related load of the entire mechanical power transmission unit was provided by the instantaneous frequency waveform for an observation period extended to 140 s. The waveform for the positive standard is stable (Fig. 5.16). For the negative benchmark, periods of monotonic decline in the instantaneous frequency (read: rotational speed) by 1.4% are evident (Fig. 5.17). Based on the experience gained in the course of diagnosing the bearing nodes of TS-11 Iskra engines [99, 114, 118, 120, 123, 136, 266], this indicates a complex bearing node degradation.

The damaged WR-24 negative standard transmission was verified at the disassembly stage. A significant level of wear was confirmed in the WR-24 transmission (Figs. 5.18 and 5.19) [99].

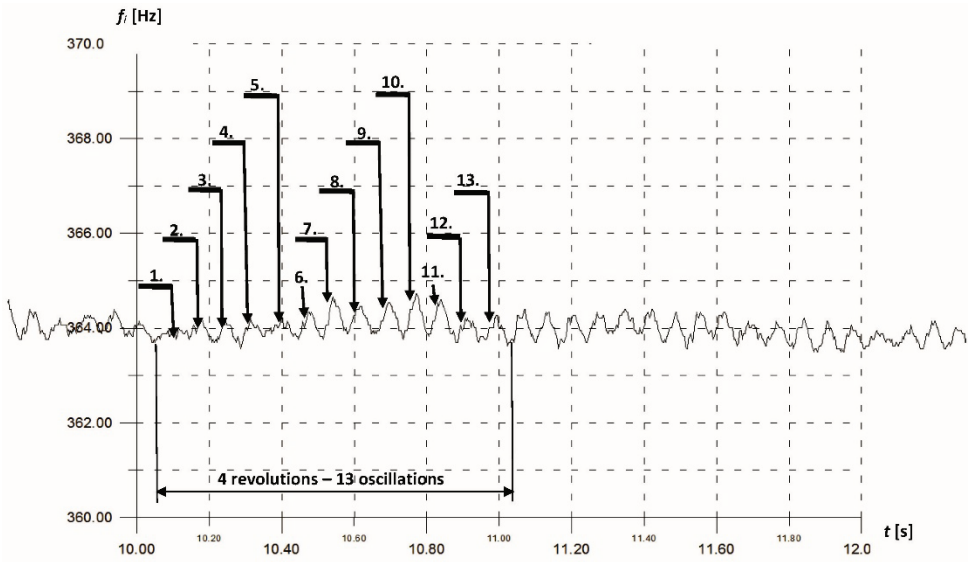

Fig. 5.14. Mi-24 No. 65 left-engine instantaneous frequency change waveform – positive standard

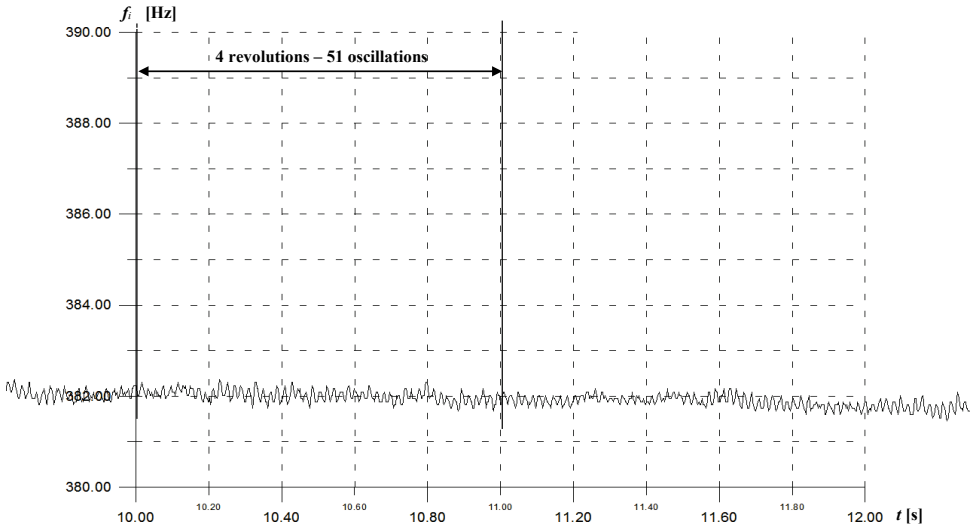

Fig. 5.15. Mi-24 No. 84 left-engine instantaneous frequency change waveform – measurement No. 3 – positive standard

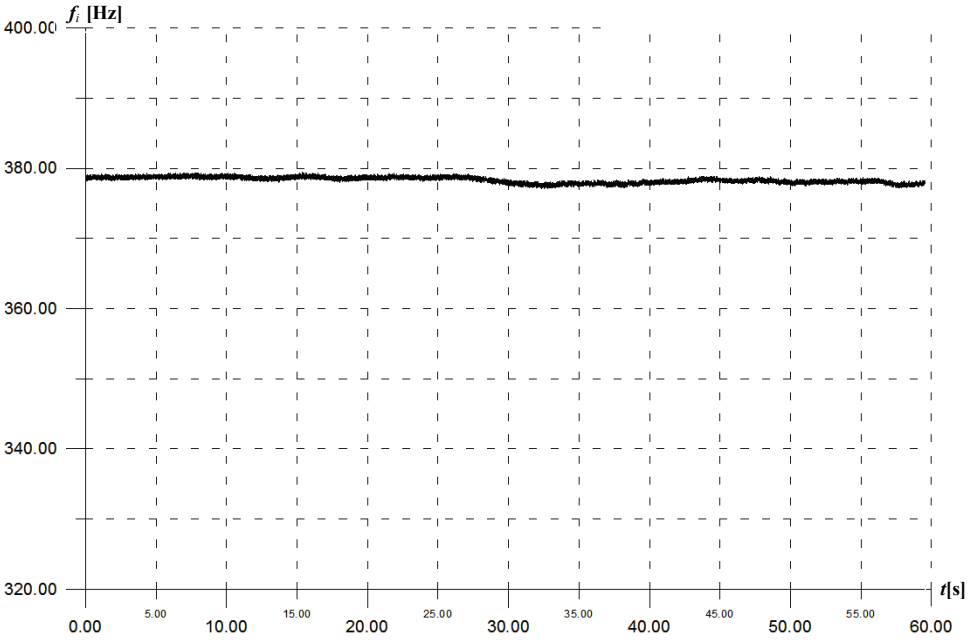

Fig. 5.16. Mi-24 No. 65 right-engine instantaneous frequency change waveform – positive standard

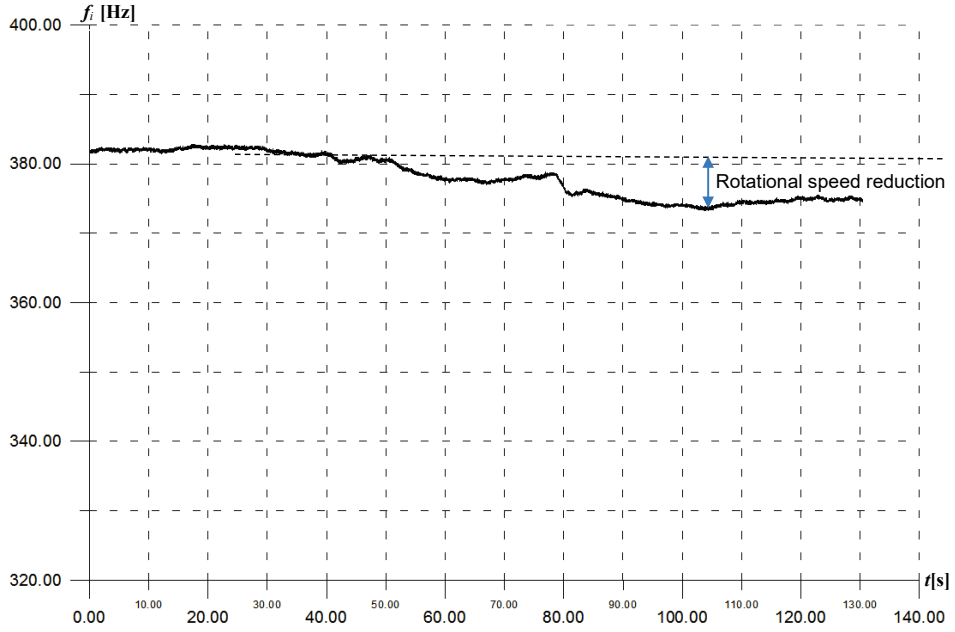

Fig. 5.17. Mi-24 No. 84 right-engine instantaneous frequency change waveform – negative standard

Fig. 5.18. Inner ring of the upper (main) bearing from the negative standard WR-24 main transmission gear: 1 – inner race flaking

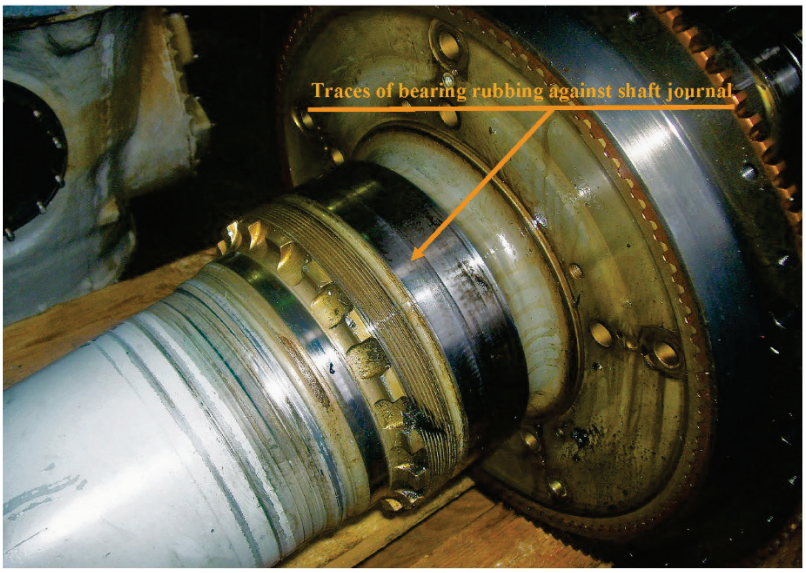

Fig. 5.19. Bearing seat of the negative standard WR-24 main transmission upper bearing

5.3.2. Diagnosing the Mi-24 generator gearbox

In the previous section, the generator gearbox (formally known as the power unit gearbox) was only one of several components transmitting the rotational motion from the WR-24 main transmission to the GT-40PCz6 generator-transducer. At the same time, continuous transmission of angular velocity between the monitored main bearing of the WR-24 transmission and the generator-transducer was assumed. A single-phase measurement of the GT-40PCz6 generator output voltage (115 V, 400 Hz) was applied in this case. The resolution of the FAM-C measurement (observability window) based on this measurement set-up is limited to relatively low mechanical primary frequencies. It is "perfect" for monitoring low-speed bearings (such as the Mi-24 helicopter main bearing, where $n = 4$ rpm, 15 rolling elements), but far from sufficient to assess the magnitude of inter-tooth backlash (small values by assumption, reaching 0.03÷0.05 of the gear wheel modulus) or observing the condition of high-speed rolling bearings. Indeed, the initial calculations [95, 98] show that the resolution of the single-phase FAM-C measurement of the generator-observer output voltage is too low. In this study, the generator gearbox will be perceived as a discontinuous mechanical model. Amongst other issues, the inter-tooth backlash in the generator gearbox will be observed herein. To this end, the author employed a three-phase measurement configuration of the FAM-C measurement, connecting not to the output terminals of the generator, but to the GT-40PCz6 generator internal excitation terminals, i.e., the so-called "exciter" (with a rated frequency of 800 Hz) [95, 98].

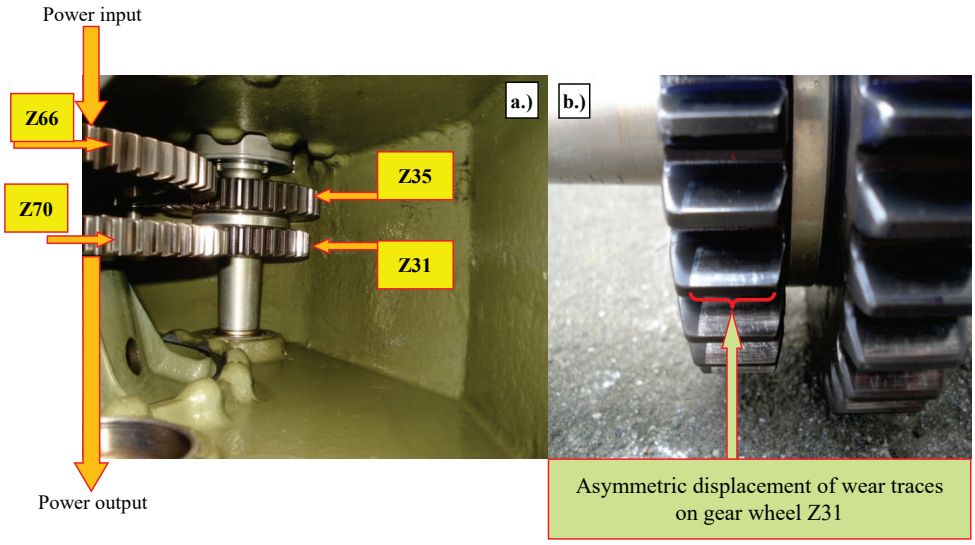

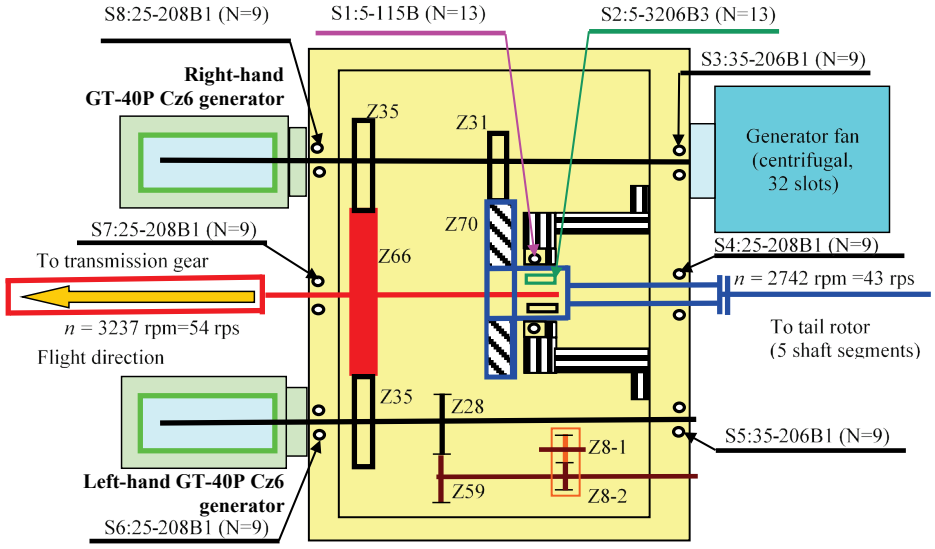

Fig. 5.20. Schematic diagram of the generator gearbox: Z66 – gear wheel powering the box, Z35 – gear wheel powering the generator, Z31 – gear wheel powering the tail rotor mechanical power transmission unit, Z70 – gear wheel associated with the tail rotor mechanical power transmission system, a) inside view of the gearbox – visible gear wheels, b) z31 gear wheel magnified, S1÷S8 – rolling bearings, N – number of rolling elements in the bearing

When analysing Fig. 5.20, it can be seen that the mechanical power input to the generator gearbox is routed from the WR-24 main transmission via a shaft. The active gear wheel in the generator gearbox is Z66, which symmetrically powers two Z35 passive gear wheels and is simultaneously supported by them. In contrast, there is no such symmetrical support at the power output – the Z70 gear wheel is supported by the Z31 wheel on one side. Therefore, radial clearance in the bearing support (Fig. 5.20, bearing S2) of the Z70 gear wheel axis will cause un-attenuated radial motion of this axis. The radial motion of the Z31 wheel axis of rotation relative to the Z70 wheel axis of rotation will translate into tail rotor angular velocity oscillations. The transfer of mechanical power between the Z31 and Z70 gear wheels is periodic with some excess power. This may also lead to an increased tribological wear rate of the Z31 to Z70 gear wheel pair. The probability of breaking the kinematic bond between the Z31 and Z70 gear wheels also increases.

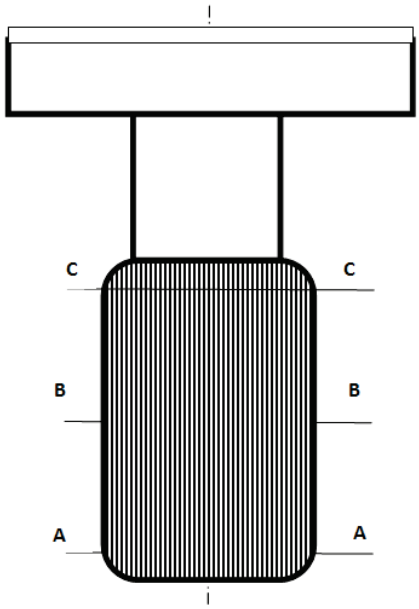

Fig. 5.21. GT-40PCz6 generator drive shaft spline measurements: A-A, B-B, C-C – consecutive planes for conducted modular pitch measurements

The repulsive forces between the Z31 and Z70 gears result in the angular motion of the longitudinal axis of symmetry of the hollow shaft that constitutes the axis of rotation for the Z31 gear. This shaft is internally hollow and has internal toothing that forms a drive sleeve for the shaft of the right GT-40PCz6 generator. GT-40PCz6 generator shaft (drive sleeve) skew leads to the generation of a particular system of forces acting on the drive shaft of this generator. This interaction is

described in subsection 3.1.6 and shown in Fig. 3.15. It causes conical abrasive decrements on the rotor shaft contact plane of the right GT-40PCz6 generator, as shown in Fig. 3.16. Therefore, when studying the severe damage to a Mi-24 helicopter [95] that involved breaking of the auxiliary rotor propulsion, the author measured the modular pitch of this rotor shaft on three planes (Fig. 5.21): A, B, C - to assess the abrasive wear on the contact plane.

Fig. 5.22 shows a polar diagram of the modular pitch values for the teeth of the GT-40PCz6 right generator shaft splines (Figs. 5.20 and 5.23.) in a Mi-24 helicopter. The contact plane material wear of the spline tooth can be seen in this diagram. The diagram illustrates the conical shape of the spline material loss – the modular pitch of the teeth on the A-A plane is clearly smaller in Fig. 22 than in the others. Pitch values on the B-B plane are already notably larger, while being the largest in C-C. This type of contact plane wear indicates significant skewing of the generator drive sleeve in relation to the generator shaft axis of symmetry. This type of wear was discussed in subsections 3.1.5 and 3.1.6 of this monograph. The consequences of the right GT-40PCz6 generator drive shaft wear presented in this chapter (Fig. 5.2) perfectly match the cases described therein (Figs. 3.15 and 3.16). Splined connection skew is most often caused by intensive spline wear [35, 41÷43, 154, 170, 247, 276]. This type of wear induces rotational speed modulation and generates systematic pulsating dynamic excesses. These can lead to sectoral wear of the transmission system at specific angular positions.

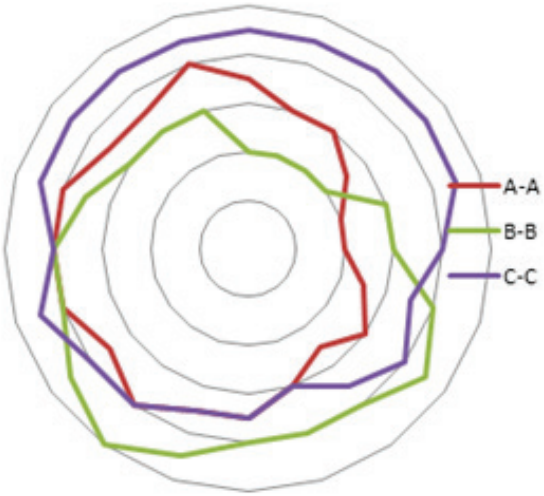

Fig. 5.22. Right generator spline wear polar diagram: A-A, B-B, C-C – successive modular pitch values (shown on the diagram as a leading radius) for consecutive modular pitch value measurement planes

When monitoring the Mi-24 helicopter generator gearbox, it is important to alert increased generator drive shaft skew relative to the drive speed. Even more important is the sufficiently early detection of excessive inter-tooth backlash between gears Z31 and Z70, especially the presence of systematic (sectoral) irregularities in that backlash at specific angular positions. This, in turn, can result in a systematic excess of dynamic power, manifested by percussive meshing of both gear wheels (Z31 and Z70). This process can induce accelerated wear of the Z31 and Z70 teeth at these angular positions and may ultimately lead to them rupturing. Even a temporary loss of the kinematic bond between these wheels poses a threat of stopping the auxiliary rotor [29]. The usual outcome is a rotation of the entire helicopter fuselage around the vertical axis, in the direction opposite to that of the main rotor. If the auxiliary rotor stopping time is long enough, this usually results in the helicopter crashing (Fig. 5.24).

Possibilities of tracking this wear type were discussed in subsection 3.3.4. Fig. 3.52 shows the instantaneous frequency waveform obtained from a measurement that was taken on the GT40PCz6 generator gearbox using the FAM-C method. It indicates material wear of the gear wheels in the generator gearbox. According to the author, spike pulses occurring periodically every several revolutions of the Z31 gear wheel prove a systematic brief disconnection of the kinematic bond between the Z70 and Z31 gearw heels [95]. Here, excessive circumferential backlash between the teeth causes dynamic excesses leading to tooth rupture (Fig. 3.53).

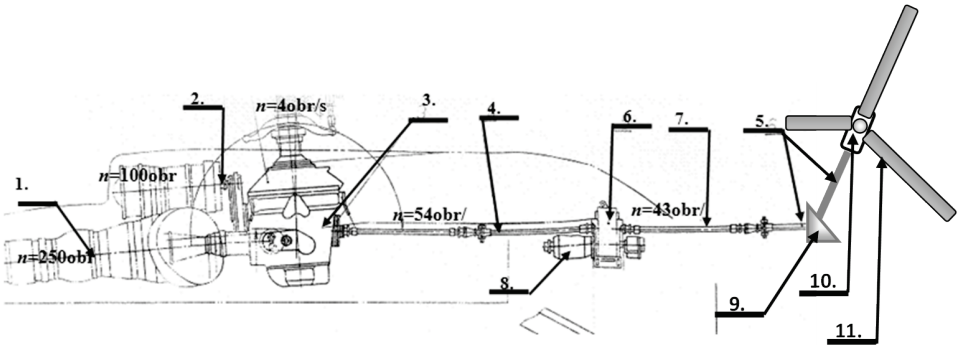

Fig. 5.23. Transmission element arrangement between the engine and the generator in a Mi-24 helicopter: 1 – TW3-117MT propulsion engine, 2 – mechanical fan, 3 – WR-24 main transmission, 4,5,7 – power transmission shaft, 6 – generator gearbox, 8 – left GT-40PCz6 generator (the GT-40PCz6 right generator is fixed to the same generator gearbox behind it), 9 – intermediate transmission, 10 – tail transmission, 11 – auxiliary (tail) rotor

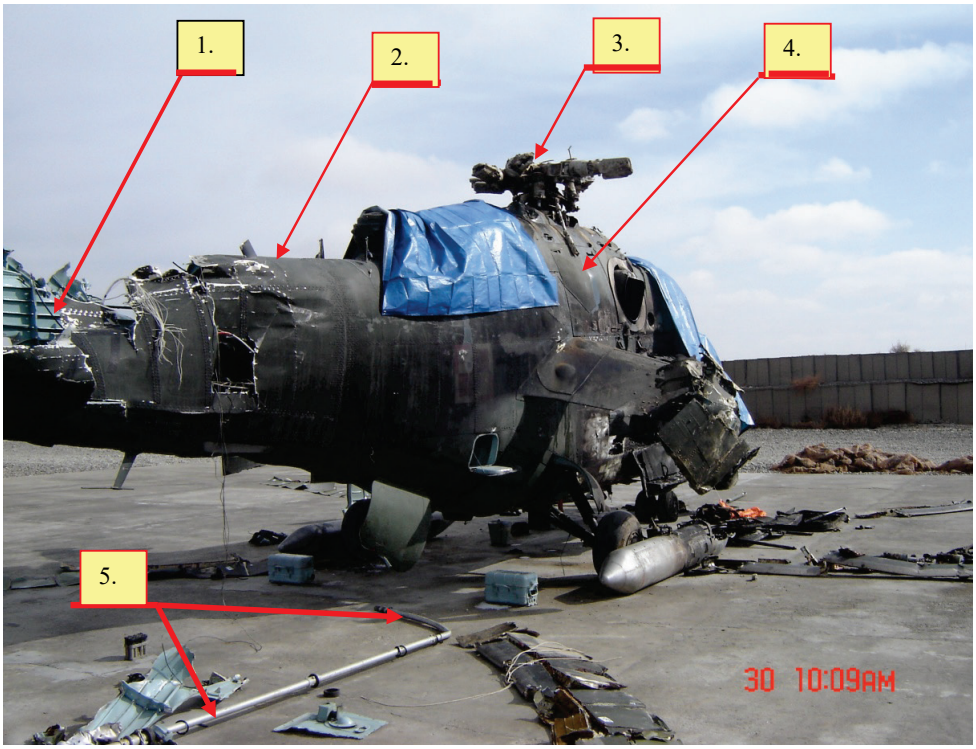

Fig. 5.24. Mi-24 helicopter with a transmission system discontinued due to internal damage in the generator gearbox: 1 – place of the torn-out generator gearbox, 2 – sheathing over a surviving transmission segment, 3 – main rotor hub after blade disconnection, 4 – WR-24 main transmission cover (movable), 5 – auxiliary rotor propulsion transmission torn out and bent as a result of the helicopter hitting the ground

5.3.3. Detecting a damaged bearing of a Mi-17 helicopter swash plate

Source literature states [225, 316] that the development of helicopters, first constructed in the same period as aircraft, has involved many theoretical and practical challenges throughout the years. The issue of control over the rotorcraft seemed the most demanding. The introduction of a swash plate allowing intermittent steering [13, 225, 237, 316], together with a three-part suspension, enabled solving this issue. The first successful, albeit very rudimentary designs started appearing after 1918 [316]. The swash plate is a mechanism that enables adjusting the angle of attack of the lifting rotor blades to suit the desired flight direction and altitude. The outcome is a change in the resultant aerodynamic force value and direction. The swash plate consists of two plates (also called “discs”):

– the lower, stationary with a variable roll and pitch angle adjusted by the pilot,
– the upper, moving – with affixed lever tips, allowing the angle of attack of individual lifting rotor blades to be changed [48, 225].

There is a rolling bearing (usually a ball bearing), also known as the "swash plate main bearing", between the two discs. It ensures the moving disc to have an appropriately low thrust torque. This bearing also transfers longitudinal forces with variable amplitudes of up to 500 kg. Furthermore, periodic control induces vibration frequency close to, and actually synchronised with, the main rotor natural frequency [225]. This significantly reduces the forces required for steering, but applies additional dynamic load on the swash plate rolling bearing. If this bearing is damaged, the control process may slow down. The steering may then become imprecise – additional broadband vibrations within the steering system may appear [225].

The Mi-17 helicopter tests using the FAM-C method involved diagnostics of three helicopters with running engines. They were conducted after connecting the FAM-C measuring system [98] to the SGS-40PU 115/200 V, 400 Hz, three-phase AC generator output voltage terminals with the following measuring configurations:

a) single-phase measurement with two-wave (half-period) counting,
b) three-phase measurement with two-wave counting.

Fig. 5.25 shows the single-phase waveform. Fading slow-variable oscillations with the following amplitudes can be seen: $A_1 = 0.8$ Hz, $A_2 = 1$ Hz, $A_3 = 0.9$ Hz, $A_4 = 0.6$ Hz and decreasing periods $T_1 = 20$ s, $T_2 = 12$ s, $T_3 = 14$ s, $T_4 = 10$ s. Oscillations of this type were notoriously excited within Mi-17 No. 2's propulsion unit and probably result from the operation of the automation system – the engine speed synchronisation system. For the sake of comparison, it should be noted that other tested engines did not exhibit an oscillatory nature of the slow-variable component. However, the considerations regarding the engine automation system go beyond the topic of this monograph.

As noted previously, the swash plate main bearing has so many rolling elements that the peripheral mechanical vibration frequencies generated by them well exceed the observability window of the onboard generator single-phase measurement. Therefore, monitoring the technical condition of the swash plate disc using the FAM-C method requires a three-phase configuration – the FAM-C measuring system is connected to the generator output terminals. Once again, the tested Mi-17 No. 2's propulsion unit provided unusual (compared to the other two) results. Namely, 2 to 11 frequency pulses with a significant amplitude were found in every third measurement image $f_i = f(t)$ (11 made) with a measurement exposure $\Delta t = 60$ s

(Figs. 5.26÷5.27). The amplitude of such a frequency pulse reached twice the steady-state frequency level. The duration of this pulse is $\Delta t_i = 0.003$ s (Fig. 5.27), corresponding to the displacement duration for one swash plate main bearing rolling element by one angular pitch[3] in its locked state (no rolling element motion on the bearing race). A return to the steady state was observed between the pulses, but the amplitude in this case is higher by several percent (Fig. 5.28). In this section of the waveform (region of increased waveform amplitude between pulses), a combination of two oscillation types is observed:

- dynamic oscillations $f_{p1} = 780$ Hz,
- slow-variable oscillations $f_{p2} = 330$ Hz.

Uniform oscillatory fluctuations were noted in the remaining waveform sections (measurement exposure time $\Delta t = 60$ s) (Fig. 5.29). Their oscillation value is $f_p = 390$ Hz.

The author believes that the occurring spike pulses (Figs. 5.26 and 5.27) are indicative of certain swash plate main bearing rolling elements becoming blocked due to surface damage. This damage can take the form of a flat grinding of the given rolling element's cylindrical surface. Such grinding was previously observed during controlled contamination of the TS-11 Iskra aircraft SO-3 engine bearing interior [266]. In contrast, fast-variable oscillations in the spike pulse occurrence region (Figs. 5.28 and 5.29) are indicative of strong rolling element skew. Experience accumulated during in the course of diagnosing the bearing supports of TS-11 Iskra aircraft engines [122, 129] enables speculating by analogy that the main bearing of the examined Mi-17 helicopter No. 2's swash plate experienced so-called "rolling element edging". This involves rolling shaft grinding, and entails a release of considerable heat amounts. Usually, a significant amount of metal filings is also produced, which increases bearing contamination.

During the "soothing" period, when spike pulses disappear, a reduction in the dynamic oscillation frequency amplitude ($f_{p1} = 780$ Hz) can be observed in the generator-transducer output voltage instantaneous frequency waveforms. This effect completely disappears after a few seconds, with only the slow-variable oscillations of $f_{p2} = 330$ Hz present (Fig. 3.30).

Conclusion – should such readings occur, the assessed Mi-17 helicopter No. 2's swash plate main bearing should be replaced as soon as possible. Further operation will be abundant with progressively enhanced tribological and thermal wear processes. These will lead to increasingly more dynamic peripheral decelerations, and, indeed, may adversely impact the technical condition of the main reduction gear components and even the entire helicopter transmission. Damage to the

[3] The swash plate main bearing has $N = 90$ rolling elements.

synchroniser crosshead bearing components can also occur. Furthermore, the yoke fixing the synchroniser crosshead arm may become loose [7, 98]. Hence, monitoring its circumferential backlash is crucial in terms of flight safety.

5.3.4. Using the FAM-C method to detect increased circumferential backlash of a Mi-17 helicopter swash plate mobile disc synchronizer

Section 5.3.3 discusses, among other notions, the role of the swash plate in controlling helicopter flight geometry. The upper moving part of the swash plate (movable swash plate disc) is pulled circumferentially by the synchronizer crosshead [7, 95, 225]. One end of this is fixed on the main rotor axis, and the other is attached (articulated) to the swash plate upper disc. Here, increased circumferential backlash of the synchroniser crosshead may hinder helicopter steering and, in particular, cause "spontaneous" flight course deviation. In an extreme case (breaking of the mechanical bond between the upper swash plate and the main rotor main shaft), this can even lead to a crash. When monitoring helicopters with the FAM-C method, discontinuities (undercuts of sine wave shape) were observed on the trailing edges (Fig. 5.31) of Mi-17 No. 1, that were similar in shape to the theoretical reference waveform shown in Fig. 3.7. Accordingly, an instantaneous frequency waveform containing undercuts evidences circumferential backlash between the inertia mass of the helicopter's swash plate and the generator-transducer. Assuming that transmission intermediates exhibit correct radial clearances (this could be assumed, as the main reduction gear had a significant residual service life), the cause could have been increased backlash in the synchroniser crosshead joint or loosening of the yoke fixing the synchroniser crosshead to the main rotor propeller head and main shafts.

A frequency waveform from a Mi-17 helicopter that does not contain the aforementioned discontinuities is shown for comparison purposes (Fig. 5.32).

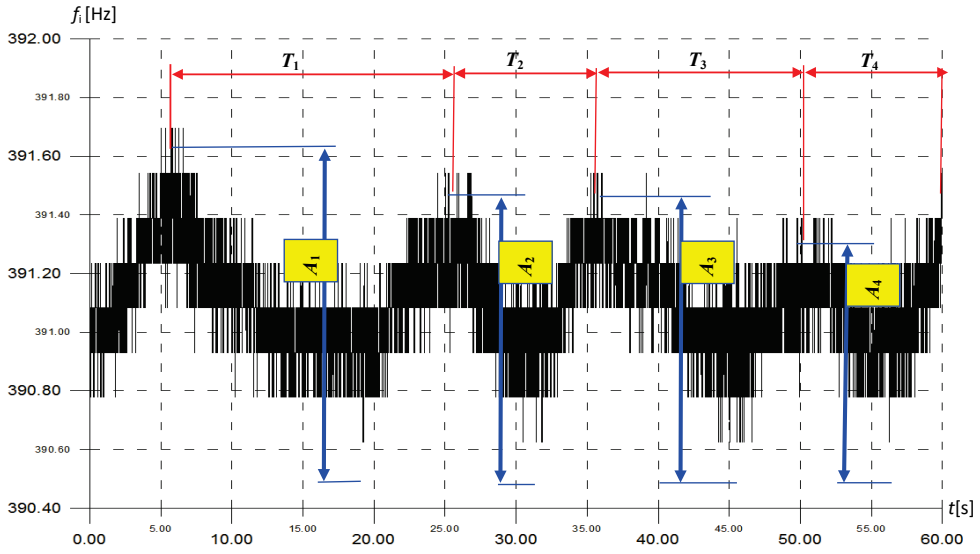

Fig. 5.25. Instantaneous frequency waveform obtained from a single-phase FAM-C measurement of the SGS-40PU generator from Mi-17 helicopter No. 2 – 60 s time window, beating-related slow-variable component visible (speed difference between the main engines). A_1, A_2, A_3, A_4 – slow-variable (fading) amplitude values

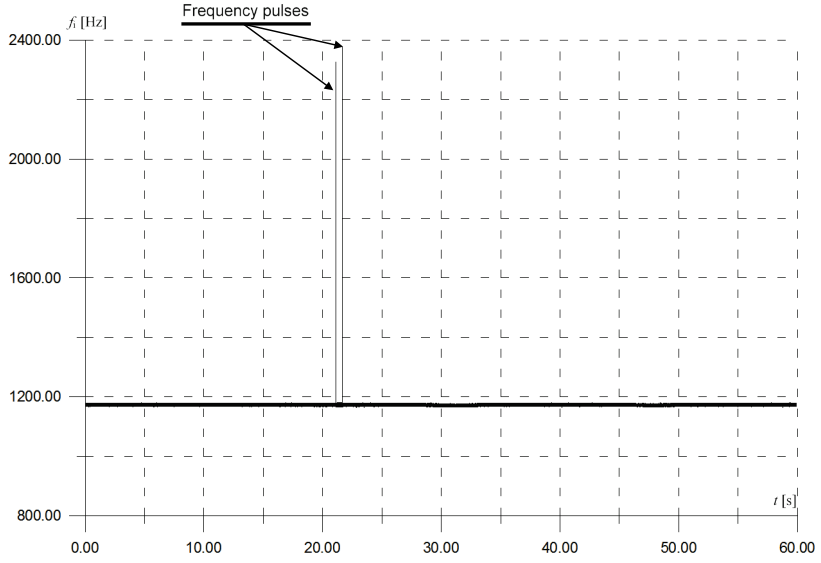

Fig. 5.26. Instantaneous frequency waveform obtained from a three-phase FAM-C measurement of the SGS-40PU generator from Mi-17 helicopter No. 2 – 60 s time window, two spike pulse visible

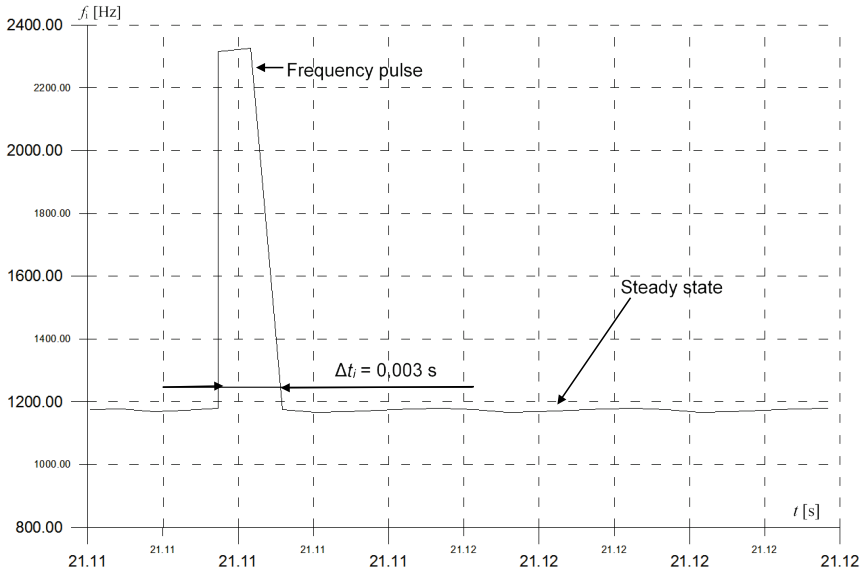

Fig. 5.27. Instantaneous frequency waveform obtained from a three-phase FAM-C measurement of the SGS-40PU generator from Mi-17 helicopter No. 2 – 0.01 s time window, one increased spike pulse visible

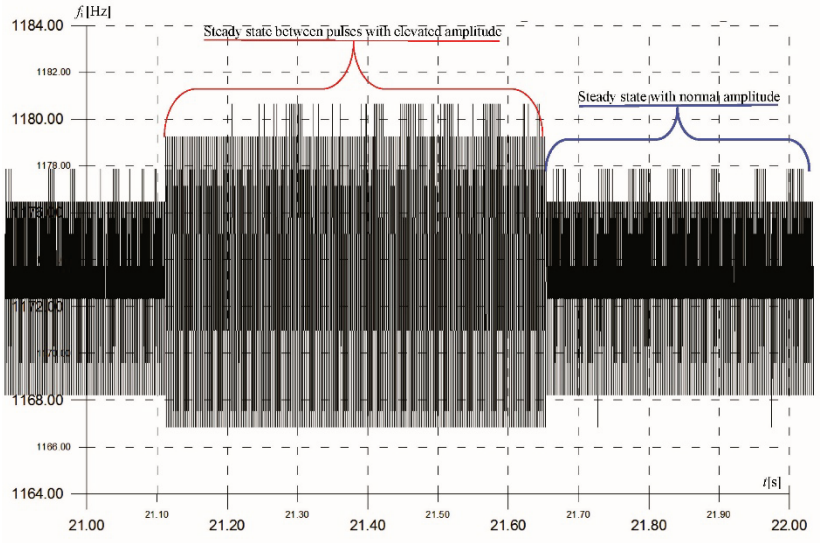

Fig. 5.28. Instantaneous frequency waveform obtained from a three-phase FAM-C measurement of the SGS-40PU generator from Mi-17 helicopter No. 2 – 1 s time window, visible changes in the medium-variable component waveform amplitude between two (not marked to shade the waveform) spike pulses (not marked to shade the waveform)

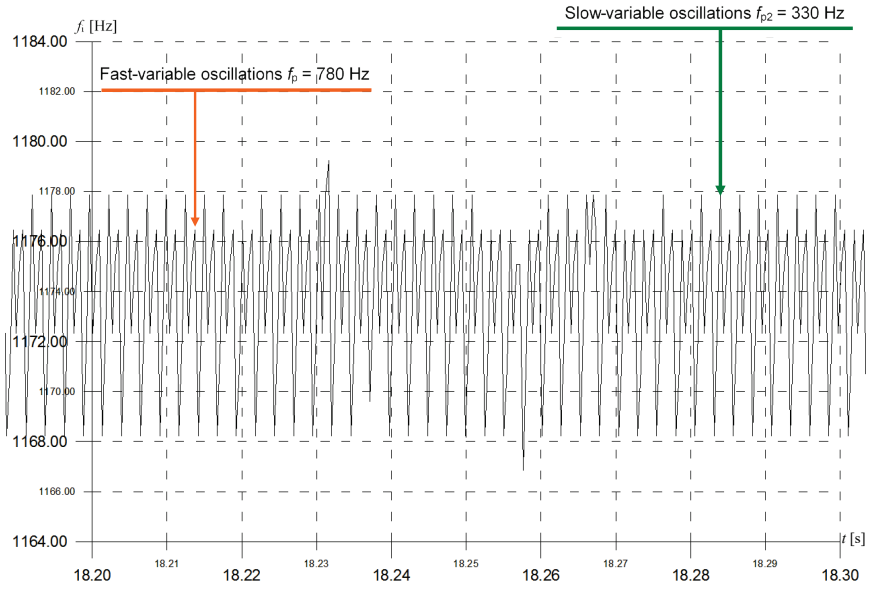

Fig. 5.29. Instantaneous frequency waveform obtained from a three-phase FAM-C measurement of the SGS-40PU generator from Mi-17 helicopter No. 2 – 0.1 s time window, waveform between two spike pulses (not marked to shade the waveform)

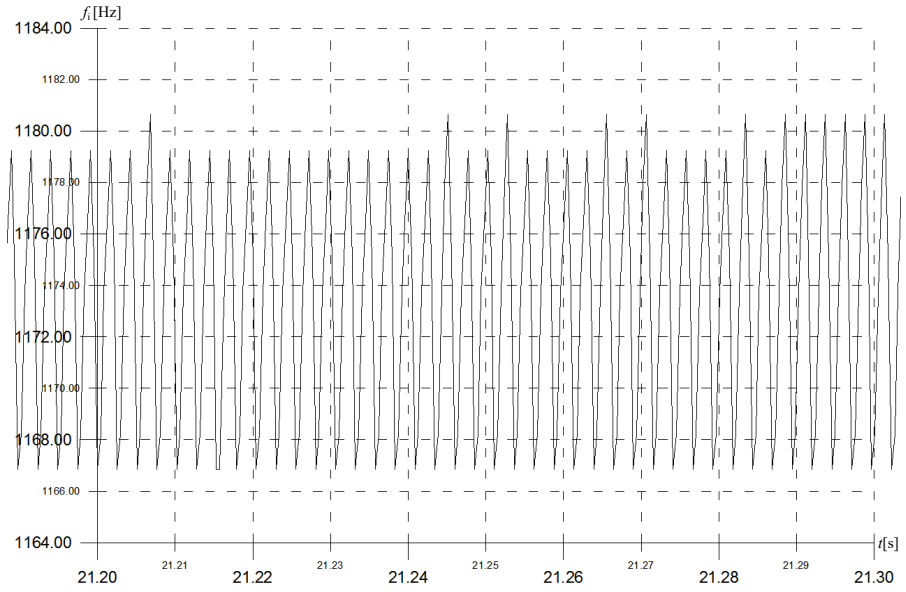

Fig. 5.30. Instantaneous frequency waveform obtained from a three-phase FAM-C measurement of the SGS-40PU generator from Mi-17 helicopter No. 2 – 0.1 s time window, in the period with no spike pulses

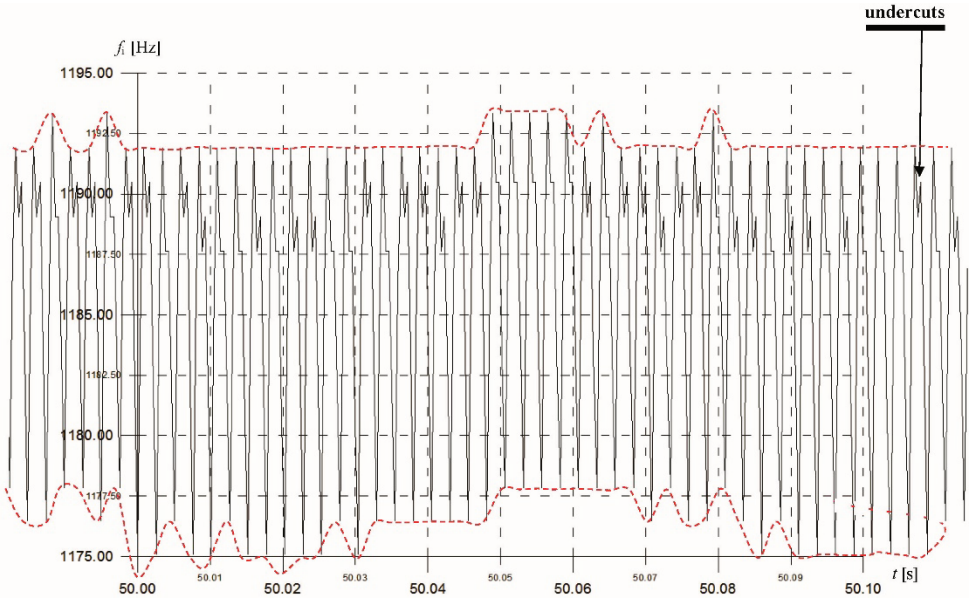

Fig. 5.31. Instantaneous frequency waveform obtained from a three-phase FAM-C measurement of the SGS-40PU generator from Mi-17 helicopter No. 1 – 0.1 s time window, visible undercuts on the trailing edge proving circumferential backlash

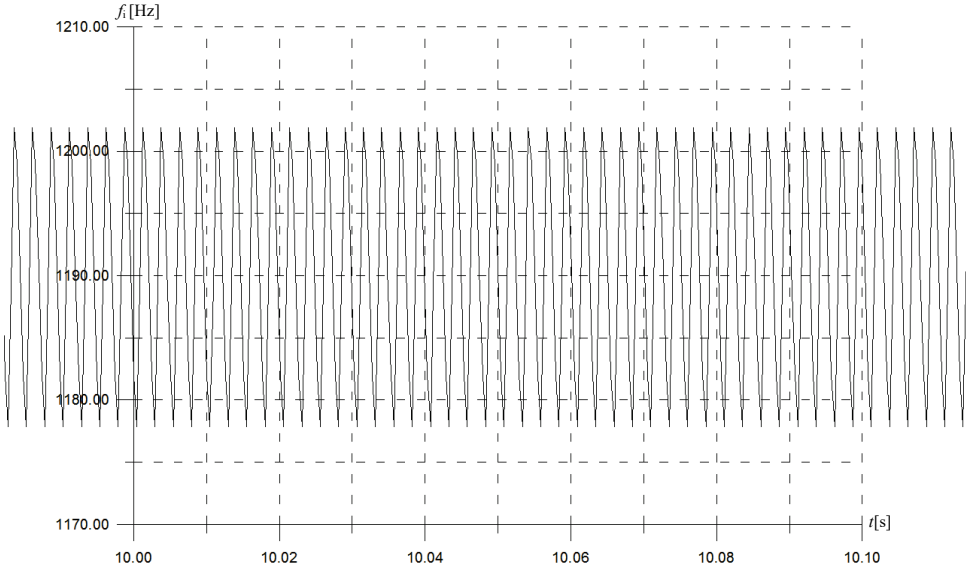

Fig. 5.32. Instantaneous frequency waveform obtained from a three-phase FAM-C measurement of the SGS-40PU generator from Mi-17 helicopter No. 1 – 0.1 s time window; sine waveform visible, uniform and stable over time

5.4. Using the FAM-C method to measure non-aviation propulsion units

5.4.1. Studying the propulsion units of marine power plants

5.4.1.1. Description of a marine power plant and its diagnosis capacity with the FAM-C method

Compression-ignition (diesel) engines have relatively low (compared to other engine types) rated main shaft speeds [28, 129]:

- marine engines 300÷800 rpm, while
- railroad vehicle engines 700÷1100 rpm,
- automotive engines 900÷1200 rpm.

This is due to the particularly large dimensions of the moving parts in marine engines.

Low rated speed is advantageous for the FAM-C method. This is because generators have strictly standardised rated speeds (regardless of the propulsion type) that are significantly higher than the rated speed of compression-ignition (diesel) engines. In consequence, slow-variable engine designers are forced to apply significant gear ratios that boosts the rotational speed to a level required for stable generator operation. This increases, directly proportionally to the gear ratio, the resolution of the FAM-C and FDM-A methods. Resolution is represented by the k_r factor [114, 129, 136]. At the same time, unexpected engine failure, especially in large facilities, can lead to significant economic losses. Therefore, the employment of low-cost, and non-destructive diagnosis methods is justified and even necessary.

In general, compression-ignition engine operation is similar to that of a four-stroke spark-ignition engine. However, it is characterised by a much higher operating pressure required to increase the fuel-air mix temperature to that of compression-ignition. Hence, diesel engine components are exposed to respectively greater loads. The most common operational disadvantages of such engines (Fig. 5.33) include:

- diesel oil injection system wear that leads to non-uniformity (formation of additional pulsed accelerations) of the engine main shaft angular velocity,
- excessive backlash between the piston pin and piston, leading to characteristic instantaneous velocity waveform undercuts,
- excessive deflection of the connecting rod leading to increased angular velocity first harmonic of the shaft with a crankshaft rated speed first harmonic frequency,
- dynamic unbalance of a moving assembly,

– excessive backlash in crankshaft plain bearing bushings,
– excessive backlash in connecting rod foot pins.

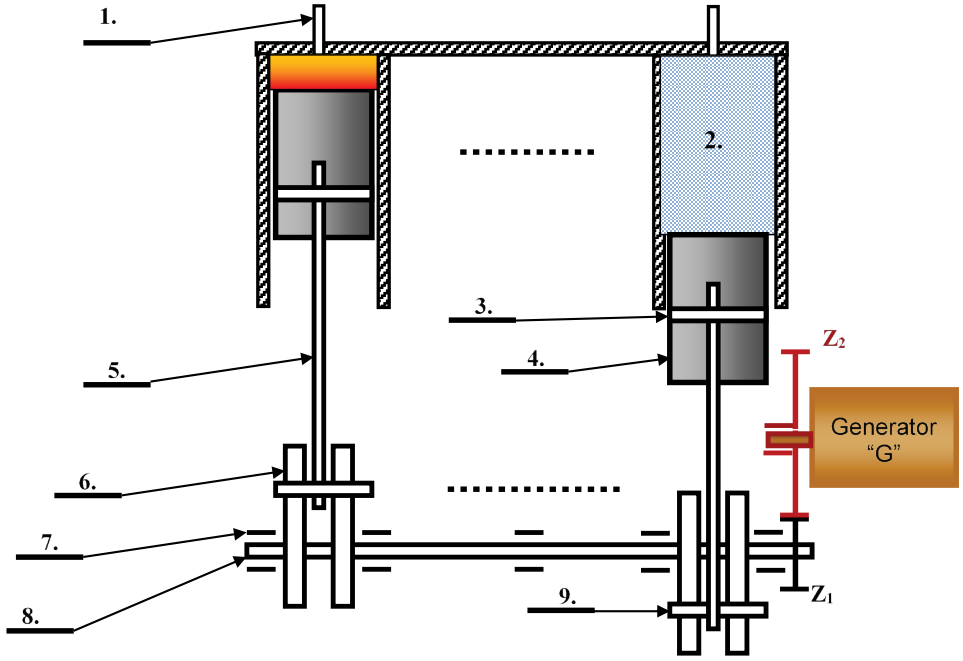

Fig. 5.33. Simplified overview drawing of a compression-ignition engine: 1 – injector tip, 2 – working medium (compressed air), 3 – piston pin, 4 – piston, 5 – connecting rod, 6 – counterweight, 7 – main shaft slide bearing bushing, 8 – main shaft, 9 – connecting rod foot pin, z_1, z_2 – transmission gear wheels, G – generator-transducer

Two identical propulsion engines per transmission are used (Fig. 5.34, detail DP, DL) to increase safety. These engines transmit power to a common SN gearbox. Due to the individual engine angular velocity variations, the outputs of their shafts are coupled to the transmission via flexible couplings (Fig. 5.34, detail SP, SL). The transmission SN distributes power extracted from the connecting rods of the two engines to:

– generator G,
– propellers SR via flexible couplings SS.

This mechanical power distribution system is the reason behind the adverse events arising in connection with incorrect installation or operation. The most common events include [44, 137]:

– lack of inter-synchronisation between engine output shaft rated speeds,

- unbalanced load of both engine shafts, resulting in excessive load on the flexible couplings and internal power losses,
- development of inappropriate flexible coupling mounting geometry,
- internal failures of the transmission gear: increased of inter-tooth backlash or tooth chipping, and skew of the gear wheel rotational axis,
- excessive torsional stress on shafts leading to their rupture, e.g., screw propeller shaft,
- uneven screw propeller shaft angular velocity, leading to propeller energy loss, which reduces ship or vessel speed.

All the failures referred to can be monitored using the FAM-C method.

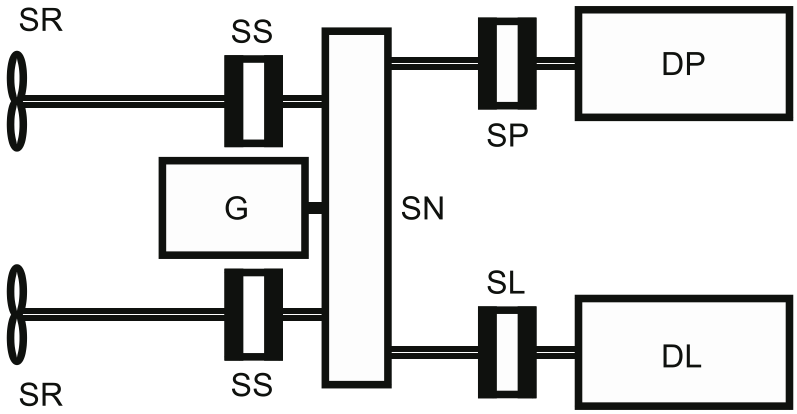

Fig. 5.34. Block diagram of a ship propulsion unit powered by two compression-ignition engines. G – generator (generator-transducer), SR – screw propeller, SS – screw propeller coupling, SN – transmission gear, SP, SL – flexible couplings of engines (right and left, respectively), DP, DL – diesel engines (right and left, respectively)

5.4.1.2. Three-phase measurements of the Pomerania ferry propulsion unit

Three-phase measurements [103, 129, 130] of each propulsion unit comprising the propulsion system were conducted under different load conditions during a typical cruise.

Observation of angular velocity pulsations induced by the operation of individual cylinder pistons (multiplication factor $k_r = 9.6$) was found to be possible.

The recorded instantaneous frequency waveform obtained through the FAM-C method in a three-phase configuration exhibits a much more complex shape than a single-phase waveform. The waveform in the three-phase configuration has three components (Fig. 5.35):

– slow-variable,
– fast-variable,
– spike pulses.

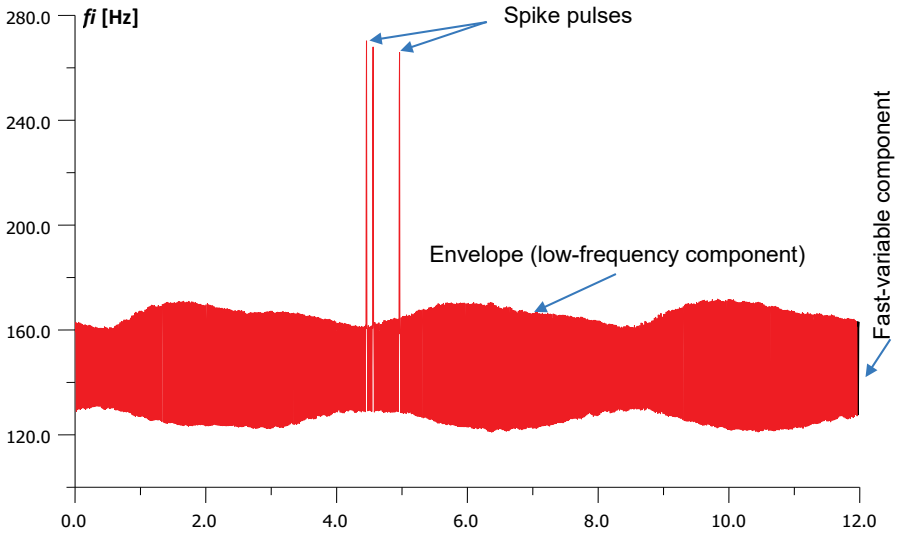

Fig. 5.35. Pomerania ferry main propulsion unit instantaneous frequency change waveform – three-phase measurement

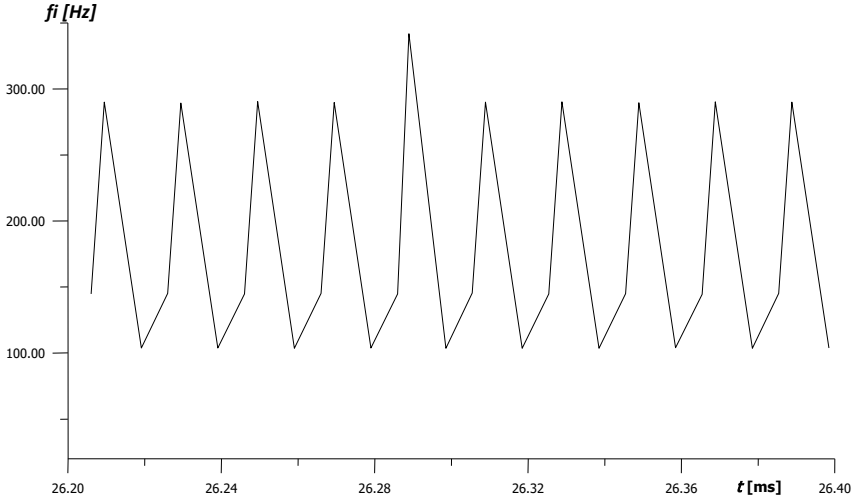

Fig. 5.36. Pomerania ferry main propulsion unit instantaneous frequency change waveform via the FAM-C method – close-up

The slow-variable component reflects the eccentricities and skew of, primarily, the SP and SL flexible couplings (Fig. 5.34), similar to the waveform in the case of single-phase measurements [114, 129, 136]. Spike pulses indicate a one-off, excessive dose of fuel injected into the cylinder. The fast-variable component represents the engine shaft speed dynamics (Figs. 5.36 and 5.37). Operating uniformity of individual cylinders can be tracked here [103, 129].

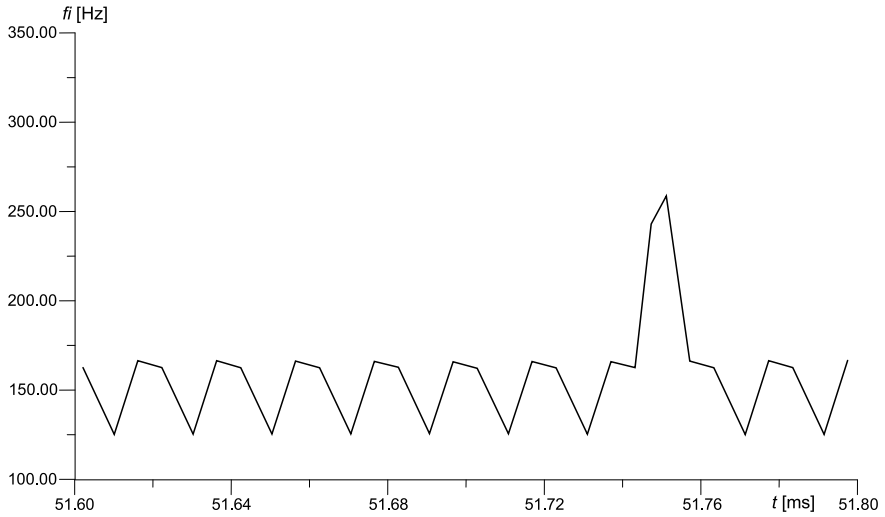

Fig. 5.37. Backup power generator instantaneous frequency change waveform

5.4.1.3. Single-phase measurements of the Polonia ferry propulsion unit

The propulsion unit of the Polonia ferry is kinematically twinned to that of the Pomerania ferry. Single-phase FAM-C measurements were conducted in this case. As previously discussed in Chapter 4 (metrological properties), the resolution of single-phase is threefold lower. Therefore, the observability band of a generator-transducer shifts towards low-frequency phenomena, and a full image such as shown in Fig. 5.35 is not obtained, but instead that of the signal envelope seen in [116, 130] is recorded. Furthermore, upon magnification, no details will be visible as in Fig. 5.36, except for the same envelope. Its amplitude provides information on the phase jitter magnitude and the rated angular velocity between the two engines (so-called "beating"). This envelope also contains fast-varying components. Once these have been decomposed into characteristic sets – images on the plane $(\Delta F, f_p)$ – it is easy, based on the data in Tables 9÷10, to calculate the values crucial to the operation of the propulsion unit (Table 11).

Table 9

Selected parameter values for chosen sub-assemblies of the Polonia ferry

Sub-assembly name	Eccentricity defect				Skew defect		
	n	f_p	T	k	f_p	T	k
	rpm	Hz	s	-	Hz	s	-
Generator shaft	1200	20	0.05	3	40	0.025	1.5
Propulsion motor main shaft	600	10.0	0.1	12	20.0	0.05	6
Power screw shaft	140	2.3	0.4286	12	4.7	0.21429	6
Pulsations induced by the 4 propeller blades	560	9.3	0.1071	3	18.7	0.05357	1.5
Pulsations induced by 6 cylinders	3600	60	0.0167	2	120	0.00833	1

Table 10

Selected design data of the Polonia ferry

Sub-assembly name	f_{NG} [Hz]	T_G [s]	i
Generator shaft	60	0.01667	1
Propulsion motor main shaft	60	0.01667	2
Power screw shaft	60	0.01667	0.46
Pulsations induced by the 4 propeller blades	60	0.01667	0.46
Pulsations induced by 6 cylinders	60	0.01667	2

Table 11

Polonia ferry coupling defect parameter values

Sub-assembly name	Eccentricity defect a [mm]	Skew value β [°]
Left engine coupling	0.195	0.017
Power screw coupling	0.602	0.011

5.4.2. Studying electromechanical transducers

To ascertain the effectiveness of FAM-C and related methods, the electrical parameters of transducers with different controlled (introduced by the testers) wear levels of electrical and mechanical components were tested. The tests were conducted using both classical (fast Fourier transform) and novel (e.g., FAM-C) methods. Actual wear levels were assessed through mechanical measurements. The tests were undertaken on PAG-1F, PT-500 and PO-750 transducers. They were prepared

for controlled application of assembly errors: eccentricity, and skew of the rotor axis of rotation with respect to the stator axis of symmetry. Single-phase and three-phase measuring systems were applied in the monitoring of these errors. Detailed properties of both measuring systems have been discussed in [112, 115, 117, 129].

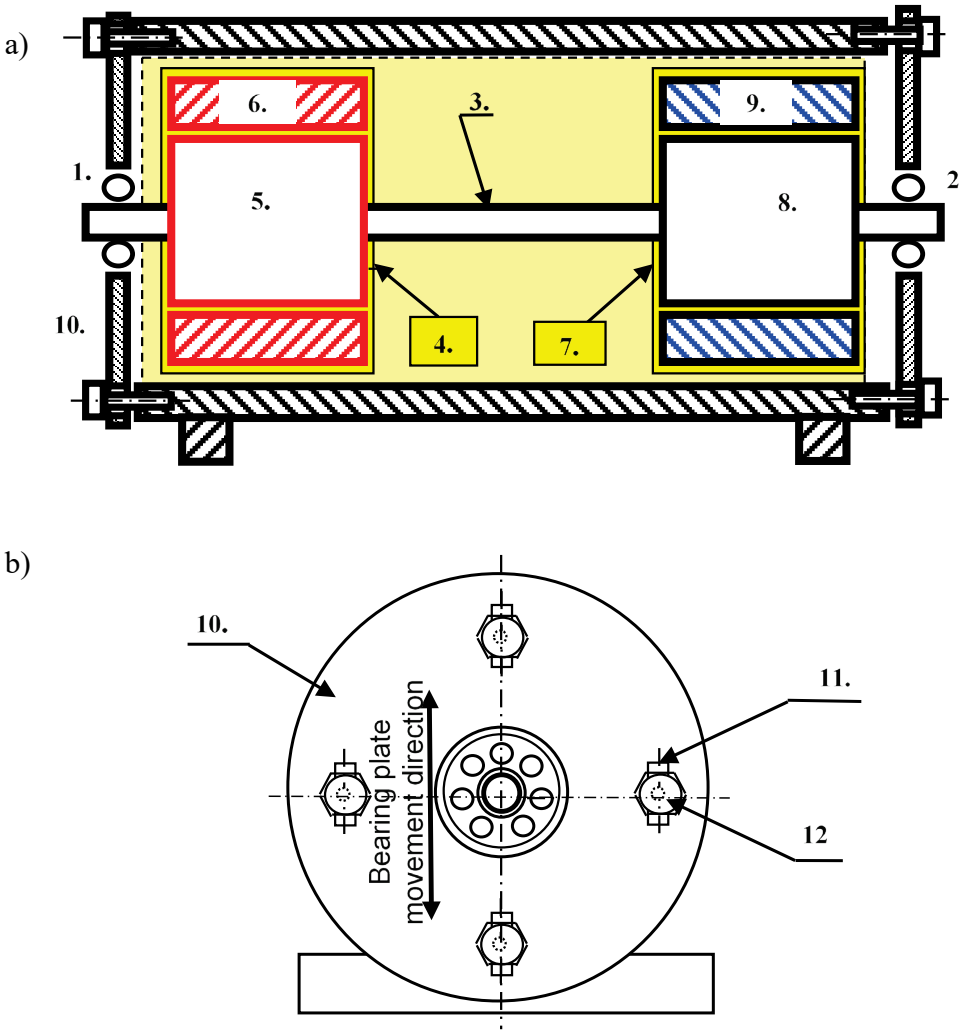

Fig. 5.38. Simplified assembly drawing of an electromechanical transducer adapted at AFIT to enable controlled application of assembly errors: a) longitudinal section, b) view from the side cover bearing shield. 1, 2 – rolling bearing, 3 – shaft, 4 – DC motor, 5 – DC motor rotor, 6 – DC motor stator, 7 – AC generator (alternator), 8 – AC rotor, 9 – AC generator stator, 10 – bearing plate (side cover), 11 – vertical milling, 12 – assembly screw

Rotor axis of rotation skew relative to stator axis of symmetry

Skewness [112] was applied for testing purposes through longitudinal vertically milling of assembly openings under the bolts securing the side cover (bearing mounting) of the machine and the cylindrical part. By moving one bearing disc (side cover) upwards and the other downwards, a measurable skew angle was obtained.

In the case of the **PAG-1F** transducer, an instantaneous frequency waveform as a function of time was obtained prior to moving the side cover, wherein modulations of approximately 75 Hz can be distinguished. This is similar to the rotor rated angular velocity first sub-harmonic. This proves the existence of low eccentricity and skew (according to calculations, the skew of the rotor rotation axis with respect to the stator axis of symmetry is about 0.0079°) of the rotor suspension relative to the stator. As soon as rotor skew reaches an angle of approx. 0.04°, the rotor rated angular velocity second harmonic frequency becomes dominant. Moreover, the instantaneous frequency waveform fluctuation amplitude increases from $\Delta F = 4.11$ Hz (0.95% relative to the average frequency value), to $\Delta F = 13.94$ Hz (1.09%).

In the case of the **PT-500C** transducer, a frequency waveform was obtained prior to moving the side cover, wherein the modulations of approximately 200 Hz can be distinguished, i.e., similar to the rotor rated angular velocity first harmonic, indicating the existence of slight rotor suspension eccentricity relative to the stator. As soon as rotor skew reaches an angle of approx. 0.2°, the rotor rated rotational speed second harmonic frequency becomes dominant (Fig. 12), and the instantaneous frequency waveform fluctuation amplitude increases from $\Delta F = 0.17$ Hz (0.04% relative to the average frequency value), to $\Delta F = 12.29$ Hz (1.02%).

In the case of the **PO-750** transducer, a frequency waveform was obtained prior to moving the side cover, wherein the modulations of approximately 175 Hz can be distinguished, i.e., similar to the rotor rated angular velocity first harmonic, indicating the existence of slight rotor suspension eccentricity relative to the stator. As soon as rotor skew reaches an angle of approx. 0.2°, the rotor rated angular velocity second harmonic frequency becomes dominant. In addition, the instantaneous frequency waveform fluctuation amplitude increases from $\Delta F = 0.24$ Hz (0.067% relative to the average frequency value), to $\Delta F = 1.87$ Hz (0.52%). Due to the failure to satisfy the Kotielnikov-Shannon condition, the data shall only be treated as informative – the assessment of the relationships between skew and frequency modulation should be conducted with the FDM-A method during machine run-up.

Upon increasing the value of the rotor axis of rotation skew angle relative to the stator axis of symmetry, an increasing amplitude instantaneous frequency waveform modulation with a period equal to the rotor rated angular velocity second harmonic is observable. What is more, the amplitude of these modulations grows along with increasing skew angle.

Rotor axis of rotation eccentricity relative to stator axis of symmetry

A parallel shift of the rotor axis of rotation relative to the stator axis of symmetry [112] was executed through longitudinal vertical milling of assembly openings under the bolts fixing the side cover (bearing housing) of the machine to the cylindrical part. A measurable eccentricity value was then obtained by displacing both bearing mountings downwards.

In the case of the **PAG-1F** transducer, a frequency waveform was obtained prior to moving the side cover, wherein the modulations of approximately 75 Hz can be distinguished, i.e., similar to the rotor rated rotational speed first sub-harmonic, indicating the existence of slight rotor suspension eccentricity and skew relative to the stator. When eccentricity values were increased to a = 0.2 mm, the instantaneous frequency waveform fluctuation amplitude ΔF increased from 4.11 Hz (0.95%), to 13.94 Hz (1.09%).

In the case of the **PT-500C** transducer, a frequency waveform was obtained prior to moving the side cover, wherein the modulations of approximately 200 Hz can be distinguished, i.e., similar to the rotor rated angular velocity first harmonic, indicating the existence of slight rotor suspension eccentricity relative to the stator, and with a frequency of approx. 200 Hz. When eccentricity values were increased to a = 0.35 mm, the instantaneous frequency waveform fluctuation amplitude ΔF increased from 0.17 Hz (0.04%) to 12.29 Hz (1.022%).

In the case of the **PO-750** transducer, a frequency waveform was obtained prior to moving the side cover, wherein the modulations of approximately 175 Hz can be distinguished, i.e., similar to the rotor rated angular velocity first harmonic, indicating the existence of slight rotor suspension eccentricity relative to the stator. When eccentricity was increased to a = 0.4 mm, the instantaneous frequency waveform fluctuation amplitude ΔF increased from 0.24 Hz (0.067%) to 0.52 Hz (0.52%).

Upon increasing the value of the rotor axis of rotation eccentricity relative to the stator axis of symmetry, an increasing amplitude instantaneous frequency waveform modulation with a period equal to the rotor rotational speed second harmonic is noticeable. The amplitude of these modulations grows along with increasing eccentricity. Based on practical measurements and theoretical calculations, the authors determined limit parameters for certain types of electromechanical transducers, and listed these in Tables 12 and 13.

Table 12

Summarized parameters of selected generator assembly failures and the parameters of their representations in electrical phenomena

	Transducer type	Mechanically measured linear displacement value		Distance between supports	D_N [mm]	β [°]	a [mm]	f_{max} [Hz]	f_{min} [Hz]	f_{sr} [Hz]	ΔF [Hz]	Failure parameters based on electrical calculations	
		A_1 [mm]	A_2 [mm]	L [mm]								a [mm]	β [°]
1	PAG-1F	0.3	0.2	145.0	55.5	0.19757	0.10	1290.32	1281.23	1285.5	9.09	0.0981	0.15506
2	PT-500C	0.35	0.35	203.3	69.3	0.19728	0.00	1224.36	1183.78	1203.2	40.58	0.0000	0.65866
3	PT-500	0.35	0.35	203.3	69.3	0.19728	0.00	1212.00	1200	1203.2	12.00	0.1727	0.19478
4	PO-750	0.5	0.0	258.0	70.0	0.11104	0.00	356.57	354.7	355.84	1.87	0.0000	0.08169
5	PAG-1F	0.01	0.01	145.0	55.5	0.0079	0.01	434.59	430.48	432.51	4.11	0.13185	0.20840
6	PAG-1F	0.3	-0.2	145.0	55.5	0.03951	0.5	1287.83	1273.89	1277.8	13.94	0.1513	0.00000
7	PT-500	0.01	0.01	203.3	69.3	0.00564	0.01	402.58	402.41	402.49	0.17	0.0073	0.00825
8	PT-500	0.35	0.35	203.3	69.3	0.19728	0.35	1208.46	1196.17	1202.32	12.29	0.17709	0.19964
9	PO-750	0.03	0.03	258.0	70	0.01332	0.03	357.77	357.53	357.7	0.24	0.0117	0.01043
10	PO-750	0.5	0	258.0	70	0.11104	0.00	356.57	354.7	355.84	1.87	0.0000	0.08169
11	PAG-1F	0.3	-0.2	145.0	55.5	0.03951	0.20	1287.83	1273.89	1277.8	13.94	0.1514	0.23925
12	PT-500	0.35	-0.35	203.3	69.3	0.00000	0.35	1208.46	1196.17	1202.32	12.29	0.1771	0.19964
13	PO-750	0.5	-0.4	258.0	70.0	0.02221	0.4	338.70	338.18	338.58	0.52	0.0269	0.02387

Table 13

List of limit parameters for selected types of electromechanical aviation generators for the FAM-C methods

Defect type	class	PAG-1F			PT-500C			PO-750		
		ΔF [Hz]	f_{sr} [Hz]	f_p[Hz]	ΔF [Hz]	f_{sr} [Hz]	f_p [Hz]	ΔF [Hz]	f_{sr} [Hz]	f_p [Hz]
1 Reduced brush pressure	A	<10	>380	0.2 ÷ 0.02	<10	>380	0.1 ÷ 0.025	< 8	>390	0.1 ÷ 0.025
	B	10÷25	350 ÷ 380		10÷25	360 ÷ 380		8 ÷ 15	370 ÷ 390	
	C	>25	<350		>25	≤360		> 15	≤370	
2 Skewing	A	< 0.3%f_s	-	400	< 0.3%f_s	-	400	-	-	-
	B	0.3 ÷ 0.8%f_s	-	400	0.3 ÷ 0.8%f_s	-	400	-	-	-
	C	0.8 ÷ 1.1%f_s	-	400	0.8 ÷ 1.1%f_s	-	400	-	-	-
	D	>1.1%f_s	-	400	>1.1%f_s	-	400	-	-	-
3 Eccentric	A	< 0.3%f_s	-	200	< 0.3%f_s	-	200	< 0.2%f_s	-	200
	B	0.3 ÷ 0.8%f_s	-	200	0.3 ÷ 0.8%f_s	-	200	0.2 ÷ 0.4%f_s	-	200
	C	0.8 ÷ 1.1%f_s	-	200	0.8 ÷ 1.1%f_s	-	200	0.4 ÷ 0.5%f_s	-	200
	D	>1.1%f_s	-	200	>1.1%f_s	-	200	>0.5%f_s	-	200

Transducer investigation during run-up

"Run-up" is a propulsion unit energy-related condition wherein the machine accelerated to rated speed is deprived of external energy supplies. The run-up time (often referred to as "coast-down time" in source literature) is the time from isolating a power source until the rotating movement of the rotating machine stops [235, 288, 289]. Two physical phenomena appear at this point:

a) **rotational speed level shifting** n (usually quasi-smooth) of individual coupled kinematic pairs, as the time counted since the cessation of external energy supply elapses, through successively lower and **lower rated speeds** (Fig. 5.39); different dynamic phenomena are observed for each of these speed levels, including the manifestation of various **local mechanical resonances** (Fig. 5.40);
b) **breakdown in the dynamics** of propulsion unit motion **into individually oscillating** (within design constraints and limits) **kinematic links**.

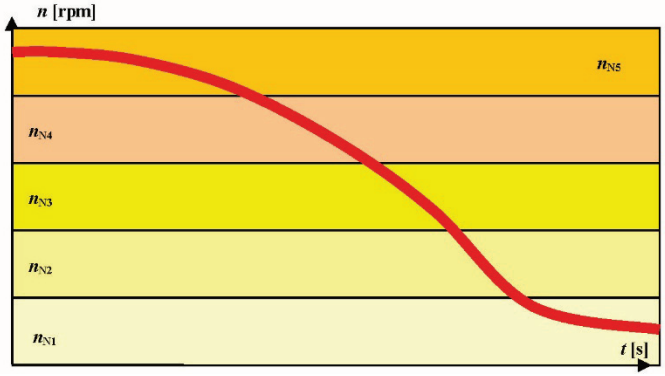

Fig. 5.39. Average rotational speed change waveform after isolating the energy source, with marked rated speed bands: $\{n_{N1}, n_{N2}, n_{N3}, n_{N4}, n_{N5}\}$ – slow-variable component

Air equipment factory manuals, as well as aircraft operation manuals, contain a number of run-up time limitations (called "coast-down time" in engine manuals) in terms of the contained rotating machinery. None of these deal with a comprehensive analysis of the run-up time angular velocity. However, the source literature holds numerous references to the potentially high diagnostic significance of such measurements and analyses [303].

According to practice and source literature data [303, 314], the shorter the run-up time, the greater the total resistance moments of a given mechanical assembly. Therefore, many manuals recommend periodic inspection of rotor bearing nodes in, e.g., gyros or turbine engines. Moreover, natural decomposition of all power propulsion components into independent kinematic pairs takes place during run-up

[314]. These pairs implement angular fluctuations, also called “free oscillations”, largely mutually independent of adjacent kinematic pairs. The attenuation duration of these oscillations depends on the dry friction component and the viscous (wet) friction component, as well as potential air damping (at higher speed levels). The frequency of such fluctuations depends on a number of factors, such as:

- moment of inertia – the greater the moments of inertia, the higher the natural oscillation period, i.e., the lower the frequency;
- elasticity – the greater the elasticity coefficient (the greater the moment of force accumulated in the component upon its deformation by a unit torsional angle), the shorter the natural oscillation period, i.e., the greater the frequency.

During run-up, the frequency of excitations acting on its individual mechanical components decreases gradually. It is therefore possible to induce and locate resonant excitations of individual generator mechanical components, e.g., bearing supports. Locating and observing these is very crucial for determining service life and making a reliable operating forecast. Mechanical quality factor Q of a resonant system is an exponent of a hazardous condition for bearing supports – if $Q > 10$, it is advisable to decommission a given unit [39, 40, 129].

If the excitation frequency is similar to the system's natural (free) vibration frequency, this may indicate a resonance hazard. Due to their step-variable cross-section, deadweight, unbalance of the suspended masses and bearing backlash, machine shafts constitute a complex vibration system. Indeed, resonant vibrations of one component impacts upon other system components. There are several critical velocities within such a system (Fig. 5.40, extremes: A_{1max}, A_{2max}, A_{3max}, A_{4max}, A_{5max}), usually calculated with approximated methods. If, for example, a certain number of rotating masses is deposited on the shaft, e.g., m_1, m_2, m_4, … , m_n, the critical velocity of the entire system is then calculated based on the Dunkerlev formula in the form [169]:

$$1/\omega_{kr}^2 = 1/\omega_{kr1}^2 + 1/\omega_{kr2}^2 + 1/\omega_{kr3}^2 + \ldots + 1/\omega_{krm}^2 \tag{3.4}$$

The stresses arising from resonant vibrations can lead to fatigue failures. The angular velocity at which resonance occurs is called the “critical velocity” (ω_{kr2}^2), and can be expressed by the formula [73,169, 260]:

$$\omega_{kr2} = (g/l)^{1/2} \tag{3.5}$$

which in engineering terms can be expressed by the relationship:

$$n_{kr} \approx 300 \cdot (1/f) \text{ [rpm]} \tag{3.6}$$

where:
f – static value of the sag in the element's symmetry axis [cm], g – gravitational acceleration.

The fact that shafts should not operate at this speed should be clearly emphasized. The rough permissible values of the sag arrow are [253]:

– machine shafts $f_{dop} = (0.0002 \div 0.0003)\ l$,
– gear transmission shafts $f_{dop} = (0.005 \div 0.01)\ m_u$,

where:
l – distance between adjacent supports, m_u – toothing modulus.

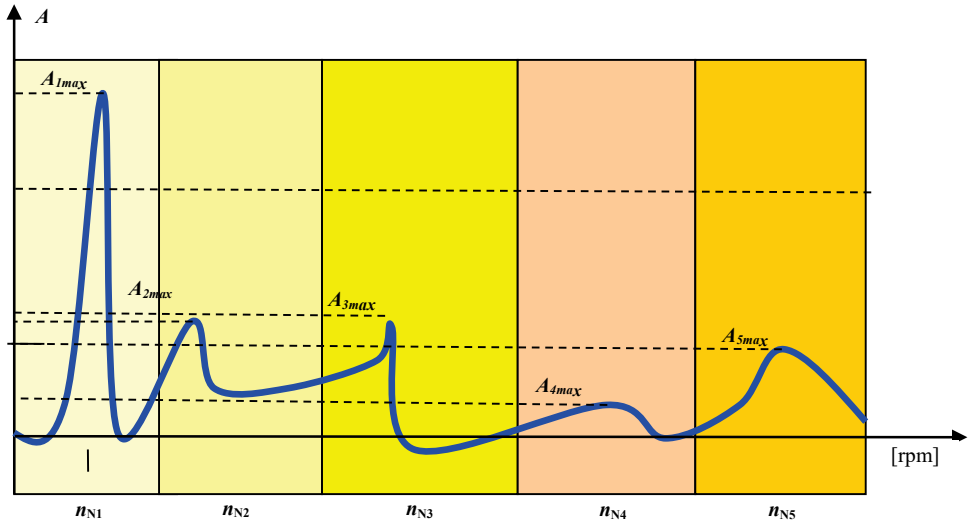

Fig. 5.40. Local resonance phenomena observed for the rotational speed after deactivating the energy source with marked rated speed bands $\{n_{N1}, n_{N2}, n_{N3}, n_{N4}, n_{N5}\}$ on a Fourier analysis image of the sample waveform $A = f(n)$

Conceptual design of testers for diagnosing the condition of aircraft transducers

Due to the significant number of electromechanical transducers installed onboard aircraft of the Polish Armed Forces and Polish Navy ships, their operation-related ageing, increasing failure intensity and economic savings, it is reasonable to develop a system for diagnosing transducers based on compact testers [112, 115, 117]. This would enable operating electromechanical transducers in accordance with their technical condition. The proposed diagnostic system, with an initial designation SD-PTE, including an electronic tester for electromechanical transducers designated ETP, and a database for data collection and recording designated BD-PTE, will allow to automate the diagnostic process, thus ensuring the correct

operation of aviation electromechanical transducers, while limiting the involvement of operators to pressing the "Start" button once and entering the factory number of the test object. The tester will employ all the diagnostic methods applied so far in the course of aircraft testing, both classical (i.e., measurement of power quality parameters included in the Defence Standards) and discrete-frequency (FAM-C and FDM-A). As part of the preparation, the authors developed and functionally verified measurement systems that enabled measurements using the FAM-C and FDM-A methods during the run-up of electromechanical transducers [112, 115, 117]. The DC motor reversibility feature would be employed in this case – the transition from motor to generator operation. Therefore, the diagnostic measurement would be implemented using the FDM-A method [6] based on analysing the pulsation component frequency dynamics [18, 20÷22]. To this end, the motor excitation winding would have to be energised upon de-energizing the transducer. The following parameters were measured:

a) total time to rotor stop (indicating overall bearing fitness);
b) characteristic set height changes.

Analysing the parameters of individual pulsation components of the electromechanical transducer diagnosing tester would allow to determine and potentially locate such failures as:

- winding short-circuit,
- winding discontinuity,
- rolling bearing wear.

The tester will enable indicating the wear degree of individual components within a transducer installed onboard an aircraft. The BD-PTE database will allow to record data assigned to individual transducers and aircraft. At the same time, statistical data processing will also be conducted therein. It will also allow to track the wear of individual components as a function of flight time, and display aggregate lists of the generator technical condition on all aircraft within a given aircraft squadron. This, in turn, will enable switching from the current system of operating generators in accordance with their service life, to operation based on their technical condition, thus providing tangible economic benefits. A significant number of transducers previously covered by a calendar-based overhaul could now be operated for longer periods before overhaul is necessitated.

6

STUDYING THE TRIBOLOGICAL PROCESSES IN ROLLING BEARINGS USING THE FAM-C AND FDM-A METHODS

6.1. Basic wear models for single-shaft engine bearings based on empirical studies, taking into account their monitoring with the FAM-C and FDM-A methods

Some cutaway aspects of wear models are briefly discussed in subsection 3.2, where the relationships between the kinematic pair defects and FAM-C and FDM-A method imaging are presented. Most relationships reviewed therein are elements necessary to understand this chapter, where the view on a bearing node is much broader – not only does it take into account the friction processes in the bearing itself, but also the geometry of the entire engine and its numerous components. Therefore, the primary author of this manuscript has suggested a working expression covering these issues, namely, "comprehensive tribological wear models".

In his studies on observations (using the FAM-C and FDM-A methods) of TS-11 Iskra aircraft SO-3/3W engine bearing node tribological processes, the author distinguished four types of rolling bearing wear models [114, 136]:

1) model of increased passive resistance,
2) model of rolling elements clamped between races,
3) model of increased radial clearance - taking into account the resonant aspect,
4) model of "increased longitudinal clearances".

The author based this division on airfield measurements involving actual objects, to facilitate developing a diagnostic decision in terms of their further operation. This is because the author realised that, making such a decision requires more than comparing individual measurement parameters obtained through FAM C and FDM-A with their limit values [129], since simple relationships (Chapter 3 of this paper) establish rather complex correlations in an actual turbine engine. These correlations will be thoroughly discussed in the following subsections. The author believes that this division has proven itself – the engines decommissioned at the author's request exhibited significant bearing node wear; moreover – most was in line with the author's predictions in the test reports drawn up at the time of engine decommissioning, i.e., well before its disassembly [114, 136, 266].

6.1.1. Model of increased passive resistance

The major phenomenon in the case of the model of increased passive resistance is frictional resistance, while the primary parameter when employing the FDM-A method is the height of the characteristic sets. When their height rises, the total resistance also esculates (Figs. 6.1 and 6.2) [129, 266]. Characteristic set heights tend to increase directly proportionally to engine operating time. This is generally true for all engine rated angular velocities (seven such values were determined in the case of TS-11 Iskra). The surge can be as intense as that in Figs. 6.1 and 6.2, which illustrate the characteristic set heights of the central bearing (for seven rated engine speeds) after 30 h of post-overhaul operation.

Experimental sequence of increasing passive resistance in an AFIT engine test house

In order to determine the total bearing resistance limit required to maintain an adequate safety margin for the engines diagnosed, a controlled central support bearing seizing experiment was conducted that involved two engines at an AFIT engine test house [266]. The test was implemented on two turbojet engines:

- with very low backlash,
- with medium backlash.

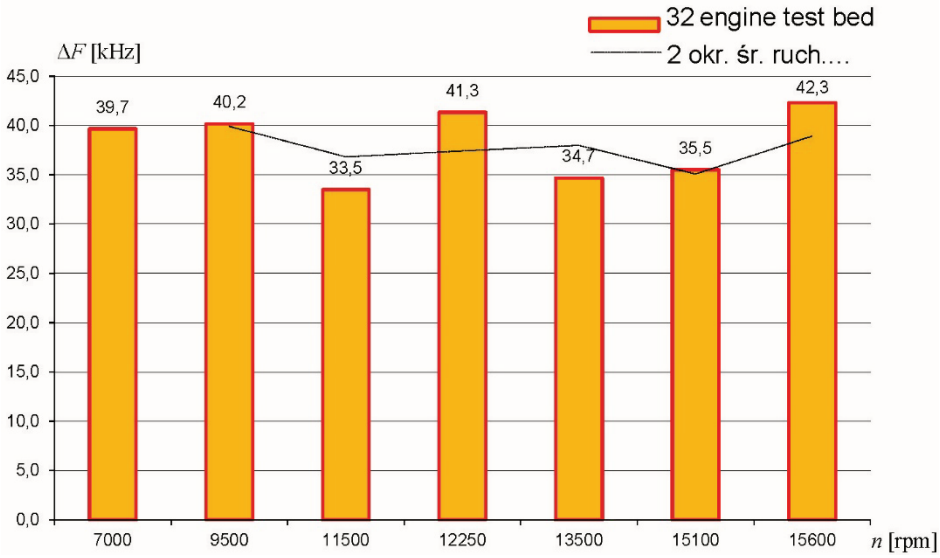

Fig. 6.1. Characteristic set height (for seven rated engine speeds) of the central bearing in engine No. 215 during a post-overhaul FDM-A test

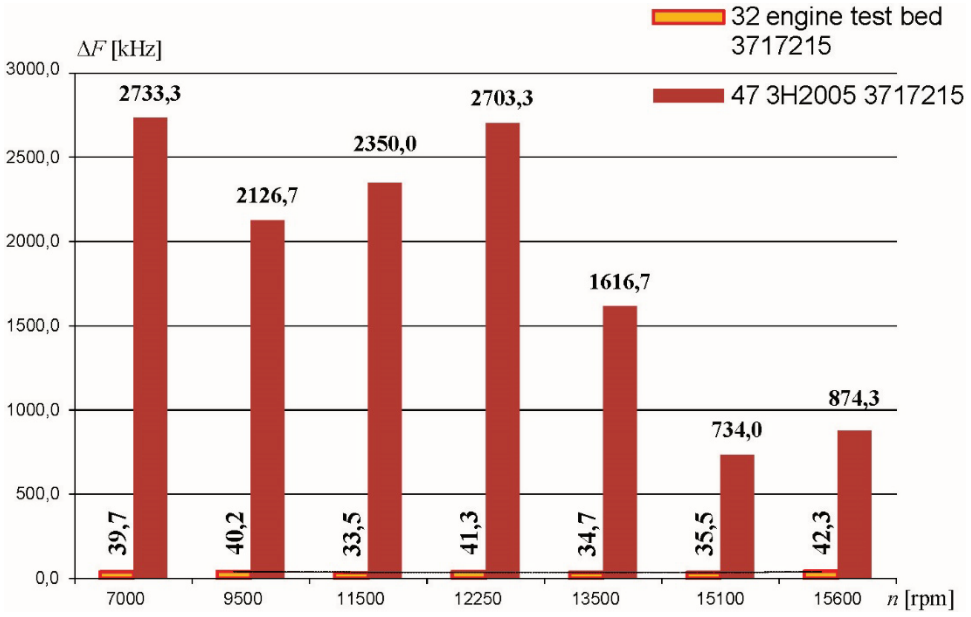

Fig. 6.2. Characteristic set height (for seven rated engine speeds) of the central bearing in engine No. 215 during the FDM-A test after 30 h of operation (post-overhaul): "32 engine test house" – after an overhaul in the engine test house, "47 3H2005" – in service after installation onboard the aircraft, after 30 h of operation

Both engines were stored without maintenance for the same period (approximately two years), which led to significant corrosion processes. Abrasive powder – a fine-grained steel-silver granulated product obtained from the milling process of the bearing cage surface – was put into both engines. The engine with very low backlash did not exhibit any signs of deterioration, despite the analogous pouring of abrasive powder – after 6 h, the test was discontinued for economic reasons. The engine with medium backlash failed within a few hours of operation (about 3 h) – certain rolling elements got blocked, and switched from rolling friction to slide friction. This was followed by a significant temperature rise in the central support bearing region, leading to softening of the journal. As in [172], pouring in the abrasive powder **at the beginning of the test** (first stage) brought about a decrease in the friction force. According to [172], the abrasive powder induces the removal of corrosion elements in the bearing, as well as the removal of lubricant surface films; however, these films have the potential to regenerate quickly at this stage. It is likely that the furrowing [56] of the rolling bearing race surfaces has not yet produced significant changes at this stage that are sufficient to hinder the rolling resistance of the rolling elements. Moreover, the abrasive powder under the rolling elements probably reduced rolling resistance. The observations with the FAM-C method indicated a decrease in the characteristic set height.

Next, at the **second stage**, after a certain period of increasing the metallic filing content in the lubricating oil, there was an intensive increase in the friction forces within the bearings – the surfaces without oxide films were subjected to adhesion [172, 266]. Adhesive bonds are formed at the interface between the bearing cage surface and the rolling element surface. Therefore, some rolling elements at this stage are permanently or intermittently blocked – locally, they slid instead of rolling on the race, i.e., a sliding contact was formed instead of a rolling contact [266]. Obviously, enhanced energy dissipation takes place in such locations – significantly more (relative to rolling friction) thermal energy is released. Adhesive bonds are also formed between the rolling element and the race. They can cause *stick-slip* friction [269]. These lead to an intensive surge in circumferential vibrations within the turbine engine rotor assembly.

Subsequently, at the **third stage**, after a certain duration of the pouring process, the frictional forces in the bearings declined – on average, the number of adhesion tacking diminishes and characteristic set heights decrease. Probably, due to a prominent temperature rise on the bearing race surface, the contact area layer becomes liquid, which considerably reduces frictional resistance, despite the fact that most rolling elements were blocked at this wear stage. After a fairly short period of time (about 30 min), the journal temperature increased so markedly that it

caused cross-softening. This induced a secondary shift in the rotor assembly mounting geometry at the central support and brought about significant engine vibration due to rotor assembly unbalance.

Extreme wear effects of the following types can also be distinguished [129]:

a) thermal: temperature rise at the splined joint between the turbine shaft and the compressor shaft (Fig. 6.3)[1], subsequent softening of the central support rolling bearing journal (Fig. 3.42), uncoupling of both shaft parts, thrust reduction, turbine build-up, air crash;
b) related to engine geometry – increasing rotor assembly unbalance due to a permanent deformation of components associated with engine rotor assembly bearing geometry;
c) related to bearing geometry – turning process fading – flat surface grinding appears on certain rolling elements (Fig. 6.4), which indicates that turning has ceased.

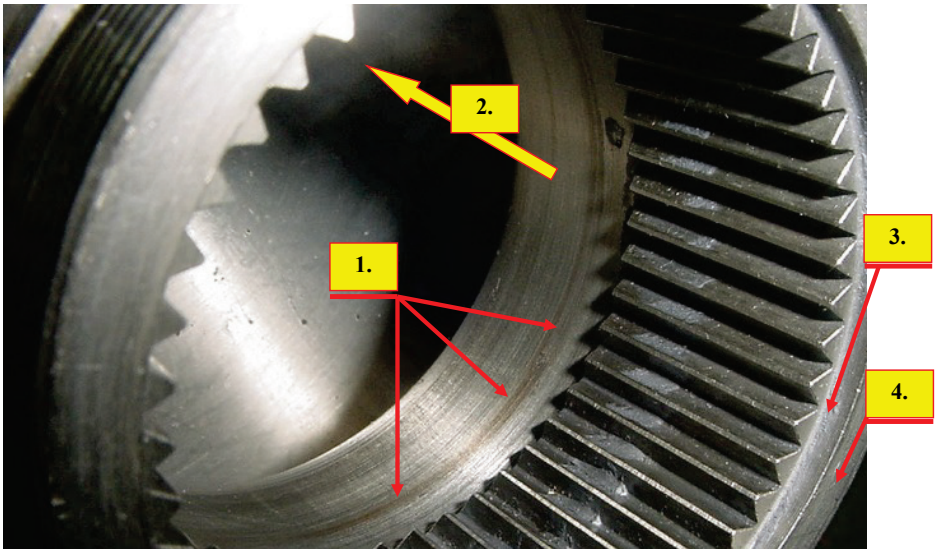

Fig. 6.3. Overheating traces inside the turbojet engine central support rolling bearing journal: 1 – discolouration ring (yellow tarnish), 2 – flight direction, 3 – central bearing journal with internal spline for connection to the propulsion turbine shaft, 4 – internal bearing race

[1] The photograph with interpretation was obtained from Maj. Eng. Albert Ostrowski. It is possible to prematurely detect such discolouration through boroscope inspections, benefiting from the fact that the engine shaft is internally hollow.

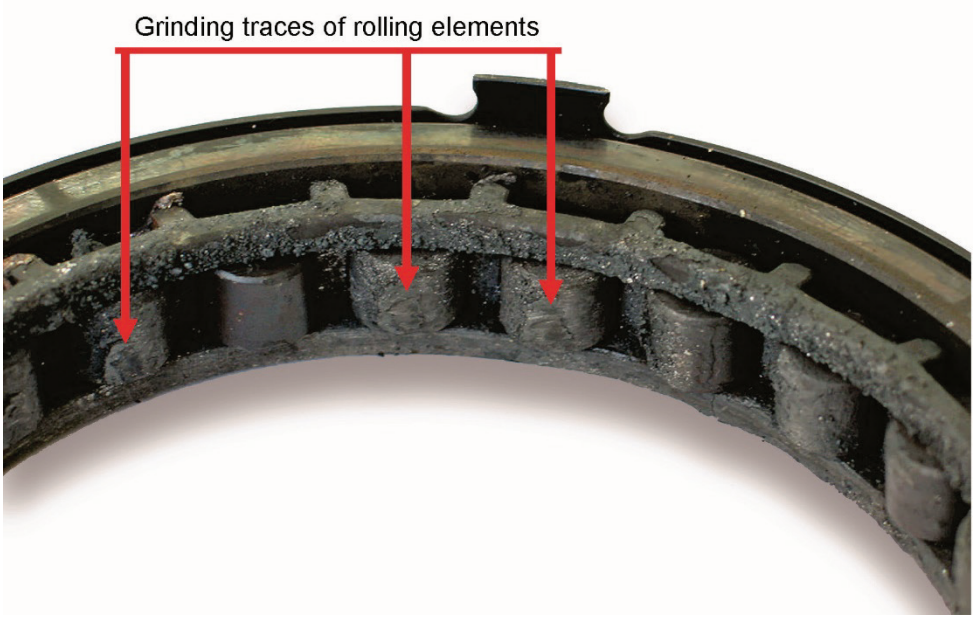

Fig. 6.4. Roller bearing after operation in an environment with increased filling content in the lubrication system

In the case of an extremely contaminated bearing, as demonstrated by tests of controlled filling content increase in an engine test house, the shape of the characteristic set height envelope in the diagram $\Delta F = f(n)$ changes. A relative climb in the characteristic set height for middle speeds (for the TS-11 Iskra engine n = 11 500 rpm) is generated. The author called this envelope "shape resonant" (see the definition in the "Basic definitions and designations" section), as it resembles the characteristics of an electrical resonant system. The relative height value expands directly proportionally to the degree of rolling bearing contamination (Fig. 6.5).

It should be stated that a characteristic with a "resonant" shape is also obtained after the cage descends on the central race (subsection 3.2.3). Therefore, it can be universally concluded that the resonant shape of the characteristic set height can indicate unnatural direct contact between rolling bearing races.

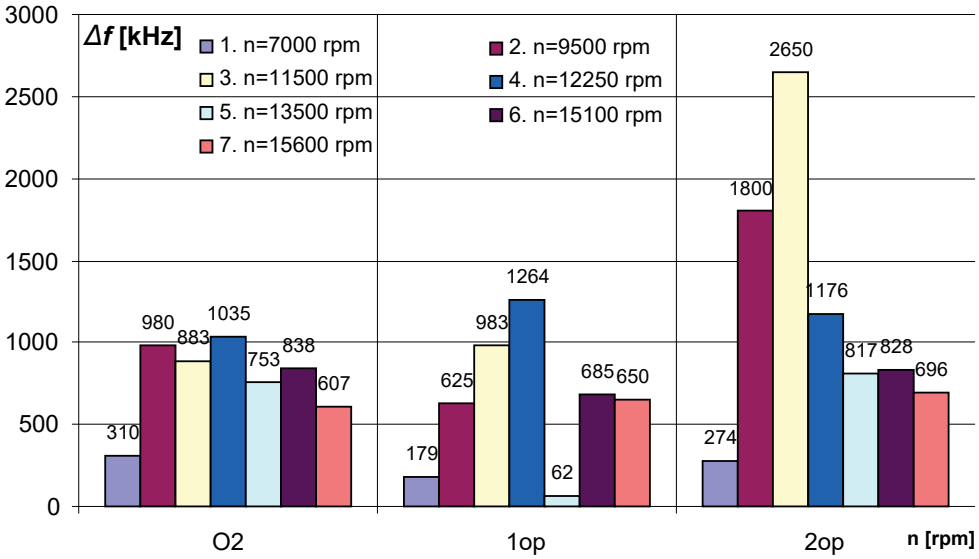

Fig. 6.5. Changes in the central and rear rolling bearing DC characteristic sets during controlled seizing of a turbojet engine: O2 – baseline, 1op – abrasive powder pouring stage I, 2op – abrasive powder pouring stage II (higher degradation rate)

6.1.2. Model of rolling elements clamped between races

There are two phenomena for this model:

- adhesive forces (the interaction of two surfaces – rolling element and race, and a rolling element and bearing cage – so close together that there is an adhesive surface bonding of material atomic structures) [15, 291],
- material heating induced upon the appearance of compressive forces[2] [182, 268].

The FAM-C method can be employed to observe [118, 119, 129]:

a) the DC characteristic set height rises with the increase in the successively induced rated speeds (Fig. 6.6),

[2] According to [176], p. 87, 4.3. Friction in rolling bearings. The genesis behind rolling bearing design was a widespread view that rolling-related frictional losses are incomparably lower than related to sliding. However, they do exist and are caused by a variety of the sources below "...When elastic bodies roll driven by a moment induced by a tangential force "S", the area entering contact is compressed, while the area leaving the contact is relaxed. As a result, material bulges in the inlet part, while there is a material deficiency on the outlet side, and the normal pressures within the contact area are no longer symmetrical relative the axis connecting the centres...".

b) the rolling coefficient p_s expands along with increasing rotational speed, an adoption of a monotonically declining characteristic follows after a destructive "backlash enlargement" (Fig. 6.7),
c) the spread of the rolling coefficient swells for a given rated rotational speed and reaches a value of $p_{smaxmax}/p_{sminmin} > 2$ (formula 3.11).

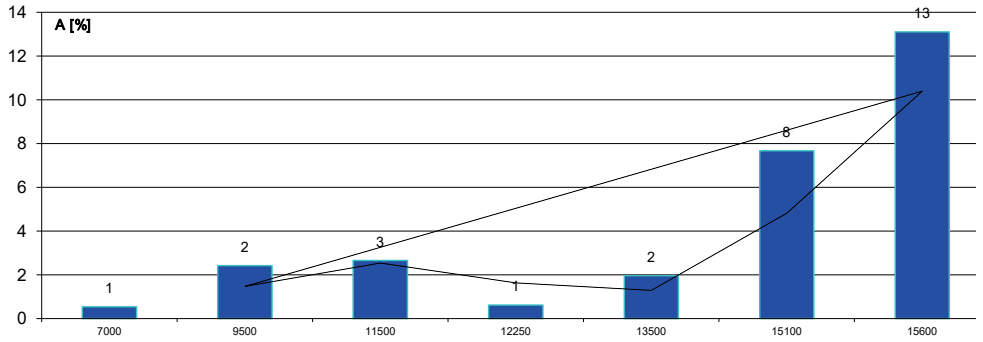

Fig. 6.6. Characteristic set height for a rolling bearing seated on a journal with excessive pressure as a function of the main shaft speed

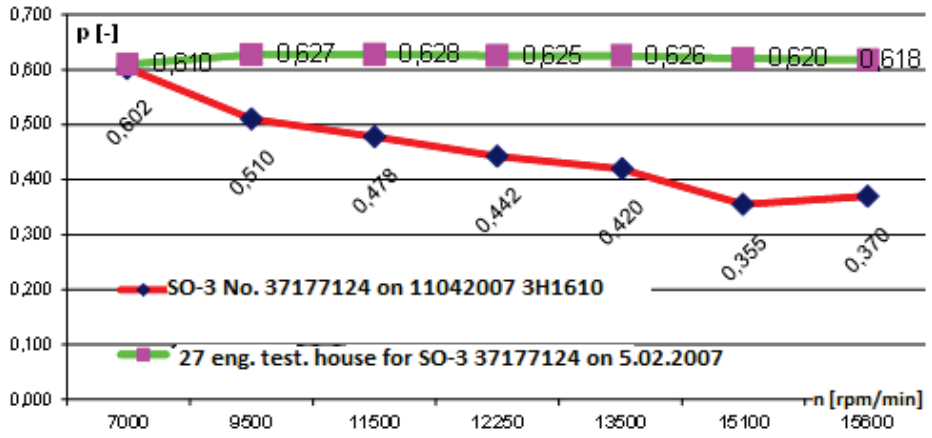

Fig. 6.7. Rolling coefficient characteristic for a rolling bearing seated with excessive pressure (green – after overhaul and excessive bearing compression) as a function of the rotational speed of the main shaft against "normal" characteristic (red), obtained after 13 h of operation

If the static[3] tilt coefficient exceeds 107% and the dynamic tilt coefficient reaches $p_{smaxmax}/p_{sminmin} \geq 3$Hz/Hz, this indicates very strong clamping of the bearing rolling elements between the races, which is destructive for bearing node durability. Reaching this parameter level qualifies a rolling bearing to be replaced. Prolonged operation of such a bearing can induce negative effects, such as excessive abrasive wear, pitting [167, 263] or even plastic changes of the rolling elements (Fig. 6.8).

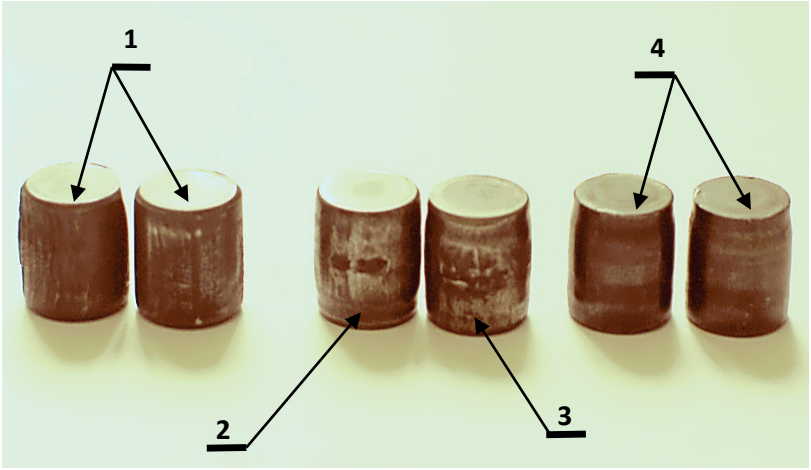

Fig. 6.8. Compared diversity of rolling element surfaces: 1 – "milling" and surface washboarding traces, 2 – pitting traces, 3 – fretting traces, 4 – conical smooth grinding traces

6.1.3. Model of increased radial clearance

The leading parameters in this model are mechanical radial clearances (mainly between rolling elements and races). Relationships can be observed [114, 123, 129, 136]:

- the DC characteristic sets height decreases[4] during operation, while individual bearing sets sometimes break up into subsets (subsection 3.2.4, Fig. 3.32) – passive resistances decrease,
- the value of the AC first harmonic increases – the values of engine main shaft suspension eccentric increase for lower rated speeds,
- the rolling coefficient value p_s decreases below the rated value p_{sN},

[3] The static tilt coefficient – quotient of the averaged rolling coefficient for the maximum rated shaft speed and the averaged value rolling coefficient for the minimum rated shaft speed – characterises the action of hydromechanical forces within a rolling bearing.

[4] The averaged characteristic set height for all rated rotational speeds reaches a level below 100 kHz.

– the increase in the average quality factor of DC characteristic sets (averaged over all rated speeds) $Q_{sr} > 11$, may be the cause for decommissioning an engine,
– the characteristics of characteristic set height as a function of rotational speed assumes a bathtub shape (Fig. 6.9).

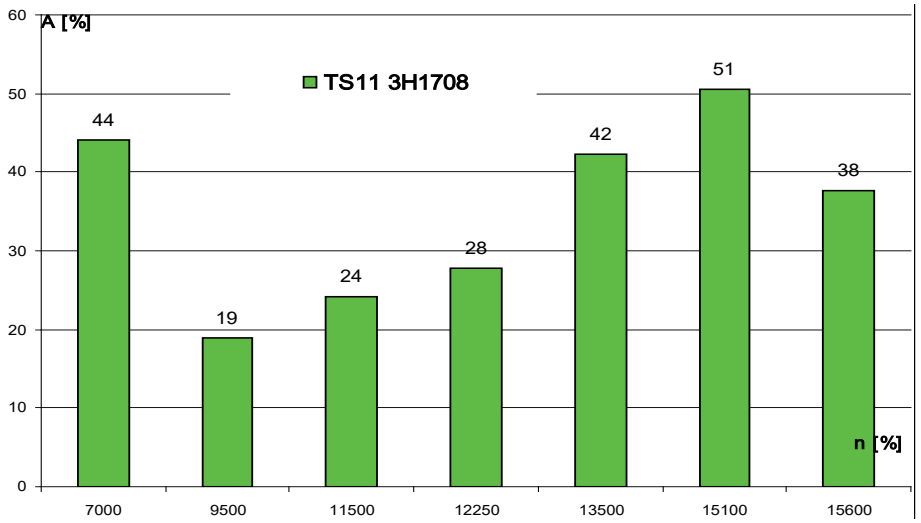

Fig. 6.9. Characteristic set of a rolling bearing with resonance

Increasing radial clearances makes the bearing more susceptible to the action of the so-called "rolling bearing underload"[5] [123, 129, 176]. Enhanced radial clearance promotes rolling bearing resonance. This resonance only occurs within a strictly-defined radial clearance range. Forces generated by resonance are largely "constrained" within the bearing volume. They lead to a systematic slow destruction of internal bearing components. Radial systematic and angular position-synchronised impacts of the rolling elements against the race and cage windows promote volumetric material decrements and induce impact forces [15, 73]. The most dangerous consequence of prolonged resonant force action on bearing elements is the disruption (rupture) of the cage separation elements. This induces pulsed deceleration forces between the races due to the direct interaction of the

[5] [176], p. 84, "Due to centrifugal force, load distribution onto individual rolling elements deteriorates, as in the case of excessive bearing clearance. This phenomenon is particularly dangerous in slightly loaded bearings, such as jet engine bearings. The increasing clearance entails a decrease in the load angle Ψ_z and only a small number of rolling parts are loaded and driven by the inner ring. In turn, due to the centrifugal force on the outer race, all rolling elements are loaded and induce motion resistance, which consequently leads the cage assembly to slide against the inner ring...".

rolling elements. This results in periodic locking forces (subsection 3.3.3) – the FAM-C method can then be employed to observe spike pulse bundles (Fig. 3.50). The number of pulses in a bundle is equal to the number of ruptured rolling elements [113, 114, 123, 129].

In the case of the model of increased radial clearance without resonance ($Q < 10$) – journal radial vibration amplitude increases, thus modulating angular velocity and escalating the torsional torque. Typically, rolling coefficients assume very small values, below the rated value, especially for the maximum rated speed of the engine. This indicates free movement of rolling elements between the races. The TS-11 Iskra aircraft engine is decommissioned if $p_{s15600} \leq 0.16$ for $n = n_{max}$ (n_{max} 15 600 rpm). The AC first harmonic value is equally important – if the first harmonic (averaged over all rated speeds) for a TS-11 engine is $h_o > 52.4$ Hz, the engine is decommissioned from further operation due to excessive radial clearance. High radial clearance induces the dynamic underload phenomenon. It involves a periodic lack of contact between a given rolling element and both races, and the cessation of rolling. This reduces the angular velocity of this rolling element. If an aircraft then begins to perform figures that require greater piloting skills, the gyroscopic precession forces (engine shaft spinning moment tends to coincide with the rudder aerodynamic force inducing moment) induce a strong compression of both races, which forces the rolling element to rapidly increase its angular velocity up the rated value. Because the rolling element has a certain moment of inertia, there is slippage between it and the race, often associated with material loss on the surfaces of mating components. This is the reason why engines with increased rolling bearing radial clearance should not be installed on aerobatic aircraft.

The FAM-C and FDM-A methods enable relatively easy identification of resonances and determination of the bearing destruction degree. The most important parameter is the quality factor Q. It is simply determined for each bearing based on the limits of its characteristic set. Various authors from this field [31, 39, 40, 176, 207] suggest that bearings that have reached $Q = 10$ should be decommissioned. The author believes that short-term (in the order of a few operation hours) overshooting of this level does not lead to visible damage. Longer operating times (over 40 h) at $Q \geq 10$, however, may lead to tangible destruction beginnings such as:

- damage to the bearing outer race in the form of so-called “false Brinell impressions” [95, 98, 114, 118, 126],
- breaking out of bearing cage separating elements [114, 136],
- fracture (breakage) of cage rings.

The first case is observable via the FDM-A method and is characterised by a systematic growth of the characteristic set quality factor up to $Q = 25$. The second

is notable by way of the FAM-C method – spike pulse bundles appear on the waveform $f_i = f(t)$. These bundles are generated every 1 revolution of the bearing journal. The appearance of such pulse bundles prompts immediate decommissioning of a rolling bearing.

6.1.4. Model of increased longitudinal clearance

A phenomenon important in this model is the multi-vector geometric displacement of engine components within the framework of increased longitudinal and transverse clearance. This applies not only to engine bearing supports, but also, among others, to both main shaft sections. The following can then be observed [122, 136]:

a) instantaneous frequency waveform $f_i = f(t)$ in the AC channel has undercuts[6] on waveform slopes (Fig. 6.10),
b) the waveform of the $f_i = f(t)$ function in the AC channel has a significant amplitude modulation depth ($p > 30$ %) (Fig. 6.10),
c) the value of the AC characteristic set height at the frequency of the first sub-harmonic is significantly higher than for other wear models. This indicates considerable skewness of the compressor shaft relative to the engine turbine shaft (subsection 3.1.4),
d) the height characteristics for DC characteristic sets as a function of rated speed (at advanced wear) has a "resonant" shape, i.e., a bulge in the characteristic set height for medium speeds is observed (Fig. 6.11),
e) the slow-variable component $f_i = f(t)$ (after increasing the time on the 0-x axis relative to the waveform in Fig. 6.10) is oscillatory (Fig. 6.12).

[6] A typical waveform has a quasi-sinusoidal shape.

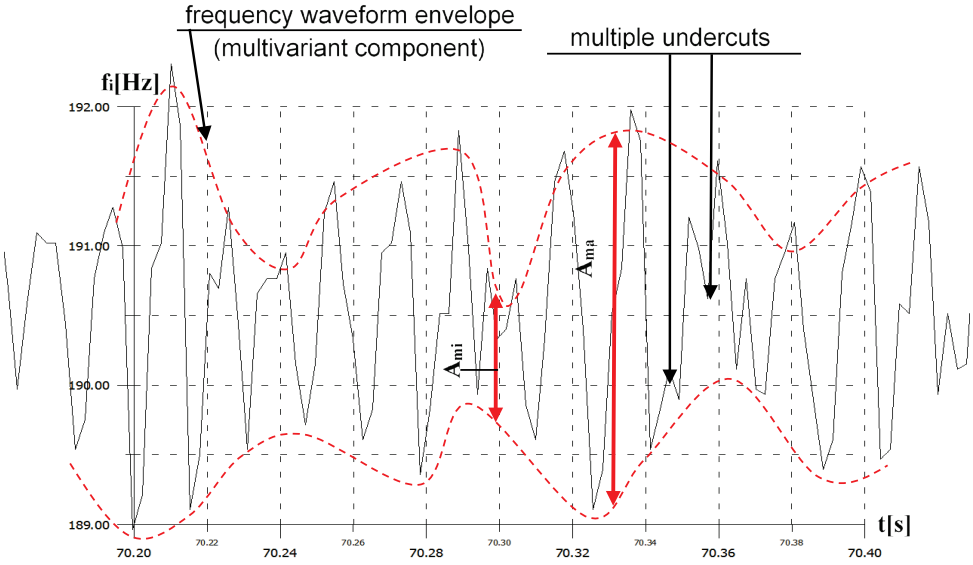

Fig. 6.10. Waveform $f_i = f(t)$ – FAM-C method – visible fast-variable quasi-sinusoidal component with multiple undercuts, amplitude-modulated by a slow-variable component

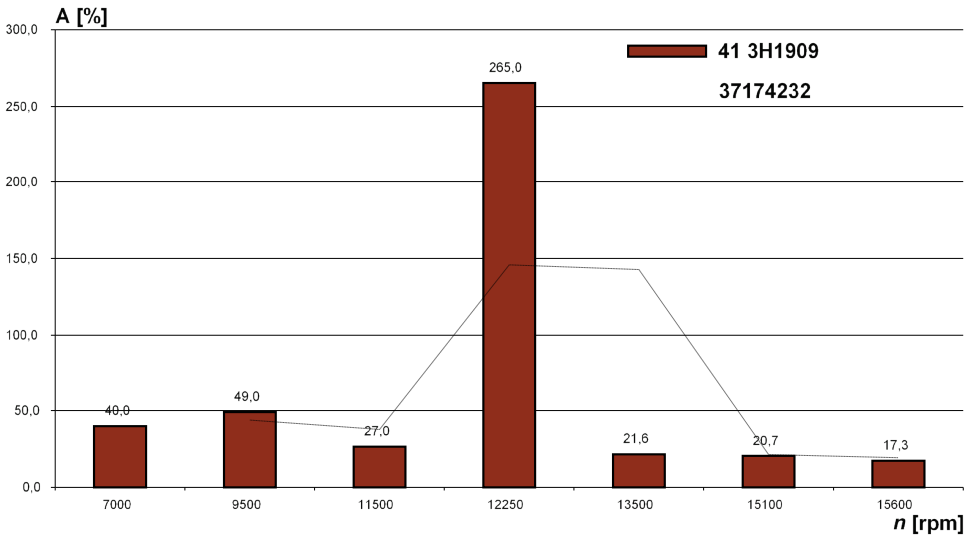

Fig. 6.11. "Resonant" shape of the AC channel characteristic set height envelope (FAM-C method) for a central bearing with increased longitudinal clearance

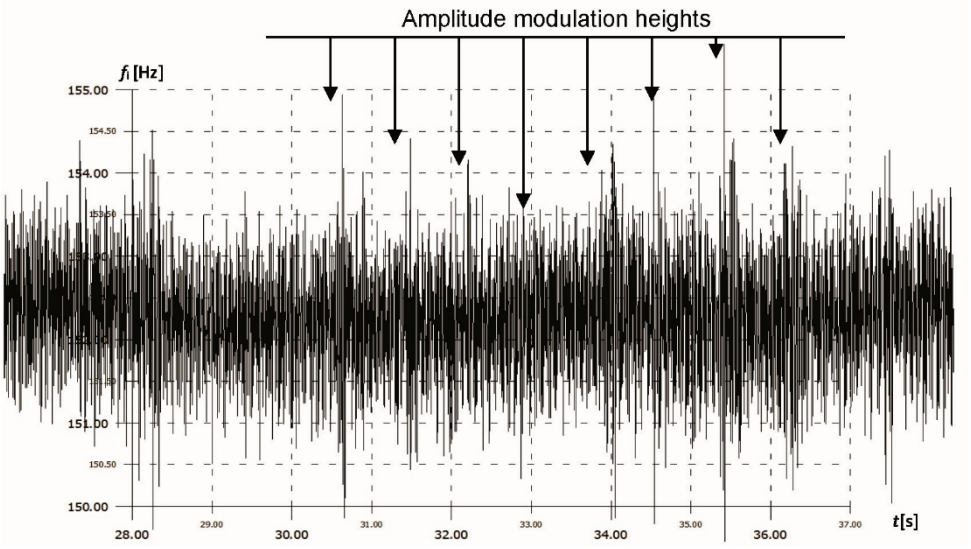

Fig. 6.12. Waveform $f_i = f(t)$ – visible slow-variable component (envelope) with significant amplitude modulation (p30%)

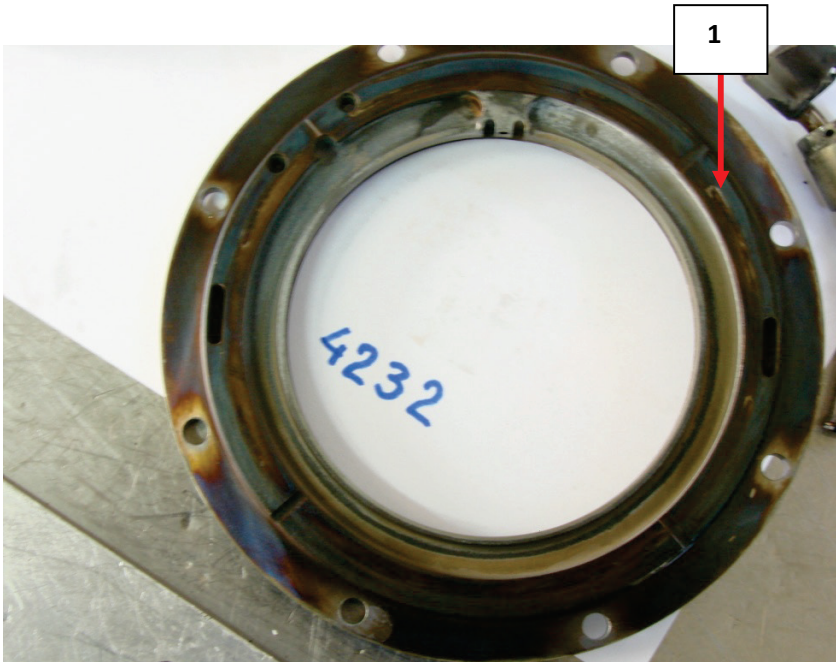

Fig. 6.13. SO-3 engine No. 22 central support rolling bearing cover with traces of mechanical impact: 1 – longitudinal force impact trace

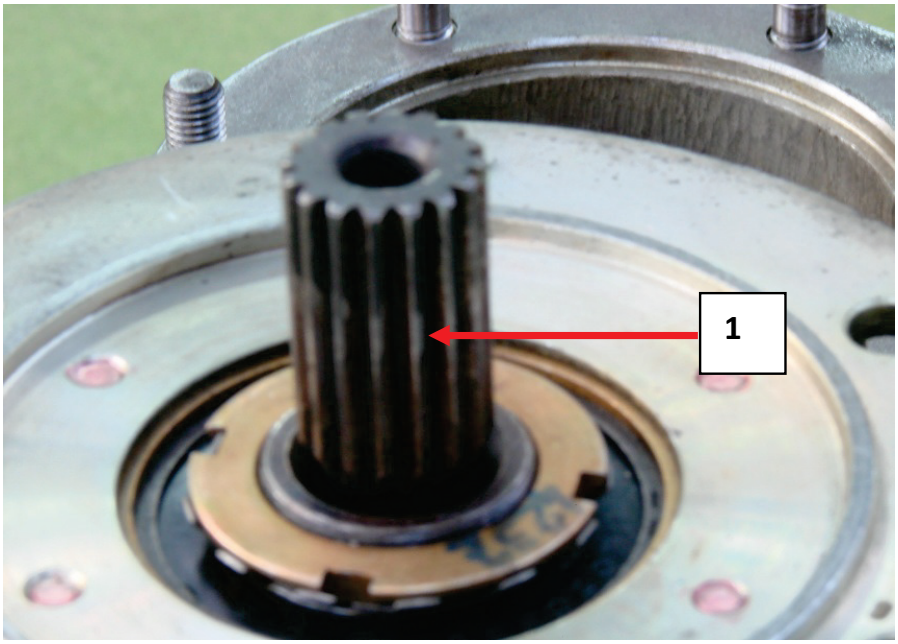

Fig. 6.14. Drive shaft of the GSR-ST-6000A generator in the SO-3 engine with barrel-shaped decrements on the spline tooth contact plane, characteristic of skew: 1 – trace of material decrements on drive shaft splines

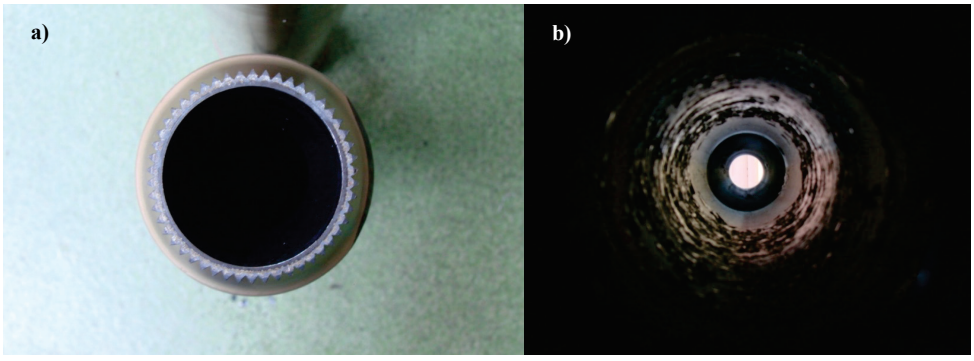

Fig. 6.15. Interior of the SO-3 engine turbine shaft with a defect involving increased central support longitudinal clearance: a) overview, b) close-up – visible flaking soot deposits

A prolonged presence of such parameters may lead to strong impacts of the bearing ring against the bearing cover (Fig. 6.13). Typically, excessive longitudinal and transverse loosening involve all moving parts of the engine, including the jet

engine turbine. This, in turn, leads to rubbing of turbine blade tips against the exhaust diffuser. Moreover, the nut connecting the turbine shaft and the compressor shaft may become loose. The transmission system and power generator splines may also develop barrel-shaped abrasive wear marks that characterize the tribological wear of a splined connection with a skew defect (Fig. 6.14). Turbine shaft (hollow) interior is blackened (Fig. 6.15) by way of visible black soot deposits. Other shafts of this type are yellow in colour. Such a case indicates that the labyrinth seal system is partially damaged, most probably under the impact of strong, dynamic skewness. This resulted in lubricating oil penetrating the shaft, after which it evaporated and formed black carbon deposits.

6.1.5. Rolling bearing tribological wear test result summary – potential assessment of the current technical condition

This chapter discusses the results of the author's research on the tribological processes occurring within the rolling bearings of a single-shaft turbojet engine. The study was conducted by applying FAM-C and FDM-A methodology, supplemented by the results of mechanical measurements. The issues presented herein expand on the considerations in subsection 3.2, where the representation of individual broadband mechanical defects in individual roller bearings on FAM-C and FDM-A images was considered. The defects in these bearings, both assembly- and wear-related, were considered individually and assigned 27 metric parameter values. These values were calculated according to previously developed algorithms by building upon $\Delta F = f(fp)$ and $f_i = f(t)$. This chapter applies these representations based on strict metric parameters (obtained from FAM-C and FDM-A measurements) to create four comprehensive tribological wear models for rolling bearings. Each of these models was described by a corresponding algorithm that takes into account 27 elementary parameters. Each has its own specific characteristics of elementary parameter changes as a function of engine main shaft rated speed and a different correlation set use for its identification (usually composed of several elementary parameters and descriptions of elementary parameter change characteristics as a function of rotational speed and as a function of operating time). In addition, each model has a different elementary parameter or group of leading parameters. To end with, each model has negative benchmarks in the form of failed engines. These are protected against third-party interference and can be subjected to additional verification through mechanical measurements at any time. Alternatively, they can be covered by additional engine test house tests after assembly, in order to assess the service life of these models. This enables correcting both elementary and complex parameters so as to extend or shorten the service life of the engines currently monitored using the FAM-C and FDM-A methods.

The diversification of tribological phenomena in the case of the presented wear models is considerable. The impacts of extreme wear on bearing support components under individual tribological wear models are also interesting:

1) Model of increased passive resistance – increase in the journal temperature up to softening value – reduction in its strength and twisting – rapid build-up of rotor assembly unbalance and, ultimately, twisting of the journal – disconnection of both shaft sections, thrust decrease, turbine build-up (displacement of the turbine shaft, together with the turbine in the direction of the thrust vector – possible after rupturing the connection between two shafts), air crash.
2) Model of clamped rolling elements – uncontrolled plastic strain of rolling elements, tearing out of race surfaces, increased airframe vibration.
3) Model of increased radial clearances with prolonged bearing node resonance (at Q >11 for Θ > 58 h) – breaking out of cage separating elements, spot imprints (false Brinell impressions) on the race, cage periphery fracture, dynamic blocking of the rotational motion, peripheral breaking out of the outer ring from the seat or the inner ring-journal press-fit connection.
4) Model of excessive longitudinal clearance – barrel-shaped wear of splines (strong skew effect), which can ultimately lead to transmission disconnection, traces of strong impacts of longitudinal bearing rings against bearing covers, uncoupling of both shaft parts (compressor shaft and turbine shaft).

During long-term diagnostic observations of individual single-shaft turbojet engines conducted with the use of the FAM-C method, it became apparent [114, 136] that, over time, one tribological wear model can shift into another. This phenomenon is covered in the subsection that follows.

6.2. Long-term tribological wear processes and their monitoring using the FAM-C and FDM-A method

Predictions regarding the future operation period were made during long-term testing of a given engine using the FAM-C and FDM-A methods [114, 136]. Trend curves obtained during consecutive periodic tests of a given engine were included in the analysis. An engine with a bearing node meeting the criteria of the model of excessive reactive drag expected to reach the predicted limit value of the characteristic set height within the operating time $\Delta\Theta_1$ was often the case. Meanwhile, the bearing had "self-cleaned" of wear products before this time elapsed. This manifested itself as an intensive decrease in the characteristic set height of the DC measuring channel. The process can be explained by the fact that the increasing wear

product concentration between bearing components initially caused passive resistance increase. At the same time, clearances increased steadily. When clearance value exceeded the statistical mean of the abrasion product element (particle) diameter, they would escape from the bearing, being washed out by the cooling oil stream lubricating the interior of bearing supports. After self-cleaning, a significant growth in the quality factor of DC characteristic sets was observed. Therefore, a bearing node previously fulfilling the criteria of a heightened passive resistance model, had later fulfilled (after self-cleaning and after radial clearance increase) the resonant model criteria. Such phenomena can be observed throughout long-term operation when $\Theta > 50$ h of flight. The shifts from one tribological model to another are interesting enough that it was decided to devote this chapter to them.

Observations show that many bearing supports that systematically increase their characteristic set heights after several tens of operation hours modify their properties – the set height, initially monotonically increasing directly proportional to engine operation hours, starts to intensively decline at a certain point of operation time Θ. Simultaneously, the height attributes of characteristic sets change shape depending on the main shaft rated speed: from resonant (dominant at stage I) to bathtub (dominant at stage II). This shape change may indicate a transformation of the rolling bearing tribological wear model from increased passive resistance, to a structure typical of the resonant model (with enhanced radial clearances). At the same time, the quality factor of such a bearing extends. If the clearance value is optimal for the resonance phenomenon [123, 129], the quality factor assumes maximum values. The average quality factor can reach $Q = 14$. (Quality factors for individual speeds reach even higher values).

Several such transformations occur during inter-overhaul engine operation – these can be represented as graphs (Figs. 6.16 and 6.17). Fig. 6.16 illustrates changes in characteristic set heights of the DC measurement channel (FDM-A method). These heights sets reflect the value of the total resistance exhibited by the SO-3/3W engine bearing supports. Based on the monitoring data for the SO-3 engine [114, 136] obtained by applying the FDM-A method, characteristic set heights A were plotted as a function of the operating time (flight hours) Θ. Fig. 6.16 contains three local maxima of the characteristic set height: the first at $\Theta \approx 140$ h, the second at $\Theta \approx 250$ h and the third at $\Theta \approx 300$ h. Moreover, the successive characteristic set height maximums for a given rolling bearing exhibit increasingly higher values:

- dla $\Theta \approx 250$ h $A_{\text{ŁP}} = 499$ kHz, $A_{\text{ŚT}} = 350$ kHz,
- dla $\Theta \approx 300$ h $A_{\text{ŁP}} = 1756{,}2$ kHz, $A_{\text{ŚT}} = 1472$ kHz.

Simultaneously, the time of occurrence for each successive maximum is shortened relative to the preceding one.

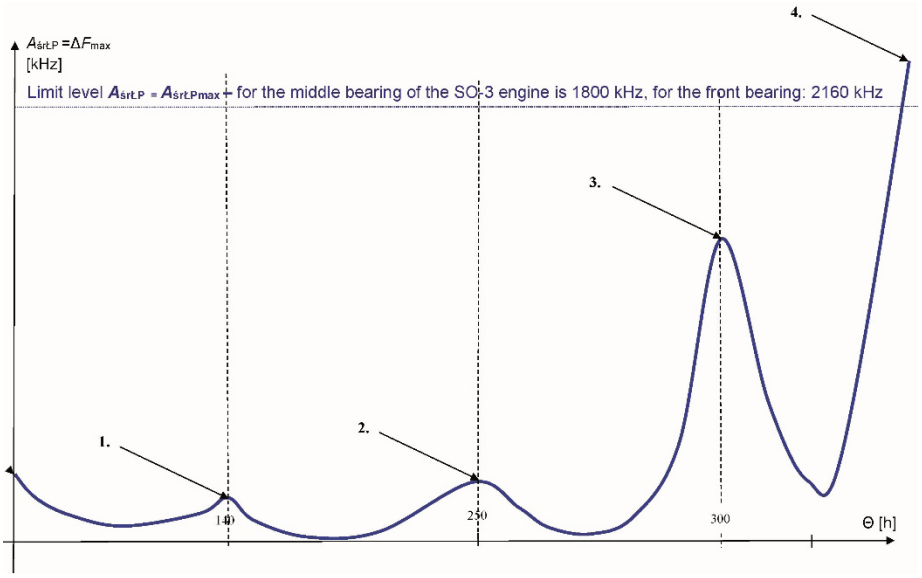

Fig. 6.16. Rolling bearing DC characteristic set height change waveform as a function of operating time ΔF_{max} = f(Θ). 1÷4 – number of the consecutive maximum characteristic set height

After long-term (400÷600 h) observation of the bearing representing the model of expanding passive resistance, the author concluded that successive local extreme values grow approximately in an exponential function. When it reaches the A_{gr} limit, the bearing must be immediately replaced. In turn, the time between subsequent extremes declines as an exponential function. Precise knowledge of these relationships will enable having the operated engine reach the limit value without jeopardizing the flight safety of the aircraft in question.

The bearing representing the model of increased radial clearance behaves in a different manner. Fig. 6.17 illustrates the change in the mechanical quality factor as a function of operating time (flight hours). Also in this case, several main parameter maximum values can be noticed. However, these maximum values expand exponentially up to a certain point only – until an extremely high value $Q = Q_3$ is reached. Once this happens, further maximum values decrease exponentially during further operation (increase in Θ). An extremely high $Q = Q_3$ is associated with a bearing reaching clearance values that are optimum for the formation of resonant states.

In order to visually synchronise the quality factor $Q = f(\Theta)$ waveform (as a solid line), together with the characteristic set height waveform $A_{ŁP} = f(\Theta)$, the latter is shown as a dashed line within the same rectangular coordinate system as a function of engine operation hours Θ (Fig. 6.17). It can be seen that waveform $Q = f(\Theta)$

is somehow shifted by 90° relative to $A_{ŁP}=f(\Theta)$. Therefore, when a bearing support assembly achieves a maximum for the $A_{ŁP} = f(\Theta)$ waveform, the minimum for $Q = f(\Theta)$ is achieved and vice versa. There are likely similar parametric substitution phenomena in the case of other wear models – one tribological wear model transforms into another [114, 136].

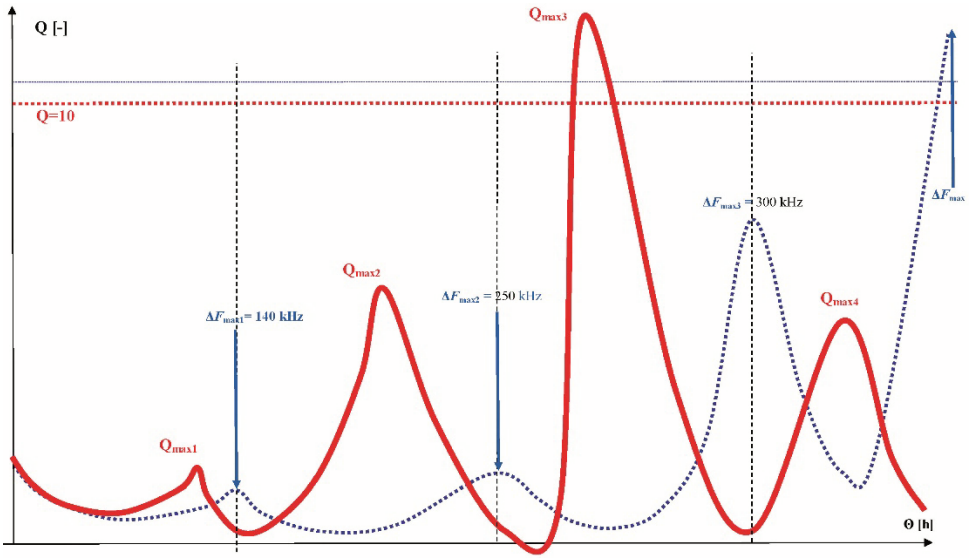

Fig. 6.17. Rolling bearing DC characteristic set quality factor Q change waveform as a function of operating time $Q = f(\Theta)$ (red solid line). Alternatively, the dashed line illustrates changes in the DC characteristic set heights, i.e., $\Delta F_{max} = f(\Theta)$

To sum up, a systematic increase in the level of the DC measuring channel characteristic set height ($A_{ŁP}=f(\Theta)$, $A_{ŁŚT}=f(\Theta)$), observed over a certain period of engine operation, does not necessarily prove that a given bearing will seize due to increased total frictional resistance. This process may be decelerated as a consequence of the wear model change (transformation to a different wear model) – e.g., characteristic set height (leading for the tribological model of increased total resistance) may reach a local maximum at a certain point, and then start to decrease. At the same time, an increase in another parameter is observed, e.g., the characteristic set quality factor Q (leading for the resonance model), which usually reaches its maximum value during operation when the first parameter reaches its minimum.

It is pretty much a rule that the model of expanding bearing support passive resistance transforms in the course of engine operation into that of increased central bearing radial clearance. The characteristic set height for that model is low, while the quality factor Q becomes the leading parameter.

Table 14

Quality factor and operating time for a TS-11 Iskra SO-3 engine

AFIT test No.	3	21	45	54	69	74	82	88
Flying time after general overhaul	189	219	234	247	253	259	283	295
DC set mean quality factor – resonance hazard	14	12.98	10.45	12.54	7.15	6.05	5.5	3.74
Product of exceeded permissible quality factor $Q_{ŁŚ}$ and operating time	90	29.7	-7.15	9.24	-23.1	-118.8	-66	-181.5

Periodic local maxima can also be encountered in the waveform of quality factor changes $Q = f(\Theta)$ – successive local maxima first start to increase, followed by a decline from a certain point onwards. The operation time Θ at which an extremely high quality factor Q occurs is related to achieving radial clearance with a value optimal for resonance induction. Based on source literature and mechanical verification of the bearing supports observed using the FDM-A method, the permissible quality factor Q_{dop} was determined at 11. However, when monitoring a certain TS-11 Iskra SO-3, the author observed Q = 10.45÷14.00 for an operation time ΔΘ = 247 h-189 h = 58 h, without external failure symptoms. Here, answer intuitive answer comes to mind that the structure would have failed after exceeding, not so much the quality factor Q, but the product of the quality factor (actually, the value over the permissible level value) and operation time ΔΘ. Such iteration totals for this engine amount to 129. The period (58 h) of exceeded bearing support quality factor above Q_{dop} = 11, the iterative sum of the products of the bearing support quality factor above Q_{dop}, and the operation time increments $Q_{dop} \times \Delta\Theta = 129$ can thus be considered as temporary limitations of bearing operation under extremely resonant conditions.

So far, the long-term processes of tribological model 1 (tribological model of increased passive resistances) transforming into tribological model 3 (tribological model of increased radial clearance) have been discussed. However, based on intuition, it can be intuitively assumed that similar transformations are possible for all tribological wear model types. The number of these combinations can be calculated from Newton's binomial $\binom{4}{2}$=6. Therefore, all that remains is proving the existence of transformations of tribological model types: 1-2, 1-4, 2-3, 2-4, 3-4.

Empirical investigations partially confirmed assumptions that other rolling bearing node tribological wear model types can also change in the course of engine operation. Another SO-3 engine is a good example. It experienced a change from a clamped bearing model to increased radial clearances [114].

A full documentation of the above and all other transformations requires a more in-depth analysis and additional research. It should be noted that the operation period between overhauls of the SO-3 engine is $\Delta\Theta = 400$ h. Meanwhile, the author can only conduct tests within 100÷200 h of operation, which hinders the analysis. In addition, the demand for a series of FAM-C and FDM-A measurements usually comes from the user in the event of experiencing unusual engine parameters (increased airframe vibrations, speed fluctuations, excessive filing content in lubricating oil, other unusual symptoms). There is no wider statistical sample of measurement results for engines with normative parameters.

Moreover, engines are often released for premature overhaul (for reasons independent of FAM-C or FDM-A test results, e.g., combustion chamber glow tube fracture, fuel system damage) without notifying the author of the possibility to conduct the test. Therefore, the possibility of monitoring certain phenomena important in terms of the theory of rolling bearing tribological model transformation is lost.

7

SUMMARY OF STUDY RESULTS – CONCLUSIONS AND FINAL REMARKS

The author's scientific accomplishments contain three main monographic studies documenting his progress in his research on the FAM-C and FDM-A methods, and representing peculiar milestones in studying their properties:

a) the PhD. thesis from 1998 [127],
b) the monograph from 2010 [129],
c) this monograph.

They all illustrate the enormous effort, primarily experimental, devoted to the development and implementation of these original methods based on the analysis of onboard generator frequency and phase modulations.

The study [127] documented the first correlations of single kinematic pairs in propulsion units with specific frequency modulation parameters. Here, the author focused on mechanical failures emitting a narrowband oscillation spectrum of speed fluctuations. Laboratory-controlled changes, e.g., shaft skew, indicated clear changes in the shape of the instantaneous frequency waveforms. These observations enabled the author to describe the mathematical relationships between the mechanical defect parameter and the parameters in the instantaneous frequency images obtained from the generator. Tracing long frequency variation waveforms was very labour-intensive, especially in the case of aperiodic mechanical phenomena such as the breaking of a shaft connection in a one-way coupling. Therefore, the author applied the discrete Fourier transform (DFT), which made it possible to track (in the FAM-C and FDM-A images) individual frequency waveform harmonics obtained from a given onboard generator. Each harmonic of this waveform reflected a different kinematic pair and a different fault type within

the propulsion unit under study. The DFT analysis did not often provide clear depictions, which hindered the analysis and making clear and accurate diagnostic decisions. An even greater issue arose when it was decided to develop the first tester for the automatic assessment of MiG-29 aircraft components, namely, one-way couplings and hydraulic block. Therefore, the author developed an original analysis method. It was employed to aid the creation of clear and easy-to-automatically analyse characteristic sets on the rectangular coordinate plane $\Delta F = \mathrm{f}(f_\mathrm{p})$.

Monograph [129] highlighted the potential of FAM-C methods in the field of monitoring aircraft turbojet engine rolling bearings. It also described three tribological models resulting from the diagnostic work involving SO-3 turbojet engines. Numerous measurements and analyses conducted on these engines emphasized the close relationship between various rolling bearing parameters seen through FAM-C and FDM-A imaging and the engine main shaft speed n. Thus, a third axis was added to the imaging in a rectangular coordinate plane – characteristic sets in three-dimensional space $\Delta F = \mathrm{f}(f_\mathrm{p}, n)$ were already obtained, Fig. 2.9. The possibilities of a three-phase FAM-C measurement with projection onto a single time axis were described for the first time. This allowed the author to apply the possibility of controlling the mechanical process measurement observability window in practice for the first time. From then on, it became possible to employ the same generator to observe slow-variable mechanical waveforms, followed by (after changing to a multiphase configuration) fast-variable ones. This paper is the first to describe the theoretical and practical application of simultaneous measurements using a DC and an AC generator.

The study precisely catalogues all imaging with kinematic pair defects described so far. It offers a pioneer subdivision of the mechanical defect classification according to the bandwidth occupied by angular velocity modulations induced by these defects. Four tribological wear models in rolling element bearings are described in detail. It is also the first to employ a fourth operating time axis Θ, which is necessary for the analysis of long-term wear predictions for turbojet engine bearing supports. While previous studies assumed that only diagnosing the kinematic pairs between the primary source of mechanical energy (e.g., turbojet engine turbine) and the generator-transducer rotor was feasible, this monograph proves that it is possible to diagnose side chains. An attempt was also made to comprehensively evaluate the errors and sensitivity of the FAM-C and FDM-A methods.

7.1. General monograph content summary

This paper proposes a multifaceted acquisition of information on the technical condition of a propulsion unit through analysing the output signal of a generator-transducer mechanically coupled to the test object. It reviews the FAM-C and FDM-A diagnostic methods. Successive transformations of the original diagnostic signal up to working out a diagnostic decision are presented. In Chapter 2, the author introduced the concept of the method, followed by (Chapter 3) creating a specific catalogue of mechanical faults and their representation in FAM-C and FDM-A. Chapter 4 analyses the metrological properties of these methods, after which (Chapter 5) a discussion of their practical applications begins. Finally, Chapter 6 highlights practical observations of tribological phenomena within rolling bearings of propulsion units tested by FAM-C and FDM-A methods. Based on the extensive research material collected, the author classified tribological phenomena occurring therein.

7.1.1. The concept behind the FAM-C and FDM-A methods

The creation and processing of a mechanical propulsion unit diagnostic signal is divided into stages:

a) Formation of the primary diagnostic signal in individual kinematic pairs of the propulsion unit under test – formation of the LF (low frequency) spectrum together with the carrier LF; the carrier frequency depends on the type of design – it can be read from the kinematic diagram of the propulsion unit in question. The LF spectrum around this carrier frequency is dependent on the type and magnitude of the kinematic defect, among other issues, the tribological process advancement or execution and assembly errors at manufacturing production or overhaul stages. Both the degree of tribological process advancement and assembly errors have a great impact on the correct operation of a given kinematic pair and, therefore, on the operational correctness, depending on the function of the entire propulsion unit. In the case of man aircraft or floating vessel designs, extensive damage to certain links can even lead to a disaster. The impact of propulsion units on operational safety is increasing in new designs due to rising speed and payload, as well as manoeuvrability and availability of transport. Therefore, the aforementioned primary diagnostic signal spectra should be particularly carefully examined in terms of their relationship to tribological processes and assembly defects. At the same time, the objective of any diagnostician should be to select diagnostic methods so that these primary spectra can be reproduced as faithfully as possible and assigned to individual kinematic pairs. This will enable reading the degree of

wear on individual kinematic pairs. Further analysis of a given propulsion unit's structural diagram allows to estimate the operational safety risk level and set out deadlines for replacing individual subassemblies within given periods, preventing the maintenance personnel from being surprised by unexpected failures.

b) Transmission of the primary diagnostic signal through the mechanical links to a generator-transducer. This transmission is a conventional concept in this monograph, which involves the transmission of angular velocity modulations from a faulty kinematic link to a generator-transducer rotor. Its meaning is more akin to a telecommunications definition than a mechanics definition. As has been demonstrated, such transmission can proceed in two ways, depending on the energy relationships between the damaged kinematic pair and the generator-transducer rotor:
   – the observed kinematic pair is in the main path of the mechanical power transmission between the primary energy source (e.g., a gas turbine and generator-transducer).
   – the observed kinematic pair is located outside the primary path of mechanical power transmission (located along the side path) – it can induce frequency-phase modulations in the generator-transducer if the moment of inertia of this pair (its vibration energy) is significant enough to modulate the kinematic chain between the side path and the generator-transducer.

   The condition of adequate stiffness of the kinematic pairs acting as intermediate links in the primary diagnostic signal transmission to the generator-consumer must be satisfied for both methods. Two mechanical parameters are included in this concept:
   – structural rigidity of intermediary elements – elements that are too flexible result in the dispersion (dissipation) of mechanical energy into heat – this is the amplitude condition, so to speak,
   – stiffness in the sense of mechanical backlash – according to the Kotielnikov-Shannon theorem, at least one period of the observed HF signal can be transmitted during one meshing period.

c) Reception of the primary diagnostic signal by a generator-transducer rotor. In this case, higher harmonics of the instantaneous angular velocity signal spectrum (LF) are partially attenuated by rotor inertia. Lower components excite mechanical angular movements of this rotor. The total (complex) LF spectrum is then summed in the generator rotor. Voltage is induced in the rotor windings due to the existence of the generator stator contributing a stable electromagnetic field. The frequency of this voltage is directly proportional to the instantaneous angular velocity of the generator rotor. Therefore, the generator frequency variation waveform reflects the HF spectrum change waveform. The

generator-transducer is a kind of a mixer-heterodyne, which transfers the high-frequency spectrum into the higher frequency range. The complex low-frequency spectrum is thus shifted into the high-frequency band. This way – according to theory – the primary signal becomes immune to interference from other sources, e.g., other mechanisms [3, 27, 228, 229, 231].

d) Transmission of the complex HF spectrum over the electrical grid of an aircraft or vessel. The electrical grid is the equivalent of an HF signal transmission medium for telecommunications transmission. As is well known [32, 35, 67, 164, 174, 195, 262], transmitting a signal over a cable network is more immune to interference than transmitting that signal over airspace. The FAM-C and FDM-A methods benefit from these properties. However, the telecommunications cable network is a network specifically designed to exchange information. Meanwhile, the electrical grid onboard an aircraft or vessel is designed and constructed not to transmit information, but to provide electricity to power consumers. At the same time, it must be as cheap as possible (cost minimization) and lightweight (weight minimization to improve aircraft aerodynamic properties), hence the need to transmit return current through the body of the aircraft. The aircraft must have a flexible body, hence the enormous number of overlap seams on the plating. These seams are simultaneously sources of sometimes significant, and, even worse, value-variable connection resistances. This raises the issue of additional modulation changes. The onboard electrical grid must offer energy distribution, hence the need for commutation systems: contactors, relays, emergency shutdown systems for certain grid sections in cases of non-compliance with quality requirements – such switching generates impulses – interference sources for diagnostic signals. In addition, the onboard grid has voltage regulation systems that act as a low-pass filters for diagnostic signals. Simultaneously, they are an automation element, characterised by significant gain and feedback, thus, in some situations, they can become a source of self-excited oscillations of the power grid.

e) Diagnostic signal detection – recovery of the original diagnostic signal (LF) from the high-frequency band. This enables recovering the original diagnostic signal (LF spectrum recovery) and analysing it. This signal will be slightly impoverished relative to the original signal because:
   – according to point c, higher harmonics of the instantaneous angular velocity signal original spectrum (LF) are partially damped by rotor inertia in the course of electromechanical processing,
   – generator-transducer primary sampling discretisation error comes into play,
   – of the digital measuring system secondary sampling discretisation error.

f) The metric parameters necessary for the quantitative evaluation of tribological processes are calculated based on FAM-C and FDM-A imaging. This analysis makes it possible to monitor the motion dynamics of individual mechanical components within the investigated propulsion unit – an attempt to discover the causes behind wear phenomena, select limit parameter values, comprehensively assess the technical condition and make short- and long-term forecasts with preventive measures proposed to a user of a particular aircraft or floating vessel.

7.1.2. Catalogue of mechanical failures and their reflections in FAM-C and FDM-A

In this monograph, the author has compiled material (to some extent already published previously under single papers) that comprehensively illustrates the relationship between the mechanical-dynamic structure of a propulsion unit and the FAM-C and FDM-A imaging. A set of defects of various mechanical components in relation to their FAM-C and FDM-A imaging and specific diagnostic identification modules has been created. This will enable faster and more efficient diagnostic decisions.

Inspired by the source literature on radio engineering and signal theory, the author proposed dividing the numerous statements into three groups of defects and failures of mechanical components imaged by FAM-C and FDM-A:

a) narrowband,
b) broadband,
c) pulsed.

The guiding idea behind this classification was organizing the observed phenomena from the perspective of the band-frequency FAM-C and FDM-A imaging nature. This division facilitates analyses and simplifies the design of semi-automatic diagnostic testers. It also simplifies the design of future FAM-C and FDM-A measuring systems based on the diversity of certain parameters, such as the time base frequency diversity depending on the nature (periodicity) of the original diagnostic signal.

7.1.3. Metrological properties

The aforementioned FAM-C and FDM-A measurements entail a variety of both methodological and apparatus errors. Knowing their nature can significantly improve the reliability of these prototype methods in the process of monitoring mechanical propulsion units. Incorrect estimation of measurement errors can result in

premature decommissioning and referral of the test propulsion unit for overhaul, resulting in unnecessary costs. An opposite situation is also possible – delayed removal of the test propulsion unit from service. This can then lead to aircraft damage and even loss of human life. Therefore, care should be taken to improve measurement accuracy (during periodic instrument calibration). It would be advisable to increase the frequency of such calibrations before each subsequent test of a given propulsion unit, when successive results indicate that the parameters of mechanical phenomena are approaching the limit value. The problem of FAM-C and FDM-A metrological analysis has already appeared in the author's previous monograph [129]. Herein, this topic has been elaborated on. In addition, a novel concept of structural control over the observation resolution related to a given mechanical motion dynamics phenomenon has been also developed. The necessity of its application arises from the fact that different types of mechanical defects induce different angular velocity modulation phenomena with different primary diagnostic signal spectral distribution bands. Adjusting the generator-transducer output signal acquisition configuration is a significant breakthrough in the author's research on the application-wise universalisation of the FAM-C and FDM-A methods for diagnosing various phenomena occurring within propulsion units. Measurement resolution can be controlled in two ways:

a) phase change – single-phase or multi-phase signal acquisition from a generator or generators of one type,
b) synchronised acquisition of signals from generators of different types.

Changing the generator-transducer signal acquisition configuration is aimed at changing not only the resolution of a given measurement channel in relation to the observed motion dynamics phenomena in given components of the monitored propulsion unit. Above all, it enables significantly shifting the observability window of the primary diagnostic signal spectrum in FAM-C or FDM-A imaging. Therefore, upon changing the configuration from single-phase (which enables observing slow-variable mechanical processes to detect and determine the value of, among other notions, increased radial clearances defect in transmission shaft mounting nodes) to six-phase, fast-variable mechanical processes become observable (with six times the frequency of mechanical processes), allowing to detect and determine the wear parameters of other mechanical components, such as certain rolling bearings.

7.1.4. Implementations and applications of the FAM-C and FDM-A methods

Chapter 3 discusses single kinematic link failures and their representation in FAM-C and FDM-A imaging. In practice, the administrator (owner) of propulsion units is interested in a comprehensive and complex diagnosis of many kinematic pairs simultaneously, and not just single isolated components. There are numerous problems associated with such a comprehensive diagnosis. The mere identification of individual characteristic sets obtained via the FAM-C and FDM-A methods with individual mechanical components for complex mechanical structures poses a major challenge for diagnosticians. Resolution control comes to the rescue. Above all, a skilfully applied change in the observability window can promote increasing characteristic set speed and their identification correctness. After selecting the observability window for motion dynamics processes of individual propulsion components, the author conducted computerised FAM-C and FDM-A measurements. The overriding objective was to determine the negative standard metric parameters for the individual components of the tested propulsion unit. The author made a final decision in terms of limit parameter values of such a standard after mechanical measurements of a disassembled propulsion unit. This enabled comparing FAM-C or FDM-A imaging with mechanical reality. The following parameters were subject to verification:

a) phases – identification correctness related to a given kinematic pair,
b) amplitudes – i.e., characteristic set heights, which are an exponent of the tribological wear level of a given kinematic pair.

Once these values are determined, it is possible to proceed with constructing a semi-automatic diagnostic tester for a given propulsion unit type. Subsection 5.2 presents two types of semi-automatic testers implemented under the author's direction:

a) DIA-KSA for a MiG-29 aircraft propulsion unit,
b) DIA-SO3 for a TS-11 Iskra aircraft propulsion unit.

This confirms the possibility of the FAM-C and FDM-A methods being applied by any aircraft technician. It does not require such a person to be familiar with the phenomena of tested propulsion unit motion dynamics or knowledge on how to convert them by a generator-transformer. Tester operation was simplified to a minimum and the signals it indicates are clear, transparent and communicative. At the same time, the testers are lightweight and compact, in the size of a pocket meter.

The following sections of Chapter 5 present what the author believes to be interesting observations of the motion dynamics of various military aircraft propulsion units conducted with the use of the FAM-C and FDM-A methods. Some of the

measurements contributed to preventing a crash, e.g. the detection of a damaged main bearing of a Mi-24 helicopter WR-24 transmission gear; the detection of increased limit backlash in TS-11 Iskra aircraft SO-3 engine bearing supports. Other research cases allowed to reconstruct the course of catastrophic phenomena *post factum*, e.g., explain the cause of a tooth breaking out in the gear of a Mi-24 helicopter; explain the cause of journal softening and compressor shaft separation from the turbine shaft in a TS-11 Iskra aircraft. Yet other FAM-C results demonstrated the possibility of monitoring the swash plate bearing and detecting increased circumferential backlash of a Mi-17 helicopter's swash plate. These are very important (one might say *critical*) components for the design of any helicopter. Disseminating the diagnosis of these components via the FAM-C and FDM-A methods during operation, including, by allocating funds to developing and implementing semi-automatic testers for technical personnel, would significantly increase flying safety.

In the case of earlier FAM-C and FDM-A applications, presented, among others, in the author's doctoral dissertation [127], it was assumed that a component to be diagnosed was located between the mechanical power source, most often in the form of a rotating gas turbine, and a generator-transducer. After compiling the results presented in Chapter 5, it can be concluded that side-chain diagnosis is also possible.

The presented methods, labelled FAM-C and FDM-A by the author, are novel solutions and still require a lot of research. They have finally found numerous applications on actual objects. The author has also provided many descriptions of laboratory tests on physical objects. This is to authenticate the effectiveness of these methods. The FAM-C and FDM-A methods were born through experimentation – hence, the rather modest theoretical and mathematical description relative to the extensive description of experimental studies and applications. Users typically report problems related to monitoring or diagnosing specific mechanical nodes of propulsion units (diagnosing one-way couplings in MiG-29 aircraft, TS-11 Iskra engine bearing supports or electromechanical transducers). Regardless of the above, the author, together with a group of colleagues, conducts his own analyses of the state of emergency of various aircraft propulsion units. He attempts to develop studies associated with monitoring numerous propulsion components, inspired by information obtained from military aircraft maintenance personnel at various levels. Typically, these are issues of complex wear that are difficult to locate with the standard diagnostic equipment available to the user. The author believes it is his responsibility to step in, with as the best-possible package of proposed diagnostic measures, primarily based on the FAM-C and FDM-A methods, when these complex wear cases have not yet escalated to life-threatening failures. Therefore, the author attempts. to the extent of his modest powers and resources, to intensify the research work on pre-selected, endangered

(according to own analyses) propulsion unit assemblies in order to be optimally prepared to monitor the multi-sector complex wear of these endangered components prior to failure. The costs associated with the cascade of such failures could be disproportionately greater than the costs of conducting diagnostic tests with the FAM-C and FDM-A methods. At the same time, knowing the diagnostic classes of tested propulsion unit individual components would enable developing effective preventive measures at an earlier stage. It is clear that in the event of a catastrophe, resources for diagnostic testing and prevention measures are usually allocated. However, in such a case, the user pressure on quick and effective results is so strong that there is no more time for basic research. Hence, this situation provides all the more reason to conduct them now, even despite the lack of resources.

On a side note of the author's technical considerations on wear monitoring of propulsion units, an economic theme comes to mind. The author's deliberations on various hazards in aircraft propulsion units, mostly old aircraft with a significant flying time and an even longer (calendar) service life (20÷35 years), are met with a frequent retort that it is necessary to replace the aircraft equipment with western equipment, preferably, of course, brand new, as soon as possible. In addition, as soon as this new equipment arrives, considerable forces and resources are allocated to it, which could be employed to develop diagnostic methods and an overhaul system. I would like to point out that this does not apply to direct expenditure on purchases only, but to funds that are many times greater, for the often necessary creation of new infrastructure from scratch.

The author is aware that such organisational moves mitigate the risk level. Indeed, it is a fact that brand new aircraft have a lower damage intensity. This has little to do with whether they were manufactured by a factory in a western or eastern country. This is simply the laws of tribology, confirmed in this regard. Long-term forecasts by US-based centres, published under source literature, suggest that service life should be extended. According to the same sources, the airframe structure can be operated for up to... 80 years. Simultaneously, the intensification of the initial failures posing a greater hazard (e.g., in the field of power grid cable operation) commences after just 11 years of operation. Therefore, the decommissioning of old aircraft designs should be moderate, based on the diagnostic data of individual flying objects and the failure statistics of the aircraft type rather than on a formal calendar or political assumptions. Unfortunately, the author does not have analogous source literature data from manufacturers of old military technology operated in the Republic of Poland. However, analysing his material related to the operation of military aircraft for 40 years, the author concluded that this old military technology was governed by the same principles as the new one – in practical terms, there were not major operational problems for the first 10 years.

The author does not intend to get into a detailed discussion of which manufacturers make better aircraft. He merely wishes to point out that redirecting some of the resources to old military aircraft propulsion unit diagnostics would enable achieving several significant structural goals within Polish military aviation:

a) refinement of diagnostic methods, e.g., FAM-C and FDM-A,
b) preventing dangerous aviation accidents associated with old military technology,
c) extending the service life of old military aircraft, which are already economically paid off,
d) enabling the development of modern diagnostic systems, starting with the creation of diagnostic systems, followed by checking them, based on novel but refined, non-interfering methods; the chance of detecting defects by personnel directly operating aircraft of old military technology will thus be balanced (the diagnostic systems of Western aircraft of new military technology are better developed),
e) gaining diagnostic experience gained on military aircraft of old military technology, through suitably intensified research, which can then be easily transferred to new military technology – the process of acquiring such experience could most likely be sufficiently advanced when new military technology enters a period of intense tribological wear.

It is known that FM modulation is characterised by a much higher resistance to interference than AM. Therefore, following prof. Cempel [39, 40], it can be assumed that even in the case of a propulsion unit that is kinematically extended, complex and concentrated within a relatively compact space, frequency modulation remains the same. Consequently, the ability to retain original diagnostic information is not lost even in the case of most extensive propulsion units. Owing to the transformation in the generator-transducer, these sets of well-preserved modulations in the low frequency bands are transferred to the high frequency band. Thus, the primary diagnostic signal gains additional protection against interference. The signal is then faithfully transmitted to all components of the aircraft or vessel electrical grid. It turns out, however, that the first discretisation of a frequency-modulated primary diagnostic signal already results in averaging of the fast-variable phenomena of the primary diagnostic signal between the crossings of the output voltage signal through the zero level. In other words, only the generator-transducer design determines if bandwidth of the primary FM-modulated diagnostic information (within the LF domain) will be transferred to HF. The generator-transducer is therefore a band-pass filter for the FM-modulated primary diagnostic signal.

7.1.5. Studying bearing node tribological processes and their changes using the FAM-C and FDM-A methods

Rolling bearing phenomena have been covered by numerous scientific publications [15, 27, 55, 56, 73, 179, 261, 269, 276]. These materials demonstrate that the theory of rolling bearing phenomena research did not begin to develop until the end of the 19th century. The following scientist particularly contributed to the development of human knowledge of rolling bearings [73, 244]:

a) German: Hertz, Tleischer, Uetz;
b) British: Archard, Hirst, Tabor, Burwell, Strang, Martin;
c) Swedish: Weibull, Lanberg, Pelgner, Winquist;
d) USA: Holm, Rubinovitz, Bayer;
e) Polish: Krzemiński-Freda, Stupnicki;
f) Russian: Kragielski, Kostecki, Solski, Ziemba, Grubin;
g) French: Courtel, Charlez Varlo.

However, the issues explored in depth by these pioneering scientists concern fragmented aspects of knowledge. There is an absence of source literature descriptions based on observations of bearing nodes in extended propulsion units. The author of this study, together with a group of collaborators, has been observing such bearing nodes for 10 years with the FAM-C and FDM-A methods [98, 99, 107, 113, 114, 119, 121÷123, 128, 129, 136, 266]. These observations enabled proposing four rolling bear tribological wear models. These models take into account not only the friction processes in the bearing itself, but also the engine geometry and its numerous components.

In addition to the four rolling bearing tribological wear models, the author presented a hypothesis on the possible transformation of one model into another for the same bearing. While observing a SO-3 engine, he noted that over a period of 400 h of operation (flight), these changes occurred at an increasing rate. At the same time, there was an intensification in wear processes, as demonstrated by a systematic increase in such parameters as the characteristic set height and quality factor.

7.2. Final conclusions – FAM-C and FDM-A methods as a novel element in the scientific theory

7.2.1. General remarks

The FAM-C and FDM-A methods were born out of practical needs – the need to monitor the motion dynamics processes of mechanical propulsion unit components, in order to identify their failure causes. Over time, the methods developed by the author to monitor the phenomena of mechanical propulsion unit shaft twisting became universal. Their development was related to the following aspects:

1) Development of measurement facilities:
   a) initially, analogue recording systems were based on loop recorders with photosensitive film recording,
   b) single-phase digital systems were employed [127],
   c) later, three-phase systems with single-axis time projection [129], synchronised multi-phase and multi-machine systems were developed,
   d) preparations are under way to start employing systems with quadrature modulation (subsection 4.3.7).

2) Diagnostic objective and task adjustment:
   a) initially, the objective was to find the causes of generator drive shaft twisting due to the wear of a single component or subassembly within a mechanical propulsion unit [80, 81, 83, 84, 125, 127, 168]. The occurrence of a single defect in the mechanical propulsion unit was assumed, which prevailed both in terms of the passive experiment (observations of shaft twisting on a MiG-29 aircraft [81, 83, 84] and the active experiment [86, 96, 127]. These were failures primarily manifested by narrowband or pulsed angular velocity modulation;
   b) an attempt was made at a later stage to create a risk area "map", looking for multifaceted causes of possible final failure of the component under investigation. These were damages that manifested themselves in a further narrowband or through pulsed angular velocity modulation;
   c) a significant stimulus to intensify the development of the FAM-C and FDM-A methods in such a multi-faceted search for the causes was the invitation of the author and a group of co-workers to inspect the technical condition of TS-11 Iskra aircraft bearing nodes; this resulted in the necessity to monitor a subassembly generating broadband angular velocity modulations.

3) Method of graphically mapping data and calculating metric parameters for diagnostic analysis:
   a) initially, frequency deviation was observed as a function of the mechanical process frequency $\Delta F = f(f_p)$ was observed in a rectangular coordinate system. The obtained points grouped into characteristic sets. Each of these sets concentrated around a specific frequency f_{poj}, characteristic of the j kinematic pair. This frequency for each kinematic pair could be calculated from the kinematic diagram of the kinematic assembly in question. This allowed to identify the characteristic set with the kinematic pair. Each characteristic set exhibited its height proportional to the defect size [127];
   b) next, upon undertaking rolling bearing technical condition monitoring, the depictions and relationships described in Section 3a were obtained, proving to be far from sufficient. Rolling bearings present numerous diagnostic difficulties due to their specific properties:
      – generation of internal resonant excitations,
      – the complexity of component motion – a local "orbital" system is created – i.e., a system of rolling elements that rotate around their own axis of symmetry and, simultaneously, move their axes of rotation at a much slower angular velocity than the bearing-supported rotor journal,
      – the action of hydro-mechanical forces – possible formation of lubricating oil wedges, which complicate the mathematical and physical relationships between rolling element angular positions as they rotate. These relationships are a non-linear function of the rotor journal speed. In consequence, there was a need to visualise the characteristic sets in the form of a deviation depending on two variables $\Delta F = f(f_p, n)$, i.e., an analysis of the sets within a three-dimensional space (f_p, ΔF, n) commenced, where n is the journal speed. In some cases with long-term monitoring, a fourth axis also appeared (f_p, ΔF, n, Θ), where Θ is the propulsion unit service life.

Therefore, phenomena from the perspective of both the FAM-C and FDM-A measurement technique and those occurring inside the mechanical propulsion unit are discussed in this monograph. According to the definition of surveillance (herein), the technique of periodic diagnostic tests via the FAM-C and FDM-A methods was adopted. The interval between successive tests should depend on the frequency of change in the mechanical processes occurring over time Θ. The operation time of the propulsion unit in-between overhauls was proposed as the total duration of the surveillance process, The author's observations show that towards the end of the inter-overhaul period, processes, e.g., tribological, the induce oscillatory parameter changes with increasing frequency, thus, the projected time between successive FAM-C and FDM-A measurements should be

induce oscillatory parameter changes with increasing frequency, thus, the projected time between successive FAM-C and FDM-A measurements should be shortened. Therefore, the images (f_p, ΔF, n, Θ) should be closely observed. It would be advantageous for the diagnostic decision correctness if the measurements were taken at a time Θ_k, which corresponds to the parameters (relevant for a given tribological wear process) reaching local extremes (subsection 6.2, Figs. 6.17 and 6.18).

7.2.2. FAM-C and FDM-A methods vs the theory of signals

When planning the test frequency, it is important to adapt the time between successive measurements $\Delta\Theta_k = \Theta_k\Theta_{k-1}$ to the periodicity of tribological processes occurring within the tested propulsion unit. Thus, instead of uniform intervals $\Delta\Theta$ = const, the author proposes to make them uniform. The challenge is the macro scale of monitoring a given propulsion unit. The issue of matching the frequency of sampling for observing the process also applies to the micro scale, and, thus, to the characteristics with an additional speed axis (f_p, ΔF, n). The time interval between successive tests must not exceed the interval between extremes. In this case, the number of engine main shaft rated speeds set by an aircraft technician can be increased to concentrate the measurements near this extreme. A similar issue is encountered in the preparation and implementation of FAM-C and FDM-A diagnostic measurement during both electromechanical sampling (implemented by a generator-transducer) and electronic sampling (implemented by a counter card time base clock).

In general, the current sampling frequency selection system applied in practice was based on the Kotielnikov-Shannon law [264, 270, 305, 306], whereby a constant sampling frequency was assumed. It establishes that the observed waveform sampling frequency must be more than twice the observed waveform frequency (process). If this condition is not met, aliasing, i.e., overlapping of spectra, follows. In practical measurements, this multiplication factor (the quotient of sampling frequency and observed waveform frequency) must be much higher if a diagnostician wants to obtain a small signal representation error – many publications recommend keeping this quotient at 10 or higher [264, 270, 305, 306].

The considerations above apply to non-synchronised sampling of the observed waveform. According to the authors of a few publications, e.g., [29, 302, 303], the Kotielnikov-Shannon condition does not apply to synchronous sampling. However, they do not provide any specific numerical relationships. The author noted that a satisfactory level of observing many mechanical faults can already be obtained with a ratio of sampling frequency to observed waveform at 1.2 (Chapter 2, relation

2.24). The FAM-C and FDM-A methods employ an onboard generator as a transducer, which implements electromechanical, synchronous sampling (owing to its rigid connection to the diagnosed propulsion unit). Therefore, the synchronous onboard generator, owing to its characteristics, executes variable sampling adapted to the dynamics of the observed angular velocity fluctuation process.

7.2.3. Onboard generator as a diagnostic transducer

A generator-transducer is a special (peculiar) element [183÷187] of a propulsion unit train that enables its monitoring and diagnosis; it has band-filter properties in relation to the primary diagnostic signal generated by individual kinematic pairs of the mechanical propulsion unit under test. Each generator type exhibits a different observability band, depending on its design parameters. The upper limit frequency of this band is defined by the relationship (2.8) and is approximately equal to half the value of the rated frequency for the generator in question. The lower limit frequency is defined by the counter card buffer capacity (subsection 4.3.3.). This bandwidth, as discussed in 4.2.3, can be adjusted (shifted towards higher f_p frequencies) through:

- changing the phase configuration (three-, two-, six-phase measurement),
- applying pilot exciter voltage (f_N = 800 Hz, U = 70 V).

Please note that:

1) In the discrete-frequency FAM-C and FDM-A methods, the measurement concept is based on simple tracking of the generator-transducer output voltage waveform zero-crossing time increments. When the carrier component is removed by the detection systems, sets of characteristic points grouped into characteristic sets are obtained. Each such set represents a different kinematic pair (with a specific rated angular velocity) modulated in a defect-specific manner.
2) Characteristic set height is directly proportional to the amplitude of angular fluctuations induced by the given defect in the case of periodic narrowband processes and certain stochastic processes (one-way couplings), and the adopted model of increased passive resistance of broadband mechanical processes. The position of a characteristic set on the abscissa axis enables locating and identifying the kinematic pair and defect type.
3) In the case of broadband processes (rolling bearing diagnosis), the position of characteristic sets is subject to displacement depending on the technical condition of the bearing. The dynamics of these changes is the most important parameter of the bearing technical condition. Ordinate values unambiguously indicate a hazard state only for the model of increased passive resistance. For

other tribological models, they have a secondary function – they notify about the tribological model type.

4) The generator-transducer is a heterodyne-modulator of primary diagnostic signals – it converts them into the high-frequency band (rated carrier frequency is f_{NG} = 400 Hz for AC generators, and f_{NG} = 1÷10 kHz for DC generators). This enables:
   – increasing primary signal immunity to all kinds of interference,
   – employing onboard power supply grid as a signal transmission medium, which makes it possible to increase the level of ergonomics and test safety – the diagnostic equipment (following the FAM-C and FDM-A concepts) can be connected anywhere within the grid.

7.3. Practical aspects of the FAM-C and FDM-A methods

At the initial phase of research into the FAM-C and FDM-A methods, it was demonstrated that they can only be employed to test rotating components of propulsion units if they are located within a kinematic power transmission system between a primary source of mechanical energy (e.g., the turbine of a turbojet engine) and a generator-transducer drive shaft [127]. Further tests on real objects have shown that it is also possible to diagnose side chains, i.e., those located outside the main chain. A prerequisite is for the vibrations induced by the component to have sufficient energy to affect the drive seat of the transducer-generator. Therefore, it was possible to detect a faulty main bearing in the Mi-24 helicopter WR-24 transmission gear, and to detect a Mi-17 helicopter swash plate worn bearing or excessive circumferential backlash in the helicopter's separator coupler.

As stated previously, the FAM-C and FDM-A methods enable obtaining diagnostic information on the condition of multiple kinematic links simultaneously. A single generator-transducer has the properties of a bandpass filter and can, therefore, provide data on the speed modulation spectrum within a specific frequency band. Developing the possibility to apply several generator-transducers simultaneously and to control the phasing of these generators significantly increases observability bands – in practical terms, a diagnostician is able to observe all kinematic pairs of mechanical propulsion units.

7.4. Final remarks

The numerous applications of the FAM-C and FDM-A methods provide strong practical foundation for the author to build their theoretical description on.

Bearing in mind that this description does not yet satisfy all scientific theory requirements, the author intends to fine-tune it and present in his next paper.

There are vast opportunities for the practical control of generator-transducer phasing, both individually (for a specific generator-transducer) and as a compilation of a set comprising several generators installed within a given propulsion unit. The author plans to introduce practical diagnostic measurements employing the concept of coherent modulation. He simultaneously intends to work on the actually expanding the FAM-C and FDM-A measurements with counter card time base generator clock frequency active control, as well as multi-vector synchronisation of this control between measurement chains.

REFERENCES

1. Abramov B.I.: *Koliebania priamozubnych zubczatych kolies*. Kharkov 1968.
2. Adams D.E.: *Health monitoring of structural materials and components. Method with applications.* ISBN 978-0-470-03313-5(HB). Chichester 2007.
3. Aleksiejew W.J., Barukow F.J. i inni: *Radioelektronika [Radioelectronics],* part. 1, WKŁ, Warsaw 1973.
4. Andrejewicz J.: *Chaos i synchronizacja w układach fizycznych [Chaos and synchronisation in physical systems]*, Monographs, Łódź 1993.
5. Andrejewicz J.: *Drgania deterministyczne układów dyskretnych [Deterministic vibrations of discrete systems]*, WNT, Warsaw 1993.
6. Antonowicz J.: *Automatyka [Automation]*, WNT, Warsaw 1973.
7. Augustyn S., Gębura A.: *Możliwości diagnozowania skrzyń napędów i zespołów transmisji śmigłowca Mi-24 metodą FAM-C [Diagnostic potential of drive boxes and transmission assemblies of the Mi-24 helicopter using the FAM-C method]*, "Prace Naukowe ITWL", Vol. 30, Warsaw 2012.
8. Ayes B.W., Arnold S., Vining Ch., Howard R.: *Application Of Generation 4 Non-Contact Stress Measurement System On HCF Demonstrator Engines*, Proc. of 10th National Turbine Engine High Cycle Fatigue (HCF) Conference. Dayton, USA, 2005, www.hcf.utedayton.com.
9. Balageas D., Fritzen C. l., Gűemes A.: *Structural health monitoring*, London 2006.
10. Balicki Wł., Szczeciński S.: *Diagnostyka lotnicza silników turbinowych w USA [Turbine engine aviation diagnostics in the USA]*. "Wojskowy Przegląd Techniczny i Logistyczny" 1996, Vol. 5.
11. Banasiuk H.: *Rozkład odchyłek wykonawczych i jego wpływ na trwałość uzębienia w kołach walcowych o zębach prostych [Distribution of execution deviations and its impact on toothing condition in spur-teeth shaft gear]*. PhD thesis. Łódź 1965.
12. Barczewski R.: *Poliharmoniczna filtracja rekreacyjna - diagnostycznie zorientowana metoda analizy sygnału [Polyharmonic recreational filtration - diagnostic-oriented signal analysis method]*. Materials of the 20th School of Diagnostics. Poznań–Zajączkowo 1992.
13. Barszewski W.: *Śmigłowiec w locie [Helicopter in flight],* Wyd. MoD, Warsaw 1956.
14. Bartosiewicz J., Stelmach A.: *Problematyka przetwarzania parametrów z pokładowych rejestratorów eksploatacyjnych lotu [Problem of processing parameters from onboard operational flight recorders]*, "Prace Naukowe – Transport", vol. 103, Oficyna Wydawnicza Politechniki Warszawskiej, Warsaw 2014.
15. Barwell F.T.: *Łożyskowanie [Bearing]*, WNT 1984.
16. Belahcen A.: *Magnetoelasticity, magnetic forces and magnetostriction in electrical machines,* Doctoral thesis,Helsinki University of Technology Department of Electrical and Communications Engineering Laboratory of Electromechanics, August, 2004.

17. Bendat J.S., Piersol A.G.: *Engineering applications of correlation and spectral analysis*. New York – Toronto 1980.
18. Berhard M. et al.: *Mały poradnik mechanika [Brief mechanic's guide]*. Volume II. *Podstawy maszyn. Maszynoznawstwo [Machinery basics. Mechanical engineering],* WNT, Warsaw 1994.
19. Będkowski L.: *Elementy diagnostyki technicznej [Elements of technical diagnostics]*. MUT, Warsaw 1991.
20. Będkowski L., Dąbrowski T.: *Model eksploatacyjny obiektu technicznego w ujęciu trójprocesowym [A triple-process technical object operating model]*. III International Scientific-Technical Conference Expo-Diesel&Gas Turbine'03. 5-9 May 2003.
21. Będkowski L., Rozwadowski T.: *Optymalizacja kontroli stanu wieloparametrowych obiektów złożonych metodą programowania dynamicznego [Optimized condition monitoring of multi-parameter complex objects with a dynamic programming method]*. "Biuletyn WAT" Vol. 1(161), Warsaw 1966.
22. Białkowski G.: *Mechanika klasyczna. Mechanika punktu materialnego i bryły sztywnej [Classical mechanical engineering. Mechanics of a material point and rigid body]*. PWN, Warsaw 1973.
23. Biarda D., Falkowski P., Gębura A., Kowalczyk A.: Patent description PL 175664B1, *Technical diagnosis of elements coupling engines, aviation combustion engine in particular, with an AC generator,* application 8/7/1996, patent granted 29/1/1999.
24. Biarda D., Falkowski P., Gębura A., Kowalczyk A.: Patent description PL 175674B1, *Technical diagnosis method for engine coupling elements, especially an aviation combustion engine with a DC generator*, application 8/7/1996, patent granting 29/1/1999.
25. Biarda D., Falkowski P., Gębura A., Kowalczyk A.: Patent description PL 175645B1, *Technical diagnosis method for engine coupling elements, especially an aviation combustion engine with a DC generator*, application 8/7/1996, patent granting 29/1/1999.
26. Biarda D., Falkowski P., Gębura A., Kowalczyk A.: Patent description PL 182554B1, *Technical diagnosis of elements coupling engines, aviation combustion engine in particular, with an AC generator,* application 19/5/1997, patent granted 02/4/2002.
27. Biela J., Macek-Kamińska K.: *Badania diagnostyczne wirników generatorów synchronicznych [Diagnostic testing of synchronous generator rotors],* "Prace Naukowe Instytutu Maszyn, Napędów i Pomiarów Elektrycznych Politechniki Wrocławskiej", No. 62, Oficyna Wydawnicza Politechniki Wrocławskiej.
28. Bielawski P., Bejger A.: *Aligment of marine generating set shafts: operational problems and inspection methods*. III International Scientific-Technical Conference Expo-Diesel&Gas Turbine'03. 5-9 May 2003.
29. Bilinkis I.: *Digital Alias-free Signal Processing.*
30. Björck A., Dahlquist G.: *Metody numeryczne [Numerical methods]*. PWN, Warsaw 1987.
31. Blade M., Mitchell W.S.: *Vibrations and Acoustic Measurement Handbook*, Spartan Books, New York – Washington 1972.
32. Bogdanow A.F., Wasim W.W., Dulin W.N. et al.: *Radioelektronika [Radioelectronics],* part 1, WKŁ, Warsaw 1971.

33. Bogdanow A.F. et al.: *Radioelektronika [Radioelectronics],* Vol. 1, 2, 3, Wydawnictwa Komunikacji i Łączności, Warsaw 1971.
34. Bomba J., Kaleta J.: *Investigation of magnetostrictive sensor to quasi-static conditions. 22nd DUNABIA-ADRIA Symposium on Experimental Methods in Solid Mechanics,* Montceli Terme/Parma, Italy 2005.
35. Borgoń J., Stukonis M., Szymczak J.: *Czy uszkodzenia połączeń wielowypustowych w silnikach lotniczych mogą spowodować wypadki lotnicze [Can failures of splined connections in aviation engines cause air accidents]*. "Informator ITWL" Vol. 311/93, Techniczne problemy eksploatacji i niezawodności wojskowych statków powietrznych, Kiekrz 1993.
36. Bukowski L., Tomaszewski H., Janowski J., Jaworski J.: *Rolling bearing technical condition monitoring method*, patent description PL173059, application No 302258, Application date 17/2/1994, application announced 21/8/1995, BUP 17/95, patent grant announcement 30/1/1998 WUP 01/98.
37. Campbell W.: *Elastic fluid turbine rotor and method of avoiding tangential bucket vibration therein*. Patent US 1.502.904. 1924.
38. Carington I.B., Wright J.R., Cooper J.E., Dimitriadis G.: *A comporison of blade tip timing data analysis methods. Proceedings of the Institution of Mechanical Engineers,* Part G, Journal of Aerospace Engineering. Volume 215, Number 5, 2001.
39. Cempel C.: Diagnostyka wibroakustyczna maszyn *[Vibroaoustic diagnostics of machines]* PWN, Warsaw 1989.
40. Cempel C.: *Podstawy wibroakustycznej diagnostyki maszyn [The basics of machine vibroacoustic diagnostics]*. WNT, Warsaw 1982.
41. Centralnyj Institut Aviacjonnogo Motopostroienia im. P.I. Baranova: *Informacjonno-izmienitielnaja sistiema kontroli a sistiema aviacjonnych i obszczemaszino-strojennych reduktorov, privodov i korbokpieriedacz*. Moscow 1990.
42. Chaimzov M.E., Kryłow K.A., Korablev A.I.: *Nadieżnost aviacjonnych raziemnych sojedinienij*. "Transport", Moscow.
43. Chaimzow M.E., Korabliev A.I.: *Rabotosposobnost aviacjonnych zubcatych sojedinienij*. "Transport" 1983, Moscow.
44. Charchalis A., Grządziela A.: *Diagnozowanie stanu współosiowości elementów transmisji momentu obrotowego metodą pomiaru sygnałów wibroakustycznych z łożyska nośnego [Diagnosing the alignment of the torque transmission components using the method of measuring vibroacoustic signals from the carrier bearing],* Problemy Eksploatacji 1999, Vol. 2.
45. Cheda W., Michalski M.: *Silniki [Engines]*. WKiL, Warsaw 1984.
46. Chwaleba A., Poniński M., Siedlecki A.: *Metrologia elektryczna [Eletrical metrology]*, WNT, Warsaw 1979.
47. Couberghe B.: *Applied frequency – domain system identification in the field of Experimental Operational Modal Analysis,* PhD thesis. Vrije Universiteit, Brussel 2004.
48. *Couplemetre type 643 pour l'helicoptere SA 330*, PUMA – SFIM, 1971.
49. Dabrowski M.: *Pola i obwody magnetyczne maszyn elektrycznych [Magnetic fields and circuits in electrical machines]*, WNT, Warsaw 1971.

50. Dadouche A., Rezaei A., Wickramasinghe V., Dmochowski W., Bird J.W., Nietzsche F.: *Sensitivity of Air-Coupled Ultrasound and Eddy Current Sensors to Bearing Fault Detection*. Tribology Transactions, 51:2008.
51. Danilin A.I., Tchernyavsky A.Zh.: *Criteria of discrete phase control of blade working condition and their feasibility in systems of turbine driven set automatic control.* VESTNIK SGAU No 1(2009), http://www.ssau.ru.
52. Dąbrowski T.: *Diagnozowanie stanu wybranej klasy obiektów technicznych w warunkach losowych zakłóceń [Diagnosing the condition of a selected technical object class under random interference conditions]*. PhD thesis. WAT, Warsaw 1977.
53. Dąbrowski T.: *Planowanie badania diagnostycznego w oparciu o chwilowe wartości cech sygnału diagnostycznego [Diagnostic test planning based on instantaneous diagnostic signal feature value]*. Biuletyn WAT Vol. 7(275), Warsaw 1977.
54. Dąbrowski Z.: *Wały maszynowe [Machine shafts]*. PWN, Warsaw 1999.
55. Deng D., Braun M.J.: *A New Model for Transition Flow of Thin Films In Long Journal Bearings.* "Tribology Transactions", 51: 2008.
56. Dietrich M.: *Podstawy konstrukcji maszyn [Machine design basics]*. T2, WNT, Warsaw 1999.
57. Drzewiecki J.: *Methodology of gaining information about engine load in particular cylinders on the basis of course of crankshaft's transient rotational speed*. III International Scientific-Technical Conference Expo-Diesel&Gas Turbine'03. May 5-9, 2003.
58. Duan F., Fang Z., Sun Y., Ye S.: *Real Time Vibration Measurement Technique Based On Tip-Timing For Rotating Blades. "*Opto-Electronic Engineering" 2005, nr 30(1), http//www.paper.edu.cn.
59. Dutkiewicz M., Radulski W., Zielek G.: *Analiza dynamiki turbozespołu w ujęciu przemysłowym [Industrial analysis of turboset dynamics]*, Elbląg 2002.
60. Dynarski P. et al.: *Podstawy transmisji cyfrowej [Basics of digital transmission]*. Wyd. Politechniki Warszawskiej, Warsaw 1999.
61. Dziama A., Michniewicz M., Niedźwiedzki A.: *Przekładnie zębate [Toothed transmission gears]*. PWN, Warsaw 1978.
62. Dzida M.: *Identyfikacja przyczyn niestacjonarności oraz niestabilności temperatury i ciśnienia gazów za komorą spalania turbiny gazowej [Identifying the causes behind non-stationarity and instability of gas temperature and pressure downstream of a gas turbine combustion chamber]*, Gdańsk 2000.
63. Dzięcioł E.: *Mikrofalowy układ homodynowy dozorujący stan techniczny turbinowej łopatki silnika lotniczego [Microwave, homodyne system for monitoring the technical condition of an aviation engine turbine blade]*. PhD thesis, AFIT, Warsaw 2003.
64. Dziurski A., Kania L., Kasprzycki A., Mazanek E., Ziora J.: *Przykłady obliczeń z podstaw konstrukcji maszyn [Examples of machine engineering basic calculations]. WNT*, Warsaw 2005.
65. Dziwoki G.: *A cost function analysis of a blind phase acquisition method*, IEEE International Symposium on Industrial Electronic, Gdańsk 2011.
66. Dżygadło Zb., Łyżwiński M., Szczeciński S., Wiatrek R.: *Zespoły wirnikowe silników turbinowych [Turbine engine rotor assemblies],* WKiŁ, Warsaw 1982.

67. Fagot J., Magne P.: *Teoria modulacji częstotliwości w zastosowaniu do łączy mikrofalowych [Theory of frequency modulation applied to microwave links]*. WKŁ, Warsaw 1965.
68. *Phase-pulse moment meter*, FRG Patent No. 206033, 1973.
69. Fellner A., Fellner R.: *Znaczenie analizy drzewa zdarzeń w wybranych aspektach implementacji GBAS [Significance of event tree analysis in selected GBAS application aspects]*, "Prace Naukowe – Transport", z. 103, Oficyna Wydawnicza Politechniki Warszawskiej, Warsaw 2014.
70. Fichtenholz G.M.: *Rachunek różniczkowy i całkowy [Differential and integral calculus]*. PWN, Warsaw 1975.
71. Flotow A., Drumm M.J.: *Engine Sensing Technology Hardware & Software To Monitor Engine Rotor Dynamic Using Blade Time-Of-Arrival And Tip Clearance*, Hood River, Or, USA, www.hoodtech.com, 2002.
72. Fonteyn K.A.: *Energy-Based Magneto-Mechanical Model for Electrical Steel Sheets*, TKK Dissertations 234, Aalto University School of Science and Technology Faculty of Electronics, Communications and Automation Department of Electrical Engineering, Espoo (Finland) 2010.
73. Furmanek S., Kraszewski Z., *Niezawodność łożysk tocznych [Rolling bearing reliability]* Wydawnictwa Przemysłowe WEMA, Warsaw 1989.
74. Ma G. J., Wu C.W., Zhou P.: *Influence of Wall Slip on the Dynamic Properties of a Rotor-Bearing System*. "Tribology Transactions" 2008, nr 51.
75. Gabelli A., Morales-Espejel G.E., Ioannides E.: *Particle Damage in Hertzian Contacts and Life Ratings of Rolling Bearings*. "Tribology Transactions" 2008, Vol. 51.
76. Gajda J., Sroka R.: *Pomiary kąta fazowego – Metody – układy - algorytmy [Phase angle measurements - Methods - Systems - Algorithms]*, Kraków 2000.
77. Gajo Zb., Kocimowski B., Kulpa K., Nałęcz M., Urbaś A.: *Sygnały i systemy. Ćwiczenia laboratoryjne [Signals and systems. Laboratory exercises]*. Joint publication edited by Jacek Wojciechowski. Oficyna Wydawnicza Politechniki Warszawskiej, Warsaw 2000.
78. Gawron S.: *Dwustopniowy, wolnoobrotowy generator synchroniczny z magnesami trwałymi [Two-stage, slow-speed synchronous generator with permanent magnets],* Prace Naukowe Instytutu Maszyn, Napędów i pomiarów Elektrycznych Politechniki Wrocławskiej, Oficyna Wydawnicza Politechniki Wrocławskiej, Wrocław 2008.
79. Gądek K.: *Wzorce czasu w metrologii cyfrowej i mikroprocesorowej [Time standards in digital and microprocessor metrology]*. Kraków 2011.
80. Gębura A.: *Biuletyn eksploatacyjny nr P/3932/E/95, dotyczy: diagnozowania sprzęgieł jednokierunkowych w przekładni KSA-2 oraz bloku hydraulicznego w agregacie GP-21 za pomocą testera DIA-KSA- C podczas eksploatacji samolotu MiG-29 [Operational bulletin no. P/3932/E/95, re: diagnosing single-way bearings in a KSA-2 transmission and a hydraulic block in a GPP-21 unit using a DIA-KSA-C tester in the course of operating the MiG-29]* Wyd. DWLiOP/ITWL, Warsaw 1995.
81. Gębura A.: *Metody eksploatacji skrzynek napędów agregatów płatowca samolotu MiG-29 według stanu technicznego [Method for condition-based operation of generator unit boxes of a MiG-29 airframe],* not published.

82. Gębura A., Lindstedt P.: *Diagnozowanie napędów prądnicy w oparciu o analizę parametrów napięcia prądnicy [Diagnosing generator drives based on the analysis of generator voltage source parameters]*. 5-th International Conference Aircraft and Helicopters Diagnostic AIRDIAG'97, Warsaw 1997.
83. Gębura A., Biarda D.: *Report on examining the causes of broken-off GP-21-3PS generator drive shafts on a MiG-29 aircraft No. 50903014615*. November 1993, not published.
84. Gębura A., Biarda D., Kowalczyk A.: *Badanie przyczyny niezdatności układu napędowego prądnicy prądu przemiennego samolotu MiG-29 (elektryczne metody pomiaru stanu technicznego układu napędowego) [Studying the causes of malfunctions of an AC generator power train in a MiG-29 aircraft (electrical methods for measuring the propulsion unit's technical condition).]*. Informator ITWL 1994, Vol. 317.
85. Gębura A., Biarda D., Kowalczyk A., Falkowski P.: *Komputerowe metody diagnozowania napędów prądnic lotniczych [Computer methods for analysing onboard generator drives]*. Materials from the 2nd School - Conference "Computer-Assisted Metrology" MWK′95 vol. 3.
86. Gębura A., Biarda D., Kowalczyk A., Falkowski P.: *Metoda FAM-C diagnozowania stanu technicznego napędu lotniczej prądnicy prądu przemiennego [FAM-C method for diagnosing the technical condition of an aviation AC generator drive]* Informator ITWL No. 338/96. 4-th International Conference Aircraft and Helicopters Diagnostic AIRDIAG′95; December 1995.
87. Gębura A., Biarda D., Kowalczyk A., Falkowski P.: *Wybrane problemy oceny niezawodności i bezpieczeństwa lotniczych skrzyń napędowych statków powietrznych metodami elektrycznymi [Selected issues of evaluating reliability and safety of aircraft power unit gearboxes with electric methods]* Informator ITWL Vol. 335/96. Materials for the VI Symposium on Systems Safety.
88. Gębura A., Budzyński P.: *Technical diagnosis method for engine coupling elements, especially an aviation combustion engine with an AC generator* - Patent description PL188758 B3, application number 333805, application date 16/6/1999,
89. Gębura A., Budzyński P.: *Technical diagnosis method for engine coupling elements, especially an aviation combustion engine with an DC generator* - Patent description PL188759 B3, application number 333806, application date 16/6/1999,
90. Gębura A., *Diagnostic of aircraft power transmission track based on the analysis of generator's frequency*, "Journal of Technical Physics", No. 1/2002.
91. Gębura A., Falkowski P., Kowalczyk A.: *Lotnicze prądnice pokładowe statku powietrznego źródłem sygnałów diagnostycznych skrzyń napędowych [Aircraft onboard generators as a source of diagnostic signals for gearboxes]* 3rd School - Conference "Computer-Assisted Metrology" MWK MWK′97 Zegrze near Warsaw, 19 ÷ 22 May 1997, Vol. 2.
92. Gębura A., Falkowski P., Kowalczyk A.: *Zastosowanie metody FAM-C do diagnozowania układów napędowych statków powietrznych [The application of the FAM-C method for diagnosing aircraft power trains]* Przegląd Wojsk Lotniczych i Obrony Powietrznej, September 1997.

93. Gębura A., Falkowski, P., Kowalczyk, A.: *Airborne generators as diagnostic sensors of a power transmission system,* 5-th International Conference Aircraft and Helicopters Diagnostic AIRDIAG'97, Warsaw 1997.
94. Gębura A., Falkowski P., Kowalczyk A., Lindstedt P.: *Diagnozowanie skrzyń napędowych [Diagnosing gearboxes]*. "Zagadnienia Eksploatacji Maszyn" 1997, Vol. 4(120).
95. Gębura A., Karczmarek K.: *Mi-24 requires transmition monitoring system* (*Mi-24 wymaga systemu monitorowania transmisji*), "Journal of KONBiN" No 4(20), Warsaw 2012.
96. Gębura A., Kowalczyk A., Biarda D., Falkowski P., Budzyński P., Pisarska K.: *Research report on: "Diagnostyka techniczna statków powietrznych. Zadanie cząstkowe: Elektryczne metody diagnozowania stanu technicznego wirujących elementów napędu prądnic lotniczych [Aircraft technical diagnostics. Sub-task: Electrical methods for the diagnostics of the technical condition of aircraft generator drive rotating elements]"*, Warsaw 1995, not published.
97. Gębura A., Kowalczyk A., Pisarska K.: *Protokół z badań konstruktorskich modelu pracującego urządzenia diagnostycznego DIA-KSA [Design test reports of a DIA-KSA diagnostic device working model]*, June 1994, not published.
98. Gębura A., Kurdelski M.: *Obciążenia układu transmisji śmigłowca Mi-24 i możliwości jego monitorowania metodą FAM-C [Mi-24 helicopter transmission system loads and its potential monitoring with the FAM-C method],* "Prace Naukowe ITWL", Vol. 33, Warsaw 2013.
99. Gębura A., Szymański M, Gajewski T.: *Report no. 47/43/2010 titled: "Realizacja pkt. 2, 3 i 4 harmonogramu projektu własnego nr N N509 360234 – Uniwersalizacja metody diagnozowania węzłów łożyskowych i elementów wirujących zespołów napędowych oparta na metodach modulacji częstotliwości FAM-C oraz FDM-A [Implementation of points 2, 3 and 4 of the original project schedule No. N N5509 360234 - Universalization of a diagnostic method for bearing nodes and propulsion unit rotating elements based on FAM-C and FDM-A frequency modulation methods]*, BT ITWL Vol. 5694/50, not published.
100. Gębura A., Markiewicz W.: *Onboard generators (alternators) as diagnostic sensors of turbine engines* (*Prądnice lotnicze jako czujniki diagnostyczne silników turbinowych*), Acta Mechanica et Automatica – Politechnika Białostocka, 2008.
101. Gębura A., Mroszkiewicz K.: *Metody FAM-C i FDM-A a zjawiska przesyłu radiowego sygnałów [FAM-C and FDM-A methods vs signal radio transmission phenomena]*, "Prace Naukowe ITWL" 2010, Vol. 27.
102. Gębura A., Pisarska K.: *Program badań konstruktorskich modelu pracującego urządzenia diagnostycznego DIA-KSA [Design test program for a DIA-KSA diagnostic device working model]*. May 1994, not published.
103. Gębura A.: *Possibilities of FAM-C method in diagnosing ship power plants*, "Polish Martime Reseach" 2003, No 2 (36), Vol. 10.
104. Gębura A., Prażmowski W., Kowalczyk A., Falkowski P., Głowacki T., Budzyński P., Pisarska K.: *Research report on: "Diagnostyka techniczna statków powietrznych.*

Zadanie cząstkowe: modelowanie matematyczne stanów dynamicznych układów napędowych prądnic lotniczych i zmian jakościowych energii elektrycznej" [Aircraft technical diagnostics. Sub-task: dynamic state mathematical modelling for aviation generator propulsion units and electricity quality changes], Warsaw, November 1996, not published.

105. Gębura A., Prażmowski W., Kowalczyk A., Falkowski P., Głowacki T., Budzyński P., Pisarska K.: *Research report on: "Określenie związków pomiędzy parametrami jakości energii prądnic pokładowych a stanem zużycia skrzyń napędowych" [Determination of the relationships between onboard generator energy quality parameters and the wear condition of gearboxes]*, Warsaw, June 1997, not published.
106. Gębura A.: *Pulsacje napięcia wyjściowego prądnicy pokładowej prądu stałego źródłem informacji diagnostycznej o stanie układu napędowego [Onboard DC generator output voltage pulsations as a source of diagnostic information on the condition of the power train]*. "Zagadnienia Eksploatacji Maszyn" 2003, Vol. 1 (133).
107. Gębura A., Radoń T., Tokarski T.: *Diagnozowanie zespołów napędowych na podstawie obserwacji zmian częstotliwości napięcia wyjściowego prądnic [Diagnosing power trains based on observing the changes in the frequency of generator output voltage]*. 2nd International Scientific and Technical Conference "Expo-Diesel & Gas Turbine'01", Gdańsk-Międzyzdroje-Copenhagen 2001.
108. Gębura A., Radoń T., Tokarski T.: *Cechy diagnostyczne parametrów napięcia wyjściowego lotniczych prądnic pokładowych prądu stałego [Diagnostic features of output voltage parameters in aviation onboard DC generators],* "Zeszyty Naukowe Politechniki Rzeszowskiej" Vol. 213, "Mechanika" V. 63, "Awionika", Vol. 2, Rzeszów 2004.
109. Gębura A., Radoń T.: *Pulsacje napięcia wyjściowego jako źródło informacji diagnostycznych o komutatorowych prądnicach prądu stałego [Output voltage pulsation as a source of diagnostic information on commutator DC generators]*. "Prace Naukowe ITWL" 2013, Vol. 33.
110. Gębura A., Radoń T.: *The diagnosis of onbard aviation generators* (pol. *Diagnozowanie pokładowych prądnic lotniczych*), Diagnostyka, nr 2/50, Olsztyn 2009.
111. Gębura A., Radoń T.: *The diagnosis of onboard generators (alternators),* "Polish Maritime Research" 2009, Vol. 16, Vol. 3(61).
112. Gębura A., Tokarski T.: *Badanie trwałości lotniczych urządzeń elektroenergetycznych. Badanie przetwornic lotniczych [Studying the durability of aviation power devices. Studying aviation converters]*, Warsaw 2000. AFIT report, not published.
113. Gębura A., Tokarski T.: *Zastosowanie metody FDM-A do oceny poślizgu łożysk tocznych i niewspółosiowości podpór łożyskowych [The application of FMD-A method for evaluating the spin of rolling bearings and misalignment of bearing supports]*. "Prace Naukowe Instytutu Technicznego Wojsk Lotniczych" 2007, Vol. 22.
114. Gębura A., Tokarski T., Szymański M., Kobylański A.: Research report No. 169/43/2009 *Weryfikacja metody diagnozowania podpór łożyskowych silników SO-3*

oraz SO-3W w oparciu o analizę sygnału wyjściowego prądnic pokładowych [Verification of a diagnostic method for SO-3 and SO-3W engine bearing supports based on onboard generator output signal analysis], Technology level IV – V, Warsaw 2009.
115. Gębura A., Tokarski T.: *Diagnosing of electro-mechanical converters by using a method of frequency modulation analysis* (*Diagnozowanie przetwornic elektromechanicznych metodą analizy modulacji częstotliwości*), „Journal of Polish CIMAC", vol. 7, No 2, Gdańsk 2012.
116. Gębura A., Tokarski T.: *Diagnosing the power plants on the basic of observaties of charges in alternator's output-voltage frequency*. III International Scientific-Technical Conference Expo-Diesel&Gas Turbine'03. May 5-9, 2003.
117. Gębura A., Tokarski T.: *Diagnozowanie elektromechanicznych przetwornic lotniczych [Diagnosing electromechanical aviation converters]* [in:] „Problemy badań i eksploatacji techniki lotniczej", Vol. 8, ed. J. Lewitowicz, L. Cwojdziński, M. Kowalski, R. Szczepanik, AFIT, Warsaw 2013.
118. Gębura A., Tokarski T.: *Fundamental laws of Rolling-Element Bearing Mechanics and Diagnostic Methods FAM-C and FDM-A,* "Solid State Phenomena" 2013, vol. 199, Trans Tech Publications LTD.
119. Gębura A., Tokarski T.: *Metody FDM-A i FAM-C w wykrywaniu i monitorowaniu silnie zaciśniętych łożysk tocznych [FDM-A and FAM-C methods in detecting and monitoring strongly clamped rolling bearings]*. "Prace Naukowe Instytutu Technicznego Wojsk Lotniczych" 2008, Vol. 23.
120. Gębura A., Tokarski T.: *Some Problems of a Diagnosis of Turbine Engine Bearings Using FAM-C Method,* "Solid State Phenomena" 2012, Trans Tech Publications LTD.
121. Gębura A., Tokarski T.: *The diagnostic of technical condition of turbine engine's bearing by means of method of alternator frequency modulation*. "Journal of Polish Cimac" Explo-Diesel&Gas Turbine'07, 2007.
122. Gębura A., Tokarski T.: *Monitorowanie węzłów łożyskowych o nadmiernych luzach podłużnyych metodami FAM-C i FDM-A* [Monitoring bearing units with excess longitudinal backlash with FAM-C and FDM-A methods], "Prace Naukowe Instytutu Technicznego Wojsk Lotniczych" 2010, Vol. 27
123. Gębura A., Tokarski T.: *Monitorowanie węzłów łożyskowych o nadmiernych luzach promieniowych metodami FAM-C i FDM-A [Monitoring bearing nodes with excessive radial clearances, using FAM-C and FDM-A methods]*, "Prace Naukowe ITWL" 2009, Vol. 25.
124. Gębura A., *Związki modulacji częstotliwości napięcia wyjściowego prądnicy z wybranymi wadami układu napędowego [Relationships between the generator output voltage frequency modulations and selected power train defects]* [in:] "Turbinowe silniki lotnicze w ujęciu problemowym", ed. M. Orkisz. Polskie Naukowo-Techniczne Towarzystwo Eksploatacyjne, Lublin 2000.
125. Gębura A.: *Biuletyn eksploatacyjny nr P/4567/E/02, dotyczy: diagnozowania sprzęgieł jednokierunkowych w przekładni KSA-2 oraz bloku hydraulicznego w agregacie GP21 za pomocą testera DIA-KSA-C wspomaganego systemem diagnostycznym DIA-KSA podczas eksploatacji samolotu MiG-29 [Operational bulletin No. P/3932/E/95, re: diagnosing single-way bearings in a KSA-2 transmission and a hydraulic block in*

a GPP-21 unit using a DIA-KSA-C tester supported by the DIA-KSA diagnostic system in the course of operating the MiG-29] DWLiOP/ITWL, Warsaw 2002.
126. Gębura A.: *Cechy diagnostyczne składowej pulsacji prądnic prądu stałego [Diagnostic features of DC generator pulsation component]*. "Prace Naukowe Instytutu Technicznego Wojsk Lotniczych" 2003, Vol. 16.
127. Gębura A.: *Diagnozowanie napędów lotniczych w oparciu o analizę parametrów źródeł energii elektrycznej [Diagnosing aviation propulsion systems based on the analysis of power source parameters]*. PhD thesis, AFIT, Warsaw 1998.
128. Gębura A.: *The FAM-C method in diagnosing aircraft and marine powerplants* (*Metoda FAM-C w diagnozowaniu lotniczych i okrętowych zespołów napędowych*), "Archives of Transport" 2004, No. 1, Vol. 16.
129. Gębura A.: *Metoda modulacji częstotliwości napięcia prądnic pokładowych w diagnozowaniu zespołów napędowych [Onboard generator voltage frequency modulation method in diagnosing propulsion units]*, Air Force Institute of Technology, Warsaw 2010.
130. Gębura A.: *Possibilities of FAM-C method in diagnosing ship powerplants (Możliwości metody FAM-C w diagnozowaniu siłowni okrętowych.* „Polish Maritime Research" 2003, No 2 (36), Vol. 10.
131. Gębura A.: *Przekoszenia połączeń wielowypustowych a modulacja częstotliwości prądnic [Skewing of splined connections and generator frequency modulation]*. "Zagadnienia Eksploatacji Maszyn" 1999, Vol. 4(120).
132. Gębura A.: *Method for detecting short-circuits in the rotor of a commutation DC generator.* Patent application PL200341 B1, application No 357584, Application date 6/12/2002, application announced 14/6/2004, BUP 12/04, patent grant announcement 31/12/2008 WUP 12/00.
133. Gębura A.: *Diagnostic properties of 3-phase alternator's frequency modulation parameters*, "Journal of Polish Cimac", Explo-Diesel&Gas Turbine'05, 2005.
134. Gębura A., Tokarski T.: *The diagnostic of technical condition of turbine engine's bearing by means of method of alternator frequency modulation*, "Journal of Polish Cimac", Explo-Diesel&Gas Turbine'07, 2007.
135. Gębura A.: *In the FAM-C method in the diagnosing of aircraft and power plants*, "The Archives of Transport" 2004, No 1.
136. Gębura A.: Research report No. 270/43/2008 *Opracowanie metody diagnozowania podpór łożyskowych silników SO-3 oraz SO-3W w oparciu o analizę sygnału wyjściowego prądnic pokładowych [Developing a diagnostic method for SO-3 and SO-3W engine bearing supports based on onboard generator output signal analysis]*, Technology level I – III, Warsaw 2008.
137. Girtler J.: *Statistic and probabilistic measures of diagnosis likelihood on the state of self-ignition combustion engines*. "Journal of POLISH CIMAC" 2007, Vol. 2, No 2.
138. Girtler J.: *Zastosowanie wiarygodności diagnozy do podejmowania decyzji w procesie eksploatacji urządzeń [Application of diagnostic reliability in decision-making within the equipment operation process]*. Materials of the Domestic Conference "Technical Diagnostics of Devices and Systems", DIAG'2003. WAT, PAN, Warsaw-Ustroń 2003.

139. Gozdecki A.: *Wpływ szybkości obtaczania przy sprawdzaniu kół walcowych na dokładność pomiaru współpracy obustronnej [Impact of reeling rate when checking cylindrical wheels in terms of bilateral interaction measurement accuracy]*. Uczelniana Lekcja Naukowa Młodych Pracowników. Poznań 1980.
140. Gozdecki A.: *Próba uzależnienia dokładności wykonania kół zębatych kontrolnych od chwilowych zmian promieni tocznych spowodowanych wybranymi błędami uzębienia kół badanych [Attempt at making the execution of pilot gear wheels independent from instantaneous changes in rolling radii due to selected tested wheel toothing errors]*. Doctoral dissertation, Poznań University of Technology, Faculty of Mechanical Engineering, Poznań 1982.
141. Gronczewski A.: *Simulation based study on the dynamics of wing-flap actuanting circuit,* „Solid State Phenomena" 2013, vol. 199, Trans Tech Publications LTD.
142. *Guidance Notes On Control Of Harmonics In Electrical*, American Bureau of Shipping, 2006.
143. Gutenbaum J.: *Problemy teorii regulatorów [Elements of the theory of regulators]*, WNT, Warsaw 1978.
144. *HCF S&T Program (1997 – 2002)*, Annual Report, htp://sinet.dtic.mil/
145. Health S., Imregum M.: *An improved single-parameter tip-timing method for turbomachinery blade vibration measurement using optical laser problems.* International Journal of Mechanical Science. Vol. 38, Issue 10, October 1996.
146. Heath S., Impregun M.: *A Survery of Blade Tip-Timing Measurement Techniques for Turbomachinery Vibration.* "Journal of Engineering Gas Turbine and Power", October 1998, Volume 120, Issue 4.
147. Heath S.: *A New Technique For Identifying Synchronous Resonances Using Tip-Timing*. "Journal of Engineering Gas Turbine and Power", April 2000, Vol. 122.
148. Hebda M., Janecki D.: *Tarcie, smarowanie i zużycie części maszyn [Friction, lubrication and wear of machinery parts]*. WNT, Warsaw 1972.
149. Hebda M., Janecki D., Pankiewicz B.: *Metoda oceny niezawodności tłokowych silników spalinowych na przykładzie badań eksploatacyjnych silników S-47 [Method for assessing the reliability of reciprocating internal combustion engines on the xample of S-47 engine operating tests]*, Materiały IV Krajowego Sympozjum Eksploatacji Urządzeń Technicznych, Vol. 5, Katowice 1977.
150. Herley C., Kovačevič, Ranchan K.: *Arbitry orfhogonaltilings of the time frequency plane*. Proceeding of the IEEE-SP. International Symposium. Victoria BC. Canada. October 4-6, 1992.
151. Hermans L., Van der Auweraer H.: *Modal Testing and Analysis of Structures under Operational Conditions*. "Mechanical System and Signal Processing" 1990, Vol. 13, No. 2.
152. Hibner C.: *Statystyczne badania dokładności kół zębatych [Gear wheel accuracy statistical tests]*. PhD thesis. Warsaw University of Technology, 1976.
153. Hill Ch.E.: *NSMS Data Acquisition Using an Alternative Multi-Point Approach.* Proc. Of 10thNationalTurbine Engine High Cycle Fatigue (HCF) Conference Dayton, USA 2005, htpp://www.hcf.utedayton.com.

154. Iwanow W.P.: *Kolebanija raboczich koles turbomaszin,* Maszinostrojenie, Moskwa 1983.
155. Izydorczyk J., Płonka G., Tyma G.: *Teoria sygnałów*, Wyd. Helion, 1999.
156. Jackson R.L., Green I.: *The Thermoelastic Behavior of Thrust Washer Bearings Considering Mixed Lubrication*, Asperity Contact, and Thermoviscous Effects. Tribology Transactions, 51: 2008.
157. Kaczorek T.: *Macierze w automatyce i elektrotechnice [Matrices in automation and electrical engineering]*. WNT, Warsaw 1984.
158. Kałek S.: *Smarowanie przekładni zębatych [Lubricating toothed gears]*. Domestic Training Conference on Operating Machinery and Equipment, POLTRIB′85.
159. Karasov M.F.: *Komutacja kolektornych maszin postojonnogo toka*, Gosudarstwiennoje Energeteciskoje Izdatielstwo, Moskwa 1961.
160. Karaś K.: *Analiza modalna – użyteczna metoda rozwiązywania problemów drganiowych [Modal analysis - useful method for solving vibration-related problems],* "Nowa Energia" 2012, Vol. 4(28), Kraków 2012.
161. Kartaschoff P.: *Częstotliwość i czas [Frequency and time]*, WKiŁ, Warsaw 1985.
162. Kasprzycki A., Sochacki W.: *Wybrane zagadnienia projektowania i eksploatacji maszyn i urządzeń [Selected issues related to the design and operation of machinery and equipment*, Częstochowa University of Technology, Częstochowa 2009.
163. Katner R., Enochson L.: *Analiza numeryczna szeregów czasowych [Time series numerical analysis]*, WNT Warsaw 1978.
164. Kayton M. Fried W.R.: *Elektroniczne układy nawigacji lotniczej [Electronic aviation navigation systems]*, WKŁ, Warsaw 1976.
165. Kirk R.G., Alseed A.A.: *Stability Analysis of a High-Speed Automotive Turbocharger*, "Tribology Transactions", 50:427-434, 2007.
166. Kisielewski P., Antal L.: *Kołysania turbogeneratora po wystąpieniu asymetrii w sieci elektroenergetycznej [Turbogenerator rocking upon asymmetry in a power grid],* "Prace Naukowe Instytutu Maszyn, Napędów i pomiarów Elektrycznych Politechniki Wrocławskiej", Vol. 62, Oficyna Wydawnicza Politechniki Wrocławskiej.
167. Kiwilsz M., Smulko J.: *Pitting corrosion characterization by electrochemical noise measurements on asymmetric electrodes.*
168. Klimaszewski S. et al.: *Analiza awarii urywania się wałków agregatu GP-21 na samolocie MiG-29 [Analysed failures of GP-21 generator shafts breaking-off onboard a MiG-29 aircraft]*" Warsaw 1994, not published.
169. Kocańda D., Mierzyńki J., Śnieżek L.: *Podstawy Konstrukcji Maszyn [Machine design basics]*. Wydawnictwo Przemysłowe WEMA, Warsaw 1989.
170. Korabliev A.I.: *Rabotosposobnost aviacjonnych zubcatych sojedinienii*, Moskva „Transport", 1983.
171. Kosowski K., Piwowarski M.: *Some results of experimental research into turbine rotor trajectory*. III International Scientific-Technical Conference Expo-Diesel&Gas Turbine'03. May 5-9, 2003.
172. Kostecki B.I.: *Trienie, iznos i smazka w masinach.* Kiev, Izdie. "Technika" 1970.
173. Kowalski M., Witoś M.: *Analiza porównawcza metody dyskretno-fazowej i modulacji częstotliwości [Comparative analysis of the discrete-phase method and frequency*

modulations], Conference "Diagnostic of Industrial Processes DPP'2001", Zielona Góra University of Technology, Zielona Góra 2001.
174. Kroszyński J.: *Współczesne urządzenia radiolokacyjne [Contemporary radar systems]*, Wydawnictwa Komunikacji i Łączności, Warsaw 1976.
175. Krysicki W., Włodarski L.: *Analiza matematyczna w zadaniach [Mathematical analysis in problems]*. PWN, Warsaw 1993.
176. Krzemiński-Freda H.: *Łożyska toczne [Rolling bearings]*. PWN, Warsaw 1985, ISBN 83-01-05532.-4
177. Krzystek R.: *Zintegrowany system bezpieczeństwa transportu, t.3 Koncepcja zintegrowanego systemu bezpieczeństwa transportu w Polsce [Integrated transport securit system. Vol. 3 Concept of an integrated transport security system in Poland]*, WKiŁ, Warsaw 2010.
178. Krzyż J., Ławrynowicz J.: *Elementy analizy zespolonej [Complex analysis elements]*. WNT, Warsaw 1981.
179. Lawrowski Z.: *Tribologia, tarcie, zużywanie i smarowanie [Tribology, friction, wear and lubrication]*, PWN, Warsaw 1993.
180. Leśniewski J.: *O objawach pewnych zjawisk dynamicznych zachodzących w obszarach styku rzeczywistego części maszyn [On the symptoms of dynamic phenomena ongoing in the actual interface areas of machinery parts]*. "Biuletyn WAT" 1984, Vol. 1(377).
181. Lewandowski W.M.: *Proekologiczne źródła energii odnawialnej [Eco-friendly renewable energy sources]*, WNT, Warsaw 2002.
182. Lewitowicz J.: *Badania produktów zużycia w systemach trybologicznych [Studying wear products in tribological systems]*. 11th Tribology Symposium; Vol. 1, 1982.
183. Lindstedt P.: *Aktywny pomiar pulsacji natężenia przepływu cieczy w instalacjach hydraulicznych za pomocą elementu korekcyjnego z możliwością zastosowania do badań diagnostycznych [Active measurement of liquid flow rate pulsations in hydraulic systems using a correction element with application to diagnostic testing]*. Kwart. Dod. Spec. AERO Technika Lotnicza Vol. 8. Warsaw 1990.
184. Lindstedt P.: *Analiza możliwości wykorzystania parametrów pracy zasobnika hydraulicznego, jako źródło informacji diagnostycznej samolotu [Analysing the potential application of hydraulic accumulator operating parameters as an aircraft diagnostic information source]*. "Informator ITWL", Warsaw 1988.
185. Lindstedt P.: *Element korekcyjny jako źródło informacji diagnostycznej [Correction element as a diagnostic information source]*. ZEM 1995, Vol. 2 (102).
186. Lindstedt P.: *Osobliwe elementy złożonych obiektów jako źródło informacji diagnostycznej [Singular elements in complex objects as sources of diagnostic information]*. "Informator ITWL", Warsaw 1997.
187. Lindstedt P.: *Methods for diagnosing hydraulic or pneumatic systems, and a diagnostic system for hydraulic and pneumatic systems*. Patent description PL 164942 b 1 1994
188. Lisiecki J.: *O metodzie magnetycznej pamięci materiału [Magnetic material memory method]*, "Prace Naukowe Instytutu Technicznego Wojsk Lotniczych" 2004, Vol. 18.

189. Łączkowski R.: *Ruchy chaotyczne dipolowego rotatora magnetycznego [Chaotic motion of a dipole magnetic rotator]*. "Przegląd Elektrotechniczny" 1993, Vol. 11.
190. Łucjanek W., Sibilski K.: *Wstęp do dynamiki lotu śmigłowca [Introduction to helicopter flight dynamics]*. ITWL, Warsaw 2007.
191. Maes S.: The *H-point theorem applied in signal processing.*Proceeding of the IEEE-SP International Symposium. Victoria BC. Canada. October 4 - 6, 1992.
192. Makusik S.: *Sprzęgła mechaniczne [Mechanical couplings]*. WNT, Warsaw 1979.
193. Malciev W.F.: *Rolikove mechanizmy svobodnego choda*. Maszinostrojenie, Moscow 1968.
194. Markiewicz W., Karpiński M., Gębura A., Prażmowski W.: *Protokół z kwalifikacyjnych badań laboratoryjnych lotniskowego urządzenia zasilania elektroenergetycznego samolotów LUZES-V [Laboratory qualification testing report covering a LUZES-V airfield power supply unit]*. Grudzień 1993, not published.
195. Maruszewska M., Sawicki J.: *Radiomechanika [Radiomechanics]*. Państwowe Wydawnictwo Szkolnictwa Zawodowego, Warsaw 1957.
196. Masłowski A.: *Identyfikacja modeli matematycznych dynamiki układów [Identifying mathematical models of system dynamics]*. Wydawnictwo Politechniki Białostockiej, 1995.
197. Mazanek E.: *Zagadnienia konstrukcyjne i wytrzymałościowe w wielkogabarytowych łożyskach tocznych wieńcowych [Design and strength issues in large-size slewing rolling bearings]*. Wydawnictwo Politechniki Częstochowskiej, Częstochowa 2005.
198. Meili Sun, Zhiming Hang, Xiaoyang Chen, Wen Wang, Kai Meng: *Experimental Study of Cavitation In an Oscillatory Oil Squeeze Film*. "Tribology Transactions", 51:2008.
199. Meisel J.: *Zasady elektromechanicznego przetwarzania energii [Principles of electromechanical energy processing]*. WNT, Warsaw 1970.
200. Mengali U., D'Andrea A.N.: *Synchronization techniques for digital receivers*, Plenum Press, New York 1997.
201. *Method of measuring torque transmitted by a rotating shaft*, US Patent No. 3817092, 1974.
202. *Torque meter on rotating shaft*, US Patent No. 3850030, 1974.
203. Mitew W.: *Maszyny elektryczne [Electrical machinery],* Vol. 1. Radom 2005.
204. Młynarczyk M., Szymański Z., Waśko S.: *Momentomierz quasi-fazowy [Quasi-phase torque meter]*. "Prace Instytutu Lotnictwa" 1983, Vol. 4, (95).
205. Moinaro F., Constanič F., Danjean A.: *Knocking recognition in engine vibration signal using the wavelet transform.* Proceedings of the IEEE-SP International Symposium. Victoria BC. Canada. October 4 - 6, 1992.
206. *Torque meter*, US Patent No. 3844168,1974.
207. Morel J.: *Drgania maszyn i diagnostyka ich stanu technicznego [Machine vibrations and their technical condition diagnostics]*. Polskie Towarzystwo Diagnostyki Technicznej, 1994.
208. Műller L.: *Diagnostyka przekładni zębatych [Toothed gear diagnostics]*. PWN, Warsaw 1992.

209. Műller L.: *Przekładnie zębate - dynamika [Toothed gears - dynamics]*. PWN, Warsaw 1986.
210. Műller L.: *Przekładnie zębate dużych mocy [High-powered toothed gears]*. PWN, Warsaw 1964.
211. Műller L.: *Zastosowanie analizy wymiarowej w badaniach modeli [Application of dimensional analysis in model studyies]*. PWN, Warsaw 1983.
212. Newman R.: *Properties of Materials Anisotropy, dynamometry, structure*, Oxford University Press, 2005.
213. EUROCADE ED-14B/RT CA DO-160B standard *Enviromental conditions and test procedures for airborne equipment*. Section 16. Power input. Alimentationelectrique.
214. Defence Standard NO-15-A200:2007 *Military aircraft. Onboard power supply systems.. Basic parameters, requirements and testing.*
215. Nowacki W.: *Teoria niesymetrycznej sprężystości [Theory of asymmetric elasticity*. PWN, Warsaw 1981.
216. Nowicki R.: *Stacjonarne systemy monitorowania i diagnozowania [Stationary monitoring and diagnostic systems]*. Materials of the 20th School of Diagnostics. Poznań-Zajączkowo 1992.
217. Nowicki R., Sordyl F.: *Wyznaczanie granic stanów eksploatacyjnych w badaniach diagnostycznych [Determining limit operation states in diagnostic studies]*. LDH Report No. 138. Poznań Universtity of Technology, 1984.
218. Ochęduszko K.: *Koła zębate [Gear wheels]*. WNT, Warsaw 1972.
219. Olchowski I.I.: *Mechanika teoretyczna [Theoretical mechanics]*. PWN, Warsaw 1978.
220. Oppenheim A.V., Wilsky A.S., Nawab S.H.: *Signals & Systems Prentice Hall.* New Jersey 1983.
221. Orkisz M., Polak Z.: *Identyfikacja toru lotu samolotu z wykorzystaniem metod sztucznej inteligencji [Aircraft flight trajectory identification using AI methods],* "Zeszyty Naukowe Politechniki Rzeszowskiej" 2004, Vol. 213.
222. Osiński Z.: *Teoria drgań [Vibration theory]*. PWN, Warsaw 1980.
223. Otnes R.K, Enochnson L.: *Analiza numeryczna szeregów czasowych [Time series numerical analysis]*. WNT, Warsaw 1978.
224. Owczarek J.: *Elektryczne maszynowe elementy automatyki [Electrical and machinery automation elements]*, WNT, Warsaw 1983.
225. Padfield G.D.: *Dynamika lotu śmigłowców. Teoria i wykorzystanie właściwości lotnych i modeli symulacyjnych* (org. ang. *Helicopter Flight Dynamic. The theory and Application of Flying Qualities and Simulation Modeling*), WKiŁ, Warsaw 1998.
226. Paduano J.D.: *Analysis of compressor system dynamics* [w:] "Active control of engine dynamics", VKI Lecture series, von Karman Institute for Fluid Dynamics, 2001.
227. Papolis A.: *Prawdopodobieństwo, zmienne losowe i procesy stochastyczne [Probability, radnom variables and stochastic processes]*. WNT, Warsaw 1972.
228. Pawłowski J.: *Wzmacniacze i generatory [Amplifiers and generators]*. WKiŁ, Warsaw 1975.
229. Pappenfus E.W., Warren B., Schoenke E.O.: *Technika jednowstęgowa [Single-band technique]*. WNT, Warsaw 1968.

230. Paszek St.: *Stany nieustalone maszyn elektrycznych prądu przemiennego [Transient states of AC electrical machines]*. WNT, Warsaw 1986.
231. Paśko M., Walczak J.: *Teoria sygnałów [Theory of signals]*. Wyd. Politechniki Śląskiej, Dział Telekomunikacja Vol. 16, Gliwice 1999.
232. Pawlak W.: *Usuwanie inercyjności pomiarowej z zapisu temperatury gazów wylotowych silnika odrzutowego w celu określenia niskocyklowego zmęczenia jego części gorącej [Removing measurement inertia from jet engine exhaust gas temperature records to determine low-cycle fatigue of its hot part]*, 3rd Domestic Conference "Technical Diagnostics of Devices and Systems", AFIT int. 330/95, Warsaw 1995.
233. Perry M.: *A Correlation approach to time-frequency representations.* Proceedings of the IEEE-SP International Symposium. Victoria BC. Canada. October 4 - 6, 1992.
234. Pintara J.: *O możliwości wykorzystania podsystemu diagnozowania wg stanu turbinowego zespołu napędowego w systemie eksploatacji statku powietrznego [On the potential application of a diagnostic subsystem according to the condition of a turbine propulsion unit within an aircraft operating system]*. [in:] "Turbinowe silniki lotnicze w ujęciu problemowym", ed. M. Orkisz, Polskie Naukowo-Techniczne Towarzystwo Eksploatacyjne, Lublin 2000.
235. Pizoń A.: *Elektrohydrauliczne analogowe i cyfrowe układy automatyki [Electrohydraulic analogue and digital automatic systems]*. WNT, Warsaw 1995.
236. pl.wikipedia.org/wiki/analiza modalna (08.11.2013).
237. pl.wikipedia.org/wiki/sterowanie okresowe (09.03.2014).
238. pl.wikipedia.org/wiki/wybieg_(technika) (10.03.2014).
239. pl.wikipedia.org/wiki/modacja koherentna (21.09.2013).
240. Plamitzer A.: *Maszyny elektryczne [Electrical machines]*. Warsaw 1986.
241. Podhajecki J., Młot A., Korkosz M.: *Comparison of displacement due to Maxwell for ces and magnetostriction in BLADC motor – static displacement.* "Prace Naukowe Instytutu Maszyn, Napędów i Pomiarów Elektrycznych Politechniki Wrocławskiej"*,* 2008, Vol. 62.
242. Polish Standard PN-ISO, April 1999. *Involute cylindrical splined connections aligned on tooth sides. Dimensions, tolerances and checking.*
243. Potapow W.N.: *Diagnostirovanie aviacjonnych elektriczeskich maszin*. "Transport", Moscow 1989.
244. Collective work: *Łożyska toczne [Rolling bearings]*. ed. "Delta Marketing", 2005.
245. Collective work: *Encyklopedia mechaniki [Encyclopaedia of mechanics]*, Warsaw 1994.
246. Proakis J.G.: *Digital communications*. McGraw-Hill, New York 2008.
247. Pronikov A.S.: *Nadieżnost maszyn.* "Maszinostrojenie", Moscow 1978.
248. Przysowa R., Dzięcioł E.: *Koncepcja wykorzystania czujnika mikrofalowego typu MUH do kontroli pracy podzespołów gorącej części silnika lotniczego [Application concept for a MUH microwave sensor to monitor the operation of aviation engine hot part subassemblies]*. "Prace Naukowe Instytutu Technicznego Wojsk Lotniczych" 2004, Vol. 18.

249. Przysowa R.: *Analiza sygnałów generowanych przez łopatki wirnikowych maszyn przepływowych [Analysing signals generated by the blades of rotor turbomachines]*. Opr. ITWL 2/34/2006, Warsaw 2006.
250. Puchała A.: *Dynamika maszyn i układów elektromechanicznych [Dynamics of machines and electromechanical systems]*. PWN, Warsaw 1977.
251. Radoń T., Gębura A.: *Uszkodzenia prądnic i styczników lotniczych w trudnych warunkach operacyjnych [Damage to onboard generators and contactors in harsh operating conditions.]*. "Prace Naukowe Instytutu Technicznego Wojsk Lotniczych" 2010, Vol. 30.
252. Rahman Md. Z., Ohba H., Yamamoto T., Yoshioka T.: *A Study on Incipient Damage Monitoring in Rolling Contact Fatigue Process Using Acoustic Emission*. "Tribology Transactions", 51: 2008.
253. Robinson W.W., Washburn R.S.: *A Real Time Non-Interference Stress Measurement System (NSMS) for Determining Aero Engine Blade Stress.* Instruments Society of America, paper 91-103, 1991.
254. Ryś J., Trojnacki A.: *Laboratorium Podstaw Konstrukcji Maszyn [Machine Design Basic Laboratory]*. Wyd. Politechniki Krakowskiej, Kraków 1994.
255. Rządkowski R., Kwapisz L., Drewczyński M., Szczepanik R., Przysowa R.: *Natural Frequencies of the Last Stage Turbine Bladed Disc of the Aircraft Engine*, 8th International Conference Airplanes and Helicopters Diagnostics, Airdiag'05, Warsaw, 27-28.10, Air Force Institute of Technology, Warsaw 2005.
256. *Self-calibrating torque meter on rotating shaft*, US Patent No. 3797305, 1974.
257. Schuster H.G.: *Chaos deterministyczny - wprowadzenie [Deterministic chaos - introduction]*. WNT, Warsaw 1993.
258. Shin Pan Seok and Cheung Hee Jun: *A Magnetostrictive Force and Vibration Mode Analysis of 3 kW BLDC Motor by a Magneto-Mechanical Coupling Formulation*, "Journal of Electrical Engineering & Technology" 2011, Vol. 6, No. 1.
259. Sidor T.: *Elektroniczne przetworniki pomiarowe [Electronic measuring transducers]*. Uczelniane Wydawnictwa Naukowo-Dydaktyczne, Kraków 2006.
260. Skalmierski B.: *Mechanika z wytrzymałości materiałów [Material strength mechanics]*. PWN, Warsaw 1983.
261. Skoć A., Spałek J., Makusik S.: *Podstawy konstrukcji maszyn. Zarys dynamiki i tribologii, elementy podatne, wały i osie maszynowe, łożyska ślizgowe i toczne, sprzęgła i hamulce [Machine design basics. Outline of dynamics and tribology, susceptible elements, machine shafts and axles, slide and rolling bearings, couplings and brakes]*. WNT, Warsaw.
262. Słuckij W.Z., Fizielson B.I.: *Impulsnaja tiechnika i osnowy radiolokacji.* Wojennoje Izdatielstvo Ministerstwa Oborony ZSRR, Moscow 1975.
263. Smulko J., Darowicki K., Zieliński A.: *Pitting corrosion in steel and electrochemical noise intensity*, Electrochemistry Communications 4(5).
264. Sobkowski J.: *Częstotliwościowa analiza sygnałów [Frequency analysis of signals]*. Wyd. MoD, Warsaw 1979.
265. Sowiński A.: *Cyfrowa technika pomiarowa [Digital measurement technology]*, WKiŁ, Warsaw 1976.

266. Spychała S., Majewski P., Szczekala M., Gębura A.: *Badania silnika 308 w hamowni WZL-3 [Studying a 308 engine at the WZL-3 engine test house]*. Warsaw 2006, unpublished.
267. Staniszewski R.: *Sterowanie zespołów napędowych [Controlling propulsion units]*. WKŁ, Warsaw 1980.
268. Styp-Reykowski M., Musiał J.: *Procesy zużywania towarzyszące tarciu tocznemu [Wear processes associated with rolling friction]*, "Problemy Eksploatacji" 2006, No. 3, Academy of Technology and Agriculture, Bydgoszcz.
269. Sung-HoonJedhg, Seok-Ju Yong: *Friction and wear characteristic due to stick-slip under fretting condition,* Tribology Transactions, 50:564-722, 2007.
270. Szabatin J.: *Podstawy teorii sygnałów [Fundamentals of the theory of signals]*. WKŁ, Warsaw 1982.
271. Szczebiakov A.A.: *Avtomatika aviacjonnych i rakietnych siłowych ustanovok.* "Maszinostrojenie", Moscow 1965.
272. Szczepanik R., Karbowiak H., Milewski R., Szczepankowski A., Szewczyk J., Zalewski J.: *Research report "Badanie zmian parametrów silnika typu SO-3 podczas próby obladzania [Studying changes in SO-3 engine parameters during an icing test]"*, lib. No. ITWL 12268/I, Warsaw 1998.
273. Szczepanik R., Kudelski R.: *System for signalling exceeded permissible vibration amplitude of turbomachine rotating blades*, patent number: 184530, application date: 13/11/1997. Szczepanik R., Kudelski R.: *Warunki techniczne na system sygnalizacji nadmiernych drgań łopatek pierwszego stopnia sprężarki silnika K-15 oraz system monitorowania widma drgań łopatek bezdotykową metodą dyskretno-fazową jako podsystem rejestratora parametrów pracy silnika S2-3a [Technical conditions for a system of excessive vibrations in K-15 engine compressor first stage baldes and a monitoring system for blade vibration spectrum with the contactless discrete-phase method as a subsystem of the S2-3a engine operating parameter recorder]*, lib. No. ITWL 11990/I, Warsaw 1997, not published.
274. Szczepanik R., Rządkowski R.: *Badania dynamiki łopatek wirnikowych silników lotniczych w różnych warunkach eksploatacji [Studying the dynamics of aviation engine rotor blades under various operating conditions*, Warsaw 2012.
275. Szczepanik R., Spychała J., Kowalski M., Dzięcioł E., Pawlak W., Przysowa R., Perz M.: *Analiza sygnałów generowanych przez łopatki wirnikowe wirnikowych maszyn przepływowych [Analysing signals generated by the blades of rotor turbomachines]*, lib. No. ITWL 2497/50, Warsaw 2006.
276. Szczepanik R., Szymczak J.: *Badanie przyczyny uszkodzenia łożyska środkowej podpory silnik typu SO-3 nr 37171219 [Studying the cause behind a SO-3 engine No. 37171219 central support bearing failure].* Warsaw 2000, not published.
277. Szczepanik R., Tomaszek H.: *Zarys metody oceny niezawodności i trwałości urządzeń lotniczych z uwzględnieniem stanów granicznych [Outline of a method for assessing the reliability and durability of aviation equipment, taking limit states into account]*. „Problemy Eksploatacji" 2005, Vol. 3.

278. Szczepanik R., Witoś M.: *Monitorowanie stanu technicznego turbinowych silników lotniczych w oparciu o metodę dyskretno-fazową i metodę portretów fazowych [Monitoring the technical condition of aviation turbine engines based on a discrete-phase method of phase portraits]*. "Prace Naukowe Instytutu Technicznego Wojsk Lotniczych" 2008, Vol. 10.
279. Szczepanik R., Witoś M., Kowalski M., Szczepankowski A.: *Method for changing the vibration frequency of a turbomachine rotating blade, an aviation turbine engine compressor rotating blade in particular*, patent No.: 189360, application date: 29/7/1998.
280. Szczepanik R., Witoś M., Szczepankowski A., Bekiesiński R.: *Sprawozdanie nr 3/34/94 z badania uszkodzenia łożyska środkowego pędni silnika SO-3W nr 48173105 [Report No. 3/34/94 on the investigation of a damage to the SO-3W engine No. 48173105 transission central gear]*, lib. No. ITWL 10943/I, Warsaw 1994, not published.
281. Szczepanik R.: *Research report "Badanie wrażliwości diagnostycznej dyskretno-fazowej, bezdotykowej metody pomiaru i analizy drgań łopatek w ocenie niewyważenia i stanu technicznego ułożyskowania jednowałowego TSO [Studying the diagnostic sensitivity of a discrete-phase, contactless method for measuring and analysing blade vibrations in assessing the unbalance and technical condition of TSO single-shaft bearing support]"*, lib. No. ITWL 11813/I, Warsaw 1999.
282. Szczepanik R.: *System diagnostyczny turbinowych silników odrzutowych SO-3, SO-3W [SO-3 and SO-3W turbine jet engine diagnostic system]*. *5th International Conference „Aircraft and helicopter diagnostic* Airdiag'97, 11-12 December 1997
283. Szelmanowski A., Michalak S., Sajda K., Gierałt J.: *Możliwości diagnozowania systemu automatycznego sterowania lotem SAU-22 na podstawie parametrów lotu [Diagnostic potential of a SAU-22 automatic flight control system based on flight parameters]*, "Zeszyty Naukowe Politechniki Rzeszowskiej" 2007, Mechanika, Vol. 71, Awionika.
284. Szelmanowski A., Michalak S., Sajda K.: *Metoda diagnozowania systemu automatycznego sterowania lotem na podstawie parametrów lotu [Diagnostic method for an automatic flight control system based on flight parameters]*, „Prace Naukowe Instytutu Technicznego Wojsk Lotniczych" 2006, Vol. 20.
285. Szklarski L., Jaracz K.: *Wybrane zagadnienia dynamiki napędów elektrycznych [Selected issues of electric drive dynamics]*. PWN, Warsaw 1986.
286. Szopliński Z.: *Badania i projektowanie układów regulacji [Testing and designing control systems]*. WNT, Warsaw 1975.
287. Tarczyński A., Qu D.: *Optimal random sampling for spectrum estimation in DASP applications*, Int. J. Appl. Math. Comput. Sci. 2005, Vol. 15, No 4.
288. Tertil Z.: *Ocena komutacji maszyn elektrycznych w warunkach przemysłowych [Assessing the commutation of electrical machines under industrial conditions],* "Przegląd Elektrotechniczny" 1982, Vol. 6.
289. Tertil Z.: *Ocena komutacji maszyn elektrycznych w warunkach przemysłowych [Assessing the commutation of electrical machines under industrial conditions]*. "Przegląd Elektrotechniczny" 1964, Vol. 2.

290. Tomaszek H., Żurek J., Jasztal M.: *Prognozowanie uszkodzeń zagrażających bezpieczeństwu lotów statków powietrznych [Forecasting damage endangering aircraft flight safety]*, Warsaw-Radom 2008.
291. Tony Ying, Uvon Tolbert, Paul Lewis, Ron Harrigal: *Micro-Adhesion in the Coining Process. Bluing on Proof Silver Coins: What It Is and How to Remove It.* "Tribology Transactions", 51:2008.
292. Topulus A., Iwanska J., Tabaczkiewicz E., Gontarz E.: *Mały ilustrowany leksykon techniczny [Small illustrated technical lexicon]*, WNT, Warsaw, 1982.
293. Trajos M., Monkiewicz W.: *Rozruch i zatrzymanie napędu elektrycznego zgodnie z zasadniczymi wymaganiami bezpieczeństwa [Start-up and shut-down of an electrical drive pursuant to essential safety requirements]*, "Zeszyty Problemowe – Maszyny Elektryczne" 2008, Vol. 79.
294. Tumański S.: *Technika pomiarowa [Measurement technique]*. WNT, Warsaw 2007.
295. *Device for measuring rotating shaft strain*. USA patent No. 3757580, 1973.
296. *Device for measuring torque with the phase shift method*. USA patent No. 3796093, 1974.
297. *Device for measuring torsional torque*. USA patent No. 3824848, 1974.
298. Wang W.: *Damage Detection of Gas Turbine Engine by Analysing Blade Tip Timing Data*. Proc. Of HUMS 2003. Conference DSTO, Australia 2003.
299. Wendeker M.: C*hwilowa prędkość kątowa i kąt skręcania wału korbowego jako sygnały diagnostyczne [Instantaneous angular velocity and torsional angle of a crankshaft as diagnostic signals]*. "Informator ITWL" Vol. 328/95; Materials of the 3rd Domestic Conference "Technical Diagnostics of Devices and Systems".
300. Witczak P.: *The Magnetostriction Forces in the Induction Motor*, COMPEL 1995, Vol. 14, No. 4.
301. Witoś M., Kowalski M.: *Aspekty metrologiczne bezdotykowego diagnozowania wirujących łopatek sprężarki [Metrological aspects of contactless diagnosis of rotating compressor blades]*. "Biuletyn WAT" 2008, Vol. LVII, No. 2.
302. Witoś M.: *Weryfikacja metod analizy danych z nierównomiernego próbkowania – rozpoznanie literaturowe [Verification of a method for analysing data from non-uniform sampling - literature review]*. AFIT report, Warsaw 2010, (not published).
303. Witoś M.: *Zwiększenie żywotności silników turbinowych poprzez aktywne diagnozowanie i sterowanie [Increasing the service life of turbine engines through active diagnosis and control]*. "Prace Naukowe Instytutu Technicznego Wojsk Lotniczych" 2011, Vol. 29.
304. Wojnar A, Zdzieborski T.: *Analiza błędów anomalnych w cyfrowych pomiarach częstotliwości [Analysing abnormal errors in digital frequency measurements]*. "Biuletyn WAT" 1974, Vol. 2(258).
305. Wojnar A.: *Statystyczna analiza przejść przez zero w teorii sygnałów [Statistical analysis of zero-crossing in the theory of signals]*. "Prace Instytutu Tele- i Radiotechnicznego" 1965, vol. 9 No. 3.
306. Wojnar A.: *Teoria sygnałów [Theory of signals]*. WNT, Warsaw 1988.

307. Woliński W.: *Analiza dokładności kinematycznej zazębienia walcowego dla modelu współpracy jednostronnej [Analysing kinematic accuracy of cylindrical meshing for a unilateral cooperation model]*. PhD thesis. Poznań 1989.
308. Wróbel T.: *Określenie liczby zębów stojana prądnicy induktorowej typu Lorentza - Schmidta [Determining the number of Lorentz-Schmidt inductor generator stator teeth]*. "Biuletyn WAT" 1971, Vol. 4(224).
309. Wróbel T.: *Prądnice zwiększonej częstotliwości [Increased-frequency generators]*. Wyd. MoD, 1972.
310. Wróbel T.: *Studium teoretyczne i eksperymentalne zagadnienia pulsacji napięcia prądnic tachometrycznych prądu stałego [Theoretical and experimental study of DC tach generator voltage pulsations*. Appendix to "Biuletyn WAT" 1974, Vol. 3(259).
311. Wróbel T.: *Studium zagadnienia pulsacji napięcia prądnic tachometrycznych o wyjściu stałoprądowym [Study of DC output tach generator voltage pulsations]*. Appendix to "Biuletyn WAT" 1977, Vol. 6(298).
312. WSK Rzeszów: *Opis silnika SO-3 [Description of a SO-3 engine]*. 2nd edition, Rzeszów 1977.
313. Zieja M.: *Analiza możliwości synchronizacji sygnałów z metod FAM-C i FDM-A – utworzenie podstaw matematycznych modelu [Analysing the potential synchronization of FAM-C and FDM-A signals - creating mathematical fundamentals of the model]* [in:] Research report No. 250/43/2008 entitled *"Realizacja pkt. 1 harmonogramu projektu badawczego własnego nr N NN509 360234 – Uniwersalizacja metody diagnozowania węzłów łożyskowych i elementów wirujących zespołów napędowych oparta na metodach modulacji częstotliwości FAM-C oraz FDM-A[Implementation of points 2, 3 and 4 of the original research project schedule No. N N5509 360234 - Universalization of a diagnostic method for bearing nodes and propulsion unit rotating elements based on FAM-C and FDM-A frequency modulation methods*], Warsaw 2008, 4426/50.
314. Zwierzchowski S.: *Kryteria i metody wyboru parametrów dynamicznych układów mechanicznych z uwzględnieniem węzłów kinematycznych [Criteria and methods for selecting mechanical system dynamic parameters, taking kinematic nodes into account]*. Habilitation dissertation.
315. Żic M.Z.: *Pieriechodnyje processy w maszynach postajannogo toka.* "Energia", Moscow 1974.
316. Żurek J. et al.: *Żywotność śmigłowców [Helicopter service life]*. Warsaw 2006.
317. Żurek Z.H.: *Badania stanu ferromagnetycznych elementów maszyn w polu magnetycznym [Studying the condition of ferromagnetic machinery elements in a magnetic field]*. "Zeszyty Naukowe Politechniki Śląskiej" 2005, Vol. 1678.

LIST OF FIGURES

Fig. 1.1. Algorithm to maintain the airworthiness of ageing AC 27
Fig. 1.2. AASP methodology structural diagram 29
Fig. 1.3. Algorithm for monitoring the airworthiness of AC structures 33
Fig. 1.4. Block diagram of a "transmitting station" used in the circulation of diagnostic information on the technical condition of a mechanical propulsion unit under FAM-C and FDM-A methods....38
Fig. 1.5. Block diagram showing the circulation of diagnostic information on the technical condition of a mechanical propulsion unit using the vibroacoustic method....39
Fig. 1.6. Reluctance sensor (CRL) in a turbine engine compressor blade grid unit as a singular element for monitoring primary diagnostic signals (individual kinematic pairs) of a mechanical propulsion unit....41
Fig. 1.7. Generator-transducer as a singular element for monitoring primary diagnostic signals (individual kinematic pairs) of a mechanical propulsion unit....42
Fig. 1.8. Compared geometry of electrical generator rotor teeth with a turbine engine compressor blade grid 42
Fig. 1.9. Compared geometry of electrical generator stator pole pieces with a turbine engine compressor body 43
Fig. 1.10. FAM-C method compared to other diagnostic methods in terms of monitoring the technical condition of a MiG-29 aircraft propulsion unit – overview 45
Fig. 2.1. Testing of the LUZES-V unit with the GTD-350 turbine engine after step-down of the current load 52
Fig. 2.2. Alternating current generator (alternator) with three pole pairs....54
Fig. 2.3. AC generator output voltage waveform with three pairs of poles at constant angular velocity without modulation 55
Fig. 2.4. Impact of a mechanical defect of the tested propulsion unit on generator-transducer voltage modulation....57
Fig. 2.5. Theoretical generator-transducer voltage modulations reflected in the waveform of time increments between successive voltage waveform zero-level crossings 58
Fig. 2.6. Theoretical generator-transducer voltage modulations reflected in the instantaneous frequency change waveform....58
Fig. 2.7. Theoretical instantaneous rotational speed changes reflected in the generator-transducer instantaneous frequency waveform 59
Fig. 2.8. Method of creating characteristic points....59
Fig. 2.9. Characteristic sets in a 3D space (f_p, n, ΔF) for typical aircraft propulsion unit failures – diagram showing characteristic set heights....62

Fig. 2.10. Example of an actual instantaneous frequency waveform – waveform from a D-10/2 tach generator in a three-phase configuration from an SO-3W engine, at main shaft speed n = 15 100 rpm 63
Fig. 2.11. Example of actual narrow-band characteristic sets obtained from a D-10/2 tach generator in a three-phase configuration from an SO 3W engine, at main shaft speed n = 15 600 rpm 64
Fig. 2.12. Rotor with four slots and a graph of electromotive force variations between commutator brushes of a DC generator 72
Fig. 2.13. Pulsation voltage component changes in the GSR-ST-1200WT commutator DC generator at minimum load (I≈1A) 77
Fig. 2.14. Pulsation voltage component changes in the GSR-ST-1200WT commutator DC generator at rated load (I≈300 A) 77
Fig. 2.15. Pulsation voltage component changes in the GSR-ST-1200WT commutator DC generator at rotor winding short-circuit 78
Fig. 2.16. Pulsation component waveform for a commutator DC generator 78
Fig. 2.17. Initial diagnostic signal lines – speed fluctuations of individual (two) kinematic pairs of the monitored propulsion unit 86
Fig. 2.18. Relationships between the main line of the carrier "wave" generated by a generator-transducer (f_{NG}) and the subcarrier frequencies of individual kinematic pairs in the propulsion unit under study 86
Fig. 2.19. Images after FAM-C or FDM-A detection 87
Fig. 2.20. Relationships between the main line of the carrier "wave" generated by a three-phase generator-transducer (f_{N3G}) and the subcarrier frequencies of individual kinematic pairs in the propulsion unit under study – basic characteristic set group 88
Fig. 2.21. Relationships between the main line of the carrier "wave" generated by a three-phase generator-transducer (f_{N3G}) and the subcarrier frequencies of individual kinematic pairs in the propulsion unit under study – full (extended) characteristic set group 89
Fig. 2.22. Images after detection of the three-phase FAM-C measurement 89
Fig. 2.23. Time base generator frequency tuning node for the imaging acquisition system (ΔF,f_p) – design – signal flow block diagram 91
Fig. 2.24. Block diagram of a faulty kinematic pair as an angular velocity modulator 93
Fig. 2.25. Generator-transducer relative to input-output signals 94
Fig. 3.1. Two shafts with an eccentricity defect connected by an "S" claw coupling 98
Fig. 3.2. Diagram of a splined connection between two shafts with an eccentricity defect, cross-section 98
Fig. 3.3. Phase diagram of a splined connection between two shafts with an eccentricity defect, cross-section 99
Fig. 3.4. Excessive wear of a gear wheel with an eccentricity defect 99
Fig. 3.5. Theoretical instantaneous angular velocity variations at an eccentric clearance connection 100

Fig. 3.6. Cross-section of the shaft-drive sleeve connection at an eccentric keyed connection with backlash 100
Fig. 3.7. Theoretical instantaneous frequency waveform for a kinematic pair exhibiting an eccentricity defect with backlash 103
Fig. 3.8. Example of an actual instantaneous frequency waveform for a kinematic pair exhibiting an eccentricity defect with backlash 103
Fig. 3.9. Theoretical pie chart (in polar coordinates) of the instantaneous frequency waveform for a pair of gears with backlash 104
Fig. 3.10. Longitudinal section of the generator shaft connection in the drive sleeve when the connection is skewed by angle β 107
Fig. 3.11. Axiomatic view of the connection between the generator shaft and the drive sleeve with a skewed angle 108
Fig. 3.12. Pie chart showing instantaneous angular velocity changes for a connection between shafts with skew 110
Fig. 3.13. Splined shaft of the SGO-8 AC generator after 800 h of operation on the LUZES-II laboratory propulsion bench with a skew of $\beta = 1.5^{o}$ 110
Fig. 3.14. Pie chart of the initial angular velocity in the case of combined connection skew and eccentricity 113
Fig. 3.15. Longitudinal section of a splined connection (generator shaft) with a drive sleeve exhibiting eccentricity and skew defects 113
Fig. 3.16. Splined shaft of a GT-40PCz6 AC generator under long-term operation with skew and eccentric displacement 114
Fig. 3.17. Displacement of two flat plates on a rolling shaft relative to each other 117
Fig. 3.18. Movement of the bearing cage relative to the inner race 118
Fig. 3.19. Variation of the rolling coefficient rating p_{sN} as a function of changes to the rolling element diameter d_k for a given inner race diameter D_w 119
Fig. 3.20. Applying the inspection mark to the inner ring and the cage of an aircraft generator rolling bearing 120
Fig. 3.21. Movement of characteristic sets at different rolling element rolling coefficient average values 122
Fig. 3.22. Kinematic overview diagram for negative misalignment of shaft supports 123
Fig. 3.23. Changes in the rolling coefficient of the SO-3 engine central bearing with a local minimum indicating misalignment 124
Fig. 3.24. Cross-section of an SO-3 type single-flow, single-shaft engine with control rollers prepared for mechanical measurement of bearing seat concentricity 125
Fig. 3.24a. Three bearing seats with the centres of symmetry marked according to the typical measurements conducted by a repair shop, but with skew bearing seat 3 forming a cylindrical surface 125
Fig. 3.24b. Three bearing seats with the centres of symmetry marked according to the typical measurements conducted by a repair shop, without skew 126

Fig. 3.25. Cooperation of a bearing at normal rolling of rolling elements between races – rolling elements drag the bearing cage with their perimeter 127
Fig. 3.26. Cooperation of rolling bearing elements after cage drops down – the cage achieves increased speed and drives rolling elements through secondary impact 127
Fig. 3.27. Rolling coefficient changes (as a function of speed) in the central bearing of an SO-3 engine with a local maximum indicating cage dropping on the inner race 128
Fig. 3.28. Rolling coefficient changes (as a function of speed) in the central bearing of a correctly operating SO-3 engine 128
Fig. 3.29. Central bearing inner race 129
Fig. 3.30. Central bearing cage – oblique view – with traces of rubbing against the journal 130
Fig. 3.31. Central bearing cage – vertical projection – with traces of rubbing against the bearing inner race orifice 130
Fig. 3.32. Central bearing cage – close-up 131
Fig. 3.33. Characteristic sets for resonant bearings 135
Fig. 3.34. "False Brinell imprints" (marked by arrows) on the race of a bearing under prolonged resonance 136
Fig. 3.35. Characterized height of characteristic sets of a correctly seated rolling bearing as a function of shaft rated speed 136
Fig. 3.36. Characterized rolling coefficient of a correctly seated rolling bearing as a function of shaft rated speed 137
Fig. 3.37. Characteristic set height of a rolling bearing seated on a journal with excessive pressure as a function of shaft speed 138
Fig. 3.38. Rolling coefficient characteristic of a rolling bearing seated on a journal with excessive pressure as a function of shaft speed 138
Fig. 3.39. Rolling element of a bearing with excessive clamp and traces of "milling" and surface rippling caused by excessive thermal energy release 141
Fig. 3.40. Characteristic sets of turbine engine No. 15 prior to long-term shutdowns 142
Fig. 3.41. Characteristic sets of turbine engine No. 215 after a 7-month shutdown without maintenance 142
Fig. 3.42. Softened bearing journal 143
Fig. 3.43. Cracked sleeve fixing the rolling bearing outer race to the turbine engine body 143
Fig. 3.44. First sub-harmonic characteristic set height after the fracture of the sleeve fixing the rolling bearing inner race to the turbine engine body 144
Fig. 3.45. Changes in the first harmonic characteristic set heights after the fracture of the sleeve fixing the rolling bearing inner race to the turbine engine body 145
Fig. 3.46. Cage-separator from a worn-out one-way coupling 146

Fig. 3.47. One-way coupling – overview diagram 147
Fig. 3.48. Set of characteristic points for a KSA-2 gearbox with a worn-out one-way coupling 148
Fig. 3.49. Images related to hydronic system air-blockage 149
Fig. 3.50. Instantaneous frequency waveform $f_i = f(t)$ of the three-phase FAM-C measuring channel for a turbojet engine, the bearing of which had five separating elements broken out 150
Fig. 3.51. Rolling bearing with a burst cage and broken out five separating elements 151
Fig. 3.52. The waveform $f_i = f(t)$ of the AC measuring channel in the case of excessive meshing backlash in a gear wheel pair of a worn-out gearbox of a Mi-24 helicopter generator 152
Fig. 3.53. Damaged gear wheel in the gearbox of a Mi-24 helicopter 153
Fig. 3.54. Examples of changes in the rupture angle of the fit (interference fit) between a journal and a rolling bearing inner ring 154
Fig. 3.55. Sample frequencies of ruptured fit (interference fit) between a journal and a rolling bearing inner ring 155
Fig. 3.56. Instantaneous frequency change waveform $f_i = f(t)$ for a DC generator pulsation example 155
Fig. 3.57. Single-shaft turbo-jet engine bearing journal after prolonged key fit between a rolling bearing inner ring and a journal 156
Fig. 4.1. Block diagram of the FAM-C and FDM-A method metrological structure 159
Fig. 4.2. Changes in the characteristic parameters of the generator output voltage frequency modulation depending on the frequency and phase relationship between the mechanical fluctuation waveform frequency and the given generator-transducer rated frequency 165
Fig. 4.3. Diagram of a bench mimicking the mechanical propulsion unit angular velocity modulation phenomena and its reflection in the FAM-C representation of an AC onboard DC generator voltage frequency modulation, enabling diagnostic system calibration 168
Fig. 4.4. Determination of the amplitude error and phase errors for a sawtooth modulating wave-form – overview drawing of single-phase, half-periodic primary sampling $k_r = 20$ 169
Fig. 4.5. Relative changes in the amplitude error for a sawtooth waveform as a function of changes in the k_r multiplication factor 169
Fig. 4.6. Relative changes in the phase error for a sawtooth waveform as a function of changes in the k_r multiplication factor 169
Fig. 4.7. Three-phase waveform and the method of counting time between zero-level crossings 171
Fig. 4.8. A three-piece signal conditioning system 174
Fig. 4.9. Determination of the amplitude error and phase errors for a rectangular modulating waveform with a 50% infill ratio – overview of single-phase, half-periodic primary sampling $k_r = 27$ 175

Fig. 4.10. Universal general block diagram of sub-assemblies housed in a measuring computer adapted to the FAM-C and FDM-A methods, showing the tested sub-assemblies for a bi-polar zero-crossing counting system 176
Fig. 4.11. Instantaneous frequency waveform for frequency modulations in the form of a rectangular waveform during a performance check of the FDM-A system under laboratory conditions 177
Fig. 4.12. Block diagram of transmission shaft torsion angle measurement using voltage frequency modulation of two different generators....180
Fig. 4.13. Voltage waveforms from two different generators employed to measure the shaft torsion angle....180
Fig. 4.14. Method of counting zero-level crossings for a three-phase AC generator....181
Fig. 4.15. Method of counting zero-level crossings for a commutator DC generator....181
Fig. 4.16. Interaction between a waveform with high frequency interference 184
Fig. 4.17. Quadrature modulation system in the FAM-C method....190
Fig. 5.1. Manner of connecting the DIA-KSA-CM diagnostic tester to a MiG-29 aircraft....197
Fig. 5.2. Operation of the DIA-KSA-CM diagnostic tester during a test at an airfield....198
Fig. 5.3. SD-KSA diagnostic system....199
Fig. 5.4. Sample view of the edition window for all measurements previously conducted with the DIA-KSA-CM on an AC with determined exceeded values in individual zones....200
Fig. 5.5. Example of a one-way coupling wear chart in a squadron database....201
Fig. 5.6. Block diagram of a field tester for short-term diagnosis of SO-3/3W engine bearing supports – mechanical wear process type recognition function – part 1. Identification of an excessive radial clearance model 203
Fig. 5.7. Block diagram of a field tester for short-term diagnosis of SO-3/3W engine bearing supports – mechanical wear process type recognition function – part 2. Identification of an increased longitudinal clearance model....204
Fig. 5.8. Block diagram of a field tester for short-term diagnosis of SO-3/3W engine bearing supports – mechanical wear process type recognition function – part. 3. Identification of an increased bearing support passive resistance model....205
Fig. 5.9. Block diagram of a field tester for short-term diagnosis of SO-3/3W engine bearing supports – mechanical wear process type recognition function – part. 4. Identification of a reduced bearing support radial clearance model....206
Fig. 5.10. Logic structure block diagram of a field tester for short-term diagnosis of SO-3/3W engine bearing supports – part 1. Formation of characteristic sets and time waveforms....211

Fig. 5.11. Logic structure block diagram of a field tester for short-term diagnosis of SO-3/3W engine bearing supports – part 2. Wear model type determination 212
Fig. 5.12. Logic structure block diagram of a field tester for short-term diagnosis of SO-3/3W engine bearing supports – part 3. Drawing up a diagnostic prediction 213
Fig. 5.13. TS-11 Iskra aircraft with a connected DIA-SO3 diagnostic tester 214
Fig. 5.14. Mi-24 No. 65 left engine instantaneous frequency change waveform – positive standard 215
Fig. 5.15. Mi-24 No. 84 left engine instantaneous frequency change waveform – measurement No. 3 – positive standard 216
Fig. 5.16. Mi-24 No. 65 right engine instantaneous frequency change waveform – positive standard 216
Fig. 5.17. Mi-24 No. 84 right engine instantaneous frequency change waveform – negative standard 217
Fig. 5.18. Inner ring of the upper (main) bearing from the negative standard WR-24 main transmission gear 217
Fig. 5.19. Bearing seat of the negative standard WR-24 main transmission gear upper bearing 218
Fig. 5.20. Schematic diagram of the generator gearbox 219
Fig. 5.21. GT-40PCz6 generator drive shaft spline measurements 220
Fig. 5.22. Right generator spline wear polar diagram 221
Fig. 5.23. Transmission element arrangement between the engine and the generator in a Mi-24 helicopter 222
Fig. 5.24. Mi-24 helicopter with a transmission system discontinued due to internal damage in the generator gearbox 223
Fig. 5.25. Instantaneous frequency waveform obtained from a single-phase FAM-C measurement of the SGS-40PU generator from Mi-17 helicopter No. 2 – 60 s time window, beating-related slow-variable component visible 227
Fig. 5.26. Instantaneous frequency waveform obtained from a three-phase FAM-C measurement of the SGS-40PU generator from Mi-17 helicopter No. 2 – 60 s time window, two spike pulse visible 227
Fig. 5.27. Instantaneous frequency waveform obtained from a three-phase FAM-C measurement of the SGS-40PU generator from Mi-17 helicopter No. 2 – 0.01 s time window, one increased spike pulse visible 228
Fig. 5.28. Instantaneous frequency waveform obtained from a three-phase FAM-C measurement of the SGS-40PU generator from Mi-17 helicopter No. 2 – 1 s time window 228
Fig. 5.29. Instantaneous frequency waveform obtained from a three-phase FAM-C measurement of the SGS-40PU generator from Mi-17 helicopter No. 2 – 0.1 s time window, waveform between two spike pulses 229

Fig. 5.30. Instantaneous frequency waveform obtained from a three-phase FAM-C measurement of the SGS-40PU generator from Mi-17 helicopter No. 2 – 0.1 s time window, in the period with no spike pulses 229
Fig. 5.31. Instantaneous frequency waveform obtained from a three-phase FAM-C measurement of the SGS-40PU generator from Mi-17 helicopter No. 1 – 0.1 s time window, visible undercuts on the trailing edge proving circumferential backlash 230
Fig. 5.32. Instantaneous frequency waveform obtained from a three-phase FAM-C measurement of the SGS-40PU generator from Mi-17 No. 1 helicopter – 0.1 s time window; sine wave-form visible, uniform and stable over time 230
Fig. 5.33. Simplified overview drawing of a compression-ignition engine 232
Fig. 5.34. Block diagram of a ship propulsion unit powered by two compression-ignition engines 233
Fig. 5.35. Pomerania ferry main propulsion unit instantaneous frequency change waveform – three-phase measurement....234
Fig. 5.36. Pomerania ferry main propulsion unit instantaneous frequency change waveform – three-phase measurement – close-up 234
Fig. 5.37. Backup power generator instantaneous frequency change waveform 235
Fig. 5.38. Simplified assembly drawing of an electromechanical transducer adapted at AFIT to enable controlled application of assembly errors....237
Fig. 5.39. Average rotational speed change waveform after isolating the energy source, with marked rated speed bands....242
Fig. 5.40. Local resonance phenomena observed for the rotational speed after deactivating the energy source....244
Fig. 6.1. Characteristic set height (for seven rated engine speeds) of the central bearing in engine No. 215 during a post-overhaul FDM-A test....249
Fig. 6.2. Characteristic set height (for seven rated engine speeds) of the central bearing in engine No. 215 during the FDM-A test after 30 h of operation (post-overhaul)....249
Fig. 6.3. Overheating traces inside the turbojet engine central support rolling bearing journal 251
Fig. 6.4. Roller bearing after operation in an environment with increased filling content in the lubrication system....252
Fig. 6.5. Changes in the central and rear rolling bearing DC characteristic sets during controlled seizing of a turbojet engine....253
Fig. 6.6. Characteristic set height for a rolling bearing seated on a journal with excessive pressure as a function of the main shaft speed....254
Fig. 6.7. Rolling coefficient characteristic for a rolling bearing seated with excessive pressure....254
Fig. 6.8. Compared diversity of rolling element surfaces 255
Fig. 6.9. Characteristic set of a rolling bearing with resonance 256

Fig. 6.10. Waveform $f_i = f(t)$ – FAM-C method – visible fast-variable quasi-sinusoidal component with multiple undercuts, amplitude-modulated by a slow-variable component 259
Fig. 6.11. "Resonant" shape of the AC channel characteristic set height envelope (FAM-C method) for a central bearing with increased longitudinal clearance 259
Fig. 6.12. Waveform $f_i = f(t)$ – visible slow-variable component (envelope) with significant amplitude modulation (p30%)....260
Fig. 6.13. SO-3 engine No. 22 central support rolling bearing cover with traces of mechanical impact 260
Fig. 6.14. Drive shaft of the GSR-ST-6000A generator in the SO-3 engine with barrel-shaped decrements on the spline tooth contact plane, characteristic of skew....261
Fig. 6.15. Interior of the SO-3 engine turbine shaft with a defect involving increased central support longitudinal clearance 261
Fig. 6.16. Rolling bearing DC characteristic set height change waveform as a function of operating time $\Delta F_{max} = f(\Theta)$ 265
Fig. 6.17. Rolling bearing DC characteristic set quality factor Q change waveform as a function of operating time $\Delta F_{max} = f(\Theta)$ 266

LIST OF TABLES

Table 1. Minimum number of generator-transducer pole pairs required to detect meshing backlash with a given backlash measurement resolution 81
Table 2. Dressing angle for selected aircraft bearing sizes 120
Table 3. Fade pulses for the SO/SO-3W engine obtained from the circuit of the GSR-ST-6000WT onboard DC generator 154
Table 4. Preset parameters (on a function generator) of instantaneous frequency sawtooth waveforms $f_i = f(t)$ 167
Table 5. Values of the FSK frequency modulation rectangular wave, set on the function generator to simulate the DC generator pulsation component frequency modulation changes caused by SO3/3W engine rotor supports at 1/10 of the process frequency for n = 7000 rpm and 15 600 rpm – preset values 176
Table 6. D-10/2 tach generator frequency parameter measurement 186
Table 7. D-10/2 tach generator output voltage measurements, tests No. 54, 69 and 88 187
Table 8. D-10/2 tach generator output voltage measurements, tests No. 52, 86 and 87 188
Table 9. Selected parameter values for chosen sub-assemblies of the Polonia ferry 236
Table 10. Selected design data of the Polonia ferry 236
Table 11. Polonia ferry coupling defect parameter values 236
Table 12. Summarized parameters of selected generator assembly failures and the parameters of their representations in electrical phenomena 240
Table 13. List of limit parameters for selected types of electromechanical aviation generators for the FAM-C methods 241
Table 14. Quality factor and operating time for a TS-11 Iskra SO-3 engine 267